EFFECT OF MICROSTRUCTURE ON HIGH-TEMPERATURE MECHANICAL BEHAVIOR OF NICKEL-BASE SUPERALLOYS FOR TURBINE DISC APPLICATIONS

A Dissertation
Presented to
The Academic Faculty

By

Heather Joan Sharpe

In Partial Fulfillment
Of the Requirements for the Degree
Doctor of Philosophy in Materials Science and Engineering

Georgia Institute of Technology

August, 2007

EFFECT OF MICROSTRUCTURE ON HIGH-TEMPERATURE MECHANICAL BEHAVIOR OF NICKEL-BASE SUPERALLOYS FOR TURBINE DISC APPLICATIONS

Approved by:

Dr. Ashok Saxena, Advisor
Adjunct Reagents' Professor
School of Materials Science and Engineering
Georgia Institute of Technology
Dean of Engineering
University of Arkansas

Dr. Naresh Thadhani
School of Materials Science and Engineering
Georgia Institute of Technology

Dr. Randy Helmink
Technology Department
Rolls-Royce Corporation

Dr. Arun Gokhale
School of Materials Science and Engineering
Georgia Institute of Technology

Dr. Richard Neu
School of Mechanical Engineering
Georgia Institute of Technology

Date Approved: June 18th, 2007

To Dr. Momm for going down
this path before me and to Graeme
for holding my hand as I took my turn

ACKNOWLEDGMENTS

Earning a doctoral degree is not an easy task; doing so when student, advisor, and campus are all in different states is especially difficult. This work would never have been accomplished without the considerable contributions of many people across the country. With sincere appreciation, I would like to acknowledge those who aided me along the way, beginning with Professor Ashok Saxena. His professionalism and dedication to his work and students are inspirational. I would like to thank Naresh Thadhani, Arun Gokhale, and Rick Neu for their time and patience as my committee members and as teachers. Susan Bowman has been invaluable as academic advisor and friend. The heart-felt kindness and dedication she shows each and every student is moving. I have to thank the members of Team Saxena, past and present, in Georgia and Arkansas, especially Kip Findley and Sau Wee Koh, the best group mates one could ever hope to have.

A NASA GSRP award initially funded this work and I would like to thank Jack Telesman, my NASA advisor, and Tim Gabb for their technical assistance. Everyone at Rolls-Royce has been so supportive, Malcolm Thomas, Mary Lee Gambone, Randy Helmink, and the technicians who were so helpful and patient. Very special thanks to Tom Hensler and Barry Holman, without whom I could not have completed this undertaking.

Finally I would like to extend my deepest gratitude to my family and friends, especially my mother and husband, for their endless love, support, and patience.

TABLE OF CONTENTS

LIST OF TABLES

LIST OF FIGURES

LIST OF SYMBOLS

w_j	neural network weight
h_j	hyperbolic tangent function for non-linear regression
H_v	Vicker's Hardness
l	length
F	applied force
t_j	actual values
y_j	predicted values
J	flux component
D	diffusion coefficient
$\partial c/\partial x$	concentration gradient
D_o	diffusion constant
Q	activation energy
R	universal gas constant
σ_y	yield stress
d	grain diameter
φ	dislocation bending angle
L'	spacing between dislocation-obstacle intersection
G	shear modulus
b	Burgers vector
ε_{COH}	coherency
r	particle radius
f	particle concentration

L	source-obstacle spacing
$\dot{\varepsilon}_{CG}$	dislocation creep rate
υ_g	glide velocity
υ_c	climb velocity
h	distance between parallel planes
ρ	dislocation density
M	number of dislocation sources
σ	applied stress
Ω	atomic volume
k	Boltzmann constant
D_L	lattice diffusivity

SUMMARY

Engineers constantly seek advancements in the performance of aircraft and power generation engines, including lower costs and emissions, and improved fuel efficiency. Nickel-base superalloys are the material of choice for turbine discs, which experience consistently high temperatures and stresses during operation. Engine performance is directly linked to operating temperatures. Consequently, the high-temperature capabilities of disc materials limit the performance of gas-turbine engines and any improvements to engine performance necessitate improved disc alloy performance.

In order to take advantage of improvements in high-temperature capabilities through tailoring of alloy microstructure, the overall objectives of this work were to establish relationships between alloy processing and microstructure, and between microstructure and mechanical properties. In addition, the project aimed to demonstrate the applicability of neural network modeling to the development and behavior of Ni-base disc alloys.

The first phase of this work addressed the issue of how microstructure varies with heat treatment and the mechanisms by which these structures are formed. Further, how superalloy compositions account for microstructural variations between alloys given the same heat treatment is also considered. To study this, four next-generation Ni-base disc alloys were subjected to various controlled heat-treatments and the resulting microstructures were characterized and their prominent features quantified. These quantitative results were correlated to chemistry and processing, including solution temperature, cooling rate, and intermediate hold temperature.

A complex interaction of processing steps and chemistry was found to contribute to all the microstructural features observed such as, grain size, precipitate distribution, grain boundary serrations. Solution temperature, above a certain threshold, and cooling rate controlled grain size, while cooling rate and intermediate hold temperature controlled precipitate formation and grain boundary serrations. Diffusion, both along the lattice and grain boundary, was identified as the necessary mechanism for evolution of the microstructure. Variations in chemistry between alloys created different amounts of γ/γ' misfit strain, which affect precipitate size and morphology.

Next, the question of how a disc alloy with different microstructures responds to constant or cyclic stresses as a function of time was addressed. To this end, mechanical testing at elevated temperatures was conducted, including tensile, hardness, creep deformation, creep crack growth and fatigue crack growth tests. Overall, mechanical properties were primarily related to the cooling rate during processing with intermediate hold temperatures being secondary. Whether the impact was positive or negative depended on the behavior under consideration. Fast cooling rates improved yield strength and creep resistance, but were detrimental to creep crack growth rates. The ability of precipitate particles to impede dislocation motion was the most frequently cited mechanism behind structure-property interaction.

Neural network models were successfully generated for processing-structure relationship, as well as for structure-property relationship. Available training data were limited, none-the-less models were able to successfully predict the expected behavior with minimal relative errors. This was achieved through careful balance between the number of input variables and the amount of training data. Despite the demonstrated

correlation between microstructure and the yield strength, microstructural quantities were not required as direct inputs. Neural networks were sufficiently sensitive as to infer these effects from processing and chemistry inputs. This result improves the efficiency of this technique, while also demonstrating the capability of neural network models.

A full program of heat-treatment, microstructure quantification, mechanical testing, and neural network modeling was successfully applied to next generation Ni-base disc alloys. From this work the mechanisms of processing-structure and structure-property relationships were determined. Further, test results were used to demonstrate the applicability of machine-learning techniques to aid in the development and optimization of this family of superalloys.

CHAPTER 1 Introduction

Ni-base superalloys are used in demanding high temperature applications such as in aircraft turbine discs that are exposed to temperatures in the range of 650ºC (1200ºF) and high stresses for extended periods of time. In order to facilitate progress in the field of modern gas turbine engines, it is necessary to reduce acquisition and maintenance costs, to improve fuel economy, to minimize emissions, and to prolong useful life of critical components within the engine. By improving the performance of nickel base superalloys, the traditional choice for key components such as turbine discs and blades, the increasing demands of the aviation and power generation field can be met. Improved superalloy performance includes an increase in the stress and temperature capabilities of the superalloy parts, which will facilitate increased pressure ratios and higher compressor discharge and turbine entry temperatures. It is suggested that alloys in these applications must improve their current temperature capabilities from about 650ºC to approximately 704ºC.

This work focuses on the high-temperature mechanical properties of next-generation Ni-base superalloys. Microstructure, especially grain size, grain boundary serration and the size, shape and distribution of γ' precipitates, are expected to directly influence the creep and creep-crack growth behavior of Ni-base superalloys. In turn, heat treatments control the microstructure of superalloys, and must therefore be carefully designed. Mechanical testing performed on specimens with known microstructures then can be used to further develop our understanding of high temperature mechanical behavior. Specifically, the interaction between damage mechanisms and alloy microstructure can be explored.

In addition, advances in the field of machine learning are applied to this work. Neural network techniques, which have been increasingly used in engineering studies, are used to model the relationship between processing and microstructure, and between microstructure and mechanical properties. These techniques have the potential to optimize the process of alloy development as well as improve alloy applications currently in use. In this way advances in turbine engine performances can be achieved in an efficient, cost effective manner.

Through our efforts to understand the role of microstructure in mechanical behavior, we hope to make improvements in superalloy performance by tailoring the microstructure of superalloy components. Based on the motivation to improve superalloy performance for gas turbine applications, the research objectives of this project are out lined as follows.

1) Quantify microstructural features and relate these to processing parameters. The effect of solutioning temperature, cooling rate and intermediate hold temperature on the microstructure of Ni-base superalloys produced via powder metallurgy are considered. Quantification of microstructural features includes grain size, precipitate size, distribution and morphology, and extent and nature of grain boundary serrations and relies on manual and computer-assisted techniques.
2) Establish relationships between high temperature mechanical properties and microstructural features. Mechanical testing is performed on specimens with systematically varied microstructures, including tensile, hardness, creep deformation, creep crack growth and fatigue crack growth. Variations in mechanical behavior are correlated to microstructural or processing parameters.

3) Demonstrate the ability of neural network techniques to model complex phenomena in the field of superalloys. Neural network models are generated which are able to predict alloy microstructure or mechanical properties from processing and chemistry inputs.

The foundation for this work lies in microstructure: establishing how to achieve a desired microstructure and which microstructure is best for alloy performance. Processing to achieve a given microstructure will vary with alloy composition. The best microstructure for alloy performance will depend on specific demands of the application. As such, metallurgists are often called to balance sometimes-contradictory demands put on engine components and must seek the optimal combination of microstructural features to meet the intended purpose. This project attempts to make this balancing act easier by improving our understanding of the mechanisms behind processing-structure and structure-property relations.

CHAPTER 2 Background and Literature Survey

2.1. Nickel-base Superalloys

Nickel-base superalloys are the traditional material of choice for turbine disc and blade applications. This project focuses on four next-generation disc alloys. This chapter presents background information on Ni-base superalloys in general and specifically for the four alloys studied. In addition, an overview of related published work on processing-structure and structure-property relations for these and related alloys is presented.

2.1.1. Brief History

The term "superalloy" applies to a group of metallic alloys that have been developed for optimal performance at high temperatures. As such, these alloys have been designed to maximize corrosion resistance, strength and creep resistance. A huge variety of superalloys have been established to date, however the group finds its roots in research on steels at the time of the First World War [1]. At this time researchers in France and the US filed the first patents for complex Fe-base alloys for land-base gas turbine engines and jet engines.

Superalloys emerged in the 1940's as the optimal material for the demanding environment in the hot section of gas turbine engines. In the decades following researchers have aggressively pursued improvements in high temperature mechanical

properties and stability, bringing about a diverse population of superalloys generally categorized by their base material for example Fe-base, Ni-base, Co-base. Driven by the demands of World War II applications, the United States and United Kingdom were the principle players in superalloy development. By the 1970's and 1980's Ni-base superalloys became prominent as corrosion-resistant, high-strength, high temperature alloys, with numerous variations commercially available.

In addition to advances based on alloy chemistry, researchers have also explored production techniques to optimize the microstructure and properties of these superalloys. Beyond traditional cast wrought methods, superalloys can be produced as directionally solidified metals, single crystal products, or by powder metallurgy. Each processing technique caters to a specific application and presents unique advantages and challenges.

2.1.2. Gas Turbine Engines

Throughout the history of superalloys, the aerospace industry can be cited as the major driver for the constant advances sought in the field. The gas-turbine engine is at the heart of the aerospace industry and constitutes a primary application of superalloys, especially Ni-base alloys. In addition to their use in jet engines, gas-turbine engines are used in marine applications, helicopters, and land-based power generation to name a few.

A brief description of gas-turbine engine operation is included to clarify the operating environment that drives alloy development and advances. Figure 1 shows the layout of a generic gas-turbine engine. Air is drawn into the inlet and compressed before being introduced into the combustion chambers. In the combustion chambers it is mixed with fuel and ignited. The resulting hot air mixture is released through the back, passing

over the turbine blades that are connected to a central shaft by the turbine discs. The blade is turned by the hot mixture and transfers this rotation to the compressor blades at the front. The color in the schematic represents the increase in temperature from the cold-section to the hot-section of the engine.

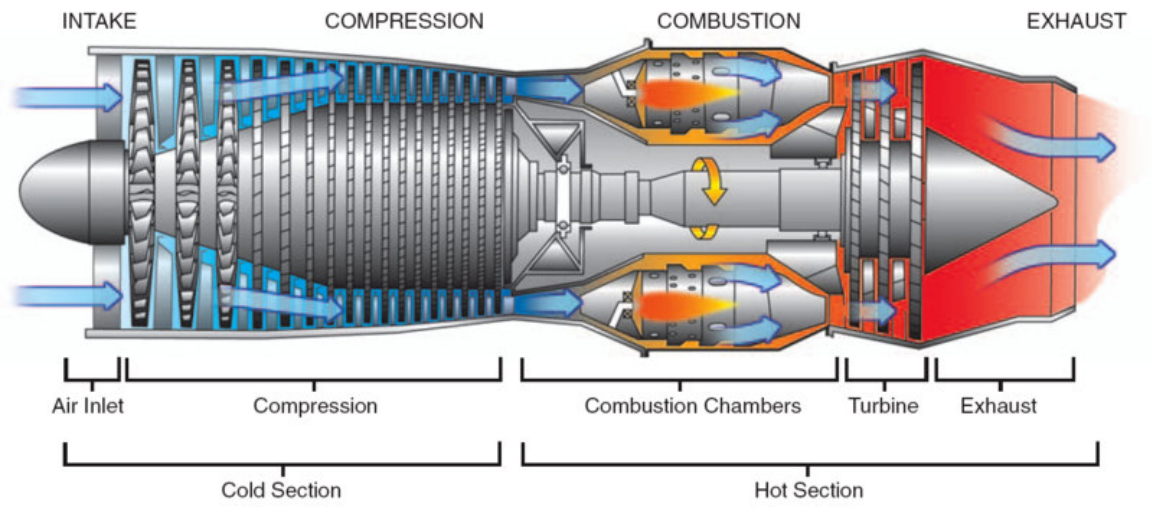

Figure 1 Schematic of gas-turbine engine [2]

The alloys considered in this study are referred to as “disc alloys”, indicative of their primary application. In Figure 1 the discs can be seen in the central part of the section labeled “Turbine”. Discs in gas turbine engines must operate for extended periods under very high temperatures and stress levels. The disc is a rotating part in the hottest section of the engine, and as such it is considered critical to the advancement of gas turbine engine performance. The outer region of the disc will generally experience operating temperatures as high as 650˚C.

Engine performance is directly related to the operating temperatures that the materials used to make its parts can tolerate. In order to improve the overall performance

and efficiency of gas turbine engines, the high temperature capabilities of disc alloys must be extended. For this reason Ni-base disc alloys are critical to the safe and efficient operation of the engine and are a primary focus of research for engineers.

Figure 2 Photograph of a typical gas turbine engine disc.

Gas turbine engine discs are thick circular discs with geometry dependent on the engine in which it is being used. In general the outer circumference of the disc is called the rim and is the location for the turbine blade attachment. The inner region of the disc is referred to as the bore and is the location for connection to the engine shaft. The intermediate area between rim and bore is called the web. The operating conditions for the rim and bore regions vary and as such the demands for the material performance do as well. The bore region does not experience the high temperatures seen in the rim of the disc, but the stresses on the bore tend to be higher. Difficulties arise because the optimal properties for each region are obtained with different microstructures. Figure 3 shows a

generic cross section for the radius of the disc with the change in temperature and mechanical property needs as a function of location. As mentioned the dimensions of the disc vary with engine size but typical diameters are in the range of 30 to 65 centimeters.

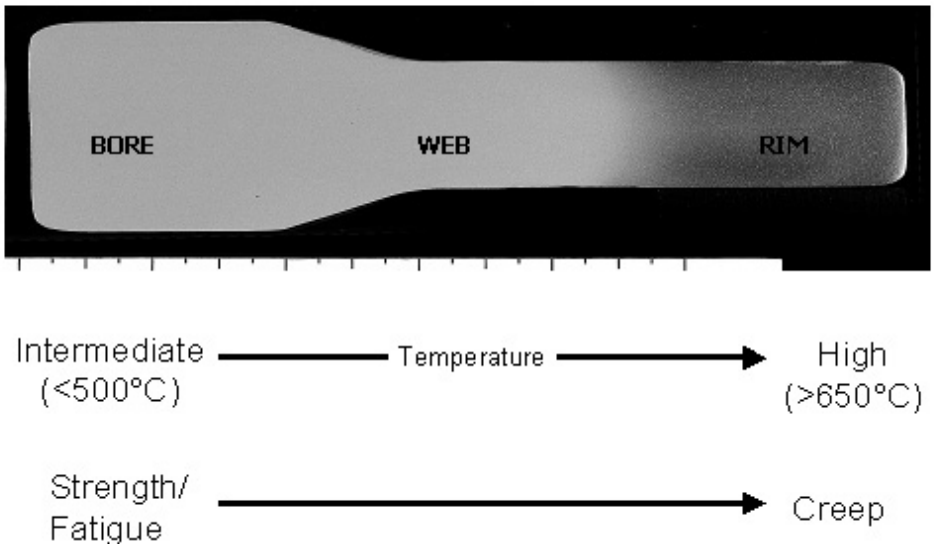

Figure 3 Cross section of generic disc with temperature and property needs outlined.

2.2. General Microstructure

The basic microstructure of PM Ni-base superalloys is a face-centered cubic, austenitic matrix phase, labeled γ, with a $L1_2$-type intermetallic precipitate phase labeled γ'. The precipitates are of type Ni_3Al, also face-centered cubic, and are an ordered phase. The difference in lattice parameter between the precipitates and matrix, referred to as 'misfit' or 'mismatch' is generally low for Ni-base alloys. The small mismatch means that particles are generally coherent with the matrix with interfaces on the {100} planes [1]. The γ' is the major strengthening phase in Ni-base superalloys. $M_{23}C_6$ and M_6C

carbides are present on grain boundaries in Ni-base superalloys and act as grain boundary strengtheners.

The γ' precipitates are traditionally categorized as primary, secondary, and tertiary, based on size or time of formation, however alternate labels such as cooling and ageing γ' are also used. For the entirety of this work the terms primary, meaning existing, large γ' precipitates, secondary, meaning moderate sized particles formed on cooling, and tertiary, meaning extremely small particles formed on ageing, will be used. Figure 4 shows an SEM image of typical γ' types in a Ni-base superalloy. Morphology of particles varies greatly, but the relative size differences between primary, secondary, and tertiary are universal and can be assessed in Figure 4 using the incorporated 1μm scale bar.

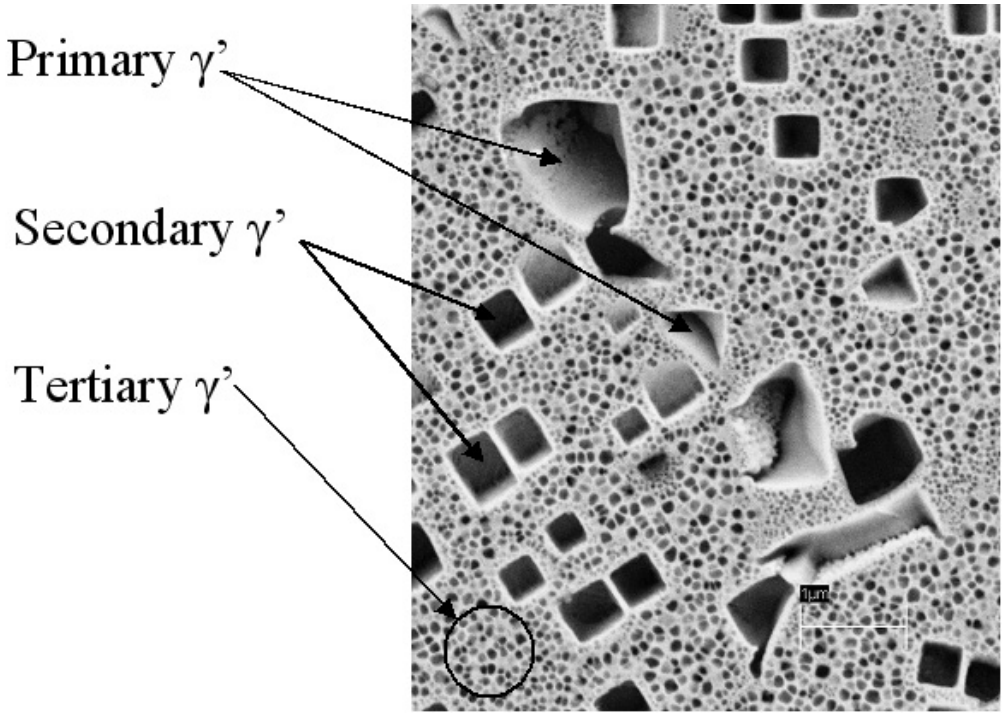

Figure 4 Example of γ' precipitate types in Ni-base superalloy.

The morphology of γ' particles varies with alloying elements and within a single alloy particle shape will change as the size of the particle changes. This can be explained if one considers the particle growth process as a balancing act between contributions to internal energy. This concept is well articulated by D. Mukherji, S. Peigert and J. Rosler who studied the morphology of γ' precipitates in Ni-base superalloys that contain W or Re. "The morphology of a coherent γ' particle depends on a large number of factors, but in general is determined by minimization of the sum of elastic strain energy of the particle, the surface energy of the particle and the elastic interaction energy between particles" [3]. Shapes of γ' prime can be spheres, lobed spheres, simple cubes, clusters of cubes, or octodendritic formations, based on the interplay of chemistry, surface and elastic energy.

2.2.1. Effect of Alloying Elements

In general the published literature is very consistent regarding the role of each element in Ni base superalloys. Madeleine Durand-Charre provides an excellent over view of the role of alloying elements in her book *The Microstructure of Superalloys* [1]. Each alloying element contributes to the overall nature and performance of the super alloy. Alloy developers must design alloy chemistries knowing how each element will affect the microstructure and therefore the mechanical properties. Aluminum increases the volume fraction of the strengthening γ' phase, as does tungsten and tantalum, which have the additional role of strengthening the matrix phase. Cobalt reduces the solubility of Al and Ti in the γ matrix and thereby maximizes the partition of these elements into the γ' phase. Also, Co is believed to reduce the γ' solvus temperature while raising the solidus. Chromium is added to improve oxidation resistance and helps reduce crack

propagation at elevated temperatures, possibly due to formation of $M_{23}C_6$ and M_6C carbides on the grain boundaries. Boron, carbon, and zirconium enhance high temperature properties, with B having the additional benefit of improving fatigue performance. B and Zr both inhibit carbide coarsening and improve grain boundary strength. Each element is included for a specific role, however a balance must be found between strength and damage tolerance in the alloy.

Table 1 Summary of effects of alloying elements

Element	*Effect*
Ni	Matrix
Al	Increase volume fraction of γ'; improves oxidation
B	Inhibits carbide coarsening; improves creep strength and
C	Carbide former
Co	Raises solidus
Cr	Improves corrosion and oxidation resistance
Mo	Matrix strengthening
Nb	Matrix strengthening; promotes γ' phase
Ta	Matrix strengthening; increases volume fraction γ'
Ti	Increase volume fraction of γ'
W	Matrix strengthening
Zr	Inhibits carbide coarsening; improves creep strength and

2.2.2. PM Processing and Heat-Treatment

Powder metallurgy processing is a multi-step processing aimed at efficiently producing a homogenous alloy material. Development of the powder metallurgy process was motivated by the ability to produced strong, fine grained materials not possible with the relatively coarse structures which results from conventional cast and wrought processes. PM processing has many advantages including production of near-net shape components, reduced chemical segregation, and increased uniformity and forgeability of

microstructures. The advantages of PM processing do not come without drawbacks, which include high production costs, the need for very fine powders, and extremely stringent process requirements [4].

Disc alloys are generally produced from pre-alloyed powders [1]. These powders are produced by vacuum induction melting (VIM) of the constituents followed by rapid cooling via gas atomization. To produce an alloy with minimal porosity and maximum homogeneity, powders must then be consolidated either by hot isostatic pressing (HIP) or by hot compaction and extrusion. This is followed by thermo-mechanical processing, such as isothermal forging, to neutralize the effect of contaminants and defects, cost-reduction through near-net production and property generation [4].

Properties of as-received PM products are generally very good, however additional heat-treatment can be applied for further tailoring of microstructures/properties. PM processing produces a fine-grained material with large primary γ' precipitates, in addition to secondary and tertiary particles, and a distribution of grain boundary carbides. Grain sizes for as-produced PM alloys are in the ranges of 7-10 μm or ASTM 8-12.

Solvus temperature is defined as the temperature at which 90-95% of the primary γ' precipitates dissolve and grain growth can occur. This study is focused on supersolvus microstructures, indicating that all materials will be heat treated above the γ' solvus temperature. The supersolvus heat-treatments applied to the materials examined in this investigation produce a larger grain size, in which the primary γ' goes into solution and so do the grain boundary carbides.

2.3. Next Generation Alloys

Researchers at NASA Glenn Research Center have developed LSHR to have optimal properties for use as a turbine disc material. The nominal composition of LSHR along with other similar alloys can be seen in Table 2. The alloy evolved from research on the Ni base superalloy, ME3 and Alloy 10, of NASA/GE/Pratt & Whitney and Honeywell Engine systems respectively. The first published information on LSHR can be found in the NASA technical memo entitled "Realistic Subscale Evaluations of the Mechanical Properties of Advanced Disk Superalloys" [5]. This memo summaries the work done on several experimental powder metallurgy disc alloys to determine various processing characteristics and high temperature mechanical properties and draws conclusions on the alloy with the best attributes for this specific high temperature application. Based on results from tensile, creep, and fatigue crack growth tests, as well as success response to various heat treatments, the authors recommended the alloy they named LSHR as being best suited for disc applications. Far-reaching testing has been conducted on the thermal and mechanical properties, characterization and processing, the results of which are available in the form of technical memos from NASA [6, 7].

Table 2 Alloy compositions by weight percent, alloy gamma prime solvus temperatures in ˚C [6, 11, 8, 21].

	Alloy Name			
Element	**LSHR**	**Alloy 10**	**RR1000**	**U720**
Ni	49.59	55.42	57.04	55.1
Al	3.5	3.69	3	2.5
B	0.03	0.03	0.02	0.035
C	0.03	0.03	0.03	0.035
Co	20.7	14.9	18.5	15
Cr	12.5	10.2	15	18
Hf	0	0	0.75	0
Mo	2.7	2.73	5	3
Nb	1.5	1.87	0	0
Ta	1.6	0.9	2	0
Ti	3.5	3.93	3.6	5
W	4.3	6.2	0	1.25
Zr	0.05	0.1	0.06	0.035
Solvus	1160	1182	1150	1190

Materials engineers at Rolls-Royce plc have developed RR1000 for use as a high-pressure compressor and turbine disc material in large civil aircraft engines. The alloy, produced via powder metallurgy, shows the high strength necessary for disc alloys and obtained by control of the γ' distributions. Developers of the alloy stated that, "In designing RR1000, the objective was to develop a misfit that contributes to strength, but to ensure that γ' remained coherent" [9]. Fine grain RR1000 has shown a 25˚C increase in temperature capability over U720Li, which is the current material used for disc applications. Large grain microstructure can also be obtained by supersolvus treatments, when improved creep properties are required of the application. The introduction of hafnium to the alloy composition has been found to contribute to improvements in crack growth and creep resistance. Successes in the development of RR1000 have led to its

introduction in multiple components on the next generation of Rolls-Royce gas-turbine aircraft engines.

Alloy10 is the product of ongoing collaborations between NASA, Honeywell and Rolls-Royce Corporation, formerly Allied Signal and Allison, respectively. It was developed for use as compressor and turbine discs in small gas turbine engines in regional jets. A high volume fraction of γ' precipitate particles, nearly 55%, is identified as being the source of the alloy's high strength. Alloy 10 is amenable to PM processing and extensive research has been conducted on the mechanical properties, processing and microstructural effects of the alloy [10, 11].

Udimet720 (U720) is a Ni-base superalloy that had been developed for cast and wrought turbine blades. From this alloy, U720Li evolved based on improved phase stability and reduced carbide and boride stringers [12]. Cast-wrought U720Li is one of the most widely used superalloys in jet engines; being used in several Rolls-Royce engines for example. The same alloy produced via a powder metallurgy route, however, has not been integrated into production parts. It does, however serve as a good benchmark material, one that is in general well known and for which variations have been widely studied.

2.4. Structure-Property Relations

This section will consider the microstructural features of PM Ni-base superalloys most relevant to the high temperature performance of the alloy. The foundation of this dissertation lies in establishing a link from processing to microstructure and then microstructure to properties. The mechanisms by which microstructural features are

formed, as well as the mechanisms by which these features affect properties, must be established experimentally and analytically. Published results on a variety of superalloys have established a precedent for this line of inquiry and techniques used in these studies have been applied or improved as part of the current work.

2.4.1. Grain size

Grain size is a major factor in alloy performance and one of the first features that should be considered. Significant effort in both research and production of alloys is directed at control of grain growth and grain size distributions. Fine grain size contributes to high strength and increased ductility in superalloys, driving the development of the powder metallurgy process that is unique in its ability to achieve a homogenous fine grain size.

Work in the first half of the twentieth century by Hall and Petch gave rise to the general relationship established to relate yield stress and other mechanical properties to grain size based on the idea that grain boundaries act as barriers to dislocation motion [13, 14]. Although later work emphasized the role of grain boundaries as dislocation sources, experimental observations confirmed the general relationship between decreased grain size and increased yield strength [15].

While small grain size (ASTM 8-12) optimizes the strength of a Ni-base superalloy disc, the opposite relationship exists between grain size and creep resistance. The creep resistance in the outer bore region is best achieved by a large grain size that minimizes the grain boundary surface area in the material. Larger grain size (ASTM 4-6) reduce the effect of grain boundary sliding, a mechanism of creep deformation [16].

Competing effects on creep resistance and strength resulting from grain size reduction are a perfect example of the need to optimize alloy microstructure. One cannot simply produce a disc with the smallest possible grain size because of the seemingly contradictory demands of high strength and high creep resistance. This balancing act of producing the optimum microstructure applies not only to grain size, but also to γ' precipitate size distribution and morphology.

2.4.2. γ' Precipitates

Much effort has focused on the understanding of growth kinetics of γ' precipitate morphology and size. This focus on the γ' phase is due to its importance as the primary strengthening mechanism of a class of materials valued for their high temperature-high strength capabilities. Recent alloy development work has focused on increasing the volume fraction of γ'. At the same time considerable effort has been put into tailoring the size, size distribution, and shape of the precipitates to optimize the strengthening effects of the phase.

The γ' particles are effectively strengtheners because of their interactions with dislocations in the material. Hardening/strengthening by precipitates can be explained bythe necessity for moving dislocations to go through or go around obstacles such as the γ' particles [17]. Particularly, at high temperatures, γ' particles are able to resist shearing by dislocations. Matrix dislocations require considerable force to create the stacking faults or the antiphase boundaries necessary to penetrate the γ' particles [1]. In order for the maximum strengthening to be achieved, a balance must be found between interparticle spacing minimized by fine particles to avoid bowing of dislocations around

the precipitates, and precipitate size which should not be so small that dislocations have sufficient leverage to shear the particles.

Numerous studies have been published which document the fundamental role of γ' size distribution on strength of Ni-base superalloys such as Rene88 DT, EP741NP, and various experimental alloys [18, 19, 21]. In all of these studies, the need for precipitate of a critical size for strengthening was highlighted. Particles must be sufficiently large to resist dislocation shearing but not so large as to allow bowing by the Orowan processes.

Results from investigations of the effect of γ' particles on creep deformation behavior indicated that heat treatments and processing routes that coarsen the particles show reductions in creep resistance [20]. This is most likely due to the inefficiency of larger particles at inhibiting dislocation motion, which is a fundamental creep mechanism.

In studies conducted on Alloy10 by researchers at NASA, improvements in time-dependent crack growth (TDCG) were directly related to the secondary γ' precipitate size distribution. They concluded that, "The larger the mean size of the cooling [secondary] precipitates the better the resistance to hold time crack growth" [11]. This improvement was attributed to the role of precipitates in determining the extent of crack tip relaxation during the creep processes, which affects the driving forces for crack growth. Thus, here is another example of competing requirements for creep deformation resistance versus high creep crack growth resistance.

2.4.3. Grain Boundary Serrations

Although the formation and effect of grain boundary serrations on mechanical properties has not been as widely considered as other features, it is nonetheless a key aspect of the structure-property relationship. The extent of grain boundary serration can be most directly correlated to the cooling rate from the supersolvus solution hold. Grain boundary serrations seem to be formed by preferential growth of γ' located on grain boundaries during slow cooling from supersolvus temperatures. This is supported by the mechanisms observed by D.U. Furrer and H. Fecht et al. in their work on PM U720. They observed from metallographic analysis that the relationship between cooling rate and precipitate coarsening and cooling rate and extent of serration formation were extremely similar. This suggested that "growth of grain boundary γ' is the cause of grain boundary serrations" [21]. As cooling rates are decreased, γ' particles are able to coarsen, especially those on grain boundaries where diffusion is accelerated. In this way the extent of grain boundary serrations formed increases with decreasing cooling rates. Figure 5 and Figure 6 show examples of smooth and serrated grain boundaries in the Ni-base superalloy LSHR.

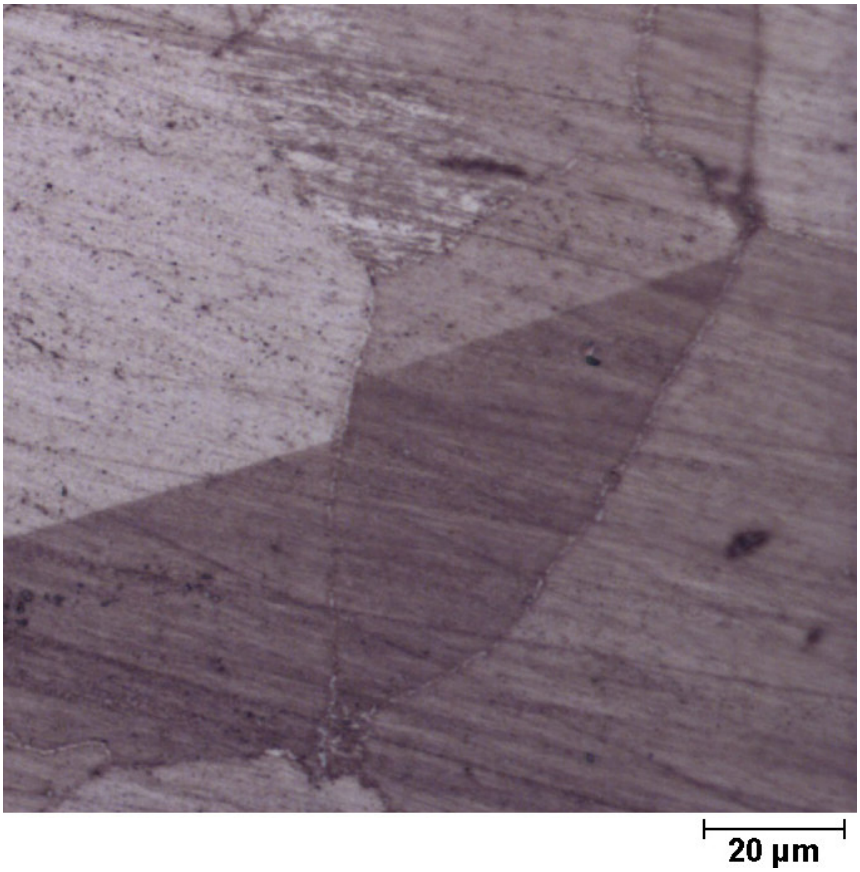

Figure 5 Example of straight (smooth) grain boundaries in LSHR.

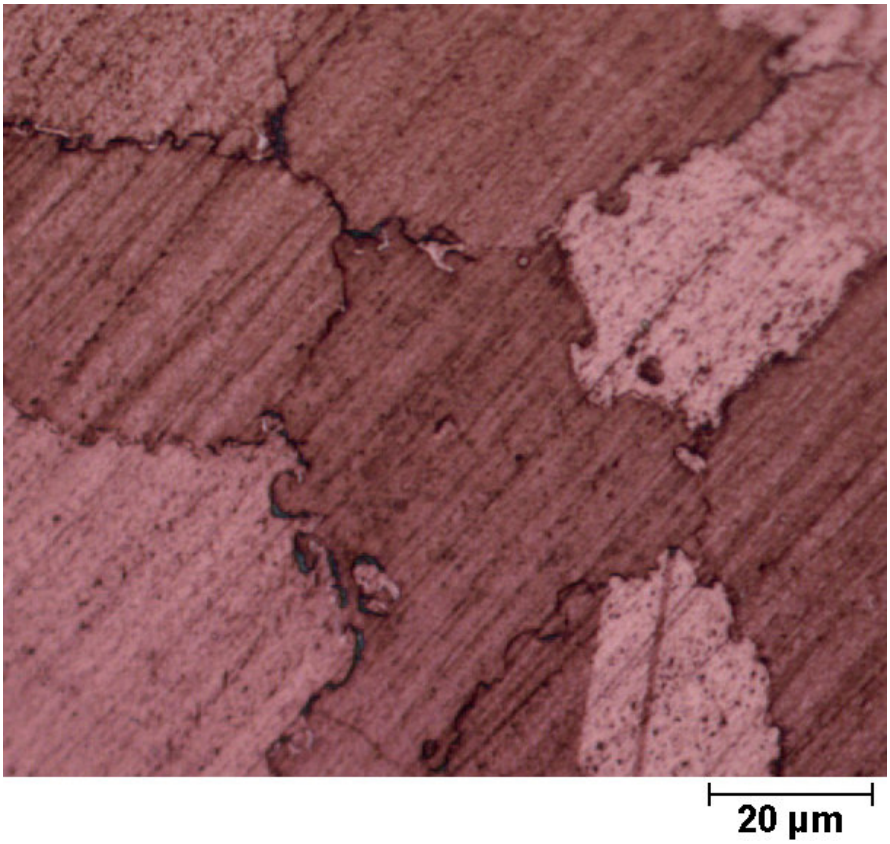

Figure 6 Example of serrated grain boundaries in Alloy10.

Research in France confirms the formation of serrations due to coarsening of γ' precipitates on grain boundaries, again highlighting the interdependence of serration formation, precipitate coarsening, and cooling rate [22]. Further work investigated the effect of these serrations on mechanical properties, specifically in a PM Ni-base superalloy [23]. Results from this work showed no clear change in tensile properties between the serrated and straight boundary material. However, creep-fatigue crack growth rates were found to be significantly slower for the serrated material. The crack propagation mode was consistently intergranular, however crack paths were more perturbed following the rough surface of serrated boundaries and thereby retarding crack growth.

These findings are consistent with results from work on Alloy10 conducted at NASA [11]. As discussed, above researchers showed improved TDCG resistance for supersolvus Alloy10 material subjected to slower cooling rates. In this work, it was noted that slower cooling rates led to preferential growth of grain boundary γ' particles, leading to formation of serrated boundaries and TDCG resistance. Serrated grain boundaries are formed by slower cooling rates, and therefore any improvements gained from this feature must be balanced with the potential loss of performance due to coarser γ'. However, improvements in TDCG were facilitated both by the serrated grain boundaries as well as by the improved ability for stress relaxation due the distribution of coarse γ' particles.

In addition to improved creep-fatigue crack growth resistance, the impact resistance also appears to be improved with increased serrations [21]. It is also hypothesized that perturbed grain boundaries can reduce creep deformation by limiting grain boundary sliding. It can be difficult at times to differentiate between the effects of serrated grain boundaries and coarsened γ' particles, both of which are dependent on cooling rate, and cannot be separated experimentally. As such, machine learning becomes an important tool in studying the effect of grain boundary serrations, as is discussed later in this chapter.

2.4.4. Hot Hardness Testing

In general, hardness data for materials can be considered as an indicator of other mechanical properties that are considerably more difficult to measure. Large amounts of data are available for hardness because hardness testing requires little material or preparation and the test itself is simple and quick. A casual survey of metallurgy texts or

industry-based literature will lead to numerous general relationships between hardness and strength [24,25]. Vast amounts of data relating hardness to strength exist for many materials, including steels, aluminum alloys, titanium alloys, bronzes, brass, etc. However, the relationships are entirely approximate and do not consider the potential effects of microstructure for a given material. In general there is no discussion beyond a basic tabulation of multiplying factors, so that issues such as mechanisms for the relationships or microstructural influences are not mentioned.

Materials scientists as early as 1961 recognized the growing interest in hot hardness measurements, fueled by the growing drive to develop high temperature materials [24]. Never the less, there is significantly less published work that uses hot hardness testing than at room temperature. In addition, the published work that does exist is more concerned with empirical observations than in investigations into the mechanisms contributing to hardness itself or the mechanisms that allow hardness to be used to predict mechanical properties such as strength or creep resistance.

A notable exception to this generalization can be found in the works published from researchers at the Bhabha Atomic Research Centre and the Indian Institute of Science [26, 27]. This work cites the increasing demand for higher temperature materials capability as the driver for developing "a rapid, inexpensive method for measuring mechanical properties at elevated temperatures" [26]. Their work demonstrates the ability of hot hardness to predict creep properties, a concept documented in work dating back to the 1950's [28]. In addition to establishing the temperature dependence of hot hardness and the relationship between hardness and creep behavior, mechanisms for each region of temperature dependence were established.

Discussions of slip systems and super-dislocation pairs, or the control of creep rate by viscous glide, for example, are included to explain the observed temperature dependence of hardness and at the same time to support the correlation between hardness and creep. It logically follows that the mechanisms underlying deformation during hardness testing must also be involved in creep behavior if a valid relationship were to exist.

2.5. Artificial Neural Networks

Materials science presents complex problems for which basic or general understanding may exist, but a rigorous mathematical treatment is lacking. This is especially true for the field of superalloys where the sheer number of variables from chemistry to processing to properties creates such a complex problem that traditional engineering methods for mechanical property predications are not practical. There is a distinct need for more reliable methods of property prediction than possible today from first principles models.

As H. K. D. H. Bhadeshia so deftly states "Neural network models are extremely useful in such circumstances, not only in the study of mechanical properties, but wherever the complexity of the problem is overwhelming from a fundamental perspective and where simplification is unacceptable" [29]. Numerous published works, not only in field of materials science but across all engineering disciplines, have repeatedly demonstrated the benefits of a NN approach to complex problems. Artificial neural networks are a powerful tool for the prediction of mechanical properties, but can also be used to gain a more fundamental understanding of the interactions between multiple variables.

2.5.1. Introduction to Neural Networks

In general a neural network (NN), also called an artificial neural network (ANN), is a method of machine learning that uses regression analysis to fit experimental data to a non-linear function. A traditional linear regression approach, which is familiar to most scientists, uses a best-fitted approach to create an equation relating inputs to outputs. While this approach can be helpful it is limited by the assumed independence of each variable, which is certainly not the case in most materials engineering problems. Further limitations are the establishment of a linear relationship prior to analysis and the implementation of a set relationship over the entire span of inputs [29].

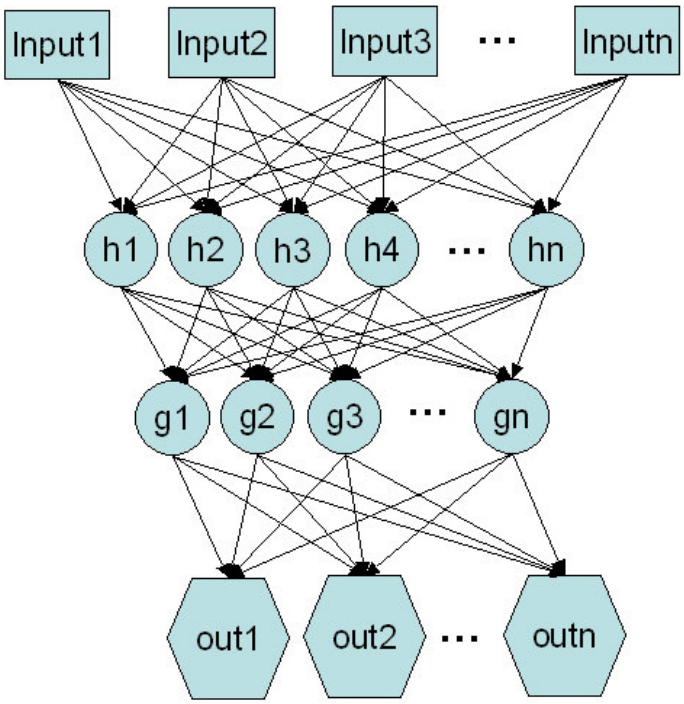

Figure 7 Representation of non-linear neural network model with two hidden layers.

A neural network is a regression method, however it overcomes the limitations mentioned above by creating non-linear relationships. Figure 7 shows a representation of a non-linear neural network, consisting of input data, an optimized number of hidden layers and output data. These hidden layers are a depiction of the hyperbolic tangent transfer functions that are the basis of the network relationships. Each node is assigned a weight, w_j, in the process of creating the best-fit non-linear relation ship. The network function can be written as

$$y = \sum_i w_i^{(2)} h_i + \theta^{(2)} \tag{1}$$

where,

$$h_i = \tanh\left(\sum_j w_{ij}^{(1)} x_j + \theta_i^{(1)} \right) \tag{2}$$

The hyperbolic tangent function is chosen based of its flexibility of shape and therefore its potential for capturing the behavior of seemingly arbitrary relationships. The nature of the NN approach as having weighted connections means "any non-linearity or inter-dependence within the relationships is necessarily incorporated within the output predictions" [30].

The process of creating a NN model involves feeding experimental data into a network to 'teach' or 'train' the nodes that relate inputs to outputs. Figure 8 illustrates the process of creating a neural network, including the steps of training the data, testing the quality of the model and applying its predictive capabilities. A subset of experimental data can be retained to test the quality of the fit generated by the model; this

subset is called the 'test data'. The overall error of a model is calculated by comparing the predicted values (outputs) of the models against the actual values, using the test data. Limitations to this description of error are present, particularly in the case of 'noisy' data or in areas where there is little input data.

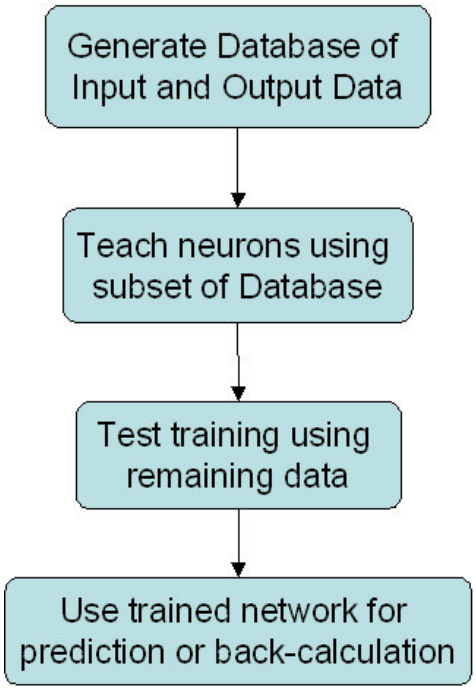

Figure 8 Schematic of general NN approach.

A Bayesian framework, as developed by D. J. C. MacKay, allows for the calculation of uncertainty in a given area, represented by error bars [31,32]. Networks with a Bayesian framework have become the most common approach for NN work in metallurgy due to their ability to extrapolate into less well-defined spaces without compromising the fit in adjacent regions of ample data. Application of a Bayesian framework has the additional advantage that the significance of each input is

automatically quantified and can be easily compared to metallurgical experience [33]. Such diverse applications as prediction of hardness of ductile irons to fatigue crack growth rates in superalloys have successfully employed Bayesian neural networks [33, 34].

Artificial neural networks exist as an entire field of study in and of themselves, thus readers desiring a more detailed discussion of machine learning or neural networks are referred to the wide amount of resources available on the Internet or to any of numerous texts on the subjects. An enlightening treatment of the topic of NN applications in materials can be found in the article by H.K.D.H. Bhadeshia, 'Neural Networks in Materials Science' [29]. The applications of neural networks in engineering in general, and materials science in specific, are numerous.

Published research, within metallurgy alone, includes dozens of applications, most notably alloy development, material processing, welds and joining, mechanical properties and microstructure. The following discussion is limited a few of the published articles which are most relevant to the areas considered in this dissertation.

2.5.2. Applications of ANN: Property prediction

A well-trained NN model can be an effective method for mechanical property prediction and as such becomes a potent tool in alloy development. Alloy development has historically been a process of trial and error guided by educated guesses. A powerful predictive tool such as an ANN greatly increases the efficiency of the development process, reducing time, effort, and cost. This is especially true for the development of

powder metallurgy alloys where in addition to alloy components, the many processing variables play an important role in the resultant alloy.

Engineers at the University of West England have conducted work in field of powder metallurgy material and process selection that demonstrates the accuracy and efficacy of the NN approach [30]. The study used a neural network to generate suggested component and processing values based on multiple inputted criteria describing the desired alloy behavior. In this approach one can see the flexibility inherent in the NN approach. Desired properties (or microstructures, etc) can be input with the output being the process necessary to achieve those properties, or process variables or alloy components can be the input with the resulting properties as the predicted output.

In this work, the network was trained with data compiled from the ample published work on PM superalloy development. The use of prior data is a key example of how the NN approach minimizes the time and cost associated with development of new alloys. From this data, a trained model with an optimized number of hidden layers and nodes was generated which was able to recommend not only chemistries and processing routes to achieve the desired alloy properties, but also predict cost savings and dimensional variation. The accuracy of the network model was established by plotting actual outcome values against predicted values.

2.5.3. Applications of ANN: Verification of mechanisms

Beyond the obvious usefulness as a means of property prediction, neural networks can facilitate the study of the fundamental mechanisms and underlying interactions of a metallurgical system. One example is that neural networks allow the user to vary input

values individually that might not be experimentally possible. Another is the use of networks to identify the primary variables of influence within a system, a primary step in the identification of underlying mechanisms. In these ways NNs become a powerful tool in the confirmation of mechanisms and interactions involved in a given materials problem. Machine learning is thereby taken from the realm of a useful industrial tool to a method of true scientific discovery and innovation.

An application of ANNs for this purpose in the field of mechanical properties of superalloys is well documented by scientist at Cambridge [34]. There, a Bayesian NN was used to analysis fatigue crack growth rates in Ni-base superalloys. In addition to the prediction of fatigue crack growth rates, based on input variables encompassing composition, heat-treatment, microstructure, and loading conditions, the models were used to estimate the effect of isolated variable that might not be possible to isolate in practice. In this way the researchers were able to demonstrate "the ability of the method to investigate new phenomena in cases where information cannot be accessed experimentally."

The effect of grain size on fatigue crack growth rates, as established in this work, serves as a perfect example of the investigative abilities of neural networks. In practice grain size is determined by heat treatment. However if one alters the heat treatment to achieve a particular grain size, numerous other factors are also changed (i.e. reduction of yield strength). The NN allows the user to isolate the grain size and change the weighting of this single feature with in the model. In this way researchers were able to demonstrate the effect of grain size alone in reducing crack growth rates, without the possible influence of other factors that would also change in experiments.

This study represents an ideal application of artificial neural networks. A database of nearly 2,000 data points was collected for training data. Many iterations of models were applied in order to achieve the best possible fit for the data. The success of a model is always limited by the quality of the input data. However this approach proved very successful in predicting full da/dN versus ΔK results for fatigue crack growth under a large variety of conditions. Due to the large amount of training data, a large number of inputs could be included. Thus predictions could be made for conditions varying a large number of parameters, including load shape, R-ratio, temperature, alloy composition, and grain size, to name a few.

Results for effect of grain size and yield strength on fatigue crack growth rate epitomize the usefulness of this approach. Typically one could not isolate the different effect that yield strength and grain size might have on fatigue crack growth rates. A change in grain size necessarily means a change in yield strength. However, with NN, the two inputs can be varied independently. Figure 9 and Figure 10 show the results for predicted da/dN curves when individually varying these inputs.

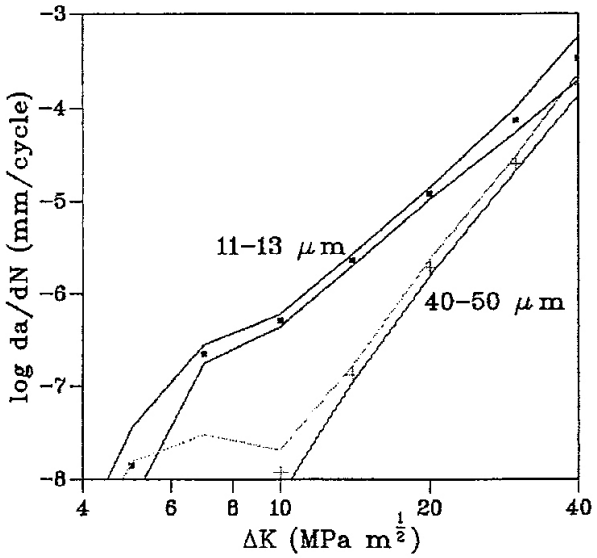

Figure 9 NN predicted fatigue crack growth rates showing effect of grain size [34].

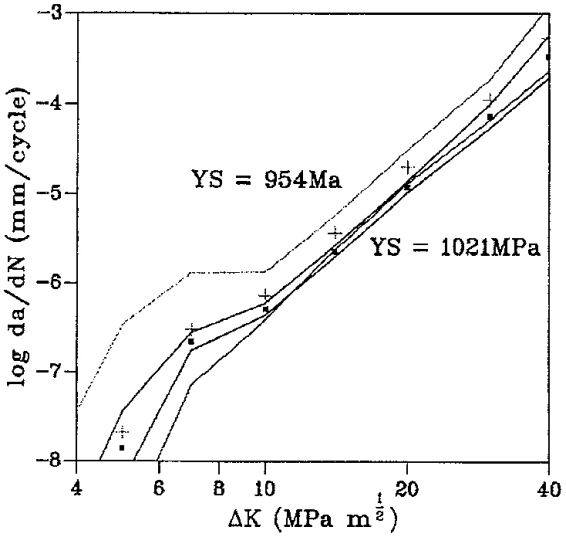

Figure 10 NN predicted fatigue crack growth rates showing effect of yield strength [34].

2.6. Summary

Through past decades advances in high-temperature alloys have been made driven by the demands of the aerospace and gas turbine engine industry. Ni-base superalloys

have emerged as the material of choice for the most arduous operating conditions. Careful additions of alloying elements have given rise to a family of alloys with superior high temperature strength, corrosion resistance, and ease of production.

The response of these alloys to thermo-mechanical processing and the mechanical properties of these alloys have been extensively studied. In addition, researchers have considered the relationship between microstructure and mechanical properties, with special attention being paid to effects of grain size, precipitate size distributions, and grain boundary formations. Classical experimental metallurgy approaches have been used, as well as the application of emerging techniques such as machine learning.

CHAPTER 3 Experimental Procedures

3.1. Materials

Four nickel-base superalloys were considered in this project: LSHR, Alloy10, RR1000, and PM U720. All of these alloys were produced via a powder metallurgy route and are under consideration for use as disc material in the next generation of gas-turbine engines. These alloys all represent various advances in mechanical properties and ease of production/machining based on changes in chemistry or microstructure from previous generations of superalloys. Their chemistries, seen in Table 2, have many similarities, with the main differences being in relative amounts of hafnium, molybdenum, niobium, tantalum, and tungsten.

LSHR, named for its characteristics of Low-Solvus and High-Refractory, was supplied by NASA-Glenn Research Center. The material used for all creep deformation, creep crack growth, and fatigue crack growth was machined from three contoured discs that also supplied the test material for NASA's studies on LSHR. Special Metals Corp. had prepared the powder material by argon gas atomization, followed by passing through screens of -270 mesh and hot compaction and extrusion in stainless-steel containers at a reduction ratio of 6:1. Wyman-Gordon Forgings isothermally forged the resulting mults into contoured discs approximately 30 cm across and 5 cm thick. The discs were subsequently heat treated at Ladish, Co. in ways deemed typical for current disc alloys in service.

The Alloy10 material was also supplied by NASA-Glenn Research Center. Special Metals Corp. prepared the material by argon atomization from re-melt stock

followed by screening to –270 mesh, canning and hot isostatic pressing (HIP) at 1093˚C and 15KSI for 3 hours. The billet material was then extruded at a 6:1 ratio at 1107˚C and isothermally forged into 35 cm diameter pancakes by Wyman-Gordon.

Rolls-Royce plc (UK) supplied the RR1000 material used in this research. This alloy was also produced by Special Metals Inc by vacuum induction melting (VIM), argon atomization, sieving, and reduction in steel cans at a ratio of 5.5:1 at 1110˚C. Again, Wyman-Gordon Forgings extruded the alloy.

PM U720 material was obtained through Rolls-Royce Corporation from material used in studies through the National Center for Excellence in Metalworking Technology. Special Metals Corporation manufactured this material from powders (-270 mesh) followed by HIP and extrusion to 15.75 cm billets. Ladish Co. forged the billet material into stage 3 turbine discs in a single stroke to final shape in a vacuum isothermal forging press. A three-step subsolvus heat treatment followed that include solutioning at 1135˚C, stabilization at 760˚C, and ageing at 649˚C.

3.2. Heat Treatment

Heat treatments for the LSHR material for creep deformation, creep crack growth, dwell, and fatigue crack growth were conducted separately from the heat treatments for the hot hardness, hot tensile and NN work. For clarification the treatment steps are described separately. Microstructural investigation was conducted to confirm the consistency of the microstructures produced.

Heat treatments of the alloy blanks for creep deformation, creep crack growth, dwell, and fatigue crack growth were conducted in a Lindberg Type 51333 5000W rated

glow-bar air furnace. Temperatures were monitored by K-type thermocouples embedded into 'dummy' blanks of the same shape and size as the actual material. Temperature versus time was recorded for the dummy blanks and the furnace using a Honeywell V5 digital strip chart recorder. All blanks were given a subsolvus pre-soak at 1135˚C for 90 minutes, a supersolvus solution soak at 1171˚C for 70 minutes followed by forced air-cooling. These times and temperatures were chosen to duplicate those applied by researchers at NASA-Glenn Research Center for their LSHR work.

The three cooling rates for creep and crack growth tests were obtained by wrapping the specimen in varying amounts of FiberFrax insulation. The amount of insulation was pre-determined with the use of dummy specimens specific to the geometry and size of the blanks. Dummy specimens were also wrapped and run with the actual specimens for further verification of the cooling rates actually obtained. These are referred to throughout this dissertation as 'fast', 'slow' or 'ultra-slow' meaning a nominal cooling rate of 3.36 ˚C/second, 1.19 ˚C/second, or .23 ˚C/second, respectively.

A matrix of 72 alloy-microstructure combinations were produced for hot hardness and hot tensile testing, as well as the microstructural quantification work. These 72 microstructures represent combinations of the four Ni-base disc alloys, three supersolvus solutioning temperatures, three cooling rates, and two secondary holds. These were run on a Vacuum Furnace Systems (VFS) HL16 with Graphoil hot zone with molybdenum elements, and 25.4 cm by 25.4 cm by 45.72 cm work zone with argon cooling capability. Temperatures and cooling rates were monitored both with embedded K-type thermocouples in superalloy dummy samples as well as the thermocouples built into the furnace itself. These were all recorded on a strip chart and manually entered into Excel.

Heat treatments were run in batches in vacuum with controlled cooling rates from the solution at hold at one of three temperatures and an argon gas fan cool following the secondary subsolvus hold at one of two temperatures. Table 3 through Table 6 show the matrix of heat-treatments in detail, with blocks of the same color being treated in the same furnace runs. Temperatures are listed in ˚C and rates are listed in ˚C/second.

Table 3 Complete list of LSHR heat treatments.

	LSHR		
	Solution	Cooling Rate	Second Hold
L1	1165	0.75	1040
L2	1165	0.75	845
L3	1165	0.416	1040
L4	1165	0.416	845
L6	1165	0.083	1040
L5	1165	0.083	845
L7	1182	0.75	1040
L8	1182	0.75	845
L9	1182	0.416	1040
L10	1182	0.416	845
L11	1182	0.083	1040
L12	1182	0.083	845
L13	1199	0.75	1040
L14	1199	0.75	845
L15	1199	0.416	1040
L16	1199	0.416	845
L17	1199	0.083	1040
L18	1199	0.083	845

Table 4 Coplete list of Alloy10 heat treatments.

	A10		
	Solution	Cooling Rate	Second Hold
A1	1199	0.75	1040
A2	1199	0.75	845
A3	1199	0.416	1040
A4	1199	0.416	845
A5	1199	0.083	1040
A6	1199	0.083	845
A7	1216	0.75	1040
A8	1216	0.75	845
A9	1216	0.416	1040
A10	1216	0.416	845
A11	1216	0.083	1040
A12	1216	0.083	845
A13	1233	0.75	1040
A14	1233	0.75	845
A15	1233	0.416	1040
A16	1233	0.416	845
A17	1233	0.083	1040
A18	1233	0.083	845

Table 5 Complete RR1000 heat treatments.

	RR1000		
	Solution	Cooling Rate	Second Hold
R1	1150	0.75	1040
R2	1150	0.75	845
R3	1150	0.416	1040
R4	1150	0.416	845
R5	1150	0.083	1040
R6	1150	0.083	845
R7	1165	0.75	1040
R8	1165	0.75	845
R9	1165	0.416	1040
R10	1165	0.416	845
R12	1165	0.083	1040
R11	1165	0.083	845
R13	1182	0.75	1040
R14	1182	0.75	845
R15	1182	0.416	1040
R16	1182	0.416	845
R17	1182	0.083	1040
R18	1182	0.083	845

Table 6 Complete PM U720 heat treatments.

PM U720			
	Solution	Cooling Rate	Second Hold
U1	1165	0.75	1040
U2	1165	0.75	845
U3	1165	0.416	1040
U4	1165	0.416	845
U6	1165	0.083	1040
U5	1165	0.083	845
U7	1182	0.75	1040
U8	1182	0.75	845
U9	1182	0.416	1040
U10	1182	0.416	845
U11	1182	0.083	1040
U12	1182	0.083	845
U13	1199	0.75	1040
U14	1199	0.75	845
U15	1199	0.416	1040
U16	1199	0.416	845
U17	1199	0.083	1040
U18	1199	0.083	845

The final heat treatment step for all material studied in this research was a two step ageing, typical of that received by production pieces. The ageing was conducted in the glow-bar air furnace mentioned above and consisted of an eight-hour exposure at 855˚C followed by a four-hour exposure at 775˚C and then air-cooling.

It should be noted that for all materials used in this research, experimental heat treatments were at temperatures in excess of the original heat treatments and that efforts were made to establish the effect of a secondary heat treatment on the resulting material. Microstructural imaging and quantification showed that there were no artifacts of previous microstructures on the investigated alloys when compared to as-forged material as well as forged and heat treated material. In other words, all material used for this study had been previously heat treated, but only to a subsolvus temperature range, where

as all microstructures considered in this work required a supersolvus solutioning, well above the high temperature in the previous exposures.

3.3. Imaging and Microstructural quantification

Several relevant microstructural features were imaged and quantified for use in this study. The techniques used for sample preparation and imaging varied based on the feature of interest. Techniques that could be applied on all four materials were sought in order to maximize consistency. ASTM standards were used for quantification of the microstructure whenever possible, although standards were not available for the quantification of some features.

Coupons of materials were cut from the tensile-bar blanks so as to assure that the measured features were the same as those of the tested material. Coupons were hand polished to 3 μm finish. The quality of results for traditional chemical etches used to resolve grain boundaries proved to vary greatly between alloys. Therefore a thermal etch was used, thus ensuring consistent exposure and results. Coupons were exposed to 704˚C in vacuum for approximately 20 minutes and remained in vacuum during cooling. Images taken by optical microscopy at 200x were used for quantification of the grain size and As-large-as (ALA) measurements. ASTM standard E112 was followed for manual grain size measurements [35]. Specifically, the circular intercept method outlined in section 14 of ASTM E112 was used. A minimum of five fields of view were used with at least 25-35 intercepts in each field. ALA measurements were made based on ASTM E930 [36]. Grains were chosen from amongst the fields of view used for intercept counts.

ASTM standards are not in place for serration quantification, so several methods were considered. The method of quantification ultimately chosen for this study was that judged to be the most consistent, objective, and widely accepted in industry and academic practice. Grain boundary serrations were characterized from optical images taken at 500x of the same specimens used for grain size measurements. Individual grain boundaries were isolated using digital photography software. Using the freeware package Image J, these individual boundaries were then converted into x-y coordinates to facilitate calculations with Microsoft Excel. Figure 11 through Figure 13 below show the typical progression from optical image to x-y coordinates for quantification.

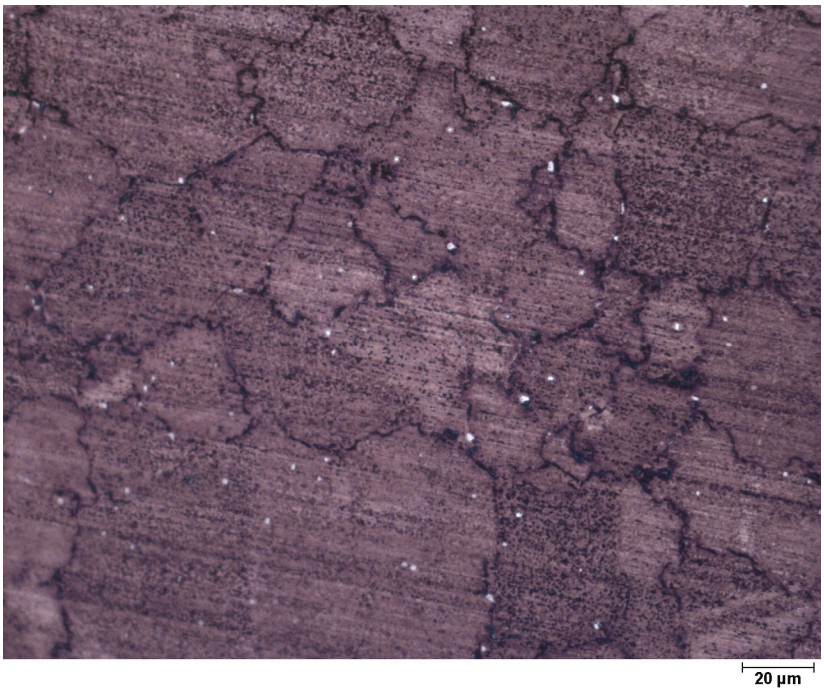

Figure 11 Typical optical micrograph showing detail of grain boundary serrations.

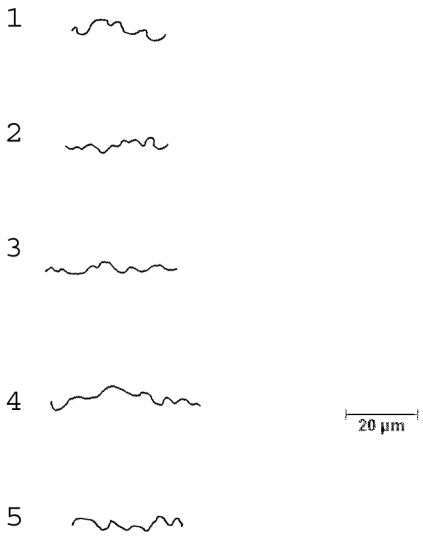

Figure 12 Results of grain boundary isolation with digital graphics software.

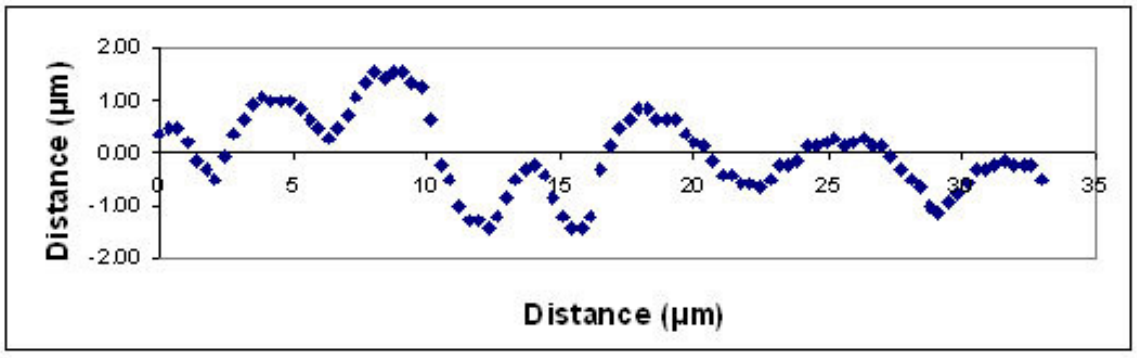

Figure 13 Serrated boundary converted into x-y plot in Excel.

For each of the 72 microstructures studied, five randomly chosen boundaries were isolated and converted into x-y coordinates. For each boundary the shortest distance between triple points, actual length of grain boundary, number of serrations, and serration amplitudes were quantified, with these numbers being used to calculate the characteristic

quantities of average serration amplitude, serration density (wavelength) and Grain Boundary Curvature Ratio (GBCR). A single serration is counted at a peak, defined by the existence of a maximum or minimum point. The amplitudes of each serration are based on the distance between the maximum point and a centerline. This centerline is defined so that an equal area can be integrated both above and below the centerline. Serration density is the number of serrations over the distance between triple points. GBCR is defined at the ratio of the overall grain length to the shortest distance between bounding triple points.

Scanning electron microscopy (SEM) was necessary for sufficient resolution to image the γ' precipitates. Specimens were mounted and polished on an automatic polishing wheel with each: 120, 320, 500, 800 and 1200 grit, then 6 μm diamond and 3 μm diamond finish. An electrolytic etch was used to remove γ matrix material and leave the precipitates in relief. The etch consisted of 10% phosphoric acid in distilled water and 3-5V were applied to immersed specimens for 5-10 seconds at ambient temperatures. Images were taken on a JEOL JSM 5900LV with a tungsten filament at magnifications ranging from 5,000x to 25,000x and an accelerating voltage of 15kV.

It should be noted that care must be taken to avoid over-etching of the samples. Because this is a γ-matrix etch, over-etching leads to the exposure of multiple layers of precipitates that will artificially inflate the volume fraction calculations. In addition, over-etching can allow particles to dislodge from the specimen surface, causing the volume fraction estimates to be too low. In this work, any specimen producing images with multiple layers of exposed precipitates or evidence of missing/dislodge precipitates were re-polished and re-etched for shorter times.

Automated image analysis routines within the ImageJ software were used to quantify secondary γ' volume fraction, precipitate size distributions and shape factors. In general, these routines began with the isolation of the γ' particles through various filtering and thresh-holding steps followed by calculations being made for each individual particle and the population as a whole. The most relevant quantities for this work were the volume fraction, calculated as an area percent, average particle size and population size distribution, based on a square area, and circularity, as defined below. For each microstructure a sufficient number of randomly chosen fields of view were considered to incorporate a minimum of approximately 200 particles.

$$Circularity = 4\pi * \left(\frac{Area}{Perimeter^2} \right) \tag{3}$$

In addition to the coupons of material specifically intended for microstructural investigation, quantification of the tested material was undertaken according to the methods outlined above. Material from the gauge and grip sections of tested specimens with tensile bar geometry were prepared and imaged to assess the extent of microstructural changes during testing in the strained and unstrained areas. Similarly, material from the failed compact type specimens was investigated.

3.4. Mechanical Testing

A thorough matrix of mechanical testing was undertaken in order to establish the link between alloy chemistry and microstructure and mechanical properties. Because

these alloys are used in the most demanding high-temperature applications all tests were carried out at 704˚C, which is approximately 30˚C above their current in-service temperature. Fracture surfaces for all tested specimens were documented.

Guidelines for testing as established by the relevant ASTM standards were followed for all tests. Specimens were blanked by wire electrical discharge machining (WEDM) prior to the heat treatments describe in 3.2 (Heat Treatment). Machining of the specimens was done on a combination of lathes, grinders, mills, and WEDM. Details of the testing conditions along with specimen geometries are in the following sections.

3.4.1. Hot Tensile Tests

Tensile tests were conducted in accordance with ASTM E8 on the tension testing of metallic materials [37]. All tests were conducted at 704˚C in air. The full set of 72 microstructures representing the four superalloys was tested with displacement measured by high temperature extensometry attached at the shoulders. Extensometer placement was factored into all subsequent calculations. The stress versus strain relationship was graphed and yield stress and ultimate tensile strength calculated for each. Specimen geometry was a reduced scale round bar with threaded grips.

3.4.2. Hot Hardness Testing

The matrix of 72 microstructures was produced specifically for use in hot hardness testing (HHT) and hot tensile testing. Heat-treated blanks were machined to dimensions of one cm by 0.5 cm by 0.5 cm to fit specimen holders for the Nikon Hot

Hardness Tester housed at the University of Arkansas. The Nikon set-up for HHT consists of two independent microfurnaces, one for the indenter and one for the specimen in the specimen holder, housed within a water-cold vacuum chamber. Three indents were made at each condition, including room temperature and 704˚C, as well as various intermediate temperatures. Heating rates did not exceed 0.5˚C per second for the specimen or the indenter.

Figure 14 Indenter and specimen vacuum chambers of Nikon HHT.

ASTM standards specific to hot hardness testing were not available; therefore the guidelines for room temperature Vicker's hardness testing were consulted where applicable. These are found in ASTM E92 [38]. A diamond tip indenter with the square pyramid geometry specified for Vickers Hardness (H_v) was used. Hardness calculations were based on the following relationship.

$$H_V = F/A = \frac{\sin(136°/2) * F}{1/2\, l^2} \approx \frac{1.854 * F}{l^2} \tag{4}$$

In this calculation, l is the length of the measured indent and F is the force applied by the diamond indenter, measured in kilograms force. This yields a unit of kgf/mm^2. Various force and time combinations were tried in order to discern the possible effects of these variables at room and elevated temperatures. The minimum time and force necessary to produce a clear and consistent indent for measurement was used. For the alloys studied this was 500 g for 5 seconds. The equipment automates indenter application and timing, although manual over-rides are available. Care was taken to ensure sufficient spacing between indents so as to avoid the effect of adjacent stress fields on subsequent indentions.

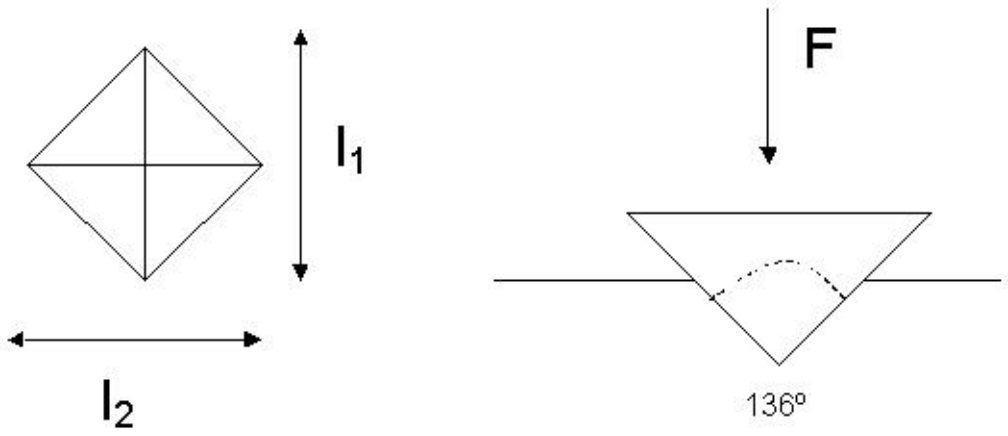

Figure 15 Indenter geometry and indent dimensions for Vicker's Hardness test.

3.4.3. Creep Deformation Tests

Creep deformation tests were conducted in accordance with ASTM E139-00 [39]. At this stage the mechanical testing narrowed in focus to the three microstructures of LSHR. Each microstructure was tested at three load levels on Arcweld Manufacturing Company Model J 20:1 lever 5500 kg capacity creep frame with ATS Series 3200 3-zone embedded element furnace. The specimen geometry consisted of a round bar with threaded grips and reduced radius gauge section. Tests were conducted at 704˚C in air, on specimens with high temperature extensometer arms attached at the shoulders. The extensometer placement being on the shoulders must be accounted for in the subsequent calculations for strain and strain rates. Extension over time was recorded from the linear variable displacement transducer (LVDT) gauges using the same digital strip chart recorded used for heat treatments. Temperature was monitored by two K-type thermocouples attached to the gauge section of the specimen. Data acquisition rates were based on the creep-regimen, with Stage I creep rates being on the order of one data point per minute and Stage II and Stage III rates on the order of one data point per hour.

3.4.4. Creep Crack Growth Tests

Creep crack growth tests were conducted on specimens having compact type (CT) geometry in accordance with ASTM E1457-00 [40]. Tests were conducted in air at 704˚C on the same tests frames as the creep deformation tests. Specimens were pre-cracked by cyclic loading at room temperature. Half of the specimens were side-grooved before testing and half were not. Temperature was recorded from two K-type thermocouples spot-welded to the face of the CT specimen. Crack tip opening displacement (CTOD) was measured at the load line using LVDTs. Crack growth was measured by means of direct current potential drop (DCPD) methods described in the annex of ASTM E1457. For the DCPD measurements, Inconel leads were welded to the specimen; a positive and negative for the constant current input and a positive and negative to read the voltage drop out. The current source was cycled off to monitor thermal voltage. In Figure 16, note the placement of DCPD leads on the top and bottom of the specimen and the left face. Also pictured is the CTOD gauge at the load line. All leads were insulated with ceramic beads.

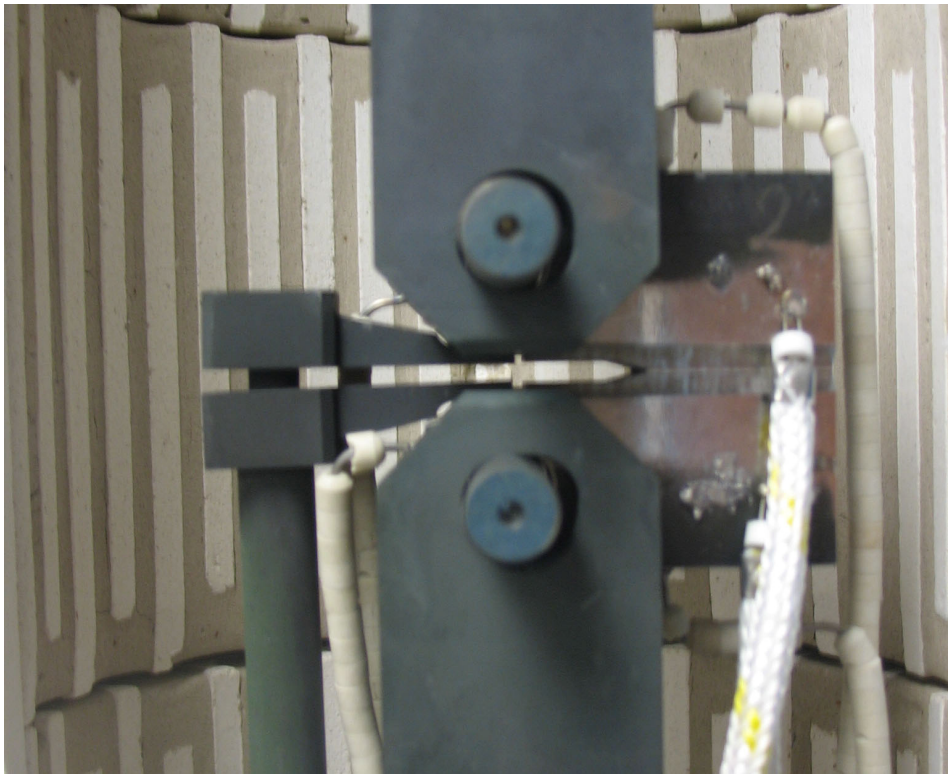

Figure 16 CT specimen in place for crack growth testing.

3.4.5. Fatigue Crack Growth Tests

Fatigue and dwell-fatigue crack growth tests were conducted on LSHR specimens having CT geometry. Servo-hydraulic frames located at the Mechanical Properties Research Lab at the University of Arkansas and at the Air Force Research Lab at Wright-Patterson Air Force Base were used for these cyclic tests. All tests were done at 704˚C in air with temperature being monitored by two K-type thermocouples. Specimens were fatigue pre-cracked at room temperature; none were side-grooved. Crack growth was measured by the DCPD method described in section 3.4.4. All tests were conducted at an R-value of 0.1, a frequency of 0.5 Hz and constant load amplitude, with a sinusoidal loading form.

3.5. Artificial Neural Networks

The results collected during microstructural analysis and mechanical testing were used to populate training and testing data sets for ANN techniques. PatternMaster was identified as the most useful software package for this project, based on its flexibility, level of user-control and the overall interface of the program. In general the NN models produced in this research were on a Bayesian Neural Network approach. Approximately 90% of the data was used for training, the remainder being used for testing of the model.

For each ANN model a database of known inputs and outputs is generated. Approximately 90% of this database is used as training data to determine the weight of the nodes. The remaining 10% is reserved to be used as 'test data' and not exposed to the model until all training is complete and weights have been established. The 10% of data used for testing is chosen randomly. From the comparison of the predicted outputs of the test data to the actual 'known' outputs values, the error of the model is measured, as described below.

Basic statistical methods were used to assess the robustness of the models. The "quality" of each model was quantified based on the deviation of the predicted output values from the actual data. A general approach of comparing the error in the predicted values from the test data for each model was applied. Graphic results typical of this approach are seen in Figure 17. The overall error described above can be written in equation format as seen in below, where t_j are the actual values and y_j are the predicted values.

$$E \propto \sqrt{\frac{1}{n}\sum_{j=1}^{n}\left(\frac{t_j - y_j}{t_j}\right)^2} \tag{5}$$

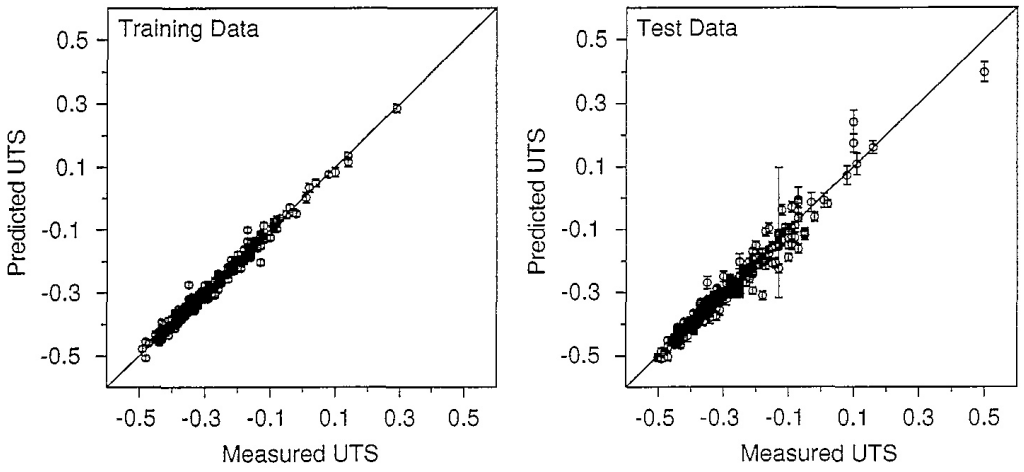

Figure 17 Typical graphic results for comparison of model predictions to actual data [41].

Various combinations of input and output data were processed to identify the most accurate and the most efficient data sets necessary for accurate predictive models. Multiple models were generated, based on the desired outputs (i.e. predicting microstructure alone, predicting mechanical properties with or without microstructure, etc). An optimized set of inputs and hidden layers was identified by minimization of error, as described above, as well as by minimizing the amount of time and computing power necessary to generate the model. Table 7 lists the complete set of potential inputs and outputs for this work. Combinations of these inputs and outputs were included in networks in the process of identifying the data required for the model that gave the most accurate results for the least number of input variables.

For each feature or property modeled the first network trained incorporated every possible input relating to the output under consideration. From this first network, the most highly weighted inputs were identified and carried into the next model. This iterative process was continued until the error, as calculated in Equation 5, was minimized. At times this would involve re-introduction of inputs previously eliminated.

Table 7 Complete list of possible inputs and outputs to ANN.

Inputs	Outputs
Alloy Components (full and subsets)	Grain Size
Solution Temperature	Volume Fraction
Cooling Rate	Average gamma' size
Hold Temperature	Average gamma' shape factor
Grain Size	GBCR
Volume Fraction	Serratin Amplitude
Average gamma' size	Hardness
Average gamma' shape factor	Hot Hardness
GBCR	Hot Yield Strength
Serratin Amplitude	Hot Ultimate Tensile Strength
Hardness	
Hot Hardness	

The weights, $w_{i,}$ as in Equation 2, for each input within each network were used to identify the primary variable of influence in a given model. The most heavily weighted input must necessarily represent the most influential component, process, etc, in the model. In this way NN models are used to investigate the fundamental mechanisms involved in structure-property relationships. The components or process steps that most affect the microstructure or the features that most influence the mechanical behavior are able to be isolated, thus illuminating the mechanisms responsible.

3.6. Experimental Procedures Summary

Four Ni-disc superalloys, supplied by NASA, Rolls-Royce Corporation, and Rolls-Royce plc, were used to conduct thorough microstructural quantification and mechanical testing. Image analysis was conducted on a matrix of 72 microstructures of the four alloys produced by heat treatments with varying solution temperatures, cooling rates and hold temperatures. Features such as grain size, grain boundary serrations, and γ' size distributions were quantified. Three microstructures of LSHR were tested. Tests conducted included hot hardness, hot tensile, creep deformation, creep crack growth, fatigue crack growth and dwell-fatigue crack growth. Where applicable, ASTM standards were followed. Results of mechanical testing are used to systematically assess the relationship between microstructures and mechanical properties. Findings from both microstructural and mechanical work were used in ANN models to create predictive tools, as well as to optimize the alloy development procedure and contribute to the fundamental metallurgical understanding of the processes involved.

CHAPTER 4 Processing-Structure Relationships

The ability to precisely control microstructure is crucial not only to industrial applications involving superalloys, but also to the fundamental scientific understanding of these materials to continuously improve them. This requires a thorough knowledge of the processing steps and the effect that they each have on the resulting alloy microstructure. The systematic variation of processing parameters and analysis of the resulting microstructural features allows us to identify the mechanisms driving certain formations. From this knowledge, processing can be optimized for production or for research on the effects of microstructure on mechanical properties, which is one of the main objectives of this thesis.

This chapter presents the outcomes for the microstructural quantifications resulting from each heat treatment. Response of each alloy to heat-treatment is considered relative to the composition and processing, as well as overall trends in the responses of the Ni-base superalloys in general. Special attention is paid to identifying the processing step that most directly influences each aspect of microstructure considered in the context of the mechanical properties of interest.

Unless otherwise noted, results for PM Udimet720 are omitted because the results of microstructural quantification indicate that the heat treatments of U720 were not executed correctly to achieve a supersolvus condition. The microstructures produced for the U720 samples had a duplex grain structure of very fine and very coarse grains. Also, primary γ' particles remained after the heat treatment indicative of inadequate exposure to supersolvus temperatures. Because of this, it became inappropriate to compare the results of the LSHR, Alloy10, and RR1000, which were fully supersolvus, with those of

the U720 material. An optical micrograph of the duplex grain size can be seen in Figure 18. Areas of extremely fine-grained material surround two very large grains at the bottom of the picture.

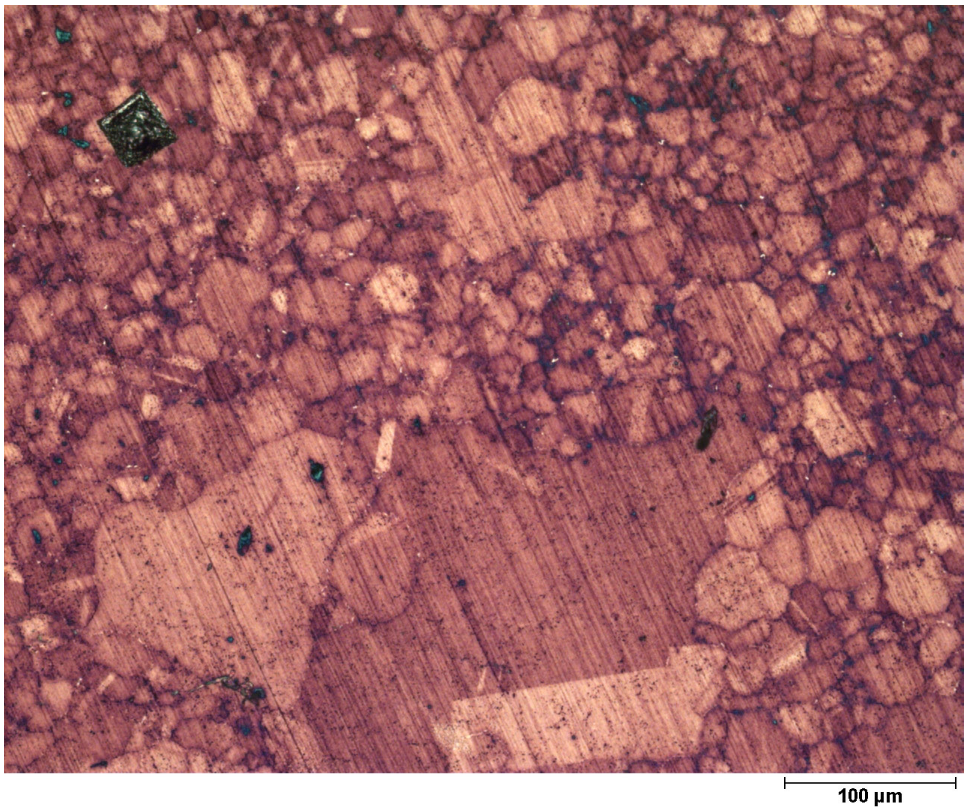

Figure 18 Optical micrograph showing the duplex grain distribution of PM U720.

4.1. Grain Size

Grain size measurements were made using the circular intercept method described in ASTM E112. Before presenting the results of these measurements, it is appropriate to discuss the capability of that measurement technique. ASTM E112 states, "it is important…to recognize that the estimation of average grain size is not a precise measurement" [35]. The grain structure is three-dimensional and there is a distribution

of sizes in the population. In addition the grains being quantified have some deviation from equiaxed and grain boundaries are not strictly straight. It is important to keep this in mind, so that we do not read too much into minor variations in values. While some variations are valid effects of processing parameters, inherent variability exist for a number of other reasons such as in the measurement process itself.

All samples were processed at temperatures that were above their respective γ' solvus temperature. Because of this a 'coarse' grain structure was expected for all heat treatments. Note that the 'as-received' material was subsolvus; meaning that it contained fine-grains with extensive grain boundary carbides and primary γ'. Grain size for as-received materials had a mean diameter of approximately 10-15 μm or ASTM 11-12. This subsolvus microstructure can be seen in Figure 19. Figure 20 shows the microstructure of a supersolvus heat-treated specimen. Note the lack of primary γ' particles and only one grain boundary visible in the slightly darker area to the bottom left corner of the picture.

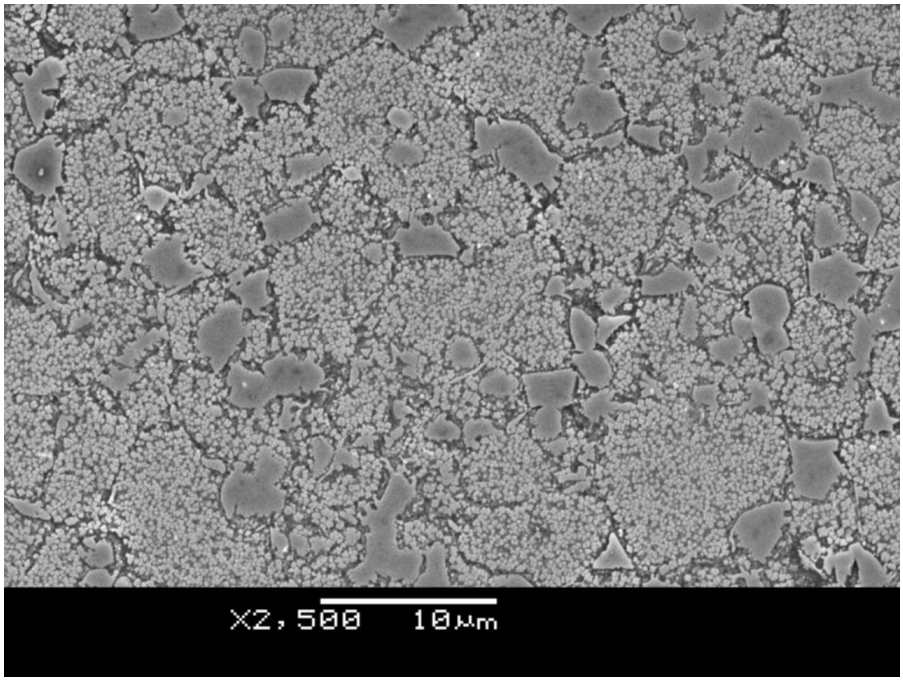

Figure 19 SEM image of as-received LSHR material. Large irregular primary γ' can be seen defining the grain boundaries of the fine grain material.

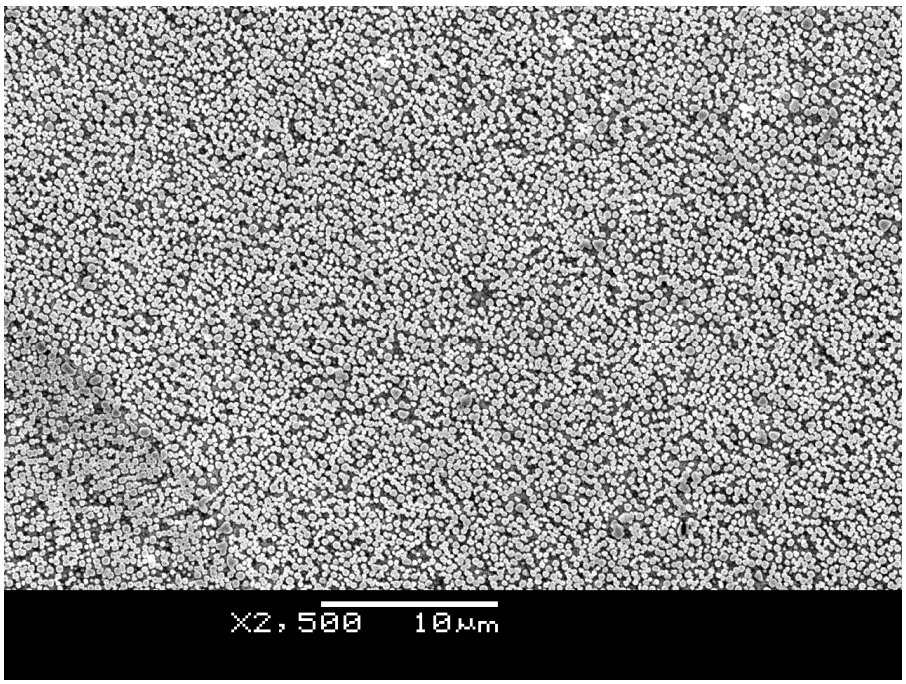

Figure 20 Low magnification SEM picture of coarse grain/supersolvus microstructure.

Grain sizes were tightly clustered between 24 and 54 μm for all materials. RR1000 produced the smallest grains for all treatments while Alloy10 produced the largest. Average grain diameters for LSHR, Alloy10 and RR1000 were 41.8 μm, 44.7 μm, and 33.3 μm respectively. In terms of ASTM grain size these sizes correspond to 5.9 for LSHR, 5.7 for Alloy10, and 6.5 for RR1000. Keep in mind that in the ASTM scales increasing grain size means a decreasing ASTM number.

Figure 21 shows grain size variation characterized by mean grain diameters graphed against the ratio of solution heat treatment temperature to each alloy's γ' solvus temperature. Grain size results are initially presented as a function of solution temperature because this step is mandatory to achieve grain growth. Looking at the results as a function of solution temperature in more detail, a trend can be identified of increasing grain size for increasing solution temperature in LSHR and Alloy10, but not in RR1000 alloy in which the grain size appeared to have remained constant with solution temperature.

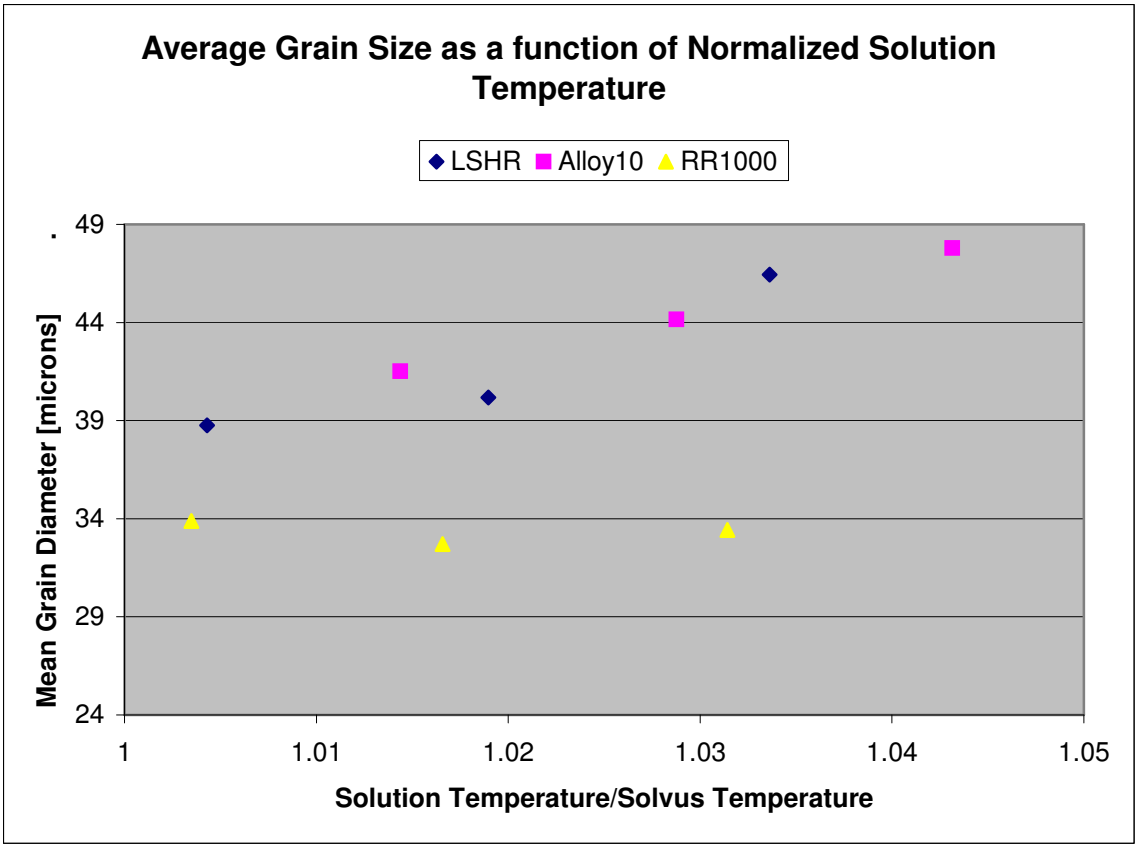

Figure 21 Graph of mean grain diameter as a function of the ratio of solution temperature to solvus temperature. Initial grain sizes were 10-15 µm.

It is not surprising that the solution temperature is the primary processing variable of those studied that determines grain size. Supersolvus temperatures cause the dissolution of primary γ' and grain boundary species which allows for grain growth. Once above the γ' solvus temperature, the trend of increased grain size with increased temperature is consistent with published results for supersolvus grain growth in PM alloys. One would expect to see an increase in grain size as a function of solution temperature, as higher temperatures promote the dissolution of grain boundary carbides and the prior particle boundaries beyond the basic dissolution of grain boundary γ', both of which are believed to limit the grain growth of PM alloys. Although one is able to

identify trends in grain size of LSHR and Alloy10 as a function of solution temperature, the results vary relatively little between the various materials.

The RR1000 grains were consistently smaller than the LSHR or Alloy10 specimens by approximately 25%. Also, the above trend of increasing grain size with solution temperature was absent in the RR1000 specimens, which seemed to maintain a constant grain diameter, regardless of solution temperature. This plateau in grain size for RR1000 is most likely attributed to the processing temperatures, which are dictated by the alloy solvus temperature. The solvus temperature for each material is based on composition; therefore differences between the compositions of the alloys will be reflected in the solvus temperature. Graphing the grain size versus the ratio of solutioning temperature to solvus temperature is expected to capture this aspect of the relationship. However, in Figure 22, we can see the grain growth trends between various alloys are distinct so normalizing the solutioning temperature with the solvus temperature does not lead to a unique relationship between grain growth and temperature. This is because grain growth also requires diffusion of alloying elements as the particles/precipitates dissolve. The rates of diffusion increase exponentially with temperature independent of the solvus temperature making the relationship between grain growth and the ratio of the temperature to the solvus temperature not unique. We, thus, plot the data in Figure 22directly with temperature to explore this relationship further.

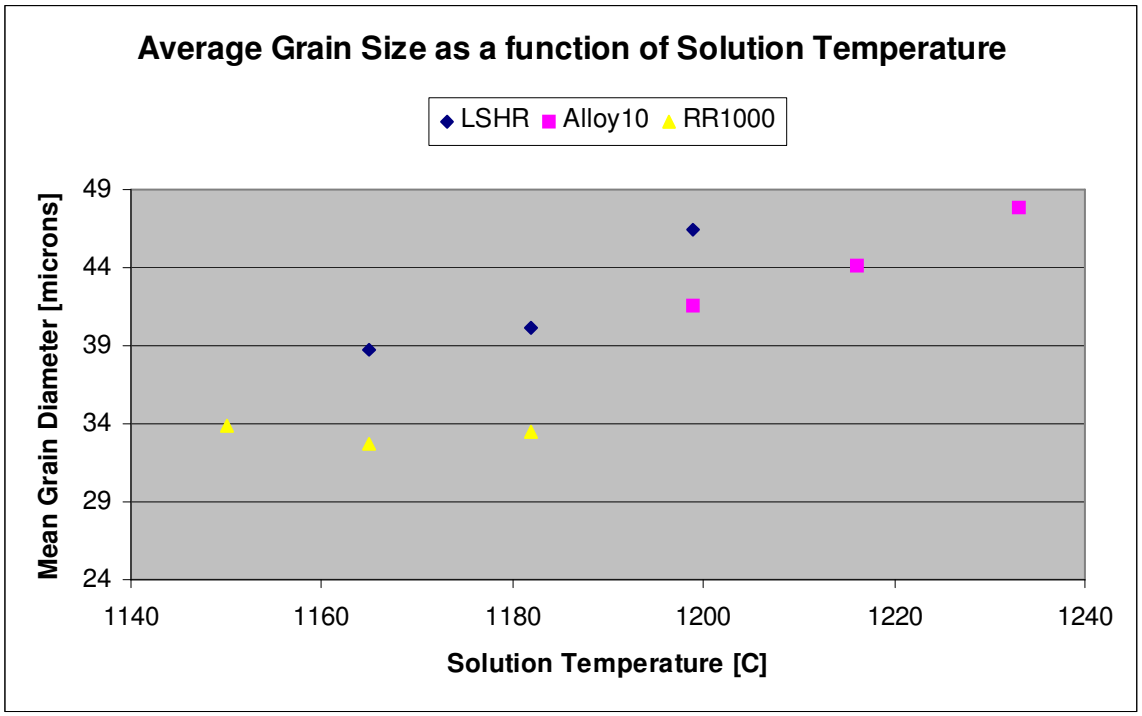

Figure 22 Grain size as a function of solutioning temperature.

In Figure 22, one can see that specimens solutioned at the three lower temperatures show no further grain enlargement, while specimens solutioned at the three higher temperatures do show enlargement as a function of solution temperature. The Alloy10, which was subjected to the three higher temperatures, clearly shows a linear increase in grain size, while the RR1000, which was only subjected to the three lower temperatures shows no additional growth. The LSHR, which was subjected to the three intermediate temperatures does not show additional growth at the lower temperatures, but does at the highest processing temperature. Thus, plotting the grain growth trends directly with temperature appear to provide a better correlation between the various alloys than with solution temperature normalized by the solvus temperatures. There seems to be a threshold somewhere between 1180˚C and 1200˚C, below which

coarsening of the grains does not occur and above which it does. This appears consistently for the alloys, suggesting that the mechanism of this is weakly dependent of compositional differences and far more strongly dependent on temperature. This is explored further in a mathematical relationship.

Fundamentally, grain growth is based on the movement of elements with in the material. As such, it is dependent on concentration gradients and governed by the flux equation. In this equation J is the flux component, D is the diffusion coefficient, and $\partial c/\partial x$ represents the concentration gradient.

$$J = -D\left[\frac{\partial c}{\partial x}\right]_t \tag{6}$$

Above the solvus temperature, concentration gradients would be generated by the dissolution of primary γ' which contain alloying elements such as aluminum and titanium. For a given alloy, the concentration gradients are the same for each set of processing conditions, but the solutioning temperature is varied. Keeping this in mind, the key term to consider in this situation is the diffusion coefficient, D. Equation 7 represents the diffusion coefficient, where D_o is the diffusion constant, Q is the activation energy, and R is the physical constant.

$$D = D_o \exp\left(\frac{-Q}{RT}\right) \tag{7}$$

These equations are included to shed light on the role of temperature on grain growth. Mass flux is a function of diffusion and the concentration gradient within the material. Diffusion in turn is an exponential function dependent on temperature. The phenomenon of additional grain growth at sufficiently high temperatures is clarified when one considers the dependence of diffusion, and thus mass flux, on temperature.

In this equation, it is the absolute temperature that is used, regardless of what the solvus temperature for the material might be. The solution temperature is chosen based on the solvus temperature of the material and it is this temperature that will limit the effective diffusion rate, and in turn the rate of flux, or mass transfer. Referring back to Figure 22, it is evident that at lower temperatures the alloys, regardless of composition, are not coarsening as they are at higher temperatures. This is attributed to the lower rates of diffusion at lower temperatures that limit the rate of flux, which is the means of structural changes in the materials. Independent of compositional variations, which may affect diffusional mechanisms, simple consideration of the absolute temperatures used for processing can account for differences in grain growth.

RR1000 has the lowest solvus temperature, which can be beneficial in regards to processing. RR1000 has the highest level of Cr, which is known to lower solvus temperatures. It is likely that in the processing of RR1000, which occurs at lower temperatures compared to the other materials, solutioning temperatures sufficient for the dissolution of grain boundary γ' are used, but these temperatures are not sufficient to facilitate rapid diffusion rates. If diffusion is limited, grain growth will be also be limited.

Compositional variations may lead to another mechanism that can limit the growth of grains in RR1000. Specifically, one must consider variations that would affect the presence of prior particle boundaries (PPBs). Published works have concluded that PM material "experiences minor grain growth after the gamma prime is in solution, limited apparently by the prior particle boundaries" [42]. As mentioned previously, RR1000 has the highest levels of Cr, which also promotes grain boundary species. It is possible that the increase in the Cr, in addition to lowering the solvus temperature, increases the amount of PPBs present during processing and heat-treatment. In this way the limiting effects of PPBs are exaggerated and results in minimization of the extent of grain growth.

Current work at the University of Cambridge has also shown a plateau in grain growth in RR100 above the solvus temperature and work there will establish the mechanisms behind this phenomenon. Grain growth is only the first of many features in which RR1000 behaves differently from the other alloys studied and compositional variations will be repeatedly referenced to explain these differences.

Having explored the variation of grain size with solution temperature, we turn our attention to the variation within a single solution temperature. Referring again to Figure 22, for each solution temperature, there are six specimens of an alloy, each having a unique combination of cooling rate and intermediate hold. Because of the variability of results for a given alloy at a specific solutioning temperature, we must conclude that additional processing parameters are affecting the grain growth. This variability of values between the six points at a given solution temperature is demonstrated in Figure

23. Error bars are included, based on the 95% confidence intervals described by ASTM E112, the specification relevant to this measurement.

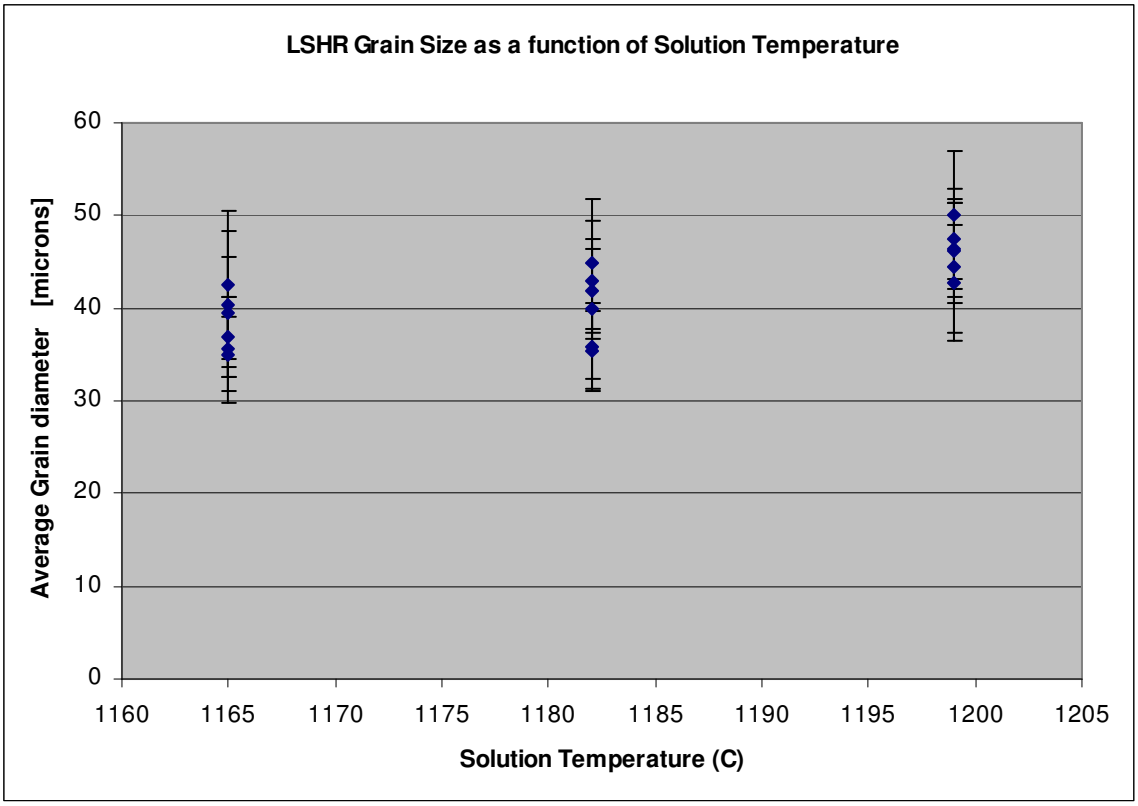

Figure 23 Variability of grain size for LSHR as a function of solution temperature. 95% confidence interval error bars are displayed.

Figure 24 isolates the effects of cooling rate and hold temperature by graphing grain size as a function of these parameters for a single solution temperature. Grain size values tend to decrease with increasing cooling rate. Physically this makes sense, as slower cooling rates would mean that the material spends more time above solvus temperatures. The proximity of values for the two intermediate hold temperatures are very close together, within the 95% confidence intervals used. We would not anticipate hold temperature having an effect, as it is well below the solvus temperatures necessary for grain growth. From this it is clear that in addition to solution temperature, the cooling

rate parameter is affecting the grain size response of the alloy. Figure 25 corroborates the variation of decreasing grain size with increasing cooling rate. Again, differences between values for the two hold temperatures are within the expected scatter for measured values.

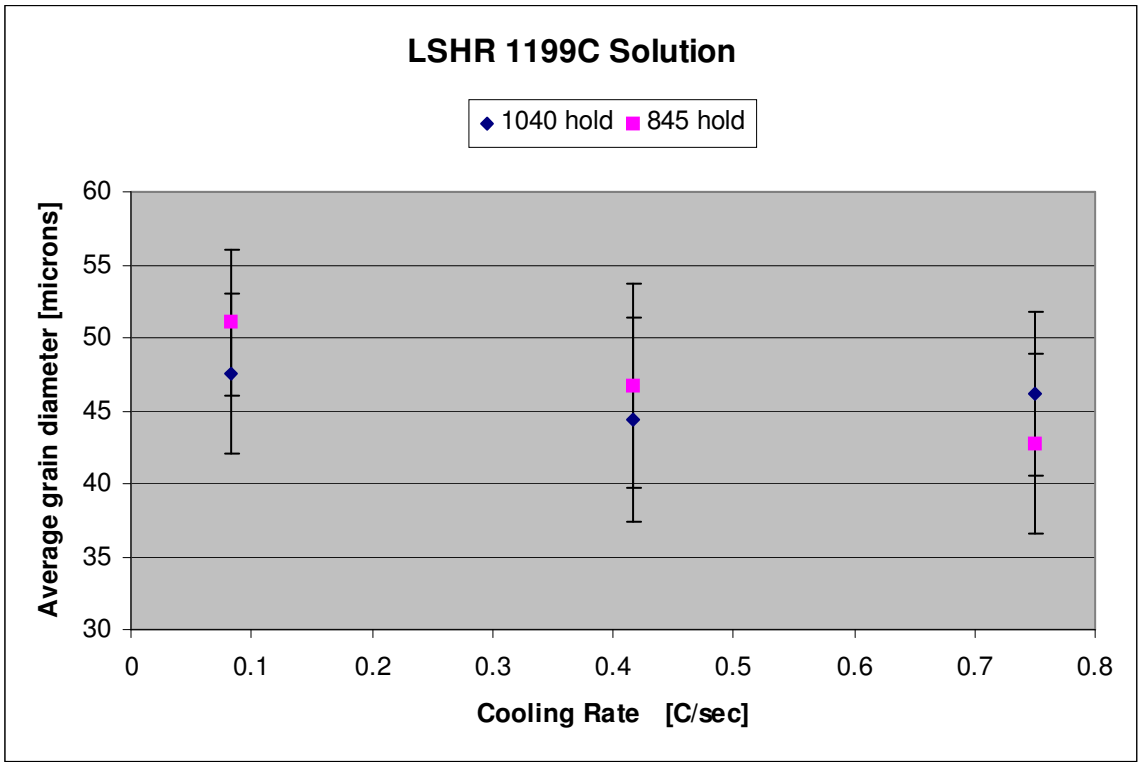

Figure 24 Variation of LSHR grain size with cooling rate for solutioning at 1199˚C.

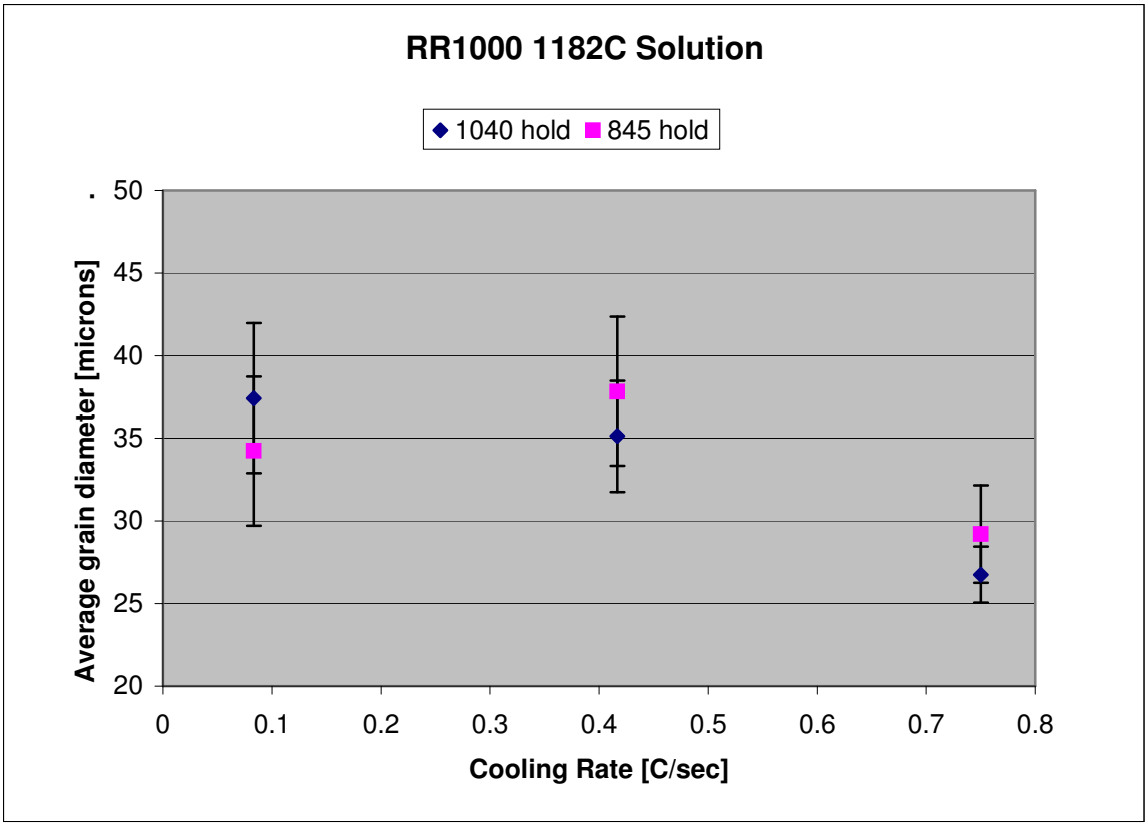

Figure 25 Variation of RR1000 grain size with cooling rate at 1182˚C.

This complex interaction is indicative of the multiple processes contributing to grain growth that are occurring simultaneously. Dissolution of primary γ', elimination of PPBs and grain boundary carbides or borides, alloying element diffusion, re-precipitation of γ', especially at the grain boundaries: all of these processes must occur simultaneously, all are uniquely affected by temperature, and all are interacting. Obviously this is an intricate balance of processes and processing; one that is difficult to assess directly.

4.1.1. ANN Predictions of Grain Size

The complexity of interactions between variables that influence the grain size make it a perfect situation to apply machine-learning techniques. The nature of the ANN approach is ideal to reconcile the interactions of these parameters. Use of ANN modeling allows us to predict grain size for a given set of processing parameters without having explicitly defined the relationship between these parameters. Using the quantified results for grain size a network can be trained so that the interaction of processing parameters is implicitly defined. Once the network has been successfully trained, the relative weights given to each connection can be used to identify the relative importance of input parameters.

Multiple networks were trained in order to establish the inputs and architecture that produced the most reliable model. In this case, architecture refers to the number of nodes in the 'hidden layer'. A balance between the number of inputs and the amount of training data must be sought. With a smaller database for training, the number of inputs must be limited for the network to be properly trained. However, sufficient inputs must be included to incorporate the relevant parameters to the phenomenon. If important inputs are omitted the model predictions for test data would become very inaccurate. The reliability or 'success' of the model is assessed by a relative root mean square error (rRMSE) as described in the experimental procedures.

For grain size, an initial network was trained using the three processing parameters and the majority of alloying elements. Alloying elements not included were those whose value varied only minimally between alloys. It was known that the training

data, in this case 47 sets, was insufficient to produce a successful model for this number of inputs. The goal of this iteration was merely to establish which inputs would be most heavily weighted in the network. These weights are taken as an indication of the importance of the input parameter to the outcome. Based on these weights, the number of inputs was pared down to better suit the size of the training database to produce the most accurate predictions.

Inputs for the most promising intermediate network were solution temperature, cooling rate, hold temperature, and weight percent of Al, Mo, Nb, Ta, Ti, and W. Calculation of rRMSE for this network generated a value of 0.13, which can also be thought of as an average error of 13%. Resulting weights from this network suggested that the cooling rate, solution temperature and the Al, Mo, and Ti content were the most relevant inputs. Figure 26 is a graphical representation of the connection between inputs, nodes, and the output. The green sliding scale at the bottom controls the weights being displayed, in order of relative 'importance'. In this instance it is showing the most highly weighted node and its connections to input values.

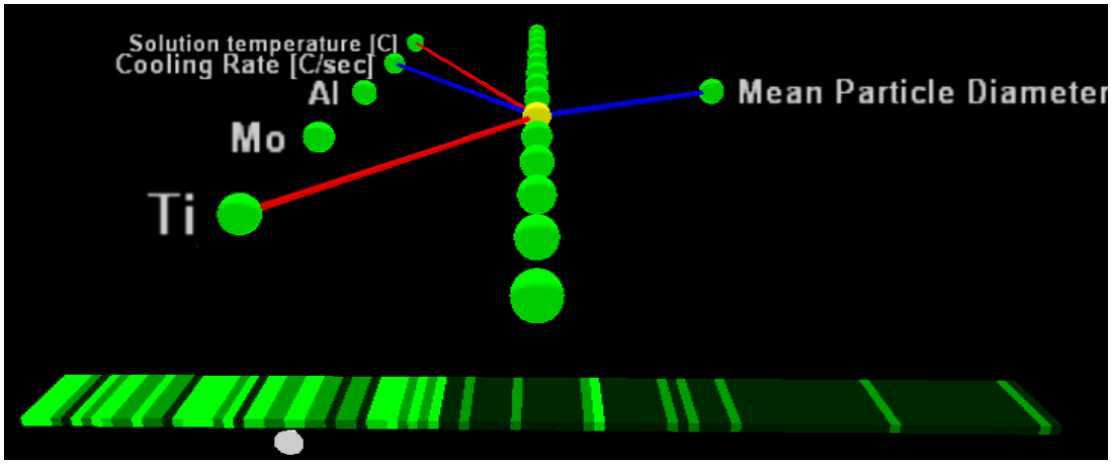

Figure 26 Graphical representation of ANN connections.

From this, further models were developed using these 5 inputs, which was a more appropriate number relative to the size of the training dataset. The most successful model for prediction of grain size based on these inputs had 14 nodes and produced an rRMSE of 0.08. Figure 27 shows the graph of actual values versus predicted values for grain size calculated from the test data. Solution temperature was the most highly weighted input, followed by cooling rate. The distribution of points both above and below the x=y line indicates that there was not a systematic bias to the results. Table 8 presents the randomly selected data set used for testing and calculation of error.

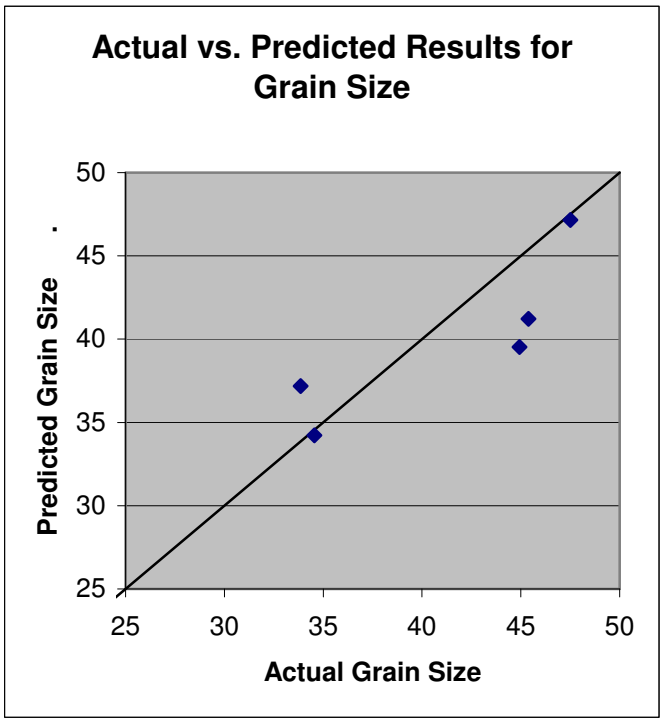

Figure 27 Comparison of actual values to ANN predicted results.

Table 8 Test data for grain size neural network model

Alloy	Specimen ID	Solution Temperature	Cooling Rate	Al	Mo	Ti	Actual Result	Prediction
LSHR	L3	1165	0.416666667	3.5	2.7	3.5	44.93215063	39.53
LSHR	L17	1199	0.083333333	3.5	2.7	3.5	47.49924689	47.155
RR1000	R2	1150	0.75	3	5	3.6	33.86411104	37.18
Alloy10	A7	1216	0.75	3.69	2.73	3.93	45.38704725	41.22
RR1000	R11	1165	0.083333333	3	5	3.6	34.55598401	34.22

This work is a good example of the application of machine learning to predict the outcome of complex metallurgical phenomenon. The results for the weighting of the inputs make intuitive sense based on our current understanding of the relevant processes. General knowledge of the physical processes taking place is consistent with the primary

inputs. We would expect grain size to scale most directly with solution temperature, as the time above solvus is required for grain growth. Further, cooling rate will determine how long beyond the solution time the sample remains above solvus. Hold temperatures, which are well below solvus, were not a necessary input into the network. The model is able to accurately predict the grain size produced for a given combination of factors. In this way the neural network is able to aid in our understanding of process-chemistry-microstructure interactions, as well as its predictive capabilities being a tool in alloy development.

4.2. γ' precipitates

Within the literature related to microstructure and behavior of Ni-base superalloys, γ' precipitates are possibly the most frequently referenced feature. They certainly play a dominant role in the results and discussion of this project. As such, the formation and characterization of γ' precipitates requires special attention.

Quantitative discussion of precipitates is concentrated on secondary γ', with limited discussion of grain boundary γ' and tertiary γ'. Examination of all micrographs confirms that the primary γ' was fully dissolved by the supersolvus heat-treatment process. Also, micrograph resolution was at times insufficient to reliably quantify tertiary γ' features; approximately 70% of the specimens have been characterized for tertiary γ'. The discussion is based on average precipitate size and size distribution, as well as particle morphology, characterized by circularity.

4.2.1. Precipitate Size

Average size and size distributions for each specimen were generated based on measurements of 100-300 individual precipitate particles to validate the use of an average size. The majority of specimens displayed a basically normal size distribution with some skewing to the right; all were mono-modal distributions. Based on the distributions, it is reasonable to use an average precipitate size to describe the results for the particle population of a given heat treatment. However, an average particle size for all specimens of a given material is not considered, due to the distinct variation of size with processing.

While grain size was most influenced by solution temperature, no discernable relationship existed between solution temperature and precipitate size distribution or circularity. This is not surprising considering that the precipitates under consideration are 'secondary' indicating their formation on cooling from the solution hold. As stated by Jian Mao, et al. "The size, morphology, and distribution of γ' precipitates that are developed inside the grains and along the grain boundaries are determined by the ageing treatment as well as the cooling process after the solution annealing" [43]. If one considers the formation of γ' as a precipitation and growth process, the growth (i.e. increase in size of particles, not number of particles) can be isolated. The γ' particles will precipitate at a distinct temperature/saturation, which the alloys experience at a distinct, singular point when the alloy crosses below the solvus temperature. Growth of the precipitated particles continues over a range of temperatures below the solvus as the heat treatment continues. Thus when considering the size or shape to which the particles have grown, it is the conditions it experiences after solutioning that are most relevant.

Therefore relationships between size and circularity, and cooling rate and secondary hold temperatures can be easily observed.

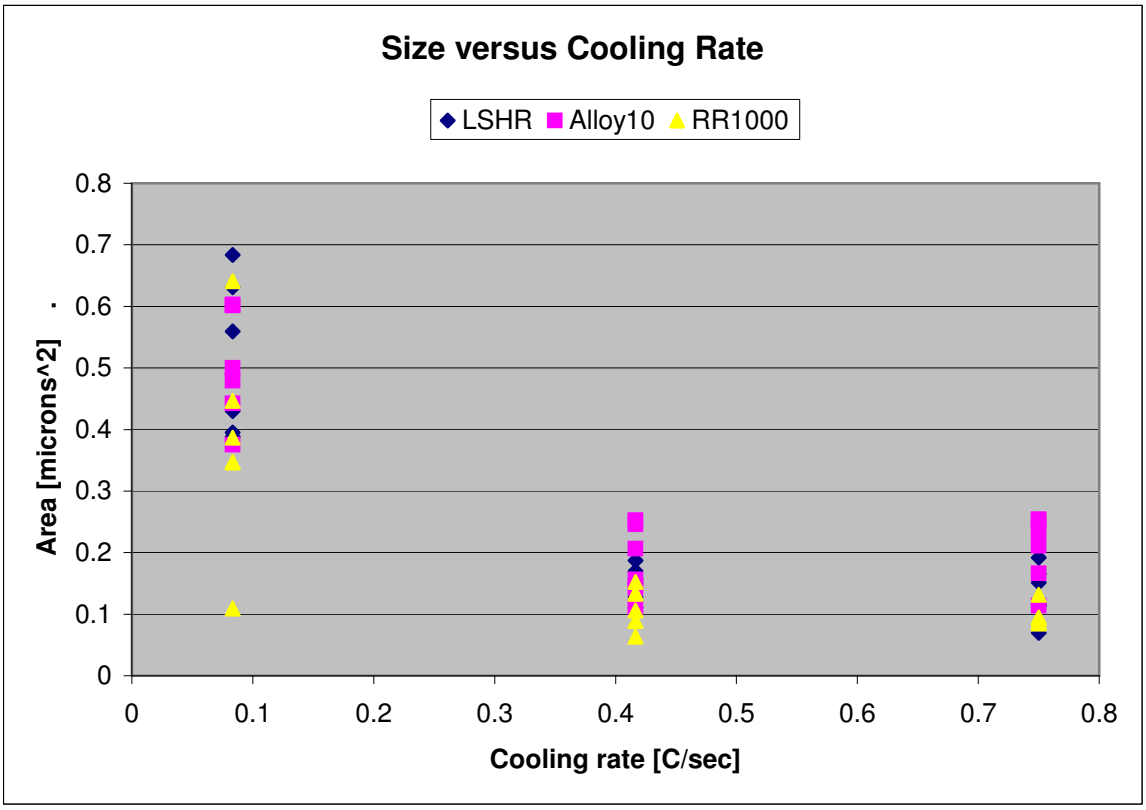

Figure 28 Secondary γ' particle size as a function of cooling rate.

Secondary γ' particle size measured as area in square microns, was less than 1 μm^2 for all heat treatments. The slowest cooling rate produced the widest spread of sizes, with a minimum size of 0.109 μm^2 and a maximum size of 0.683 μm^2. The intermediate and fastest cooling rate produced the similarly sized particles, having the least spread, particles ranged from 0.069 to 0.465 μm^2.

In general precipitate size decreased with increasing cooling rate. Intuitively this is consistent, as the material would spend less time at the high temperatures necessary to

drive the diffusion that causes precipitate growth. One might also expect a larger precipitate size for the material with a higher secondary hold temperature, since diffusional growth activity would be favored at the higher temperature. However, as can be seen in Figure 29, there is no correlation between secondary γ' particle size and secondary hold temperature. To understand why this is the case, one must keep in mind that the precipitates under consideration are "secondary γ'", also referred to as "cooling γ'". These particles are formed during the cooling process. It is the "tertiary" or "ageing γ'" which would be affected by the secondary hold temperature.

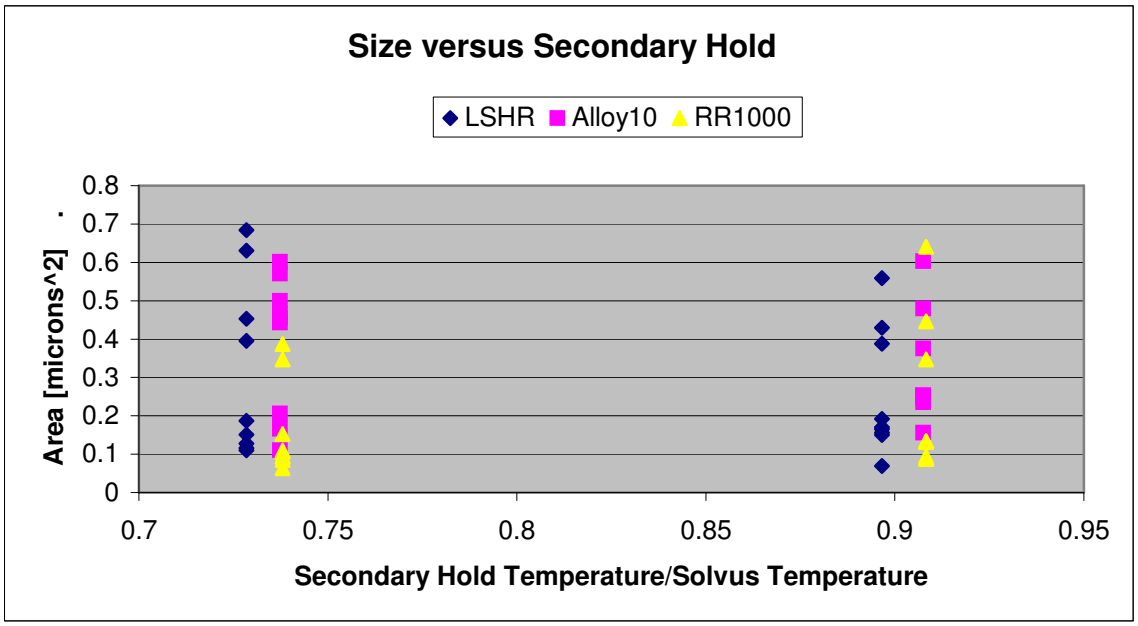

Figure 29 Precipitate particle sizes as a function of the ratio of secondary (post-solution anneal) hold temperature to solvus temperature.

Tertiary γ' was visible in the majority of SEM images, but at times not with sufficient clarity to be quantified with statistical relevance. Average sizes were calculated based on 20-60 tertiary particles for select specimens. Calculations could be

skewed towards the larger tertiary particles, as these are more likely to be visible in the micrographs. Also, the particles had to be outlined manually before automated measurements were taken. This could lead to a higher level of inaccuracy than measurements of the secondary γ' particles, where outlining and measuring were both automated. Therefore, values for the fine tertiary γ' should be taken as estimates.

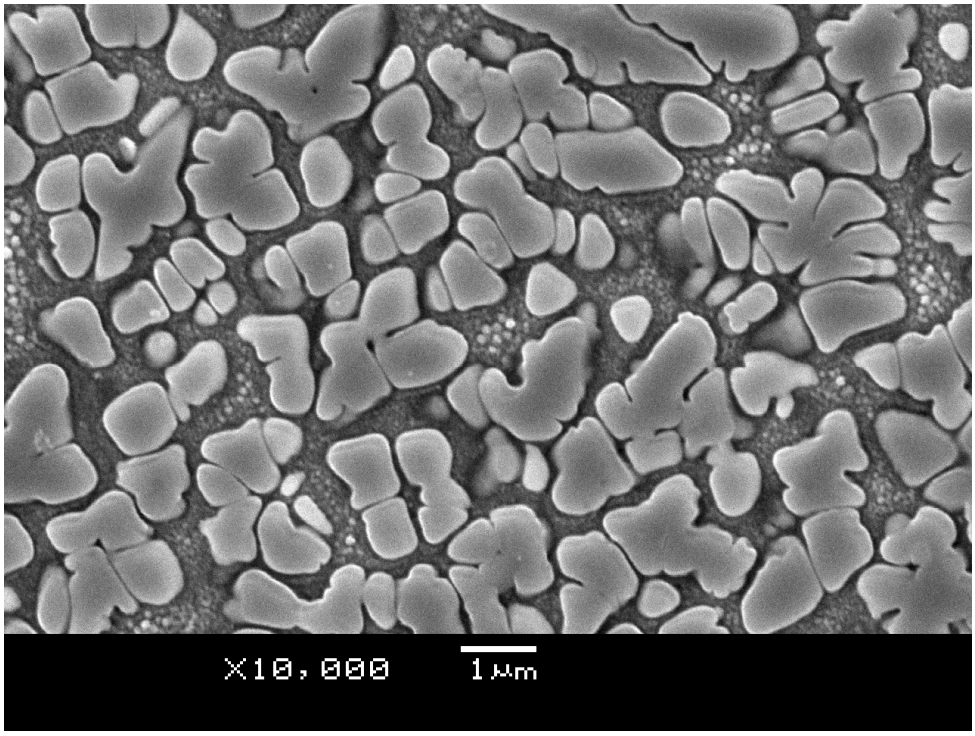

Figure 30 SEM image showing the fine tertiary γ' in the channels between large, pseudo-dendritic γ' in Alloy10.

Tertiary γ' size decreases with increasing cooling rate, much like the secondary γ'. The average tertiary particle sizes incorporating all alloys, for the slow, intermediate, and fast cooling rates were 0.0057 μm^2, 0.0035 μm^2, and 0.0027 μm^2, respectively. Although over all secondary γ' size varied by alloy, tertiary γ' sizes were similar, regardless of alloy type. As fully expected, there was no correlation between solution

temperature and tertiary γ' size. These results can be seen in Figure 31, graphed as a function of cooling rate.

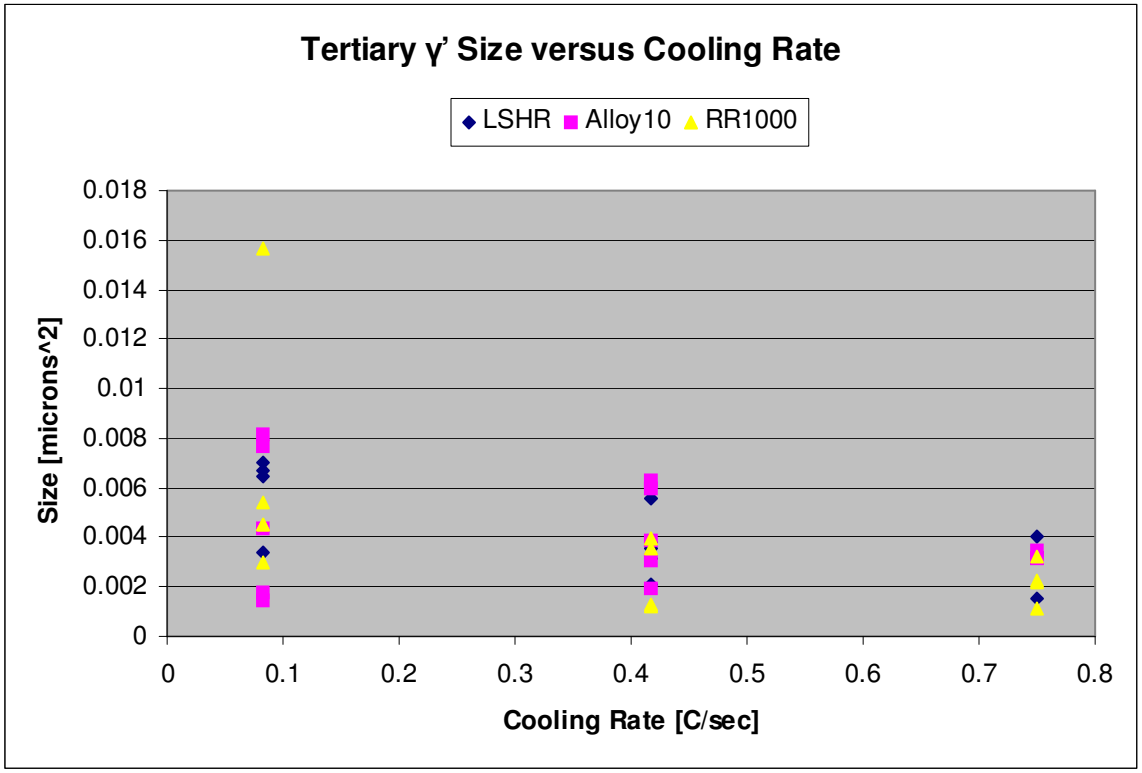

Figure 31 Tertiary γ' size as a function of cooling rate.

Pair-wise comparison of tertiary γ' size versus secondary hold temperature for a given cooling rate indicates that the higher hold temperature produces a smaller precipitate size. This trend is obvious for the intermediate slowest cooling rate, as can be seen in Figure 32. The correlation seems weaker for the faster cooling rates. At higher temperatures one might expect increased coarsening. Therefore, this result can seem counterintuitive, but is easily explained. The higher secondary hold temperature was 87-90% of the solvus temperatures for these alloys while the lower hold temperature was 71-73%, depending on the alloy. At such high temperatures it is likely that some γ'

particles, especially the very fine γ', are being resolutioned into the matrix. They would then re-precipitate and be coarsened with cooling from hold, which is a more rapid rate than the controlled cooling from solutioning. The lower secondary hold seems to be low enough that resolutioning does not take place and the tertiary particles are simply coarsened.

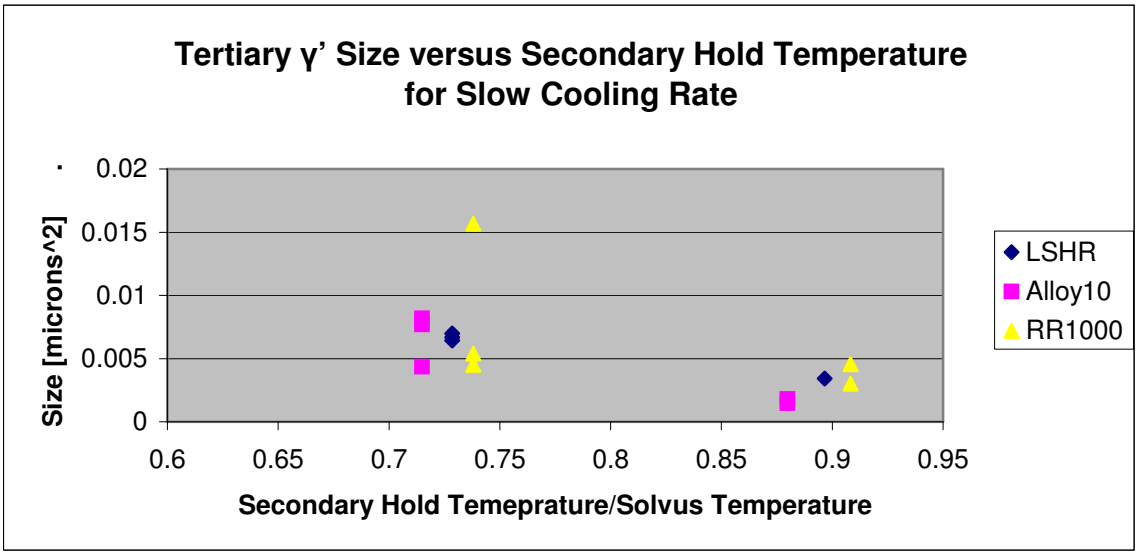

Figure 32 Pair-wise comparison of tertiary γ' size versus secondary hold temperature for a single cooling rate.

Grain boundary γ' particles were not thoroughly quantified in this project, although some estimates were made for select specimens. In addition, micrographic evidence confirms that grain boundary γ' coarsens as a function of cooling rate. Grain boundary γ' in specimens cooled at the fast and intermediate rate were generally around 0.6 microns^2 for LSHR and Alloy10. At the slowest cooling rate, grain boundary γ' averaged as large as 5.5 microns^2 for the Alloy10 and LSHR; and 0.9 microns^2 for the RR1000 specimens. These results reflect the trend reported for the secondary and tertiary

γ’ where the fast and intermediate cooling yielded similar values, with the slow cooling being distinctly different.

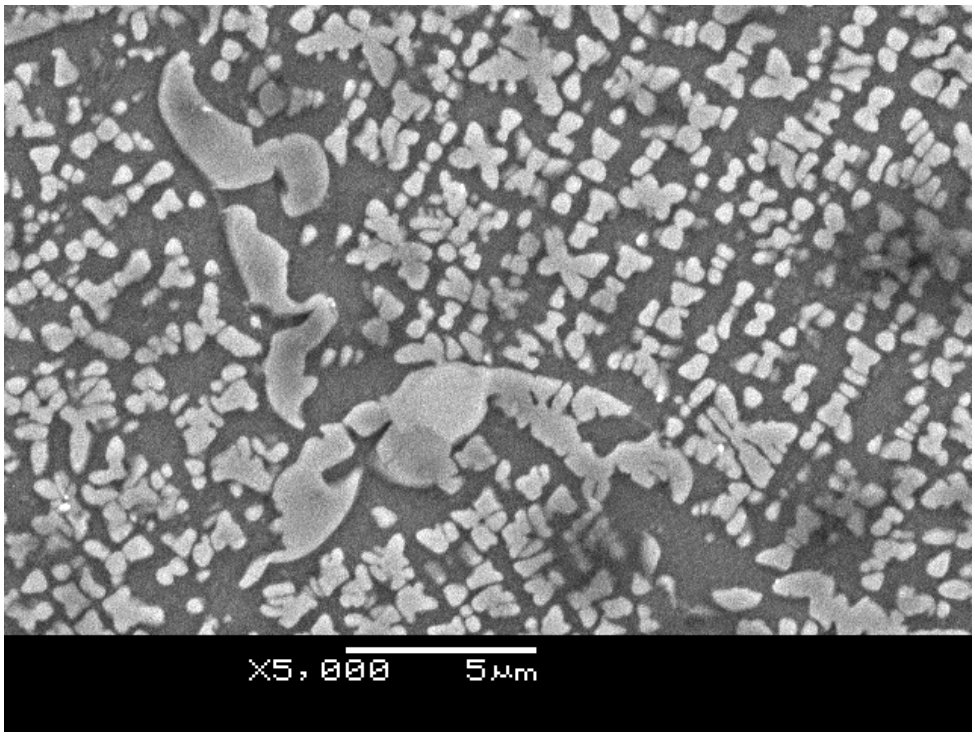

Figure 33 SEM image of grain boundary γ' for slow-cooled LSHR.

For the LSHR specimens cooled at fast or intermediate rates, grain boundary γ’ particles were 3.5-4 times larger than the secondary particles. For Alloy10, the grain boundary particles were approximately 2.5 times larger than the secondary particles for fast and intermediate cooling. For both LSHR and Alloy10 receiving the slowest cooling rate grain boundary γ’ particles were 10 times larger than the secondary γ’ on average. RR1000 material showed the smallest difference of all the alloys between the secondary γ’ size and the grain boundary γ’ particles. Even at the slowest cooling rate the grain boundary particles were only about twice the size of the secondary γ’.

The difference in size between grain boundary γ' and secondary γ' is due to the faster diffusion along the grain boundaries. The boundaries serve as an accelerated path for diffusion of γ'-forming elements, thus, γ' particles adjacent to the grain boundaries are coarsened more rapidly than the particles within the bulk of the grain.

4.2.2. Precipitate Morphology

As with size, precipitate circularity showed no universally concrete trends. However, general observations can be made. For example, the results for circularity for the specimens with the slowest cooling rate stand out as having the lowest values, indicating the most deviation from a circular precipitate shape. This holds true for all three materials and is a result of the increased amount of time that each slow-cooled specimen is exposed to higher temperatures. As with particle size, the increased exposure to high temperatures allows for increased opportunity for thermally accelerated processes, such as diffusion, to take place.

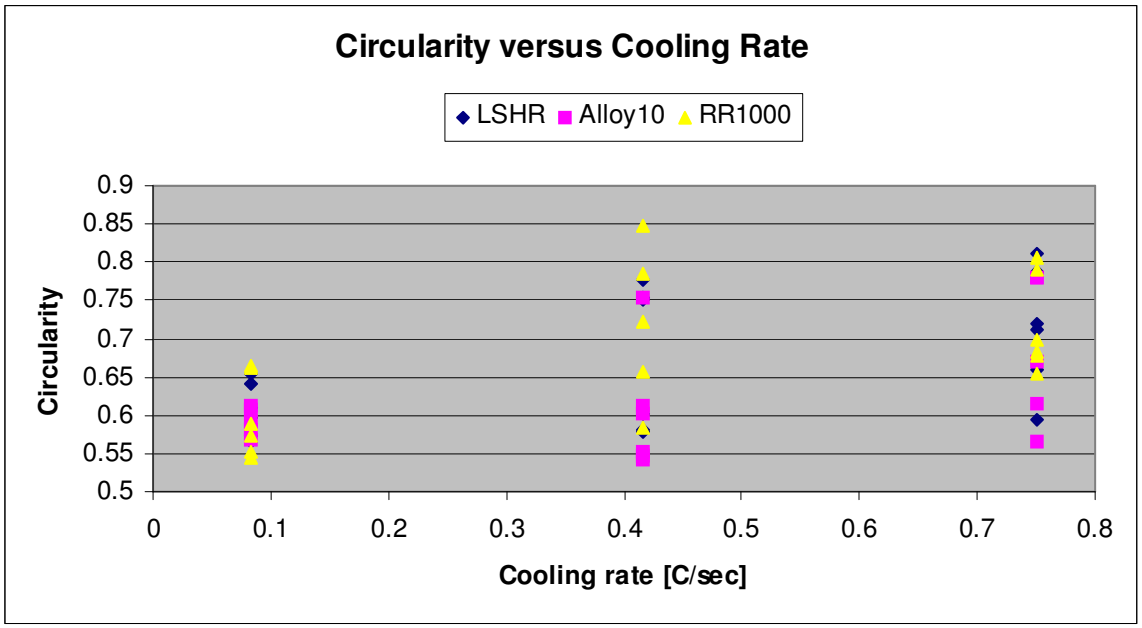

Figure 34 Circularity as a function of cooling rate after supersolvus solutioning hold.

When considering Figure 28 or Figure 34, one must keep in mind that for a given cooling rate, additional processing variables are being iterated. In other words, for the six specimens of each material processed at a specific cooling rate, there are six unique combinations of solution temperature and secondary hold. For example, Figure 35 shows the variation of circularity with cooling rate, with all other processing variables held constant. This explains the spread of values for a given alloy at a given cooling rate. Also it is evidence of the complex interactions involved in the processing-structure paradigm. Such observations validate the application of machine learning to untangle the complex multi-variate relationships.

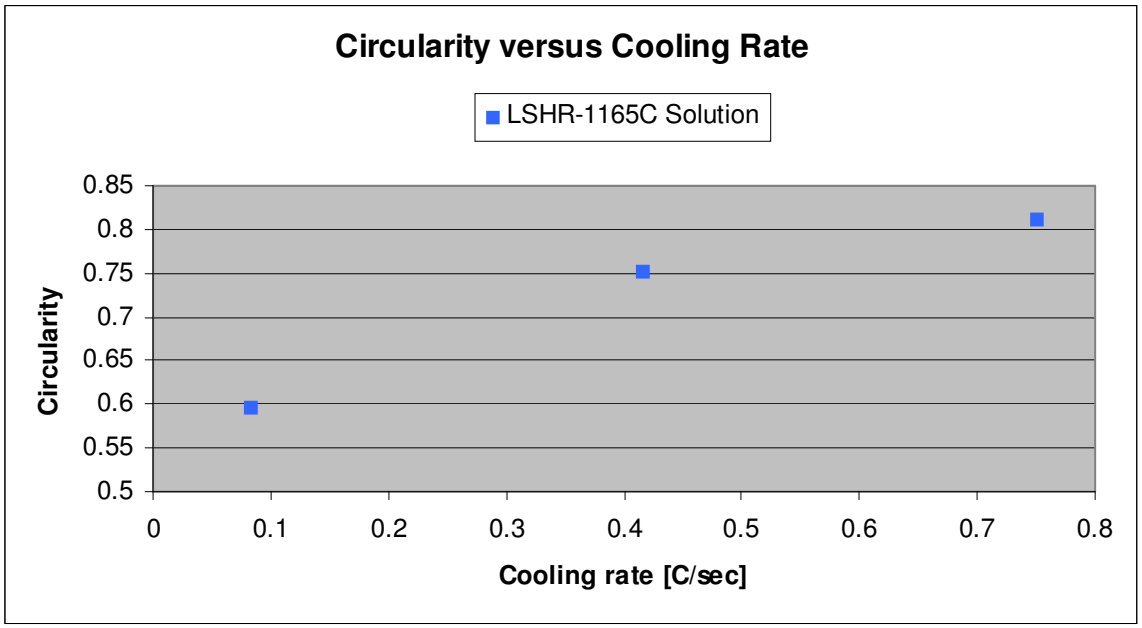

Figure 35 Circularity versus cooling rate for a single solution temperature of LSHR.

Regarding the quantity of circularity, it is important to consider that a given numerical value of circularity does not represent a unique shape. It is only the ratio of area to perimeter, standardized by that of a circle. It is therefore possible for two irregular particles to produce the same value of circularity, but to be entirely different shapes. When considering the highly irregular shapes that may be produced by precipitate growth, circularity should not be the sole factor for assessment of precipitate morphology. Lacking a more precise or robust numerical quantity to describe particle shape, some qualitative discussion of morphological differences is in order. In this context, although the trends mentioned are not invalidated, differences between precipitate formations in each alloy can be made more obvious by qualitative assessment.

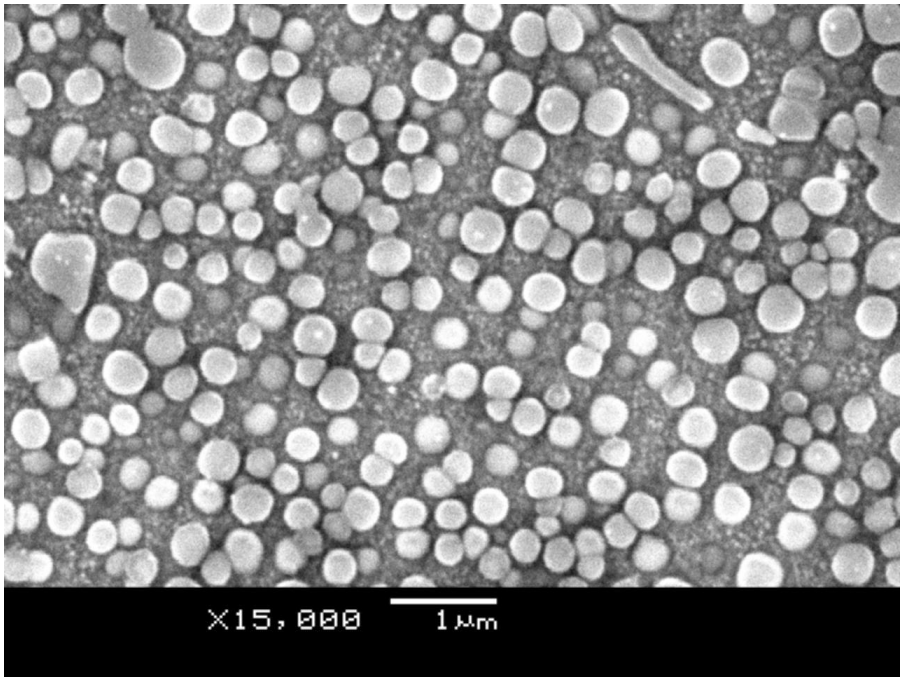

Figure 36 SEM of fast cooled RR1000 showing preserved round precipitate shape.

Initially, all precipitates are spherical, forming into alternative shapes as the particle grows with cooling and ageing. The initial spherical shape is preserved in the fast cooled specimens. An example of this for can be seen in Figure 36. The SEM images in Figure 37, Figure 38, and Figure 39 are representative of the shape ultimately assumed by the γ' particles in each material. A complete set of images can be found in the appendix. For this discussion these images will be taken as descriptive of the shapes seen for all larger precipitates of a given material.

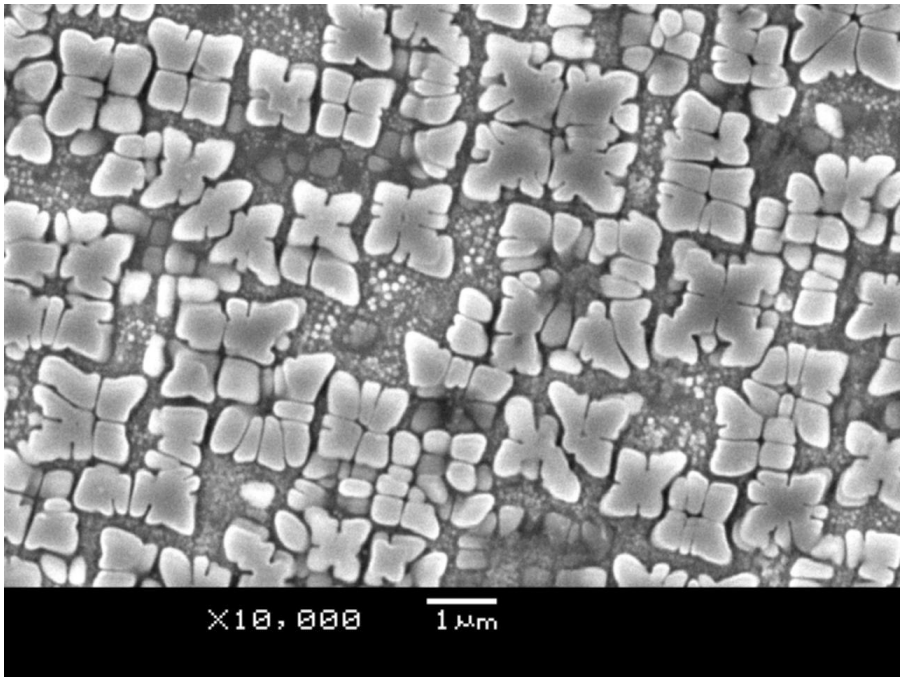

Figure 37 SEM image of slow cooled LSHR showing γ' precipitates in relief.

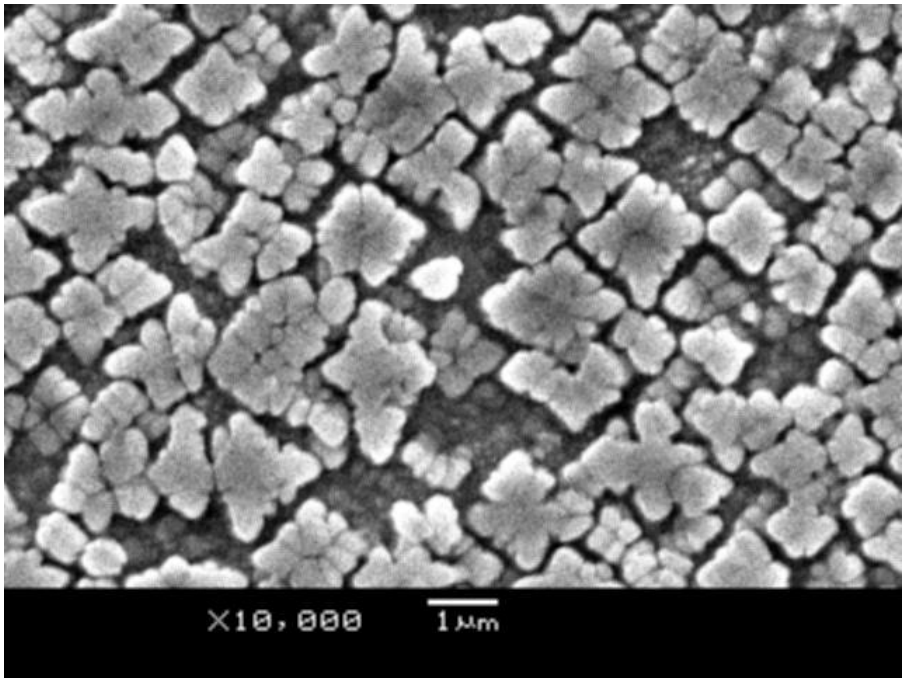

Figure 38 SEM image of slow cooled Alloy10 showing γ' precipitates in relief.

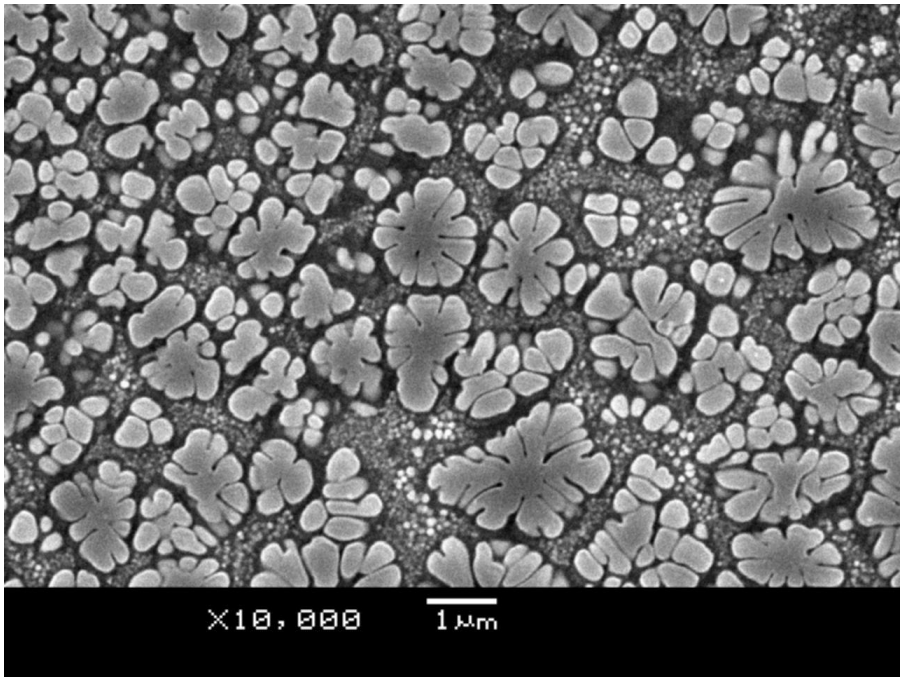

Figure 39 SEM image of slow cooled RR1000 with γ' in relief.

From the graphs of size and circularity as a function of cooling rate, one can see that all of the values are somewhat similar. Size, as described by the cross sectional area, can be simply assessed from numerical values. However, the distinct differences in particle shape, which are not obvious from circularity values, become strikingly apparent when looking at SEM images of the microstructure. LSHR and Alloy10 form distinctly cubic precipitates (seen as square or diamond in cross-section). Both show a distinct tendency to form a pseudo-dendritic structure by preferential growth on the corners of the cubic precipitates. The RR1000 material, on the other hand, shows little indication of cubic or pseudo-dendritic formation. Instead, the spherical particles seem to form a still-spherical lobed structure, sometimes referred to as flower-like.

The difference in morphology can be explained by the difference in composition. These compositional differences result in a change in γ/γ' lattice parameter differences,

also referred to as misfit, that causes a shift in the balance of factors that dictate the morphology of the particle. These include surface energy of the particle, the elastic strain energy and interaction between particles. This misfit can be either negative or positive, depending on which lattice parameter is larger. In the case of nickel-base superalloys both the γ matrix and γ' precipitates are face-centered cubic (FCC) phases, so that the precipitates tend to be coherent with the matrix. Internal stress fields are generated by the accommodation of both the coherency and lattice mismatch.

During the growth process of the γ' particles, morphology will develop so as to minimize the combination of surface energy and lattice strain (due to misfit). Based on this, the morphology of the LSHR and Alloy10 suggests that there is high lattice strain due to a large misfit. The growth of cubes with pseudo-dendritic arms takes place along crystallographically relevant directions. The exaggerated growth of the arms will take place in orientations within the FCC crystal lattice that minimize the internal stress fields generated. The nature of the cubic lattice is reflected in the cubic precipitate shape and the perpendicular orientation of the arms and branches off of the arms. The high misfit dominates the development of the particles. The formation of cubic particles creates more surface area (i.e. increased surface energy). Despite this increase, this shape is still energetically favorable due to the decrease in lattice strain.

RR1000, on the other hand, forms with no apparent crystallographic orientation. This indicates that there is low misfit and therefore small internal stress fields generated by the precipitates. Precipitates are not encouraged to grow on distinct crystallographic planes in order to minimize strain. Instead, particles maintain a spherical morphology, which minimizes the surface area for a given particle size.

Table 9 Selected components in weight percent, atomic number and radius in angstroms.

	LSHR	Alloy 10	RR1000	Atomic #	Atomic Radius [Å]
Ni	49.59	55.42	57.04	28	1.62
W	4.3	6.2	0	74	2.02
Hf	0	0	0.75	72	2.16
Mo	2.7	2.73	5	42	2.01
Ti	3.5	3.93	3.6	22	2
Al	3.5	3.69	3	13	1.82

Differences in tungsten, molybdenum, and hafnium content are most likely to cause variation in lattice misfit. These heavy elements are considered efficient matrix hardeners [1] and occur in varying amounts in LSHR, Alloy10, and RR1000. Table 9 summarizes the alloy content and the nature of the nickel matrix, as well as the heavy elements being considered, and the primary precipitate formers. RR1000, which seems to have the lowest misfit, does not contain any tungsten, only a small percent of hafnium. LSHR and Alloy10 contain relatively large amounts of these 'large' elements. Having these elements in the matrix, which are at least 24% larger than the nickel atoms that make up the majority of the matrix, is likely increase the lattice parameter of the FCC matrix. At the same time, we note that all three alloys have similar amounts of Ti and Al which combine with Ni to form the γ' phase. Therefore, they should have similar γ' lattice parameters. However, the addition of large, heavy elements to the matrix of LSHR and Alloy10 will cause an increase in their γ matrix lattice parameters that does not occur in RR1000. Since misfit is based on the difference in lattice parameters, LSHR and Alloy10 would have higher misfit than RR1000. This leads to increased internal lattice strain and consequently more cubic and pseudo-dendritic precipitate morphology.

4.2.3. ANN predictions of Precipitate Size

Application of the ANN technique was not successful for precipitate size prediction. Assessments of error for the multiple iterations of modeling attempts ranged from an rRMSE of 1.21 at worst to 0.33 at best. These values are 5-10 times worse than the error for grain size predictions discussed in the previous section. Figure 40 shows the predicted versus actual values for test data of average precipitate size for the most successful model generate. This iteration had an rRMSE of 0.33. The predicted values are consistently lower than the actual values.

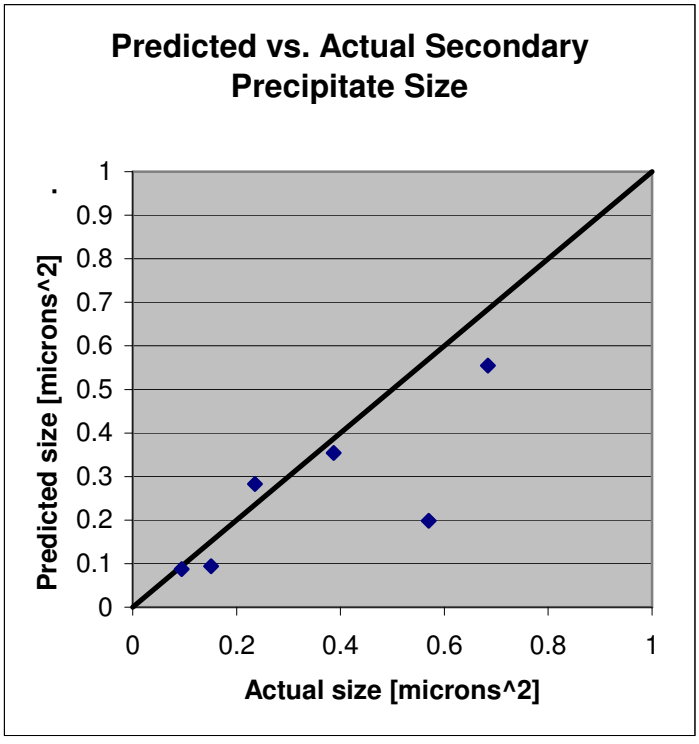

Figure 40 Graph of actual versus predicted values of secondary γ' size.

One factor that must be considered is the relative range of the output values. Predictions for an output whose range of values in the training data is very tightly clustered will naturally have less error. All combinations of inputs point to a similarly valued output, so any trained prediction should be in the relative area of those values. In other words, if all of the possible outcomes are tightly grouped, there is less opportunity for predictions to be made outside of the range. The network must be well trained in order to make predictions for results that can vary greatly. In this case it is not sufficient to merely predict a value in the general area of all of the known results.

The relative variation in precipitate size with processing and chemistry was much greater than the variation in grain size. Grain size results being so tightly clustered means that a relatively small error can be achieved just by making predictions near to the clustered results. On the other hand, precipitate size values covered a relatively wide range, leaving large room for error in predictions. This tells us that in order to make accurate predictions for a property that can vary widely, a more thoroughly trained network is necessary. Although the predictive capabilities of this work were not successful, the work does help to define the limitations of the neural network technique. In this way it teaches us how to improve on the technique for future applications.

The primary lesson to be learned from this effort is the importance of an adequate database, particularly when dealing with complex phenomenon. This modeling had the same amount of training data as the grain size work, but was unable to define the relationships successfully. One of the first networks trained, which was only intended for identifying relative importance of inputs, was most successful. It included 9 inputs, about twice the number appropriate for the amount of training data. However, subsequent

models, which reduced the number of inputs to a number more appropriate for the amount of training data, had an increased error. This tells us that the interactions of parameters controlling precipitate size are sufficiently complex as to demand several inputs into the network. In this case, it is necessary to have a proportionally larger training database. For a network to predict precipitate size at least 9 inputs were necessary, so that the training base should have been about twice as large as the existing one.

In order to train successful models to predict γ' size, a larger database of training data must first be generated. To make the effort most useful, this data should incorporate an optimized range of input parameters. The use of design of experiment (DOE) methods in the planning of data generation is highly encouraged. In this way the resources applied to experimental work can facilitate the generation of a neural network most successfully.

In addition, every effort should be made to minimize the scatter in the training data. The quality of the model is limited by the quality of the training data on which it is based. Training data that incorporates large amounts of scatter cannot define the complex relationships that need to be captured by a neural network. In the particular case of γ' precipitates this includes consistency in heat treatment, sample preparation, and imaging, as well as adequate sample sizes for quantification.

With the incorporation of larger training sets of quality data, neural networks may be more successfully applied to the prediction of γ' size. This effort is deemed to be worthwhile based on the importance of γ' on the high temperature mechanical properties discussed in the next chapter. The distribution and morphology of γ' in these superalloys will be consistently cited when explaining variations in strength, creep deformation, and

crack growth. Therefore further development of neural networks for this facet of microstructure should prove beneficial.

4.3. Grain Boundary Serrations

Grain boundary serrations were quantified from optical microscopy images using ImageJ software (a freely distributed, open source code program). Features quantified included an average wavelength and amplitude for the serrated boundary as well as the grain boundary curvature ratio (GBCR). GBCR is the ratio of actual length versus shortest distance between end points. Thus, GBCR values closest to 1 indicate the least amount of serration.

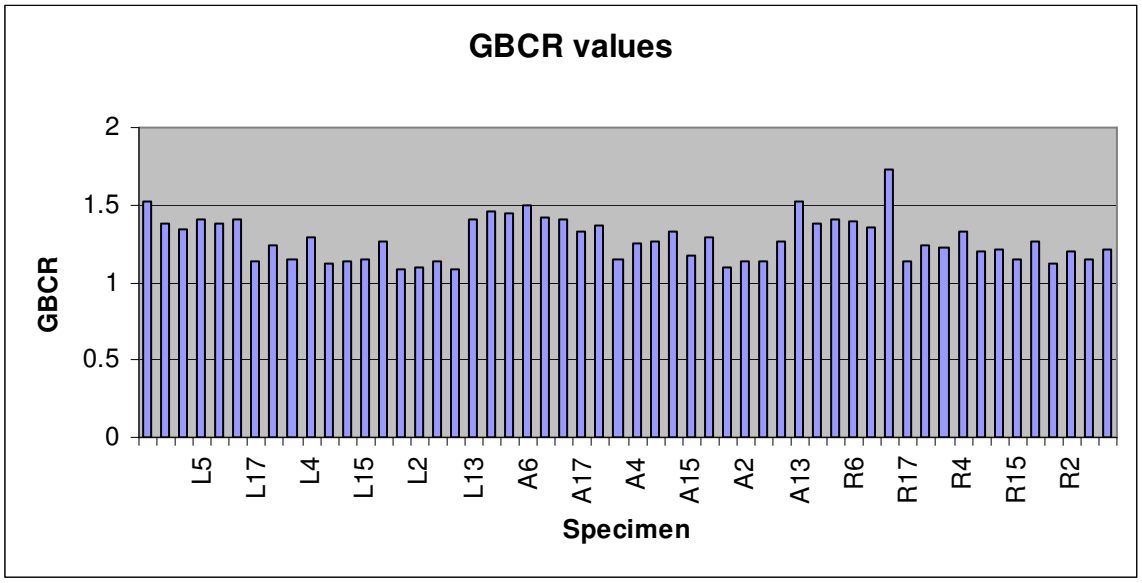

Figure 41 GBCR values for all specimens.

All values for GBCR fell between 1.08 (least serrated) to 1.74 (most serrated). Similar values for GBCR were measured for each material. For each material, the results

seemed to cluster into three groups. This is most likely linked to the processing variables influencing the serration formation. Cooling rate is the obvious choice, because there are three groups for each material corresponding to the three cooling rate variations.

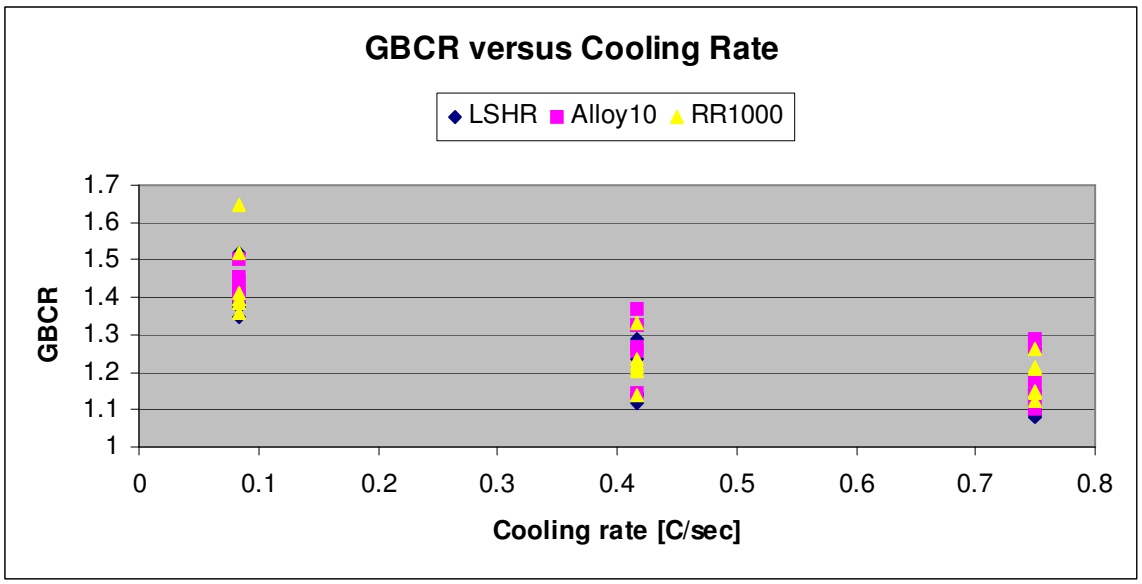

Figure 42 Extent of grain boundary serration presented as GBCR versus cooling rate.

Figure 42 illustrates the values of GBCR as a function of cooling rate. For the most rapidly cooled samples GBCR values were tightly clustered between 1.08 and 1.28. Samples cooled at the intermediate rate had GBCR values between 1.12 and 1.36, while the slow-cooled specimens were from 1.34 to 1.73. Figure 43 shows the optical micrograph of the specimen with the highest GBCR value. This specimen, R18, was subjected to the highest solution temperature and the slowest cooling rate.

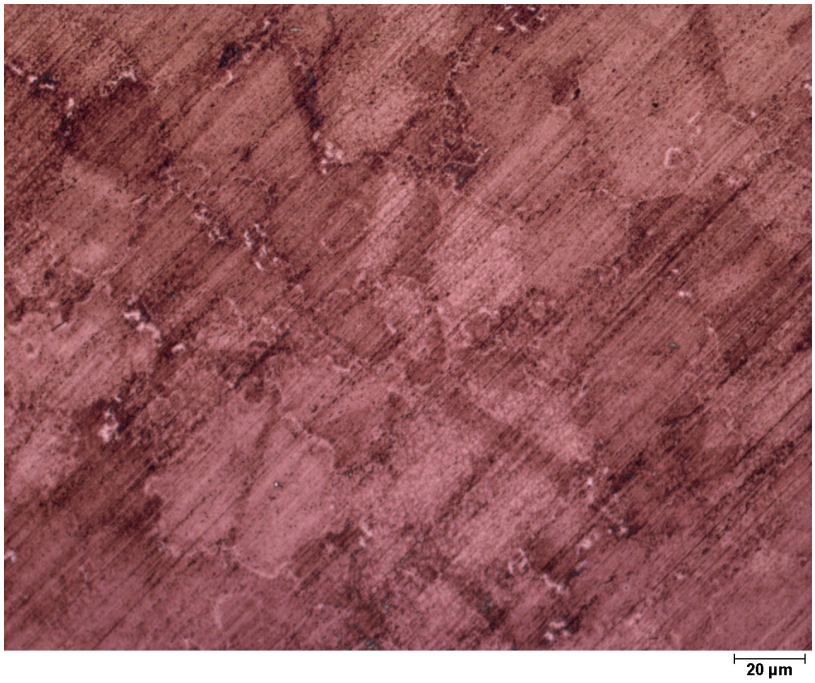

Figure 43 Optical micrograph of RR1000 specimen showing a wide extent of serrated grain boundaries.

While GBCR is a good indicator of the extent of grain boundary serration, it does not provide a quantitative description of the nature of the serrations. For this, one must consider the results for average serration wavelength and amplitude. These can be seen in Figure 44 for each material. Values fell within similar ranges for each material, with values for Alloy10 tending to be higher than those for the other materials. Again, clustering of results indicate cooling rate is the key process variable affecting these quantities. Figure 45 and Figure 46 show them as a function of cooling rate.

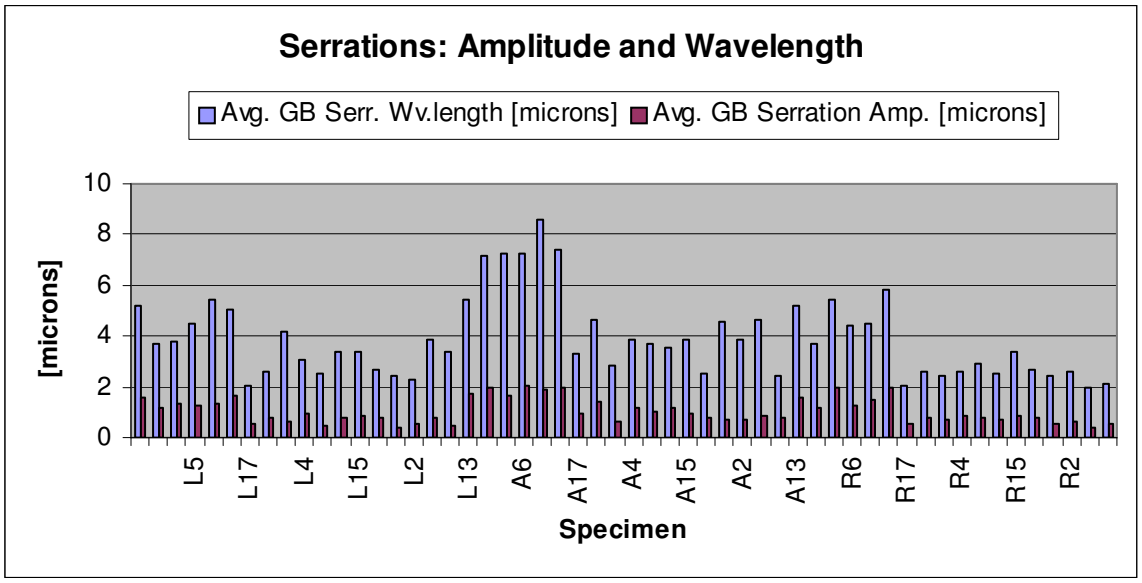

Figure 44 Average wavelength and amplitude results for all specimens.

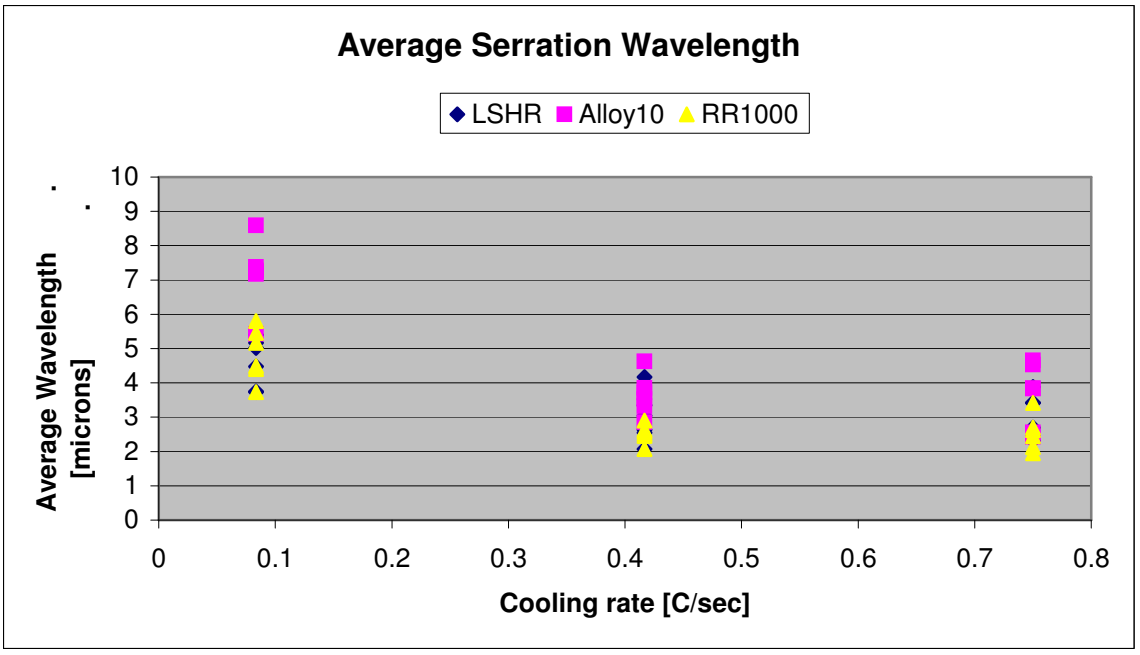

Figure 45 Average serration wavelength as a function of cooling rate.

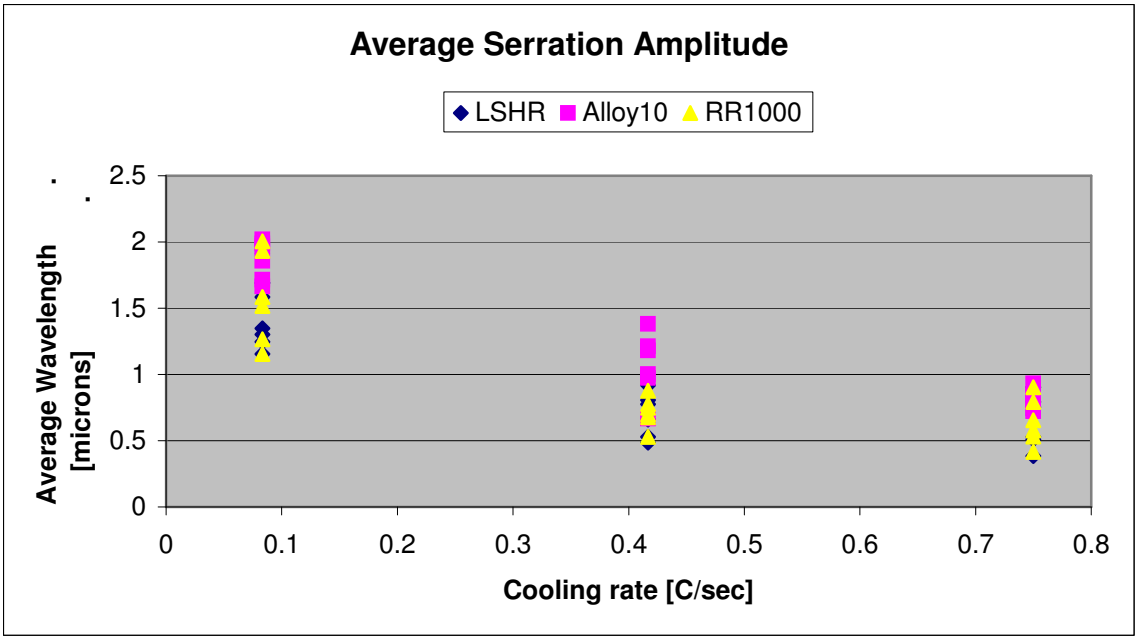

Figure 46 Average serration amplitude as a function of cooling rate.

Previous work has suggested that grain boundary serrations are formed by the coarsening of γ' particles that are in contact with the grain boundaries [23]. As discussed in the previous section, particle size was linked to cooling rate. Thus it is not surprising that serration formation and precipitate size show the same correlation to cooling rate in this work. One cannot, however, plot the results for serrations (either GBCR or amplitude) as a function of particle size, like those charted in Figure 28. These particles are the secondary γ' particles that are within the bulk of the grains and not the ones that lie along the grain boundaries. The γ' particles which grow on the grain boundaries and cause the serrations to form, are generally much coarser than the secondary γ' particles because of the enhanced diffusion of the solute atoms along the grain boundaries as described earlier in the section

While these grain boundary γ' are larger and have additional diffusional contributions, they are still affected by the cooling rates during the heat-treatment.

Figure 47 shows the typical formation of grain boundary γ' in contrast with those formed in the interior of the grains. One can see how the coarse grain boundary γ' would lead to the formation of serrations by pushing out the grain boundaries. As noted before, these coarse particles of γ' would be affected by cooling rate just as the secondary γ' particles are, with the additional factor grain boundary diffusion contributing to their coarsening. Thus, it makes perfect sense that grain boundary serrations are strongly influenced by the cooling rates.

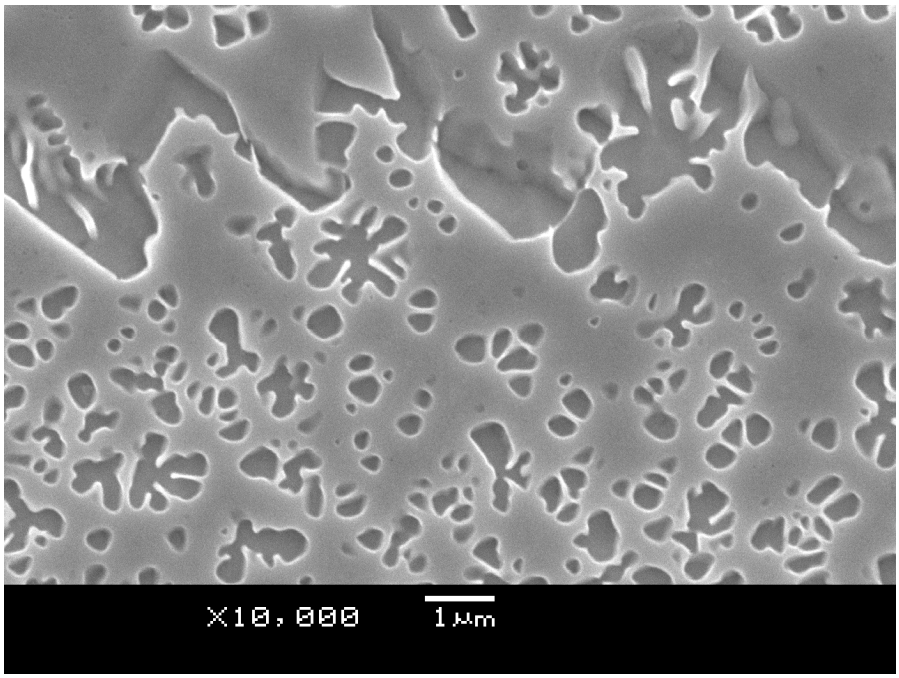

Figure 47 Heat-treated RR1000 material showing grain boundary γ' formations. γ' is etched out, γ matrix is in relief.

The one among adjacent grains the particle is coherent with determines the direction in which the grain boundary particle grows. The grain boundary γ' will coarsen preferentially into the grain that it is coherent with based on the same principles of minimizing free energy that control morphology. Since adjacent grains are distinct in

orientation, the particle can be coherent with only one of the two grains adjacent to a boundary. This is especially the case in powder metallurgy alloys, which are consolidated from discrete powder particles. As the randomly distributed grain boundary particles grow into one of the adjacent grains, serrations are created. It then follows that slower cooling rates that allow for greater coarsening of the grain boundary particles increase the extent of serration of the boundary.

4.3.1. ANN predictions of Grain Boundary Serrations

ANN techniques were successfully applied to the prediction of extent of grain boundary serrations. The ability of a well-trained model to make predictions showcases the usefulness of this tool in the field of metallurgy. Also, the steps taken to create a well-trained model can guide us in future efforts.

Efforts to create a NN model for serration predictions illustrate perfectly the need for balance in this technique. The minimization of the number of inputs to suit the size of the training dataset must be reconciled with the inclusion of all of the relevant inputs. An initial model with nine inputs (three processing parameters and six elements) was generated to obtain an idea of the most relevant inputs. This initial model had an rRMSE of 0.076, which is actually quite good. A subsequent model narrowed down the input to the three processing parameters and only two elements. In doing so the rRMSE more than doubled for the same testing data. Although five inputs would have been appropriate for the amount of training data, it is clear important inputs had not been included. When developing a NN model, we must always keep in mind that it is based

on actual physical processes. Mathematical and computing convenience cannot come before accurately capturing the physical phenomena.

The most successful model for prediction of extent of grain boundary serration was based on solution temperature, cooling rate, hold temperature, and weight percent of Al, Nb, and Ta. The rRMSE for this model was 0.052. The input elements are those involved with segregation into the γ' phase. The importance of these elements in predicting GBCR is consistent with the physical mechanisms of serration formation. Coarsening of grain boundary γ' particles causes serrations to form, thus the amount of elements involved with this process would be necessary for predictions.

Figure 48 shows the predicted versus actual values for the best and worst neural network models of grain boundary serrations. This visual representation clearly shows the improved accuracy for the 6-input model. By failing to include a single relevant input, the relative error of predictions can be tripled. This fact serves as a warning for future work that utmost care must be made to include the correct inputs. Also, it illustrates the sensitivity of the technique, making it clear that neural networks are truly rooted in the physical phenomena. It has been shown to be able to capture the reality of each facet of the complex metallurgical processes that relate alloy chemistry, heat-treatment, and microstructure. Table 10 lists the input data and actual and predicted outputs for testing data of the model with the minimal error.

Table 10 Best Model (6 input) test data and results.

Alloy	LSHR	LSHR	Alloy10	Alloy10	RR1000	RR1000
Specimen ID	L4	L7	A2	A3	R8	R15
Solution Temperature	1.00431	1.01897	1.014382	1.014382	1.01747	1.03231
Cooling Rate	0.41667	0.75	0.75	0.416667	0.75	0.41667
Hold Temperature	0.72845	0.89655	0.71489	0.879865	0.73799	0.9083
Al	3.5	3.5	3.69	3.69	3	3
Nb	1.5	1.5	1.87	1.87	0	0
Ta	1.6	1.6	0.9	0.9	2	2
Actual Result	1.23733	1.08099	1.289184	1.327803	1.2058	1.2016
Prediction	1.329	1.109	1.243	1.2	1.197	1.206

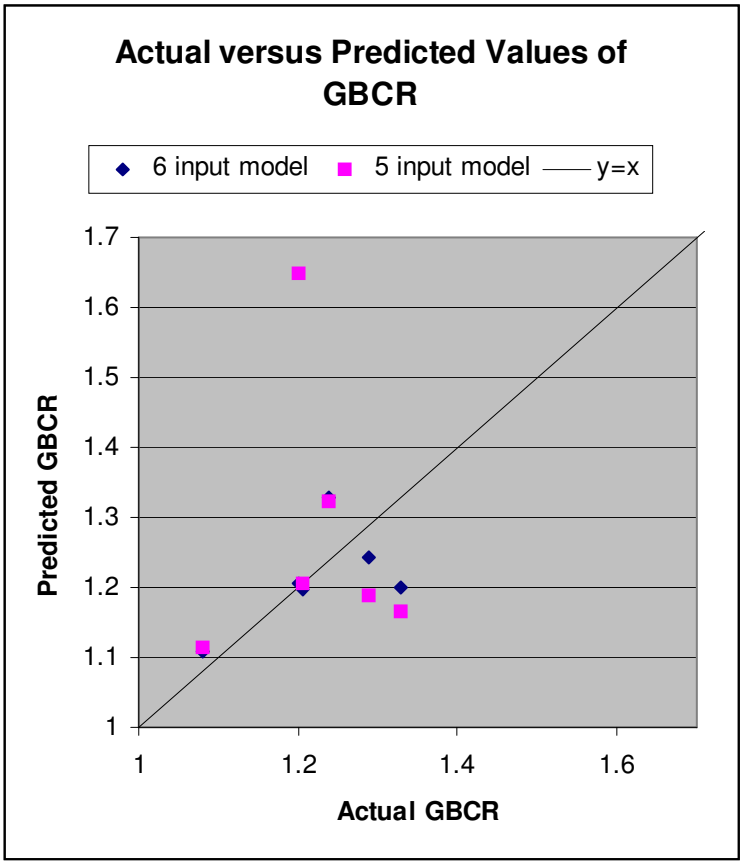

Figure 48 Predicted versus actual values of GBCR based on NN output.

4.4. Summary of Heat Treatment and Microstructure

Results of microstructural quantification are reported for heat-treated specimens. Variation of microstructure with processing was discussed. Solution temperature was the primary factor controlling grain size variations, while cooling rate had the strongest effect on γ' size and morphology as well as grain boundary serration formations. In all features controlled by cooling rate, less variation is seen between the fast and intermediate cooling rates, as compared to the slow cooling rate, which demonstrated a greater change in the relevant microstructural characteristics such as grain boundary particle size and secondary γ' size and grain boundary serrations. This indicates a non-linear relationship between cooling rate and these microstructural features. A non-linear relationship would be consistent with the form of the equation describing diffusion rate.

RR1000 consistently produced the smallest values for microstructural quantities: grain size, γ' size, GBCR and serration amplitude. At the same time, Alloy10 produced the largest values for these quantities. The lower grain size can be attributed to the fact that RR1000 is solutioned at a lower temperature. However, the γ' size at the grain boundary and the interior are dependent primarily on the cooling rates suggesting that the diffusion kinetics for RR1000 are slower than for the other materials. This fact must be kept in mind when planning processing steps to assure that the desired microstructure can be achieved.

Artificial neural network techniques were applied to generate predictive models for grain size, secondary γ' size, and grain boundary serrations. The accuracy of the ANN predictions differed for each feature, although the same sized training database was used. This is indicative of the varying levels of complexity in the processes being

considered. Models predicting grain boundary serrations were the most accurate, likely because this process was most simple. The training data was sufficient for the limited number of input parameters necessary. Attempts to generate a network for precipitate size were largely unsuccessful. Insufficient data was available to train the model for the number of relevant input parameters. Also, the variability in the training data contributed to the inaccuracy of the predictions. Despite the inaccuracy in the predictions, the work on this model was valuable for demonstrating the limitations of this approach. Lessons learned from this effort can be used to optimize the use of the ANN approach on future work.

The results of the processing-structure investigation are summarized in Table 11. These conclusions should be used when choosing a heat treatment to achieve a specific microstructure. A detailed understanding of the role of processing parameters in the formation of microstructures requires a full understanding of the mechanisms driving their formation. In this way, investigation of processing-microstructure relationships contributes to the fundamental understanding of superalloys as well as facilitating efficient production.

Table 11 Summary of results for processing-structure investigation.

Microstructural Feature	Relevant Processing Step	Relationship	Comments
Grain Size	Solution Temperature	Higher Temperatures, Larger Grains	Temperatures must be above 'threshold'
γ' Size	Cooling Rate	Faster Cooling rates, smaller γ'	Applies to secondary, grain boundary, and tertiary γ'
γ' Shape	Cooling Rate	Slower cooling, less circular/more lobed or armed	LSHR and Alloy10 tend to cuboidal/pesudo-dendritic; RR1000 remains circular, but lobed
GB Serrations	Cooling Rate	Slower cooling rates, more serrations	Dependent on GB γ'

CHAPTER 5 Structure-Property Relationships

Ni-base superalloys are used in the most demanding areas of gas turbine engines. These alloys must perform for extended periods at extremely high temperatures and stresses. Therefore it is crucial that these alloys have optimal high temperature properties and that these properties be well understood. High temperature mechanical testing is conducted to better understand the relationship between microstructure and mechanical properties. This serves to optimize the performance of the materials through control of processing variables. At the same time, a more fundamental understanding of the mechanisms of high temperature deformation and crack growth can be achieved. This can be used to tailor processing as well as make the development of new alloys more efficient.

Testing was conducted to capture the effects of microstructural variations on mechanical properties. Tests conducted included hot tensile, hot hardness, creep deformation, creep crack growth, and fatigue crack growth. Results for each and discussions pertaining to these results, especially on the relevant role of microstructure, are presented in the following sections. The goal of this work was to establish mechanistic understanding to the extent possible and develop semi-empirical relationships between alloy microstructure and high temperature mechanical properties.

5.1. Hot Tensile Properties

Tensile testing is the corner stone of mechanical testing programs. This test establishes the response of a material to uniaxial loading. It is a relatively simple test to perform, yet provides a wealth of information on material behavior. Innumerable studies of superalloys have established the superior strength achieved with fine-grain materials, while coarse-grain is optimal for creep resistance. Given that fine grained is best for strength; these tests were concentrated on establishing how to optimize strength within the limitations of a coarse-grain material. In other words, it sought to establish what microstructure (and related processing steps) produced the best high temperature tensile strength properties in material that had already been optimized for creep performance.

For this project tensile tests were conducted at high temperatures to assess the yield strength and ultimate tensile strength of LSHR, Alloy10, RR1000 and U720 at operating temperatures. Results from tensile tests clarify applicable strengthening mechanisms by establishing correlations between processing parameters and microstructural features and strength. The best microstructure for strengthening of coarse-grained material is suggested.

5.1.1. Tensile Testing Results

Tensile tests were conducted on the full set of 72 specimens at 704˚C in air. All results are presented graphically in Figure 49 and Figure 50. Of the four alloys tested LSHR showed the highest values for ultimate tensile strength (UTS) and yield strength (YS). Although the difference in UTS results between alloys was greater than the difference in YS, this trend was consistent for both. The highest value for UTS of LSHR

was 1278.2 MPa and the lowest was 1148.5 MPa. Yield strengths ranged from 958.3 MPa to 787.3 MPa for LSHR. Alloy10 values were slightly lower than those of LSHR. The highest Alloy10 UTS and YS were 1202.3 and 911.4 MPa respectively while the lowest Alloy10 UTS and YS were 1080.9 and 754.2 MPa. RR1000 and U720 had similar values, although the UTS values for RR1000 tended to be higher over all. The highest UTS values for these alloys were 1204.4 MPa and 1215.4 MPa respectively while the lowest UTS values were 1096.2 MPa and 1045.8 MPa. A single outlier can be identified in sample A16 that exhibited an unusually high strength, which was from Alloy10 material that received an intermediate cooling rate and 845˚C hold temperature.

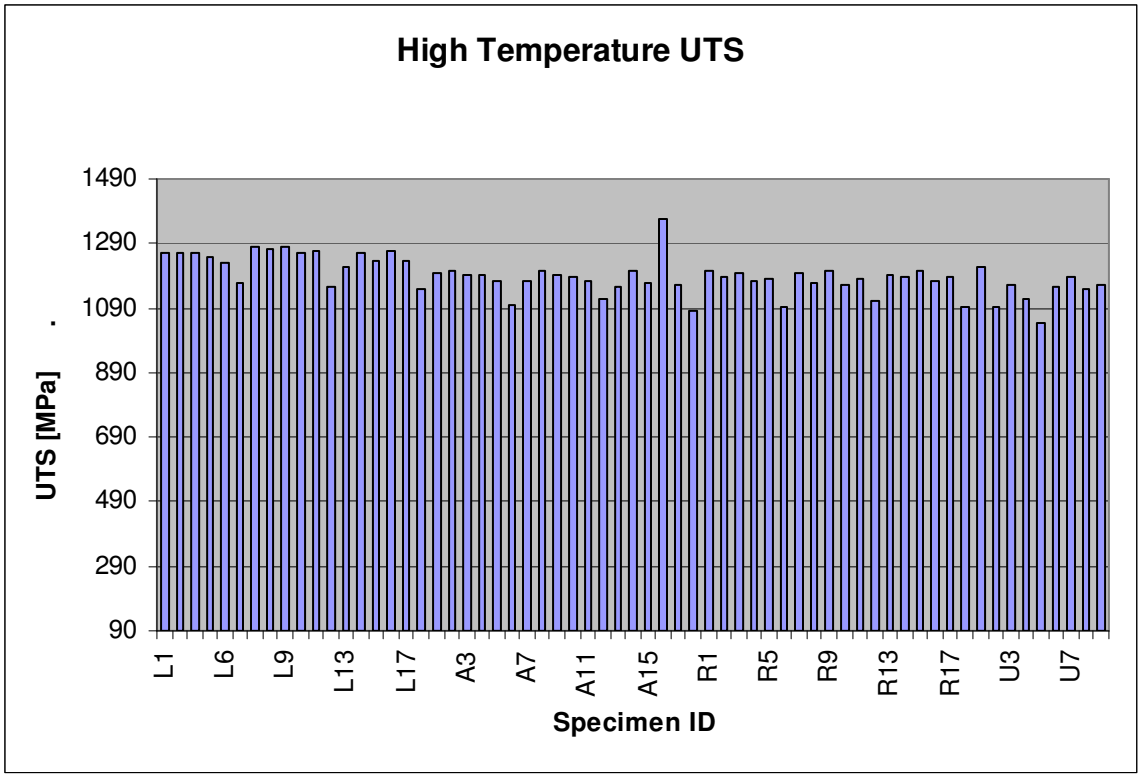

Figure 49 Full results for ultimate tensile strength.

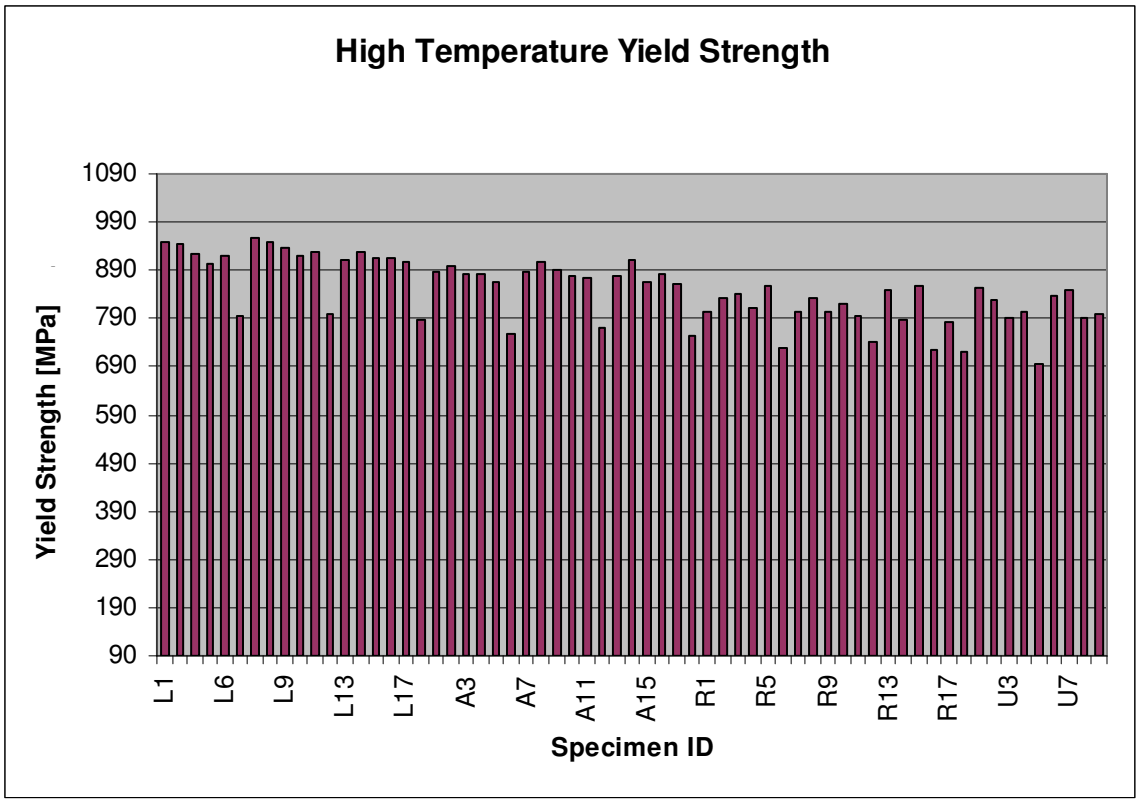

Figure 50 Full results for yield strength (0.2% offset).

Hot tensile testing results varied by alloy composition and by heat-treatment and microstructure. Multiple mechanisms must therefore be invoked in order to account for these variations. These mechanisms operate in parallel and encompass grain size effects, solid-solution strengthening, and precipitate hardening.

A single processing variable cannot be pinpointed as the primary influencer of hot tensile properties. Results for hot tensile tests show no correlation to solution temperature and only a weak correlation with either cooling rate and after solutioning and secondary hold temperature. Overall, specimens cooled at the slowest rate produced the lowest values of UTS and yield. Intermediate and fast cooling rates produced similar results to each other. Also, lower UTS and YS values resulted from materials subjected

to the 845˚C hold, as opposed to the 1040˚C hold. The effect of secondary hold seems to be more pronounced within the slow cooled specimens. This can be seen clearly in Figure 51. As one might expect, specimens receiving both the slow cool and the lower hold temperature had the lowest values for UTS and yield. These trends were consistent for all four alloys.

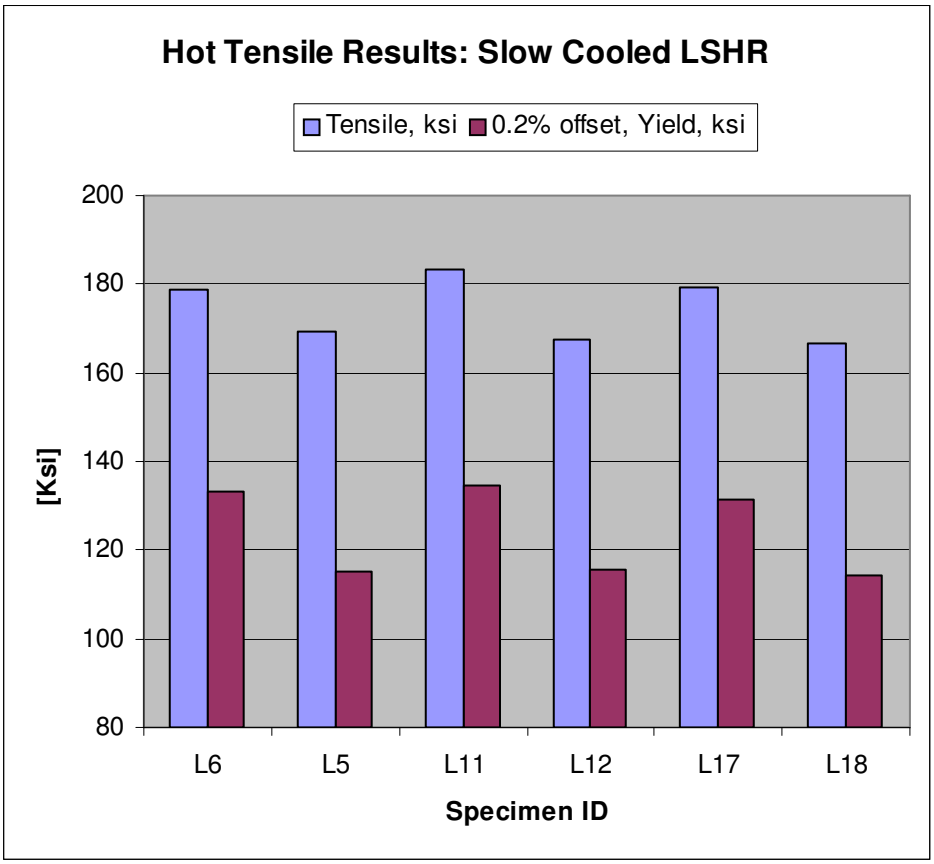

Figure 51 UTS and yield for slow cooled LSHR specimens. L6, L11, and L17 had a 1040˚C hold, the others were held at 845˚C.

5.1.2. Influence of Grain Size

It is not entirely surprising that hot tensile results did not correlate to grain size, despite the long established Hall-Petch Relationship. Hall-Petch describes a correlation between grain size and strength, seen below, where σ_y is the yield stress, σ_o and k_y are constants, and d is the diameter of the grain. This equation, particularly the inverse square-root dependence of YS on grain size is based on the strengthening model that requires the applied stress to overcome internal stresses created by dislocation pile up at grain boundaries for plastic deformation to initiate. Such phenomenon is characteristic of single-phase materials that do not have particles or precipitates that interact with mobile dislocations during plastic deformation.

$$\sigma_y = \sigma_o + \frac{k_y}{\sqrt{d}} \tag{8}$$

In theory, this relationship is likely to apply over the full range of possible grain sizes in these materials. However, the range of sizes studied in the work is too narrow to make an appreciable difference. Results from the previously referenced tensile testing of LSHR by NASA show that deformation in fine-grained material consistently produced higher strengths than coarse-grain LSHR tested under the same conditions. In this case, a reduction of average grain size from 31 μm to 7.3 μm resulted in an increase in tensile strength of 150-200 MPa. This was an improvement in strength of approximately 10% for a 75% decrease in grain size. So, one can still argue that the dependence of strength in these materials with grain size is at best weak. In this project, however, variation in grain size for the microstructures under consideration was limited to less than +/- 5 μm or

approximately 10%. If there were to be a grain size effect on strength it would be very limited because of the minimal variation. In fact, the variation in strength among materials with different grain sizes would be on the same order as statistical variation in results or instrumentation error.

Furthermore, the Hall-Petch equation describes a relationship between strength and grain size with a power-law decay function. As such, the variation of strength with grain size becomes vanishingly small as the value of d increases. This work is on supersolvus material whose grain sizes are very large. Mathematically, this would lead to minimal differences in strength based on the form of the relationship. In his text on mechanical behavior, Courtney suggests that for grain-size strengthening to be appreciable, grain sizes must be below 5 μm in diameter [44]. The grain sizes for the specimens tested are at least 7 and as much as 10 times larger than this. This would lead us to conclude that at the sizes under consideration, grain size strengthening would not be significant.

Variation of strength with grain size is not accounted for by the Hall-Petch relationship, listed above. The equation is included to explain why a correlation may be anticipated by metallurgist and at the same time clarify why this correlation was not found. Variations in grain sizes considered in this work are very minor. When this is considered in conjunction with the form of the Hall-Petch relationship, which is a power-law decay function, we would not expect to see a significant variation in YS. Also, as stated above, this relationship is based on a strengthening model of dislocation pile-up at grain boundaries. The Ni-base superalloys under consideration in this work are

precipitate strengthened, which de-emphasizes the strengthening mechanism on which the Hall-Petch relationship is based.

A correlation between high-temperature yield and tensile strength and cooling rate and secondary hold temperature indicate that γ' precipitates, both secondary and tertiary, could be the microstructural feature influencing the strength in this regime. Using theories on strengthening mechanisms in Ni-base superalloys, one can explain the observed variation of strength with γ' size. In this situation, the primary γ' precipitates have been eliminated. As stated above, there are only minimal changes in grain size between the specimens (less than +/- one ASTM number), so that the Hall-Petch effect is deemphasized. Solid solution strengthening will vary between alloys, but should not vary between different heat treatments. Finally, there is shearing of secondary and tertiary γ', which do vary greatly between the specimens tested.

5.1.3. Influence of Solid-Solution Strengthening

Independent of microstructural variations, tensile properties for each alloy type were clustered. LSHR and Alloy 10 have similar γ' distributions, however the results for LSHR, which has the highest fraction of alloying elements, were consistently higher than results for any other tests. This suggests the importance of the contribution of solid solution strengthening to the tensile properties of the alloys.

Table 12 Weight percent of solute elements listed with atomic radius.

Alloy Name					
Element	**LSHR**	**Alloy 10**	**RR1000**	**U720**	**Atomic Radius [Å]**
Ni	49.59	55.42	59.5	55.1	1.62
Co	20.7	14.9	18.5	15	1.67
Cr	12.5	10.2	15	18	1.85
Mo	2.7	2.73	5	3	2.01
Nb	1.5	1.87	0	0	2.08
Ta	1.6	0.9	2	0	2.09
W	4.3	6.2	0	1.25	2.02

Solute elements such as Cr, Co, Mo, W, and Ta are added to Ni-base superalloys to enhance strength, especially at high temperatures. These elements are summarized in Table 12. Increases in yield strength are achieved by the generation of internal stress fields and the resulting interaction energy between the dislocation and solute atom. Solute atoms and their stress fields are able to impede dislocation motion in the matrix. For example, solute atoms will interact attractively with edge dislocations thereby increasing the flow stress necessary to for the dislocation to move past the particle. This impedance of dislocation motion is the fundamental means of strengthening.

The extent of the atom-dislocation interaction includes factors such as size and modulus of the solute atom, the nature of the dislocation and the symmetry and density of stress fields. Solute particles can be smaller or larger than the matrix. In the case of LSHR solute atoms are larger than matrix atoms, producing a positive dilation. Strain fields can have spherical or tetragonal symmetry, which will alter dilation. A full treatment of this can be found in [44]. For this work it is sufficient to note that an increased concentration of solute atoms increases the solid solutioning effect. Thus, one would expect improved strength for LSHR, which has the highest alloying content.

Results for hot tensile tests clearly show the superior high temperature tensile strength of LSHR. Improvements are more pronounced in ultimate tensile strength, than in yield strength. Testing conducted at NASA-Glenn Research Center corroborates the superior strength of LSHR. Results from this work claimed strength values that "exceeded those of ME3 and Udimet720" [7]. With the highest content of matrix-solute elements, LSHR saw the biggest improvement from solid solution strengthening.

These improvements by solid solution strengthening are only one aspect of high temperature strength. It must be considered in parallel with the effects of precipitate strengthening, which is discussed in the following section. Solid solution strengthening is a function of alloy composition, while precipitate strengthening is affected by composition as well as microstructure. As with most high temperature mechanical properties, especially in highly complex material systems, multiple mechanisms tend to operate simultaneously.

5.1.4. Role of Precipitate Strengthening

The extent to which the γ' particles contribute to the strength of the material is based on the volume fraction of the phase, the size distribution and precipitate spacing. γ' particles act as obstacles to the motion of dislocations. The factors mentioned determine the coherency strain of the alloy and the stress necessary for dislocations to bend around or shear through the obstacles. Maximum impedance of dislocation motion should produce the maximum values for strength. Thus an optimal size and distribution of secondary and tertiary γ' particles would be sought to optimize this property. The

correlations observed in the data between cooling rates and hold times and strength suggest how to achieve this.

Faster cooling rates produce higher values for YS and UTS. Faster cooling rates necessarily mean smaller secondary γ' precipitates, suggesting that fine γ' are better obstacles to dislocation motion. At the same time, a lower hold temperature, which produced the larger tertiary γ', produced lower strength materials. The combination of these observations confirms that an optimal size and distribution of γ' precipitates are necessary to optimize strength. Fast cooling rates along with higher temperature holds, which produce finer secondary and tertiary particles produce microstructures that lead to high temperature tensile strength. This is based on strengthening mechanisms involving dislocation-obstacle interactions as discussed in more detail below.

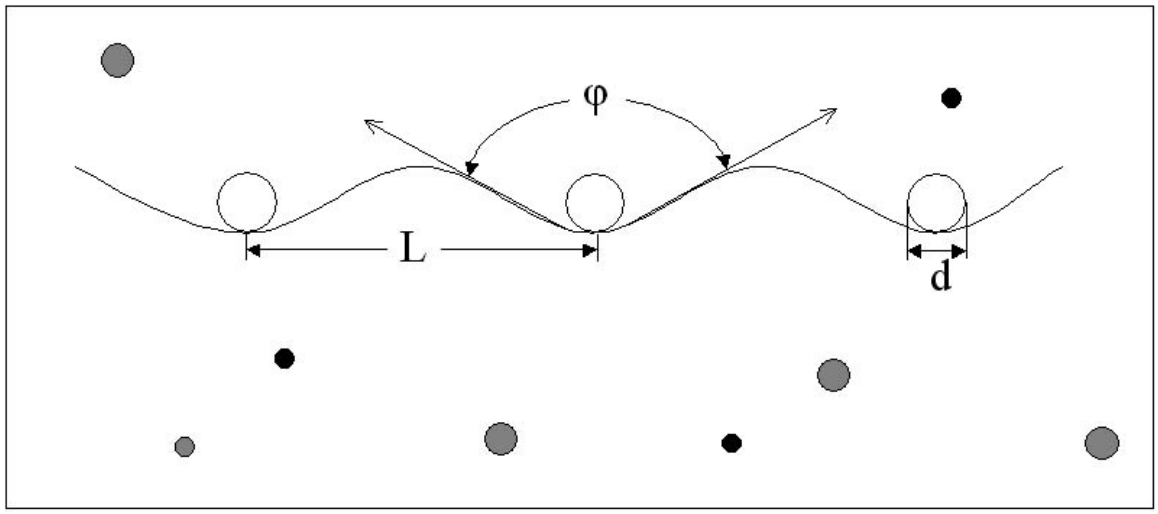

Figure 52 Schematic of dislocation-obstacle interaction. Dislocation (line) motion is towards top of page. Circles represent obstacles to dislocation motion which cause bending.

These observations are consistent with the simple model of dislocation-obstacle interaction. For deformation to occur, a dislocation must move through a field of

obstacles, in this case γ' precipitates. When the dislocation encounters an obstacle, it must bend and either loop around or shear through the particle, in order to continue. Figure 52 illustrates the movement of a dislocation through a dispersion of obstacles. The angle φ describes the amount of bending of the dislocation. "Stronger" obstacles will better resist penetration by dislocations so that the angle φ will approach 0. "Weaker" obstacles will have a large angle φ and the dislocation line will remain straighter.

$$\tau \cong \frac{Gb}{L'} \cos \frac{\varphi_c}{2} \tag{9}$$

Equation 9, based on calculation of the stress necessary to operate a Frank-Reed source, clarifies the effect of obstacle strength and spacing on the shear stress necessary for a dislocation to proceed [44]. It is based on dislocation line tension calculated as $Gb^2/2$, where G is the shear modulus and b is the Burgers vector. L' is the average spacing intersection of the dislocation line with obstacles. Optimal alloy strength will be achieved for the maximum value of shear stress necessary for dislocation motion. Based on Equation 9, this would be achieved by decreasing obstacle spacing, L', and minimizing φ_c.

In Ni base-disc alloys, secondary and tertiary γ' precipitates act as obstacles to dislocation motion. Their efficacy is based on the strength of the particle, the particle spacing, and volume fraction of particles. Based on the relationship to cooling rate and hold time, it is concluded that finer particles are most effective. For a given volume fraction, smaller particles would increase the number of particles and decrease the

particle spacing. This would offer many, more closely spaced particles impeding dislocation motion. In this way, L' would be minimized, increasing the stress necessary for dislocation motion and therefore strengthening the alloy.

In addition to γ' particles affecting dislocation motion by acting as obstacles, they also impede motion by creating internal stress fields within the grain. Smaller precipitate phase particles are more likely to maintain coherency with the matrix. This coherency strain, which is generated from the mismatch between the lattice parameters of particle and matrix, produces the stress fields. The internal stresses that are generated will contribute to strength by increasing the stress necessary for dislocation motion. This effect is described by Equation 10, which relates the increased resolved shear stress to coherency strain, ε_{coh}, where r is particle radius and f is particle concentration.

$$\tau_{coh} \cong 7\left|\varepsilon_{coh}\right|^{3/2} G\left(\frac{rf}{b}\right)^{1/2} \tag{10}$$

The maximum stress to move a dislocation is achieved by increased values for coherency strain, particle radius, and particle concentration. This must be balanced with the loss of coherency that occurs for large particles. In other words, dislocation motion will be most impeded by a large number of particles that are as large as possible but not so large that coherency is lost.

Equations 9 and 10 are both included to elaborate on the factors which contribute to increasing the applied stress necessary to move dislocations. The terms included in both equations help to relate the phenomena to physical quantities. Equation 9 describes the resolved stress necessary to move a dislocation past an obstacle. Its calculation involves the shear modulus of the material, the Burgers vector, but more importantly the

obstacle spacing and dislocation angle, which is dependent on the obstacle strength. This term quantifying obstacle spacing can be directly related to the spacing of precipitate particles, which from this research are deemed to be the dominant obstacle to dislocation motion.

The inclusion of Equation 10 which clarifies the effect of coherency strain caused by precipitate particles to the critical resolved stress necessary to move a dislocation underscores the importance of particle size for them to remain effect obstacles. The introduction of internal stresses due to coherency strain strengthens the material

Both of the equations high-light the physical, microstructural quantities involved in strengthening these superalloys. Moreover, when considering both, we must reconcile the contributions of each with the potentially contradictory implications of each. Because of the dependence of equation 9 on obstacle spacing, a rapid cooling rate has been suggested to maximize strength. This rapid cooling rate would decrease the value of L', obstacle spacing, and thereby increase τ. However, a rapid cooling rate necessarily decreases the particle size so that the contribution of r, particle radius, to τ in equation 10 is decreased.

In addition to facilitating a theoretical discussion of the relationship between microstructure and strengthening mechanisms, Equations 9 and 10, together with numerical data, have the potential to be used to quantitatively assess the contradicting effects of microstructure on strength. Specifically regarding microstructures controlled by cooling rate, these equations can be used to quantify the optimal combination of obstacle spacing and size necessary to maximize strength.

5.1.5. Neural Network Model of Yield Strength

Neural Network models were generated to predict yield strengths of these Ni-base superalloys. This effort was deemed very successful, as the error for the models was no higher than 0.0587 and as low as 0.028. This level of error is lower than that achieved for predictions of microstructural features, but was achieved using similarly sized training sets.

The preliminary model, generated to identify the principle inputs necessary, had an rRMSE of 0.056. This is a very low error value, despite the relatively high ratio of inputs to training data. Although further refinement was possible, this preliminary network can be considered as highly accurate. Based on the weights assigned the inputs in this initial run, inputs were pared down to include the three processing parameters and weight percent of Co, Cr, and W. Intuitively these inputs make sense, as these elements are commonly associated with strengthening mechanisms. Specifically, W was previously discussed for its role in solid-solution strengthening and differences in strength amongst the alloys tested.

Reducing the number of inputs had a minimal impact on the relative error level of predictions of yield strength; rRMSE rose slightly from 0.056 to 0.058. While the ratio of inputs to training data was improved, the level of accuracy was not. This suggests that the system is sufficiently defined by the existing data. At the same time we can conclude that the omitted inputs do not weigh into calculations of predicted values significantly.

As has been mentioned, the predictions of a neural network are only as good as the training data from which the network is generated. In the first two models discussed, the complete set of results for LSHR, Alloy10, RR1000, and PM U720 were included in

the construction. However, as pointed out early in the discussion, the heat treatmed PM U720 material never reached a fully super-solvus state. As such, many microstructural features were present in the U720 material that were not a factor in the others. Therefore, it is likely that factors contributing to the strengthening of U720 are very different from the other materials. If this were the case, then the inputs would not be weighted similarly for U720 as for the other materials, which do have the same structure and mechanisms. By reducing the number of inputs, those relevant to the U720 are likely excluded.

To further consider this, an additional network was trained. This network used the pared down set of inputs, but omitted the U720 specimens from the training and testing data. This combination resulted in the most accurate model, having an rRMSE of 0.028, half that of the previous networks. Figure 53 shows the actual versus predicted values of YS for this network. Values fall equally above and below the y=x line, indicating that there is no systematic skewing of the predictions. Table 13 and Table 14 list the details of test data used for models of yield strength with and without PM U720.

This example illustrates the sensitivity of the network to the training data on which it is based. In the process of optimizing the number of inputs, it is important to consider whether the mechanisms that underpin the processes are consistent. It is a classic case of comparing apples to apples.

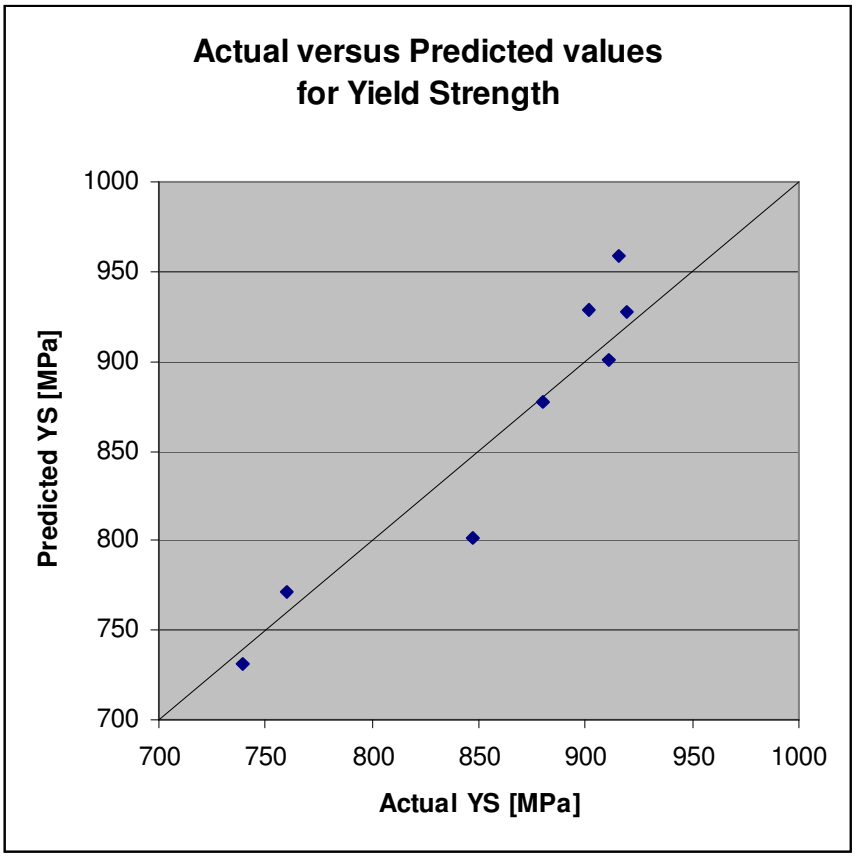

Figure 53 Actual versus predicted values of YS.

Table 13 Details of test data for model not including PM U720.

Alloy	LSHR	Alloy10	Alloy10	Alloy10	RR1000	RR1000
Specimen ID	L15	A6	A10	A14	R11	R13
Solution Temperature	1199	1199	1216	1233	1165	1182
Cooling Rate	0.41667	0.08333	0.416667	0.75	0.08333	0.75
Hold Temperature	1040	845	845	845	845	1040
Co	20.7	14.9	14.9	14.9	18.5	18.5
Cr	12.5	10.2	10.2	10.2	15	15
W	4.3	6.2	6.2	6.2	0	0
Actual Result	915.523	759.719	880.3638	911.387	739.726	847.273
Prediction	958.26	770.94	877.7	901.24	731.01	801.83

Table 14 Inputs and predict and actual outputs for test data including PM U720.

Alloy	Specimen ID	Solution Temperature	Cooling Rate	Hold Temperature	Co	Cr	W	Actual Result	Prediction
LSHR	L4	1165	0.41667	845	20.7	12.5	4.3	901.7352	926.51
LSHR	L6	1165	0.08333	1040	20.7	12.5	4.3	919.6596	917.97
LSHR	L15	1199	0.41667	1040	20.7	12.5	4.3	915.5232	929.52
Alloy10	A6	1199	0.08333	845	14.9	10.2	6.2	759.7188	776.56
Alloy10	A10	1216	0.41667	845	14.9	10.2	6.2	880.3638	880.64
Alloy10	A14	1233	0.75	845	14.9	10.2	6.2	911.3868	910.75
RR1000	R11	1165	0.08333	845	18.5	15	0	739.7262	724.86
RR1000	R13	1182	0.75	1040	18.5	15	0	847.2726	812.61
PM U720	U17	1199	0.08333	1040	15	18	1.25	867.2652	771.95
PM U720	U5	1165	0.08333	845	15	18	1.25	837.621	713.61
PM U720	U7	1182	0.75	1040	15	18	1.25	847.2726	831.58

It is very important to note that for all of these networks, no microstructural quantities were inputted. Although this project focuses on the effect of microstructure on mechanical properties, it is not necessary to include microstructural parameters in the models. This is not an indication of the relative importance of their impact; rather it is an indication of the power of the neural network approach. Microstructure is a product of the processing and chemistry of the material. Processing and chemistry are the inputs used for the networks. The network is able to infer the effect of microstructure from the inputs. This is a powerful conclusion because it can eliminate the time spent on quantifying microstructural features. Microstructural quantification can be a very time consuming task and the results of which are easily skewed by small variations in technique. Further, we have discussed that some features, such as tertiary γ' size, were not quantifiable with available techniques. By using processing and chemistry parameters as inputs, the effect of these features is included, whereas using inputs such as secondary γ' size would completely eliminate the possible contribution of the non-quantified features. The ability of the network to incorporate these effects based on primary variables saves time, as well as eliminating a possible source of inaccuracy.

To corroborate these statements, networks were constructed using the results of microstructural quantification, in place of processing variables. The most accurate model from these efforts had and rRMSE of 0.084. This is a level of error 1.5 times greater than that of the least successful model using processing parameters as inputs. By using more fundamental inputs, i.e. processing variables, neural network models can be generated more efficiently and with a higher level of precision.

5.1.6. Summary of Hot Tensile Testing

Results for each specimen are based on contributions from several strengthening mechanisms. Although grain size effects are minimal in this testing, the combined effects of solid solution strengthening and precipitate hardening produce varying tensile strengths. LSHR appears to have the best characteristics for high temperature tensile strength. Its composition includes a high weight percent of matrix solute elements so that it benefits the most from solid solution strengthening. In addition, rapid cooling rates produces a fine dispersion of γ' particles which optimizes the effect of precipitate strengthening. Alloy10 contains the lowest levels of solid-solution strengthening, however the efficacy of its γ' particles give it tensile capabilities similar to those of LSHR. Despite relatively high levels of solution strengthening elements, RR1000's tensile properties were inferior to those of LSHR and Alloy10. The low misfit strain in the alloy, combined with alternative γ' morphology in the latter are likely responsible for this. Variations between alloys and heat treatments all operate on the same principles of dislocation motion and the impedance thereof.

A fast cooling rate generates a dispersion of fine particles thus, maximizes the contribution of γ' particles to strength. It is able to optimize particle spacing and coherency so that both contributions to the stress required for dislocation motion is maximized. This effect was seen in the results of the hot tensile testing where fast cooled specimens, with hold temperatures that minimized tertiary γ' size, produced the best results.

A multitude of factors dictate the precise events that take place including the strength of the obstacle, obstacle spacing, the nature of the dislocation, the dislocation density, temperature, residual stresses in the matrix, etc. For example, the strength of the obstacle dictates the amount of bending necessary before the particle is sheared. The volume fraction of γ' controls the frequency with which dislocation meet obstacles, while the density of dislocations influences the force applied by the dislocations. The structure-property relationship under consideration in this section, namely γ' effects on tensile strength, directly affect the obstacle size and spacing. By controlling the cooling rate and hold temperatures, γ' size and distribution can be optimized to impede dislocation motion. In this way Ni-base disc alloys can be processed to achieve optimal high temperature strength, within the limits on strength imposed by the supersolvus solutioning.

Machine learning techniques were successfully applied to the prediction of yield strength values. Neural networks were able to accurately predict yield strength from inputted values of solution temperature, cooling rate, hold temperature and weight percent of Cr, Co, and W. Microstructural quantification results were not necessary as inputs for these models. This underscores the power of neural networks to infer the effect

of microstructure from primary variables. This eliminates the expenditure of resources on microstructural quantification, and at the same time reduces the sources of inaccuracy.

5.2. Hot Hardness

Hot hardness testing was characterized in order to establish a relationship between high temperature hardness and strength and creep properties for nickel disc superalloys. Hot hardness test were conducted on small coupons of each material in vacuum at a range of temperatures from approximately 24˚C to at least 704˚C. Results varied between alloys and for the various heat-treatments within each material. Outcomes are summarized and discussed in this section. Full results are located in the appendix. Figure 54 shows a typical indent, in this case in RR1000 material. Note the scale of the indent relative to the grain size.

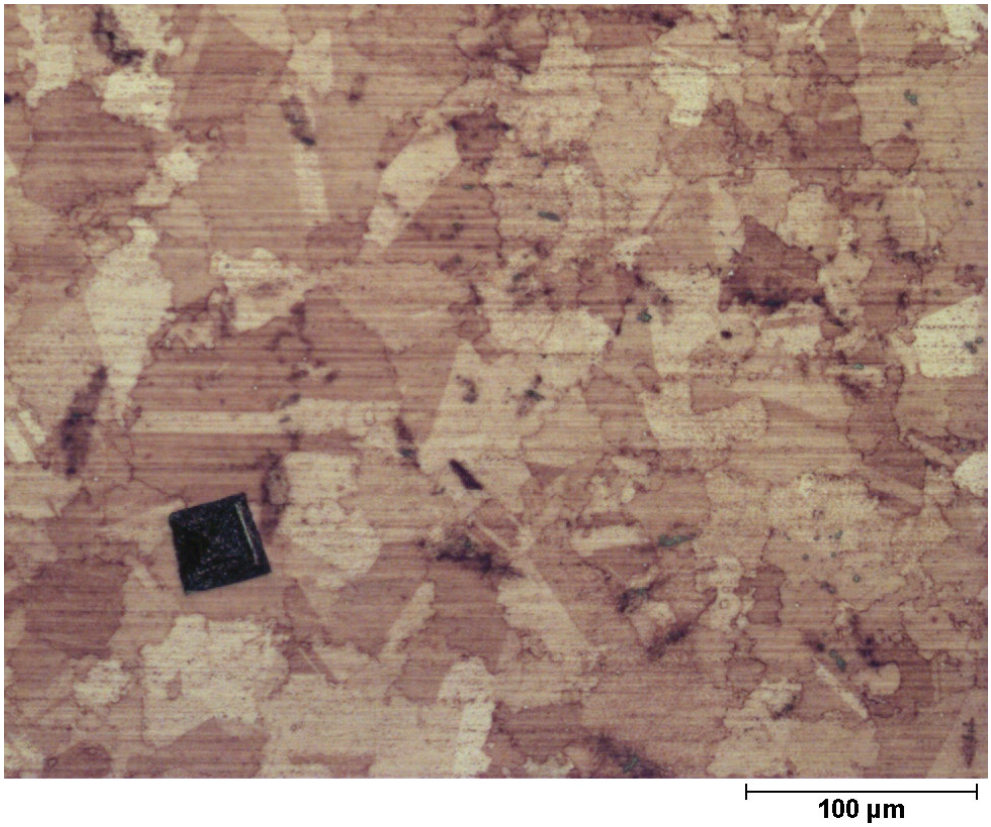

Figure 54 RR1000 hot hardness specimen.

5.2.1. Hot Hardness Results

A decrease in hardness with increasing temperature was seen for each material tested. Hardness measurements at 400˚C and 700˚C were approximately 13.5% and 21% lower than the room temperature hardness values, respectively. At room temperature LSHR had the highest values for hardness on average, while Alloy10 and RR1000 had similar values. However, at elevated temperatures Alloy10 had the highest hardness measurements, with LSHR and RR1000 being similar.

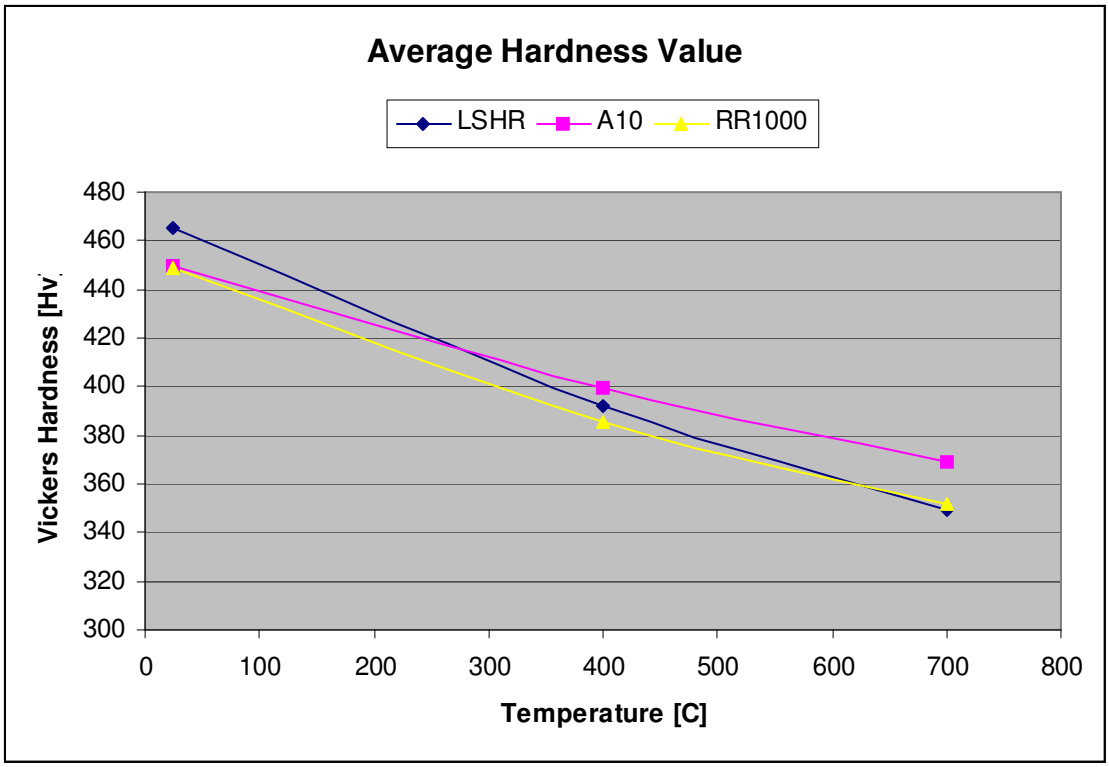

Figure 55 Average of results for hardness testing as a function of temperature.

The values above are averages for all specimens of a given material. By taking these averages variations between hardness and heat-treatments are lost. Figure 56 shows the actual results for hardness at three temperatures for LSHR. One can see that there is variation from specimen to specimen. This can be scatter, or it can be a correlation to processing variables and microstructure.

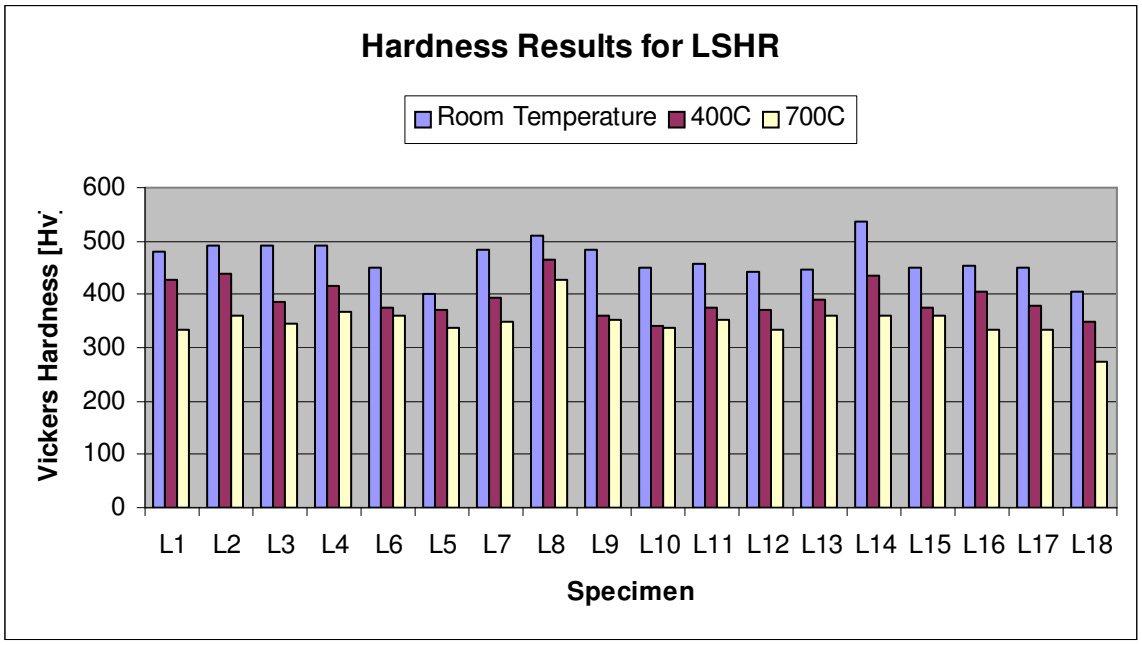

Figure 56 Results for LSHR at room temperature, 400C, and 700C.

Little correlation to processing or microstructure was identified for the hot hardness results. As with hot tensile, a single processing parameter is not influencing the hardness results. A loose correlation to cooling rate and secondary hold temperature can be seen. Of the sets of specimens solutioned at the same temperature, the hardest specimens for each set were those cooled at the fastest rate and held at the lower temperature. Again, this indicates the impact of secondary and tertiary γ' on this mechanical property. In terms of microstructure, this might suggest that smaller sizes of the secondary and larger tertiary particles produce a harder material. However, plotting secondary γ' precipitate size versus hardness gives no indication of a relationship. Volume fraction of γ' also varies with cooling rate and hold temperature and since there is no evidence for a relationship between precipitate size and hardness, we then consider a possible relationship between volume fraction of secondary γ' and hot hardness.

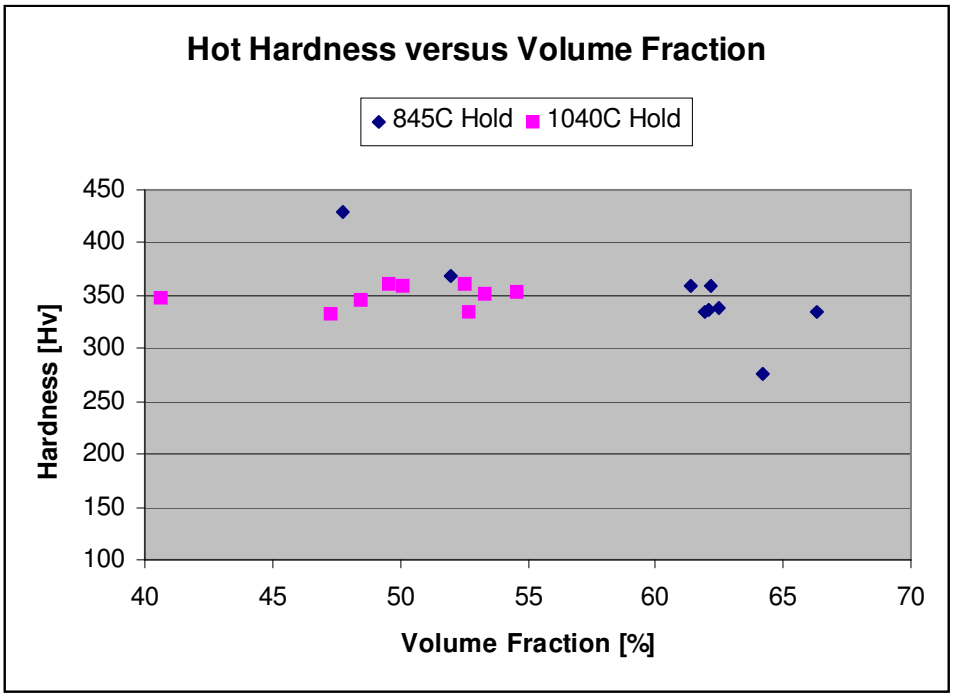

Figure 57 Hot hardness as a function of volume fraction of secondary γ' for LSHR.

Figure 57 shows the graph of hot hardness versus volume fraction of secondary γ', separated by hold temperature. For clarity a single alloy is seen in this graph, LSHR. In general, it can be seen that the higher intermediate hold temperature yields a lower volume fraction of secondary γ'. Different trends seem to exist between volume fraction secondary γ' and hardness, depending on the intermediate hold temperature. Hardness results for specimens held at 845˚C range from 275 to 429 Hv. Results for specimens held at 1040˚C are tightly clustered between 332 and 360 Hv. For the lower hold temperature, the data suggests a weak trend of decreasing hardness for increasing volume fraction. However, this trend is not at all apparent in the higher hold group, where results are consistently around 350 Hv, regardless of volume fraction.

As discussed in the previous chapter, the higher intermediate hold temperature has the effect of resolutioning smaller precipitate particles. From the graph of hardness

versus volume fraction, it is clear that holding material at the higher temperature lowers the volume fraction and, in effect, normalizes the hardness of the material. All of these observations, however, are based on volume fraction secondary γ'. Due to the relative sizes of tertiary γ' and dislocation, it is likely that volume fraction of tertiary γ' is more relevant. TEM images would be necessary for a discussion on the effect of tertiary γ' volume fraction and size distribution. At this time, we can observe that hold temperature is clearly affecting the hot hardness results and that this is likely linked to the effect of intermediate hold on volume fraction of precipitate phase.

Hot hardness values are based on manual measurements of indent diagonals. These measurements are made at temperature through a built in microscope. If there are variations of hardness with microstructure, it is likely that the resolution of the equipment is unable to capture it. In addition, there can be larger degree of inaccuracy in manual measurements of this type. Although multiple indents were taken for each condition, the results are inconclusive. Similarly, volume fraction measurements are directly affected by sample preparation techniques. Slight variations in polishing and etching of specimens for imaging can easily skew results for volume fraction. In order to produce accurate results concerted effort must be made to prepare and image the specimens in a consistent manner.

Variation in hardness with grain size might be intuitively expected. However, two factors make this data incapable of capturing such a trend. The first is that grain size variations were minimal for the test material. As was noted in the discussion of grain size effects on tensile strength, this testing was limited to supersolvus material with a very narrow variation in size. The accuracy and resolution of indent measurements

would likely be insufficient to capture subtle effects from small grain size variations. In addition, the average indent diagonal length was nearly identical to the grain size diameters of the specimens being tested. Thus each indent would only be encompassing, if not a single grain, only a very few. If the material being tested were fine grained, so that many grains were indent at once, grain size variations may be more likely to be resolved.

5.2.2. Correlation to Hot Tensile

Hot hardness tests were conducted in an attempt to correlate results to hot tensile tests and thereby provide an alternative test for ascertaining strength properties at elevated temperatures. Hot hardness tests would require less material than tensile tests and the same specimen could be used for testing at multiple temperatures. Unfortunately, there was no discernable relationship between hardness and yield strength or UTS at 704˚C. For example, LSHR had the highest results for high temperature tensile tests. However, it did not stand out as the hardest material. This typifies the lack of correlation found in these results. Figure 58 and Figure 59 show the results for hot hardness versus UTS and versus YS respectively.

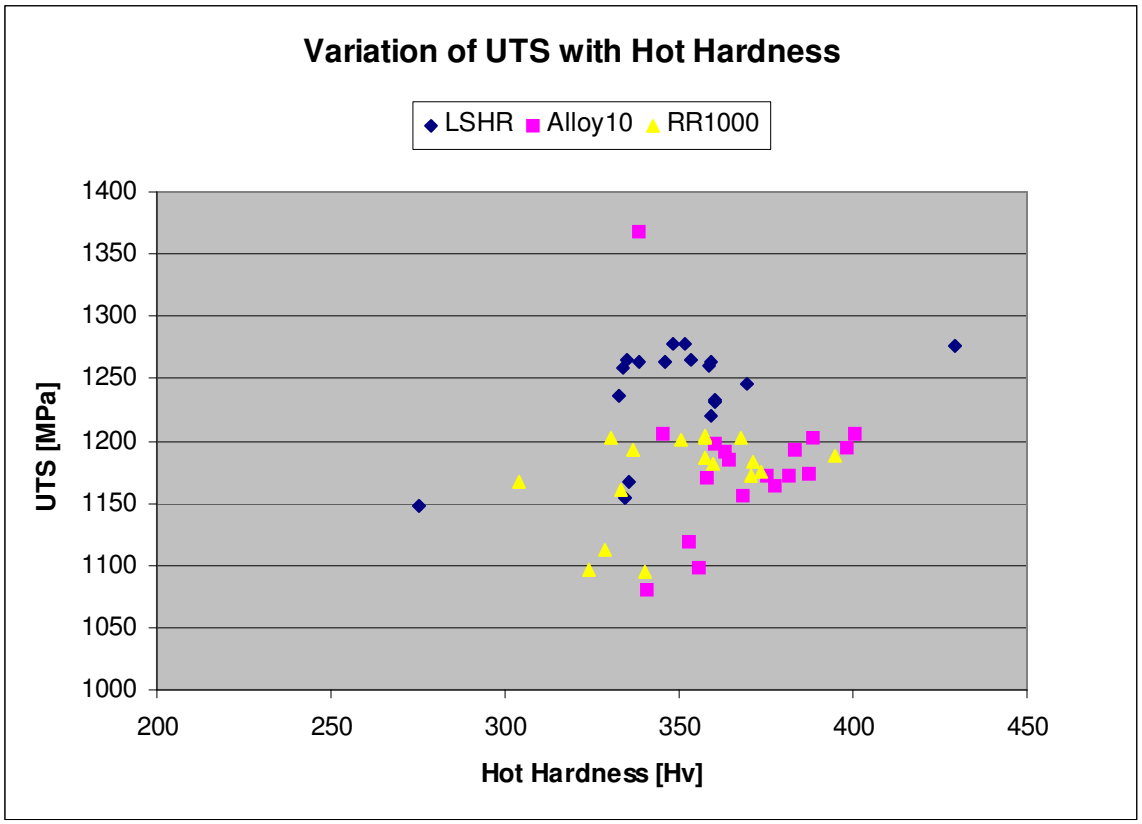

Figure 58 Hot Hardness versus UTS at 704˚C.

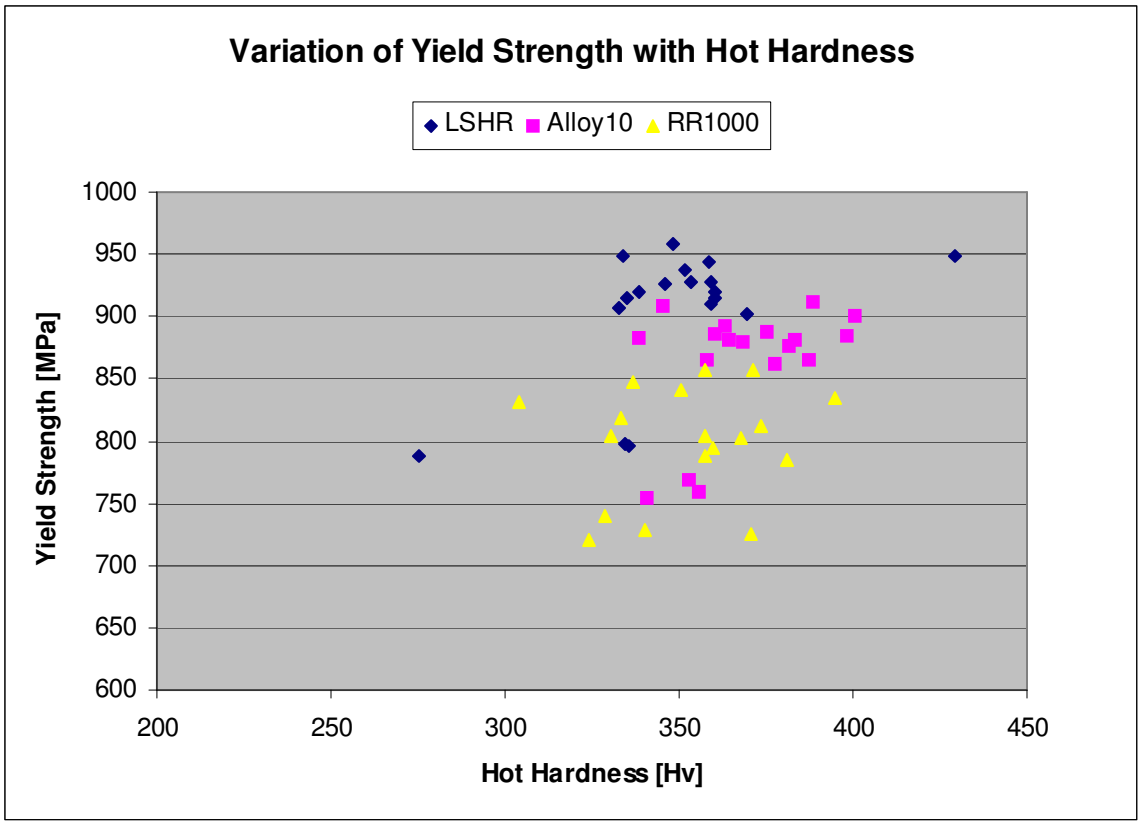

Figure 59 Hot Hardness versus UTS at 704˚C.

The lack of correlation between these properties suggests that they are based on different mechanisms and relate to the microstructure of the material differently. While it would have been beneficial to find a more efficient means of assessing material strength, hot hardness measurements are not a viable alternative. In addition to not finding a correlation, lab equipment to make hot hardness measurements is rare. At present there are less than half a dozen operable Nikon QM hot hardness testers worldwide. Further, Nikon no longer supports the equipment nor do they produce replacement parts. Other avenues must be pursued in order to establish a more material efficient means of assessing strength.

5.3. Creep Deformation

Creep deformation occurs when materials are subjected to stress at elevated temperatures for a period of time. As such, it is a time-dependent deformation mode. Understanding the creep deformation behavior of Ni-base superalloys is crucial since these materials are intended for high temperature applications. Creep must be considered as a potential failure mode for materials operating at low stress levels and high temperatures for long periods of time. This is certainly the case for aircraft disc applications.

Microstructural variations can noticeably alter the creep behavior of these alloys, so processing variables that influence the microstructure must be considered in optimizing creep properties. As mentioned previously, coarse-grain microstructures have been proven to provide superior creep resistance. The creep deformation tests conducted for this work sought to establish what further refinements could be made to the microstructure to improve creep resistance. It was hypothesized that a distribution of fine precipitates would be optimal. Creep mechanisms active within the grain would involve dislocation motion. Impeding this motion to reduce creep rates would be similar to the impedance of dislocation motion to improve strength. Hence a similar microstructure would facilitate this.

Creep deformation tests were carried out on the LSHR material for three different microstructures at various stress levels. All tests were carried out at 704˚C in air. The following section presents the results and discusses the effect of microstructure on the creep behavior of the material. Complete charts for creep deformation results can be found in the appendix.

5.3.1. Microstructures Tested

The variations in microstructure investigated in this section were only those related to cooling rate, while all other processing parameters were held constant. Thus, the three microstructures tested had the same grain size, but different γ' sizes and some variation in grain boundary serration formations. However, the cooling rates considered here were much more rapid than those in the matrix of microstructures discussed above. As such, the extremes of coarse γ' shape, morphology or extensive serrations are avoided. In general, all microstructures subjected to creep testing were consistent with those that would be produced by industry procedures and use. High magnification SEM pictures of γ' (in relief) for each cooling rate tested are in Figure 60, Figure 61, and Figure 62. Tertiary γ' particles are only visible in the slowest cooled specimen. Figure 62 shows an example of grain boundary γ' particles that have a highly irregular morphology.

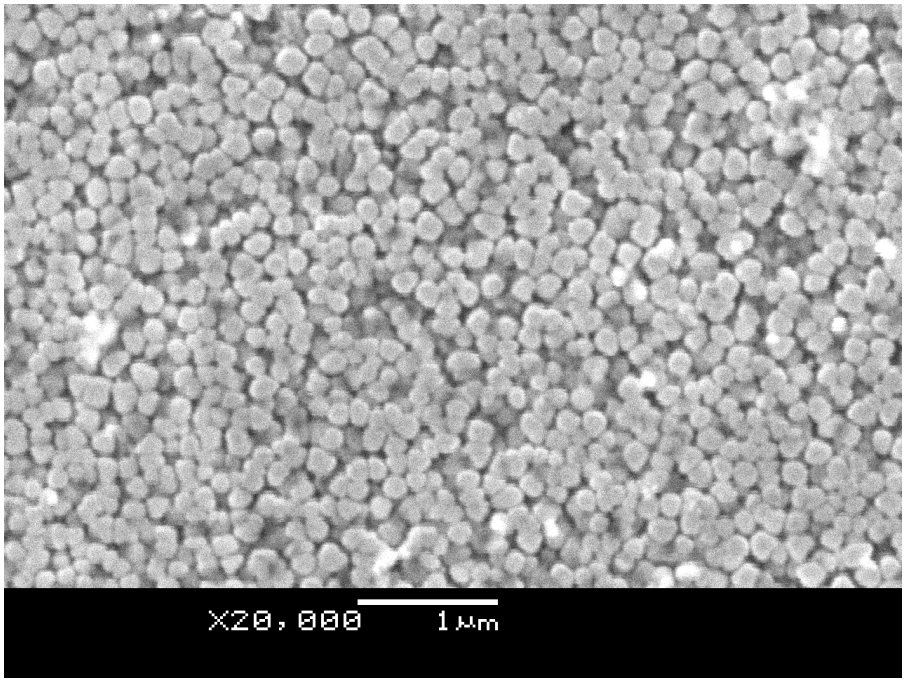

Figure 60 γ' microstructure of fast-cooled LSHR for creep and crack growth testing.

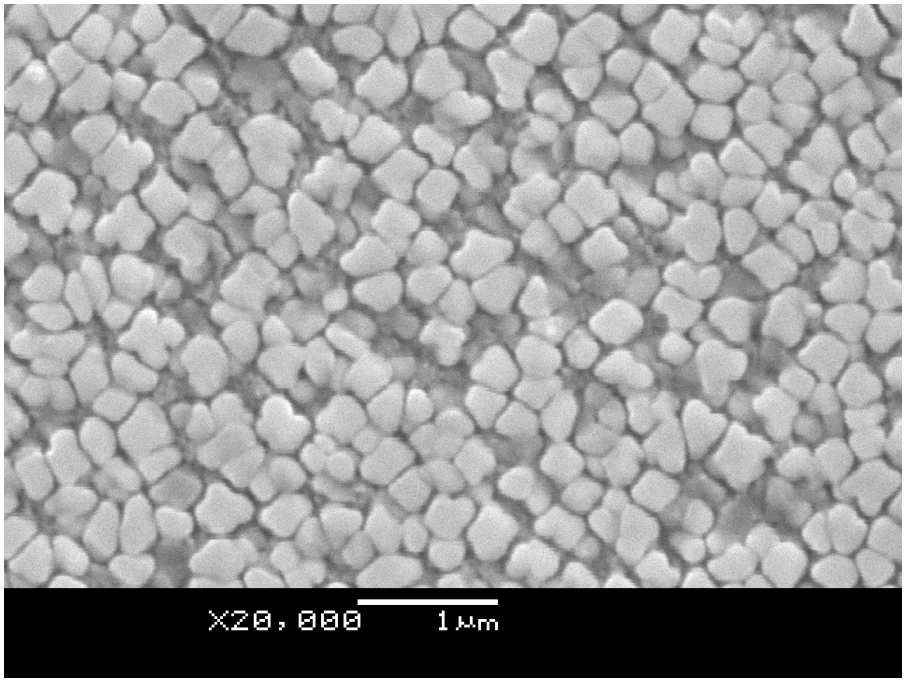

Figure 61 γ' microstructure of slow-cooled LSHR for creep deformation and crack growth testing.

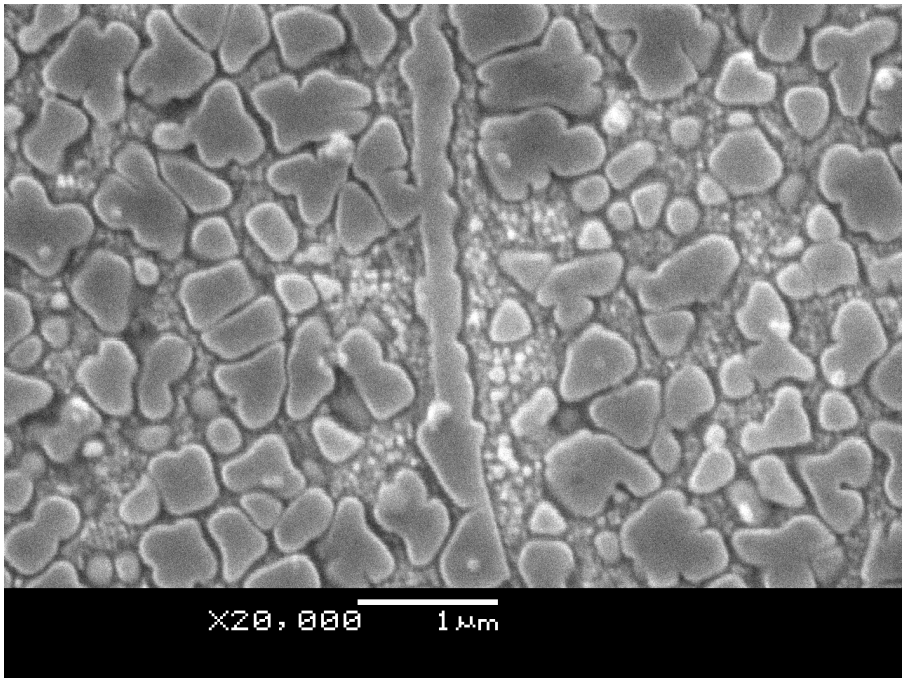

Figure 62 γ' microstructure of ultraslow-cooled LSHR for creep deformation and crack growth testing.

Figure 63 presents the relationship between the sizes of grain boundary and secondary γ' particles and cooling rates in the three heat treatments that were chosen for creep deformation testing. Particle coarsening as a function of cooling rate was consistent between the different sets of heat-treated specimens. Two of these cooling rates were faster than any used in the matrix of 72 specimens. The resulting precipitates sizes are therefore proportionally smaller. This result underscores the reproducibility of the microstructural results. Figure 64 displays the GBCR values as a function of cooling rate. Again, these values fit the same trend identified in the full microstructural investigation. Because cooling rates were more rapid, the extent of serrations was much less then previously mentioned results. For all γ' sizes, as well as GBCR, the slowest cooling rate showed the most pronounced differences. This was consistent with the previously discussed results.

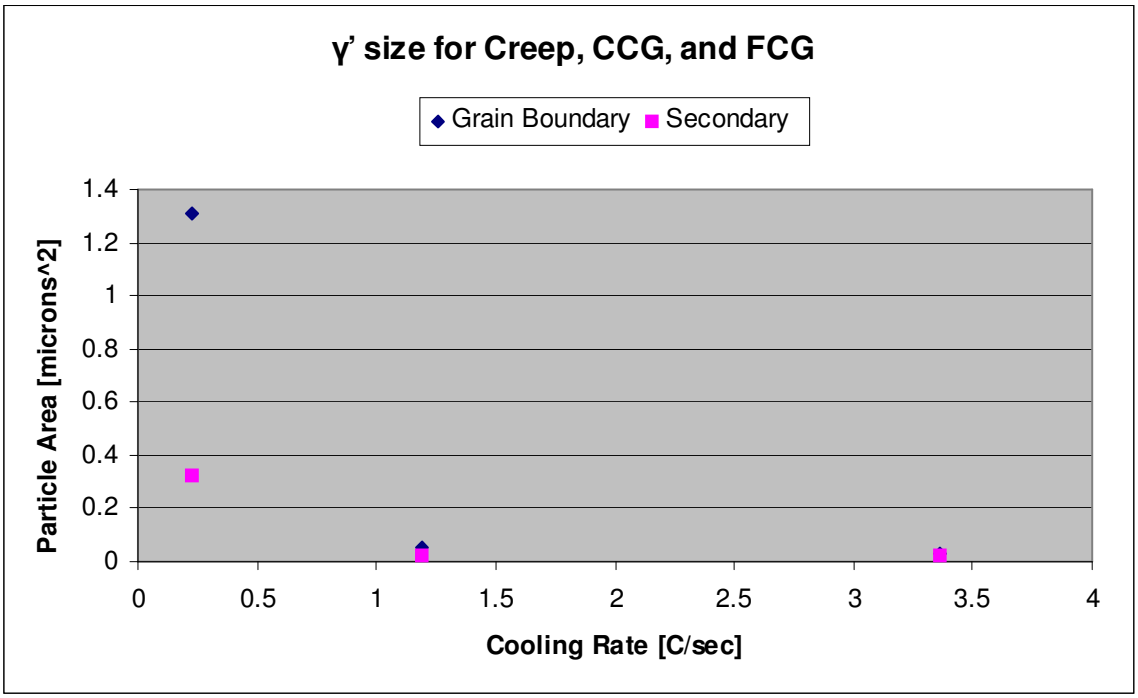

Figure 63 Variation of precipitate size with cooling rate for mechanical testing specimens.

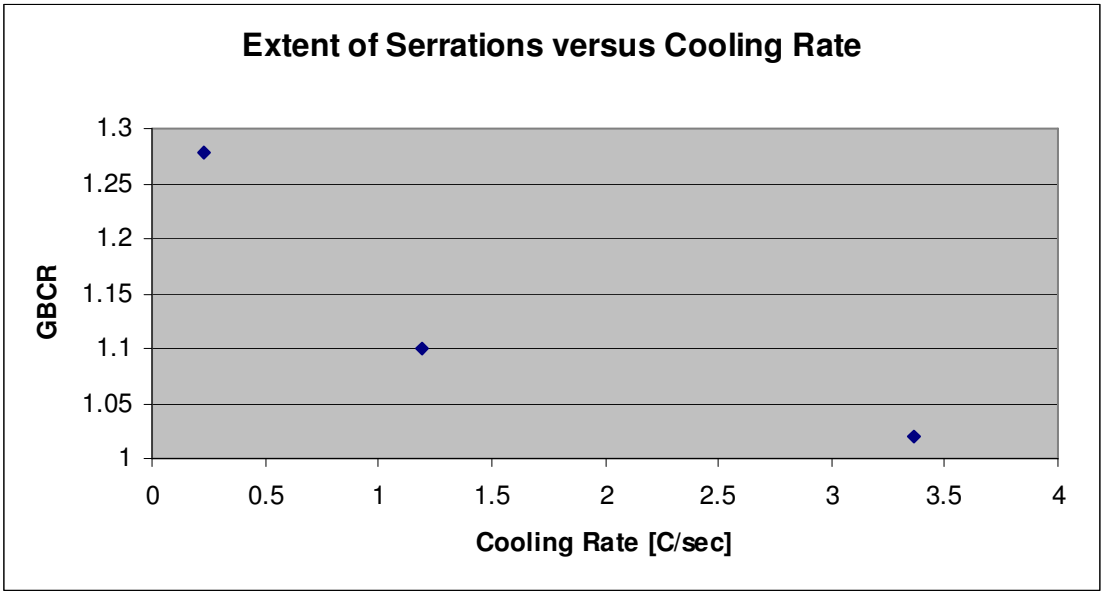

Figure 64 Variation of GBCR with cooling rate for mechanical testing speciemens.

5.3.2. Results

All tests were conducted in air at 704˚C and were allowed to continue to failure. As expected, for a given microstructure, time to reach a given percent creep strain decreased with increasing load. Tests conducted at the lowest stress level, ~685 MPa, reached 1% creep in ~250-380 hours and ultimately lasted ~1100-1350 hours. At the highest stress levels tests reached 1 % in as little as 10 hours and failed after ~100 hours. The notable exception to this was the fast cool specimen, which did not reach 1% creep until after the slower cooled specimens had failed, and did not reach failure until ~400 hours. For the three microstructures tested, Figure 65 shows the time to 1% creep for various load levels and Figure 66 shows time to failure.

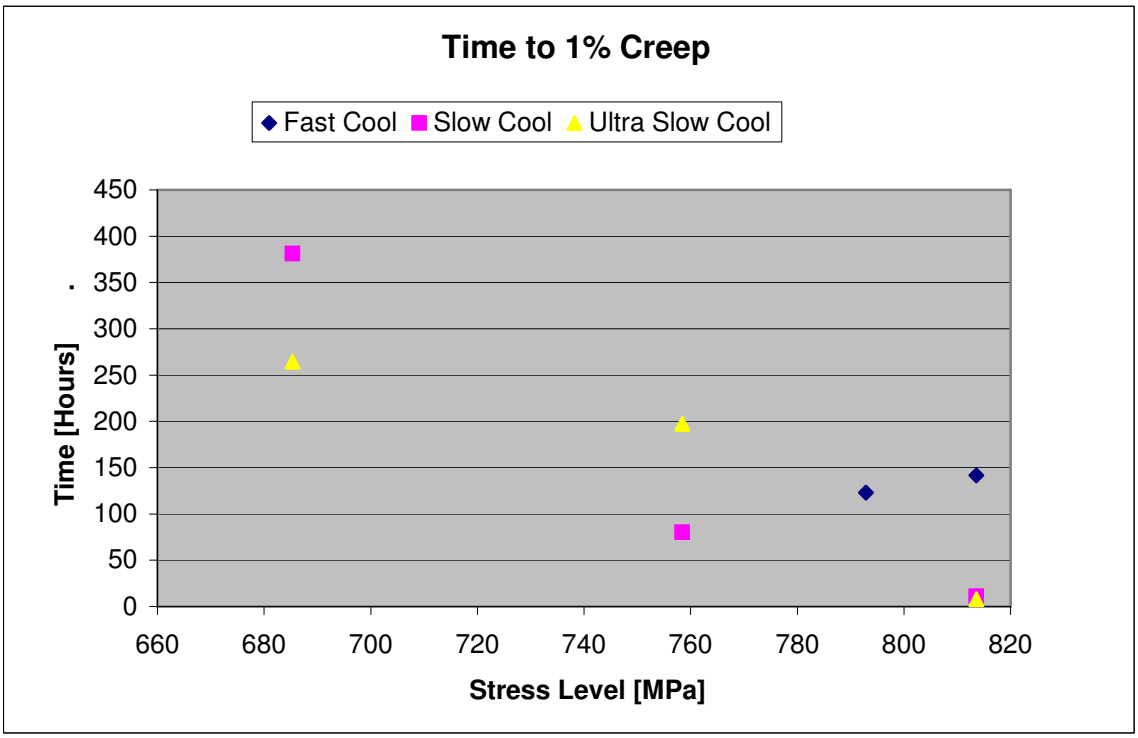

Figure 65 Time to 1% creep as a function of stress level for three microstructures of LSHR.

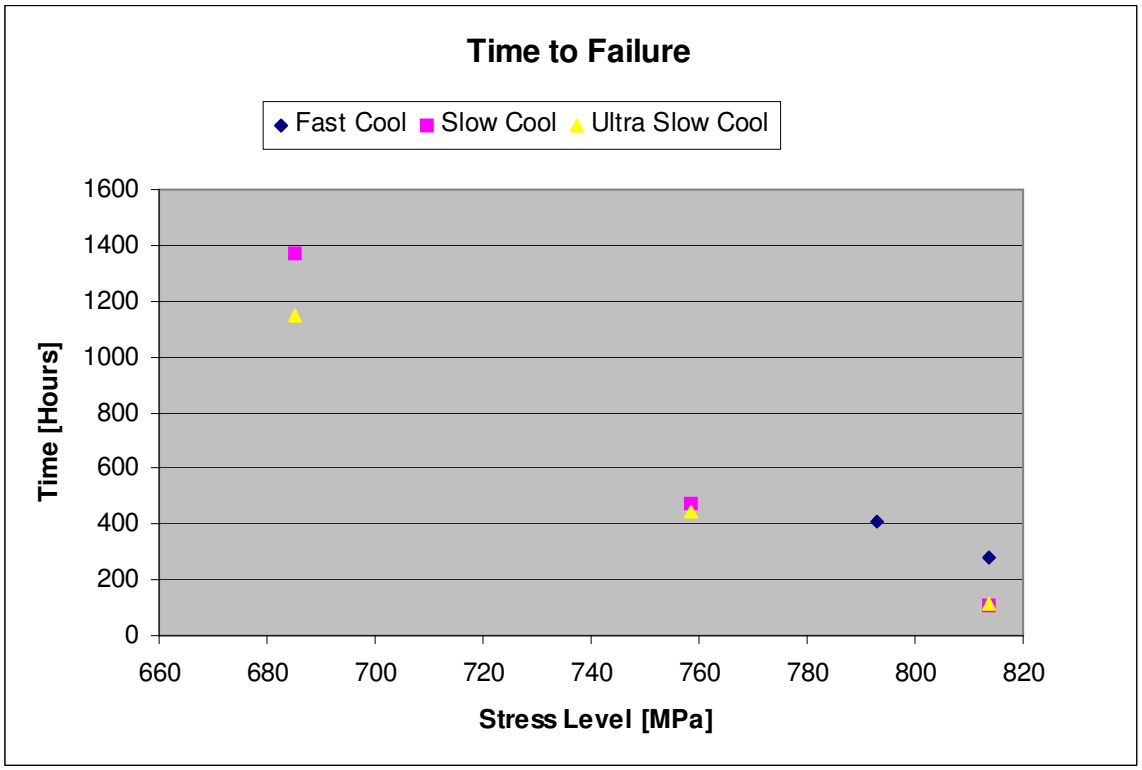

Figure 66 Time to failure as a function of stress levels for three microstructures of LSHR.

For all of the creep tests conducted, a faster cooling rate (i.e. smaller γ' precipitates) produced longer times to a given percent creep or failure. This suggests that a fast cooling rate produces a microstructure optimized for creep deformation resistance. A consideration of the creep mechanisms active in this regime is necessary to justify why small γ' is optimal.

5.3.3. Discussion of Mechanisms

During creep deformation processes, multiple mechanisms can be taking place concurrently or sequentially. While multiple mechanisms are operating at the same time, some are more relevant than others given the microstructure in question. Creep

mechanisms can be grouped into those that are diffusion based, involving flow of vacancies and interstitials, and those that are dislocation based. Ultimately, grain boundary sliding will be involved in either group to accommodate the change in structure that is the creep deformation.

This discussion of creep mechanisms is somewhat simplified due to the constant grain size for each specimen. All of the LSHR samples had a coarse grain structure (~ASTM 5.5 +/- 0.5). Coarse grains necessarily indicate a low grain boundary density. Grain boundaries are a major factor in creep deformation, as they act as an excellent source or sink for vacancies. In this way they facilitate deformation mechanisms based on diffusional flow, such as Nabarro-Herring (NH) creep. NH creep operates on the vacancy concentration gradient between the material that is under tensile strain versus that which is under compressive strain. Creep deformation occurs as the flux of vacancies goes from the tensile areas to the compressive, which is the equivalent of a mass flux in the opposite direction. In this way material is transported and the material elongates in the direction of applied stress. Grain boundary sliding must then occur to facilitate grain contiguity. For the tests considered in this section, grain boundary density remains consistently low among specimens. Thus, the discussion need not focus on the NH creep mechanism since it is, in this situation, a constant.

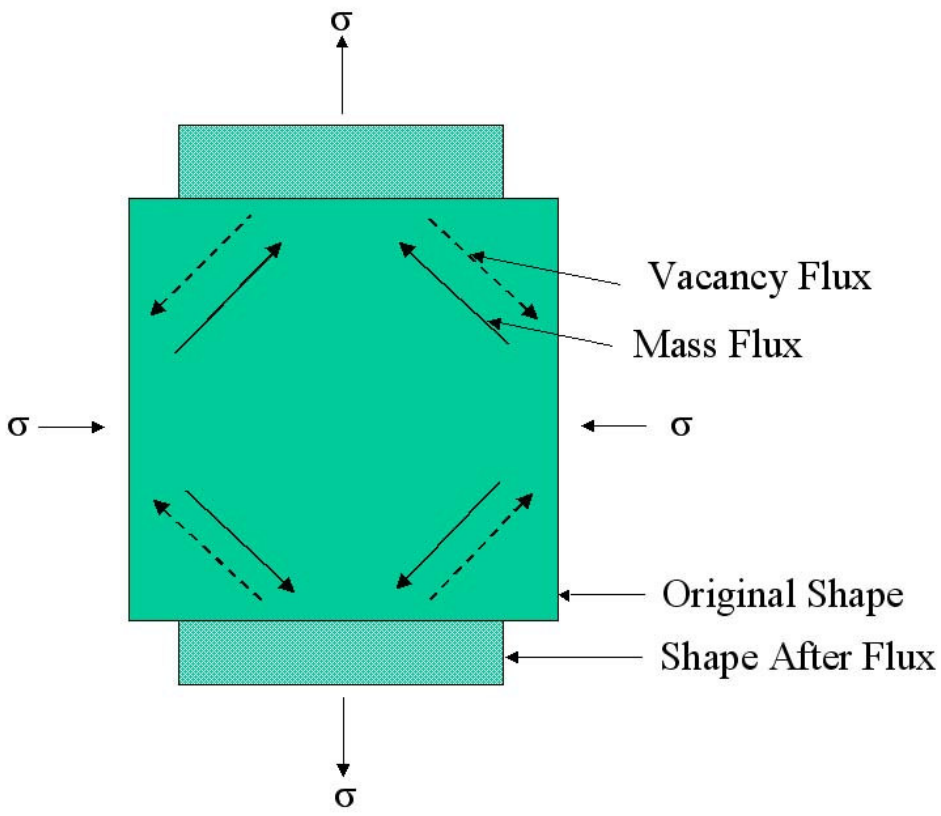

Figure 67 Schematic of the NH diffusional creep in a single 2-D grain.

A similar argument can be made for the minimal role of Coble creep in this situation. Like NH creep, Coble creep is driven by the gradient in vacancy concentration. Grain boundaries are even more important to Coble creep, as the mass transport resulting from vacancy motion is along the boundaries. Having moved material away from the boundaries and extended the grain in the direction of applied stress, grain boundary sliding must occur to accommodate the change in shape of the grains. Again, because the material is coarse grained (therefore minimizing grain boundary density) the effects of Coble creep are minimized. The variation of creep resistance for the microstructures tested would not be attributed to changes in the Coble creep.

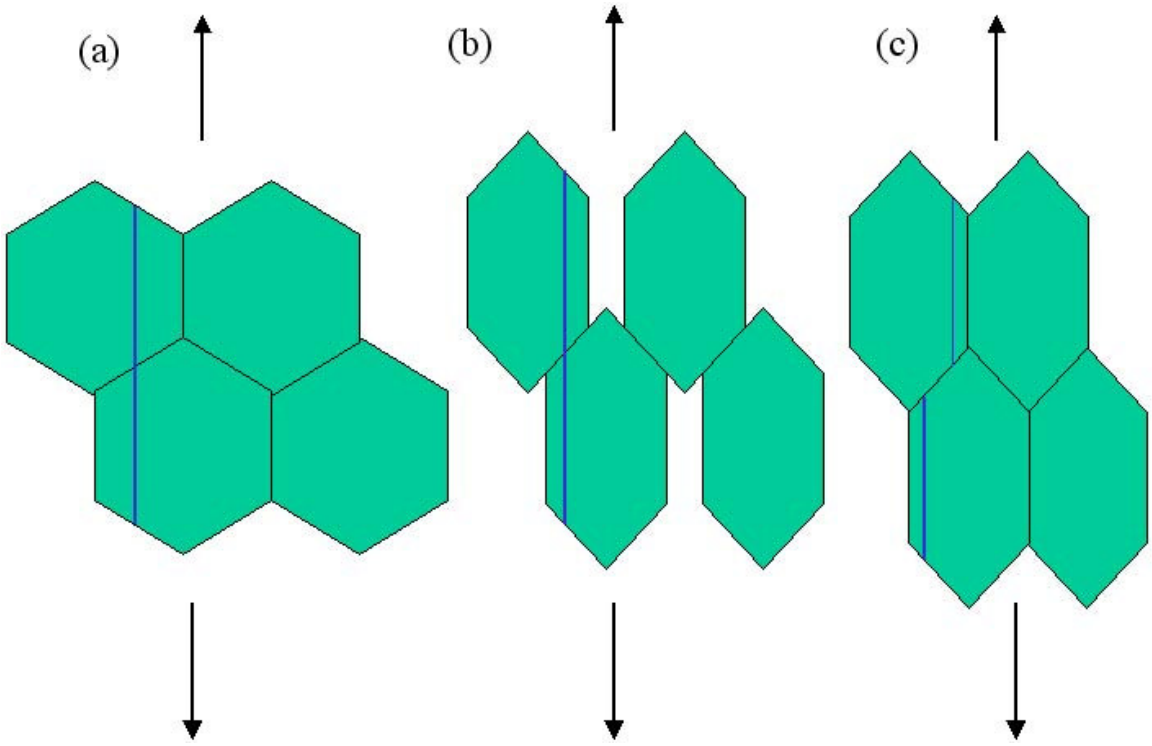

Figure 68 Schematic of diffusional creep process shown for four 2-D grains. (a) stress is applied (b) grains deform by mechanisms described previously creating gaps between grains and (c) grain boundary sliding occurs to maintain contiguity of grains.

Having discussed which creep mechanisms are not significant, namely those based on mass transport dependent on grain boundaries as a source/sink for vacancies, it is still necessary to identify which mechanisms are being affected. For this, one must consider creep mechanisms that operate on an intragranular basis. Although diffusional flow still occurs, dislocation creep is the primary creep mechanism affected by variations in γ' size and morphology.

Dislocation creep generally occurs under conditions of moderate applied stress at temperatures sufficient for thermal activation of certain processes. Dislocation creep is generally attributed to a number of mechanisms. One of these mechanisms is called "solute drag" creep. Solute drag creep is so named for the effect of solute atoms on edge dislocations. In general, size misfit between the two leads to restriction of dislocation

motion, but at higher temperatures solute atoms are mobile and can move along with the dislocations, causing a 'drag' effect on their motion. During stage 1 creep, the number of dislocations increases while the concentration of solute atoms remains constant, thus the relative amount of drag decreases. The solute drag mechanism is identified by an increase in creep rate during stage 1 creep prior to steady state due to the decrease in the drag effect. An increase in creep rate prior to steady state creep was not seen to occur in the creep deformation tests conducted, and therefore solute drag creep is not considered. The more likely mechanism of dislocation creep applicable to the situation at hand is dislocation climb-glide.

The details of mechanisms responsible for dislocation climb-glide creep have not been firmly established, although the basic physics behind the process is understood. Put simply, dislocations are emitted from a source and move through the grain until they encounter an obstacle at which point they climb in order to surmount the obstacle. The dislocation motion is driven by the applied stress. For strain to continue at a constant stress such as during creep deformation, dislocations must be eliminated as the source produces more. This occurs when the dislocation climbs to a parallel plane and interacts with other dislocations. There they are annihilated by interaction with other dislocation and the addition of atoms or vacancies. This process can be seen schematically in Figure 69.

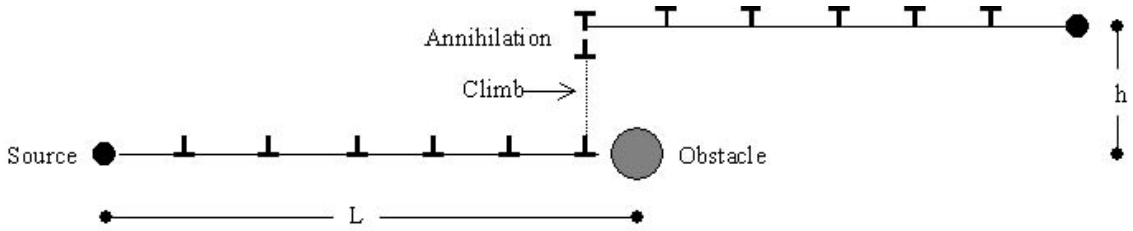

Figure 69 Schematic of the mechanisms driving dislocation climb-glide creep.

Dislocations emitted from the source, such as a Frank-Read source, glide a distance, L, until they encounter an obstacle. At the obstacle, the dislocation climbs to a parallel plane separated by a distance h. On the parallel plane the dislocation will interact with other dislocation. Depending on their relative types, annihilation will occur by the addition of atoms or vacancies to the terminations of the dislocations. Mass transfer must be involved regardless. The source cannot emit dislocations limitlessly. The annihilation of dislocations is necessary to prevent pile-up and for continued strain without raising the stress level.

It is proposed that γ' precipitates act as obstacles to dislocation motion within the context of dislocation creep. Creep test results showed that specimens with a more rapid cooling rate produced the slowest creep rates and longest times to failure. Rapid cooling rates produce a fine dispersion of precipitate particles. These precipitates act as obstacles to dislocation motion, forcing them to climb. This contributes to the reduction of dislocation creep rates. This reduction in creep rate is made obvious in the derivation of dislocation creep rate, $\dot{\varepsilon}_{CG}$. The following derivation is based on that found in the mechanical behavior text by Courtney [44].

$$\dot{\varepsilon} = \rho b v_g \tag{11}$$

Equation 11 describes the general calculation of strain rate for dislocation creep. The term υ_g is the glide velocity, which is more rapid than the climb velocity, υ_c. The two can be related however, as $\upsilon_g = (L/h)\,\upsilon_c$. The dislocation density is represented by ρ and can be calculated by multiplying the number of dislocation sources, M, by the spacing distance L and the loops per source, which is proportional to L/h. This allows Equation 11 to be written in the following form.

$$\dot{\varepsilon}_{CG} \sim \frac{ML^3}{h^2}\upsilon_c \tag{12}$$

Physical considerations can be incorporated that allow υ_c to be rewritten. Based on the idea that dislocation climb is driven by applied stress and facilitated by mass transfer, the climb velocity would be proportional to lattice diffusivity and applied stress. That is $\upsilon_c \sim D_L\sigma$. Further, the applied stress can be written in its normalized form, $\sigma\Omega/kT$, which incorporates temperature dependence. Ω is atomic volume and k is the Boltzmann constant. With these substitutions, one arrives at a convenient form of climb-glide creep rate. This is seen in the following equation.

$$\dot{\varepsilon}_{CG} = \frac{D_L ML^3}{h^2}\left(\frac{\sigma\Omega}{kT}\right) \tag{13}$$

Lowering strain rates are an indication of improved creep performance. If the γ' particles are able to act as obstacles to dislocation motion, then minimizing the distance L between these obstacles will improve the creep performance of the alloy. From the derivation of dislocation climb-glide strain rate above, the L term is in the numerator and

taken to the third power. The effective inclusion of obstacles at small spacings has the potential to drastically reduce creep rates by minimizing this term. This conclusion is consistent with the observation of reduced creep rates for specimens receiving a rapid cooling rate, which produces the smallest γ' particles. This derivation is included to spell out the effect of microstructure, specifically precipitate particles as obstacles to dislocation motion. Quantitative use of this derivation, using creep rates from testing, has the potential to confirm which population of particles is acting most effectively as obstacles. This approach becomes difficult, as it would also require numerical quantities for physical features such as M, the density of dislocation sources and D_L, the lattice diffusivity. Even without quantitative treatment, this derivation provides insight on the role of obstacle spacings in creep rates. It can facilitate a theoretical discussion of effect of microstructure on creep deformation by spelling out the contributions of physical quantities.

The variation of minimum creep rates from the testing with cooling rate was not linear. This supports dependence of dislocation creep rates being dependent on a L^3 term, which is also not linear. Also, this is consistent with the three dimensional nature of creep phenomena, especially when mechanisms are based on microstructural features.

The effect of obstacle spacing in this derivation is consistent with that in the discussion of strengthening mechanisms in 5.1.4. In both cases the minimization of the obstacle spacing term causes an improvement in alloy performance, either by increasing the resolved stress or decreasing the creep rate. This consistency is due to the similar mechanism of dislocation-obstacle interaction in both

Due to the scale on which these mechanisms are taking place, it is hypothesized that tertiary γ' are the dominant in the role of obstacle. Secondary γ' size and spacing are significantly larger and are unlikely to be involved in the climb-glide mechanism as presented. Extremely high-resolution SEM or TEM images would be necessary to provide valid quantification of tertiary γ' for the microstructures under consideration. In addition, TEM techniques would be necessary to document the dislocation-obstacle interactions, if it is possible to do so at all.

Dislocation creep still requires grain boundary migration to occur to maintain contiguity. The climb-glide process in areas adjacent to the grain boundaries can be facilitated by grain boundary migration. If migration does not take place at rates needed to accommodate the creep rates in the grain interior, then grain boundary cracking will occur. It is the coalescence of these grain boundary cracks that is ultimately responsible for the failure of the material under creep loading conditions. Investigation of the fracture surfaces of the creep-ruptured specimens illustrates this.

5.3.4. Creep Rupture Fracture Surfaces

Figure 70, Figure 71, and Figure 72 show the surfaces of specimens failed by creep rupture at ~814 MPa at 704˚C. Microstructure and creep rates for each varies because they are for fast, slow and ultra slow cooled specimens, respectively. However, all of them show typical intergranular creep failure. This is indicated by the faceted contours on the surfaces that correspond to grain boundary surfaces. This failure mode is based on the coalescing of cracks on the grain boundaries. These cracks form when grain boundary sliding does not take place to offset creep deformation and maintain a

continuous material. Intergranular creep failure is expected for conditions with moderate stresses and high temperatures, such as those used for testing.

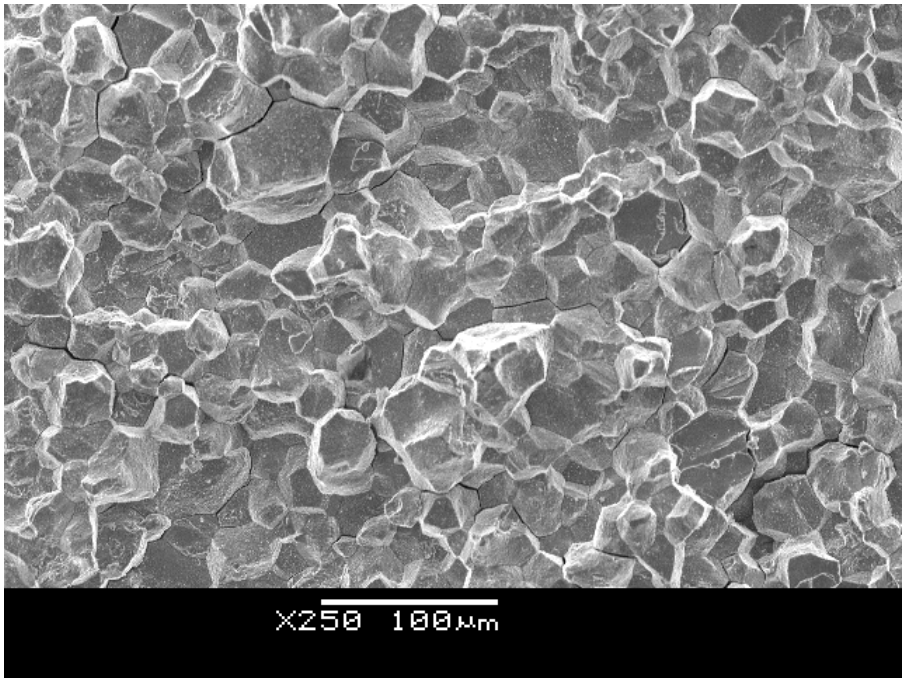

Figure 70 Surface of fast-cooled specimen after creep rupture.

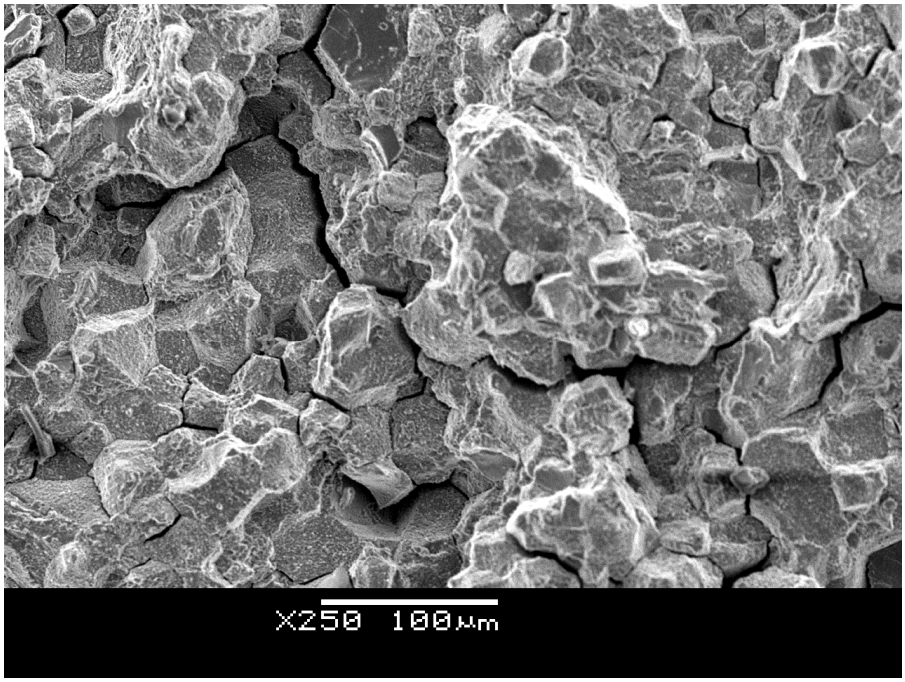

Figure 71 Surface of slow cooled specimen failed by creep rupture.

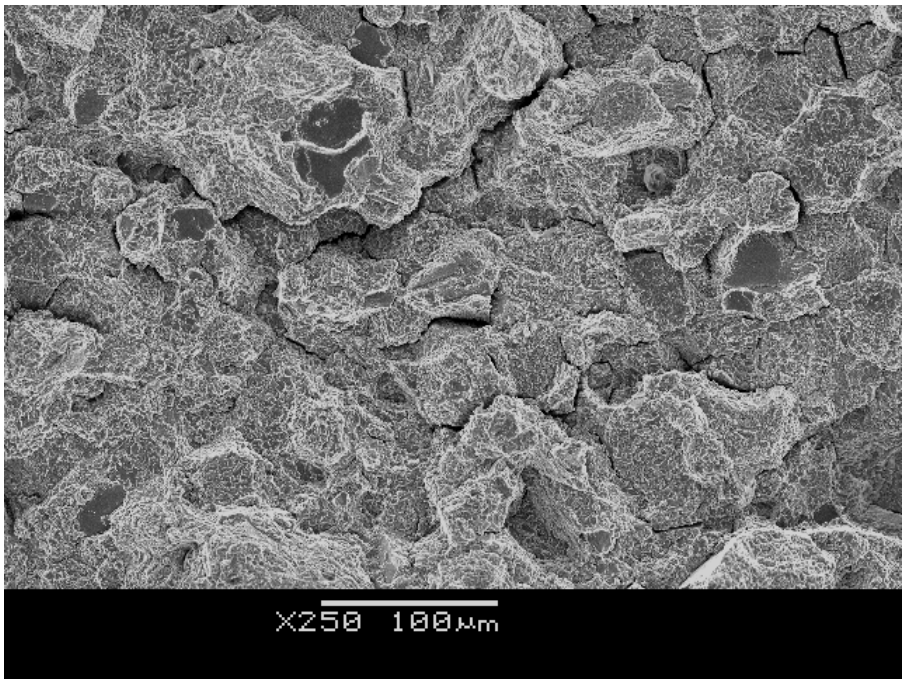

Figure 72 Surface of ultra-slow cooled specimen failed by creep rupture.

Although these three images show 100 percent intergranular failure, it is interesting to note the differences in the surfaces of the grains. The faceted surface of the fast cooled specimen appears to be very smooth. For each subsequent decrease in cooling rate, the grain surfaces seem to become increasingly rough. This is a manifestation of the increase in grain boundary serrations. Up to this point, serrations have been quantified and discussed based upon two-dimensional corollary. However, because the creep failure takes place intergranularly, one is able to see the actual grain boundary surface. On this plane, the variation in the extent of serration, seen as roughness, with cooling rate is visually exposed.

5.3.5. Summary of Creep Deformation Results

Results from creep deformation testing of variations of coarse grain LSHR suggest that rapid cooling of specimens improves the creep capabilities of the alloy at 704˚C. Creep strain rates were minimized and time to 1% creep and time to failure were extended. Grain size remained constant for each specimen tested, so improvements to creep must be a function of mechanisms internal to the grain. This is attributed to the role of γ' particles as obstacles to dislocation motion within the context of dislocation creep.

Dislocation climb-glide and the possible role of microstructure in this creep mechanism have been explained. The potential to link creep performance, as strain rate to microstructural variables has been established. Based on current understanding, dislocation creep rates are reduced and the creep strength improved by minimization of spacing between obstacles that force the dislocation to climb. Further, creep deformation

testing at additional temperatures and with variation of γ' size (cooling rate) must be completed to justify the inclusion of microstructural parameters in strain rate calculations. SEM and TEM techniques should be applied to evidence the interaction of γ' and dislocations.

In the mean time, it is sufficient to note the phenomenological evidence for improved creep resistance with a dispersion of fine γ'. This relationship can be incorporated into improvements in alloy performance by tailoring alloy heat-treatment appropriately. This improvement to alloy performance could be effective and inexpensive, as it involves no change to alloy composition or solutioning.

5.4. Crack Growth Testing

Crack growth testing is becoming increasingly prominent in industrial settings. As engineers better understand the mechanisms of crack growth phenomenon this crucial feature can be better incorporated into superalloy component design. The aeronautics industry relies on a damage tolerance design approach, meaning that parts must retain their integrity in the presence of a crack or flaw until the damage can be detected. This approach supports a philosophy of cause-based retirement of components, which optimizes the factors of cost and safety. A full understanding of crack growth behavior is crucial to the successful application of this approach.

Crack growth tests involve more complex specimen geometry and can require more complex test set-up. Like tensile testing or creep deformation several mechanisms can take place during the crack growth. However, in crack growth additional consideration must be given to loading arrangements and environmental effects. The

same material will behave differently under steady versus cyclic loading. When this is compounded by the effect of varying microstructures, crack growth becomes a very complex problem.

These tests were conducted on compact type (CT) specimens that had been pre-cracked. Therefore, crack initiation is not a parameter. Crack propagation is the primary consideration, either as crack growth rate as a function of time, da/dt, for creep crack growth tests or crack growth rate as a function of cycles, da/dN, for fatigure crack growth tests. Just as material response varies with the type of loading, so too should the microstructural effect on behavior vary with the type of loading. The mechanisms driving each behavior will determine the effect of the microstructure.

5.4.1. Creep Crack Growth

Results from creep crack growth testing indicate a significant difference in crack growth rates for specimens of different cooling rates. Crack growth rates for slow cooled specimens were an order of magnitude slower than were the fast cooled specimens. Estimates of creep crack growth rates were made based on the amount of stable crack growth and the time to failure. These are graphed as a function of initial stress intensity factor, K, in Figure 73. Both specimens are nominally identical and were subjected to the same load. However, the rates in the slow-cooled specimen with the more serrated grain boundaries was an order of magnitude slower.

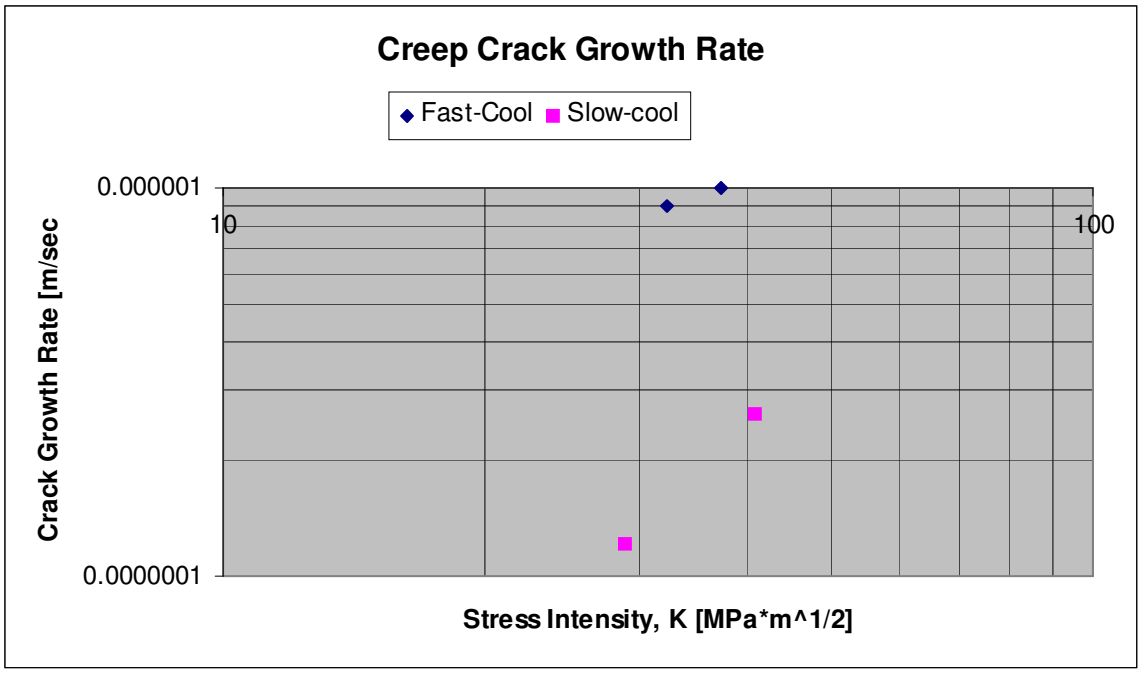

Figure 73 Graph of estimated crack growth rates for creep crack growth tests as a function of initial stress intensity factor.

Figure 74 shows a low magnification image of a creep crack growth fracture surface. Stable crack growth, indicated by intergranular fracture can be seen transitioning into unstable, transgranular growth immediately before failure. Figure 75 shows a higher magnification image of the stable, intergranular crack growth typical of all four creep crack growth tests. As with the creep deformation fracture surfaces, the texture of grain facets in the transgranular fracture surfaces indicates the extent of serrations.

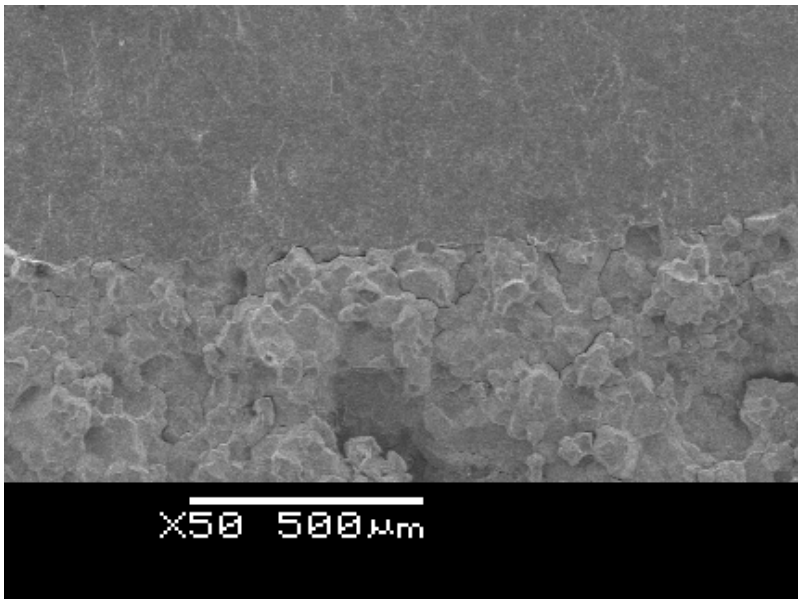

Figure 74 Low magnification SEM image of transition from stable (intergranular) crack growth to overload in slow-cooled supersolvus LSHR.

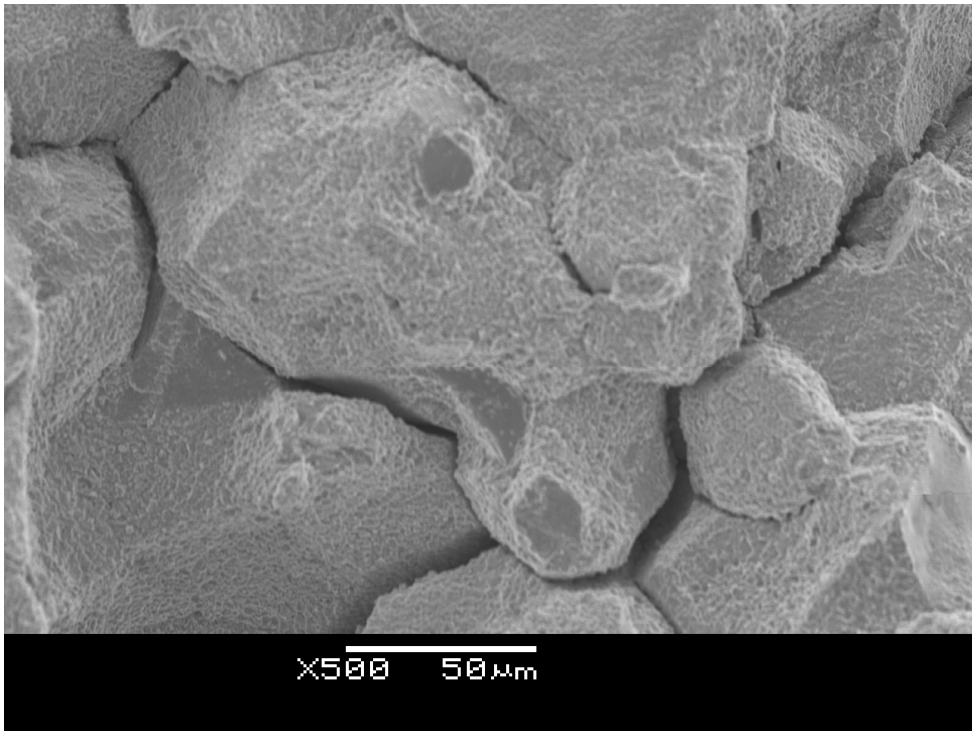

Figure 75 Close up of intergranular creep fracture surface of slow cooled LSHR creep crack growth test specimen.

It was anticipated that slow-cooled specimens with more extensive grain boundary serrations would have slower crack growth rates. Indications from creep crack growth testing show that slow cooled specimens resist creep crack growth better than fast cooled specimens. Estimated creep crack growth rates were slower for the two tests on slow cooled specimens. This suggests that improved crack growth resistance can be achieved with a microstructure that includes serrated grain boundaries and coarser γ' particles. This is based on the effect of cooling rate from solutioning on the superalloy and the subsequent crack growth behavior.

Cooling rate variations alter the size and distribution of γ' as well as the grain boundary serrations. Consensus in the field of crack growth suggests that the vulnerability of grain boundaries to environmental attack controls the crack growth behavior. As such, grain boundary serrations are suspected to play a role in any variation in crack growth behavior. It is hypothesized that serrated grain boundaries create a longer, more torturous path for oxygen diffusion. This diffusion leads to grain boundary embrittlement, which encourages void/crack formation at the grain boundaries. This theory is consistent with the nature of the fracture surfaces documented as well as the crack growth rates for a given microstructure.

Many challenges were encountered in the creep crack growth testing of LSHR. Although valuable results were still achieved, steps should be taken to avoid these problems in the future. Two factors limited the success of these tests. The primary factor was limited instrument resolution and the other was error in pre-cracking of the specimen.

DCPD measurements were taken to monitor crack growth during the tests. However, recorded readings of potential drop did not resolve any change in voltage during the test. Fracture surfaces, on the other hand, indicate that stable crack growth did occur. Improved resolution of DCDP signals is absolutely necessary in further testing to better monitor the progression of crack growth and produce full crack growth rate curves.

Fatigue pre-cracking led to highly tunneled and overly long pre-cracks. Crack fronts tunneled extensively for all specimens. Also, the pre-cracks exceeded anticipated lengths so that initial K levels for testing were higher than intended. Because stress intensity factors were much higher than intended, the crack growth tests were accelerated and failed quickly. Tests on slow cooled specimens hung for a few hours before failure, fast cooled specimens tested for approximately one hour before failure. Problems with pre-cracks were exacerbated when side-grooves were made in the specimen. This process extended pre-cracks further and tunneling persisted. In future testing, minimal pre-cracking should be attempted and side grooving should be omitted. Confirmation of initial crack size should be made so that tests can be run at lower initial stress concentrations. This should lead to longer tests with more clearly delineated stages of crack growth.

At this time, data suggests a significant impact of microstructure on creep crack growth behavior. Results suggest a relationship between lower crack growth rates and more extensive grain boundary serrations. Because of the order of magnitude improvement that was seen, we strongly recommend more tests be conducted. However, the microstructural features that affect creep crack growth rates cannot be identified with certainty until further testing is conducted. Improved resolution of potential drop

measurements is necessary to produce useful results for creep crack growth studies. Consistent pre-cracking, free of tunneling, will also be necessary for accurate results.

5.4.2. Fatigue Crack Growth

A da/dN versus ΔK curve was generated for fast and slow cooled LSHR. These can be seen in Figure 76. Results for fatigue crack growth rate for both microstructures were very similar. There does not appear to be any major differences between the FCGR behavior of the slow and fast cooled materials. Any definite conclusions about relationships between fatigue crack growth rates and γ' size cannot be made based on such limited data. Not only are more tests necessary, but also testing of microstructures with greater variations should be included among the test conditions.

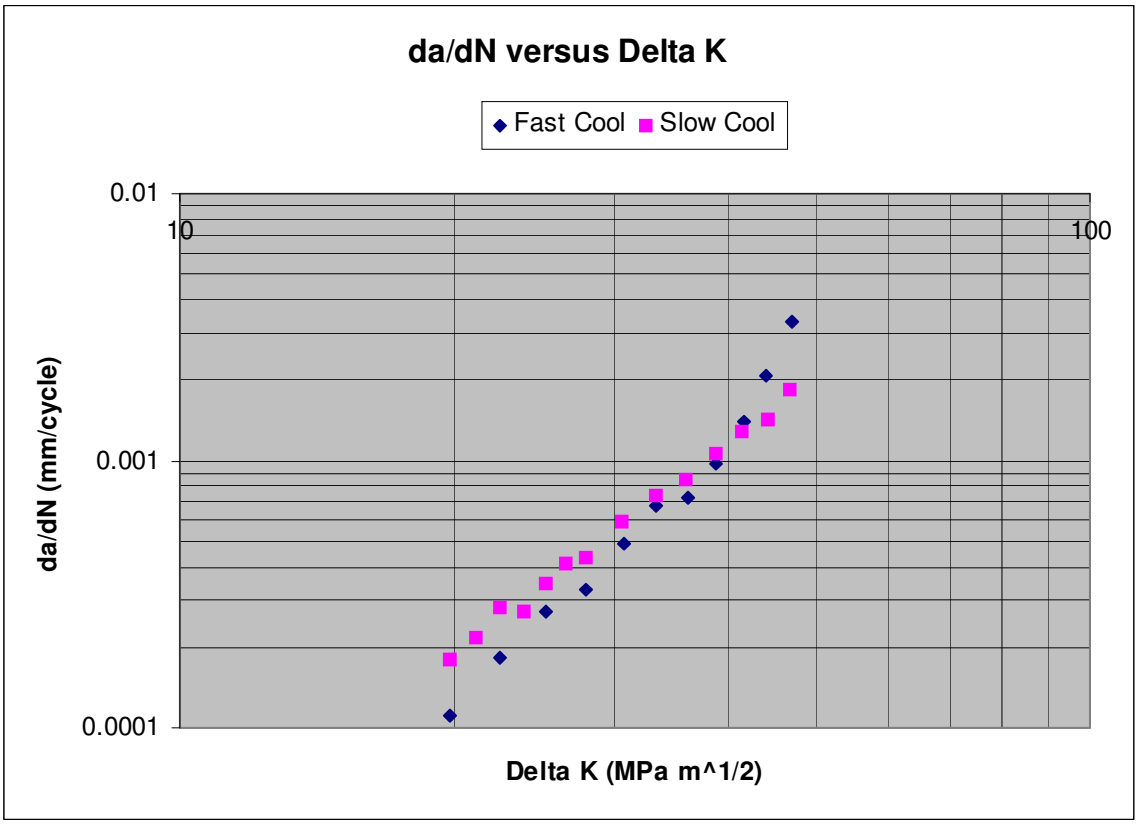

Figure 76 Fatigue crack growth rates for fast and slow cooled LSHR.

SEM images of fracture surfaces are seen in Figure 77 and Figure 78. Fracture surfaces for both fatigue crack growth specimens are similar. Striations are visible on both, with similar texture and spacing. Cracking perpendicular to primary crack growth takes place at intervals along striations on both specimens. Crack growth was transgranular in both cases. Transgranular crack growth is expected for this type of fatigue crack growth testing. Fracture surfaces also indicate that there was no discernable variation in fatigue crack growth behavior for these two microstructures.

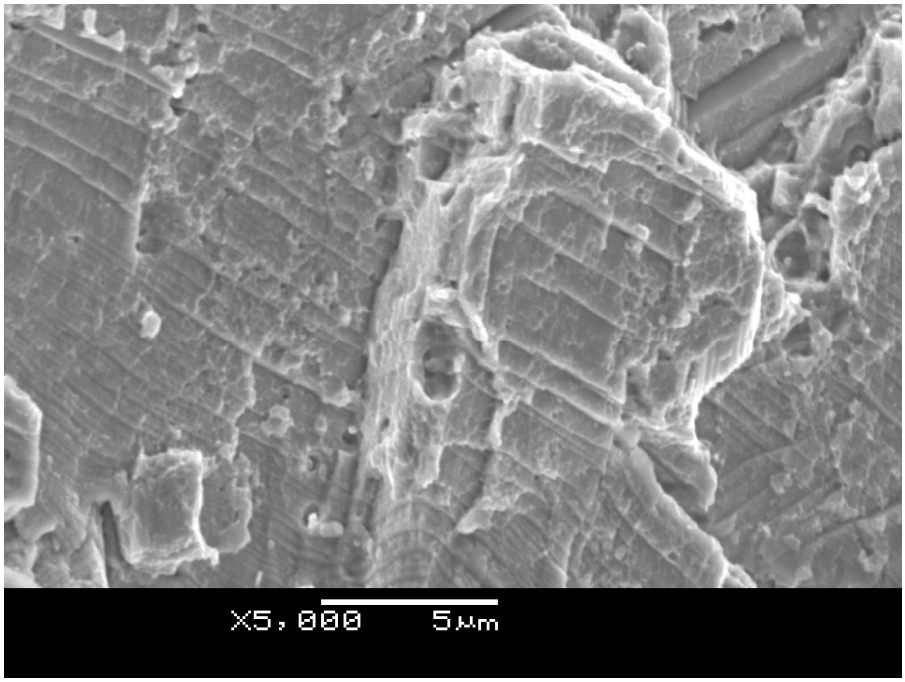

Figure 77 Crack growth fracture surface of fast cooled LSHR subject to fatigue loading.

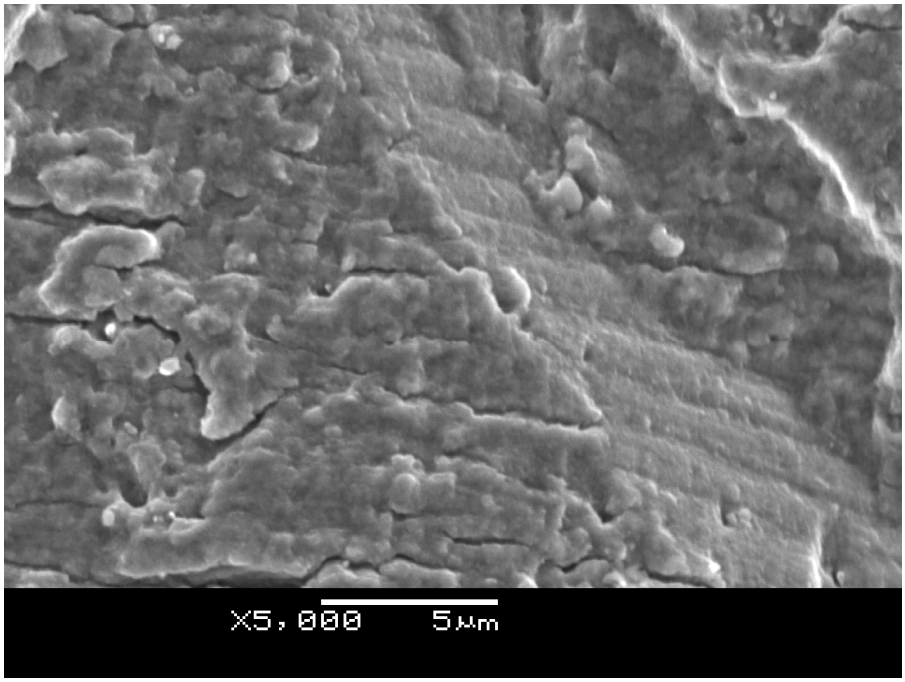

Figure 78 Crack growth fracture surface of slow cooled LSHR subject to fatigue loading.

Results from testing indicated that the variations in microstructure tested did not affect fatigue crack growth rates. The two microstructures produced da/dN versus ΔK curves that were virtually identical, any differences being well within the scatter expected. These results were consistent with unpublished results on coarse grain RR1000 material. Tests were conducted on various cooling rates of supersolvus solutioned RR1000. Fatigue crack growth rates for these tests fell very closely. From these tests of RR1000, as with the LSHR, there was no evidence that microstructure affect crack growth rates.

5.5. Summary

In general the results presented in this section confirm the ability to tailor alloy performance for a given application by manipulating microstructure. Thus, engineers can enhance material performance in an efficiently and gain a deeper understanding of the mechanisms controlling the mechanical behavior of the alloys. This aspect of the research incorporated several types of high temperature mechanical tests on a variety of microstructures that were produced by varying alloy chemistry and heat treatments. The correlations between microstructure and mechanical properties were discussed in the context of deformation and failure mechanisms. Qualitative descriptions of the correlations established from the results of this study have been briefly described in Table 15.

Table 15 Summary of results for structure-property investigation.

Mechanical Property	Relevant Processing Step	Relationship	Comments
Hot Tensile	Cooling Rate-γ' size/distribution	Smaller γ' improve strength	Alloy chemistry important
Hot Hardness	No correlations	n/a	No correlation to microstructure or chemsitry
Creep Deformation	Cooling Rate-γ' size/distribution	Smaller γ' improve creep resistance	γ' alter dislocation creep rates
Creep Crack Growth	Cooling Rate-grain boundary serrations	Serrated boundaries reduce creep crack growth rates	Rate of oxygen diffusion at grian boundaries affected by serrations
Fatigue Crack Growth	No correlations	n/a	Fast and slow cooled produce same FCG rates

Mechanical tests conducted included high temperature tensile, hot hardness, creep deformation/rupture, creep crack growth, and fatigue crack growth. Heat treatment of specimens for mechanical testing was varied in order to study the effect of microstructural changes on mechanical behavior. Tensile and hardness tests incorporated the full compliment of 72 conditions that included four alloy chemistries and various heat treatments including solutioning temperature, cooling rates and intermediate thermal hold temperature. Creep and crack growth tests were limited to supersolvus LSHR material with varying cooling rates. The choices of these tests were limited by availability of materials and time available to complete the project. The relevant microstructural feature depended on the behavior being considered and the mechanisms involved, although the interaction of moving dislocations with γ' obstacles was a common theme.

Tensile testing produced results for yield strength and UTS at 704˚C. LSHR had the highest results across the board; this is likely due to solid solution strengthening. Microstructural effects on yield strength involved variation of γ' precipitate size and distributions, but not grain size. Faster cooling rates and higher hold temperatures, which

produced the finest distributions of γ', produced the highest strength materials. The opposite was also true; slow cooled specimens that had the largest precipitates had the lowest strengths. The ability of γ' particles to interfere with dislocation motion is the basis for this strengthening. ANN models were able to successfully predicted yield strength. Microstructural quantities did not need to be input as the model was sufficiently well trained so as to infer their influence from the processing and chemistry variables that were included.

Hardness testing was conducted in an attempt to correlate high temperature hardness to strength. This was not achieved as hardness results did not correlate with any other factor, microstructural or mechanical. Hardness values did decrease with increasing temperature for all materials but no systematic variation with material or microstructural feature could be established. Accuracy of measurements and relative indent size were an issue.

Creep deformation testing indicated improved creep resistance for specimens with fine γ', i.e. specimens with a more rapid cooling rate. This improvement is attributed to the role of γ' particles as obstacles to dislocation motion within the context of dislocation creep. The coarse grain material means lower grain boundary density which minimizes the effect of diffusional creep. Rapidly cooling the alloy from supersolvus solutioning forms numerous closely spaced particles that impede dislocation motion. Therefore an ideal alloy for creep deformation resistance would be given a supersolvus heat-treatment to create a coarse-grained structure and cooled rapidly to minimize precipitate size.

Creep crack growth rates were estimated for slow and fast cooled supersolvus LSHR. These suggest that slow cooled specimens are able to resist creep crack growth better than fast cooled specimens. Creep rates in samples with more serrated boundaries and larger γ' were an order of magnitude slower. It is hypothesized that the slowing of diffusion of oxygen through the grain boundaries serrations is responsible for improved crack growth resistance. More crack growth testing in air and in vacuum is necessary to confirm this.

The results from cyclic crack growth testing were inconclusive. One test on slow cooled LSHR and one test on fast cooled produced very similar results. This would seem to suggest that, despite the obvious effects of grain size on fatigue crack growth, precipitate size or grain boundary formations do not affect cyclic crack growth resistance. Again, further testing will be required to confirm this conclusion.

Overall, cooling rate was the most dominant processing parameter affecting mechanical properties. The variation of γ' sizes and distribution and grain boundary serrations with cooling rate affected the mechanisms controlling strength, creep and crack growth properties. Secondary hold temperature played a relatively minor role. Once above the solvus, solutioning temperature (via grain size) does not seem to affect mechanical behaviors. The obvious effect of microstructure on mechanical properties highlights the need for special attention to be paid to superalloy component processing. In addition, it illustrates the opportunities for improvement in alloy performance with simple adjustments to processing steps.

CHAPTER 6 Conclusions and Future work

The objective of this work was to systematically study the relationship between processing parameters and microstructure, and microstructure and mechanical properties in Ni-base disc alloys. Efforts were concentrated on high-temperature mechanical testing of supersolvus heat-treated materials. Microstructures resulting from various heat-treatments were documented and quantified. Quantified results were discussed based on the mechanisms of formation. Results from mechanical testing were presented as a function of processing variables or microstructural quantities. The relationships amongst these properties were presented in the context of damage mechanisms and their interactions with microstructural features. From this work several conclusions can be drawn.

1. Grain size results were most directly linked to solution temperature, with the additional influence of cooling rate. For all alloys additional coarsening as a function of solution temperature was only seen at higher temperatures.

2. Secondary γ' precipitate size was a direct function of cooling rate. Larger particles resulted from slower cooling rates. Grain boundary γ' scaled with cooling rate in the same way as secondary, although it is significantly larger due to the addition of grain boundary diffusion.

3. Processing variables controlling the morphology of secondary γ' particles include cooling rate secondary hold temperatures. For all specimens, rapidly cooled

specimens produced spherical precipitates. Precipitate particles from slower cooled specimens showed increasingly complex shapes. In addition, variations in morphology as a function of alloy composition were evident. This effect of composition is likely due to the variation of misfit between matrix and precipitate with variation in alloy chemistry. LSHR and Alloy10 showed pseudo-dendritic geometries indicating higher levels of misfit strain, as compared to RR1000 which did not grow in crystallographically relevant directions.

4. Extent of grain boundary serrations increased as a cooling rate decreased. As cooling rate decreases, average grain boundary γ' size increases, which is the cause of grain boundary serrations.

5. Large precipitate particles were detrimental to the high temperature tensile strength of all alloys tested. Rapid cooling of specimens decreases precipitate spacing and thereby improves both yield strength and ultimate tensile strength.

6. No evidence was found to relate hot hardness measurements to alloy composition or microstructural features. Further, no correlation was established between hot hardness and UTS or yield strength values for tests at the same temperature.

7. Increased cooling rate from supersolvus hold temperatures produce microstructures with better creep deformation resistance. Decreases in the

precipitate spacing increased the impedance of dislocation motion through the material, thereby decreasing strain rate.

8. Creep crack growth rate decrease significantly in specimens given a slow cooling from supersolvus solutioning. Intergranular fracture surfaces suggest the importance of grain boundary serrations in this phenomenon.

9. Limited data can be used to train ANN models that are capable of predicting output with minimal error.

In addition to the specific conclusions listed above, general conclusions from the research are as follows.

1. Superalloy microstructures are a result of the complex interactions between alloy chemistry and heat-treatment processing. Often multiple mechanisms are operating simultaneously in the formation of a given feature, so that a single processing parameter cannot be identified as the controlling factor. For example, grain size was seen to be a function of solution temperature and, to a lesser extent, cooling rate. γ' precipitate size and distribution, on the other hand, were strongly affected by cooling rate, but their morphology was dependent on chemistry. Ultimately, however, the complex relationships between chemistry, processing, and microstructure are justified by the physical process taking place.

2. ANN techniques are a powerful tool in consolidating the complex interactions that go into formation of microstructure. This tool can be successfully used to make predictions of the microstructural features based on input variables describing processing and chemistry. The quality of the predictions is only as good as the training data and network construction. Therefore, attention must be paid to not over extending the training database, while at the same time including all relevant input parameters. Failure to do so can cripple the predictive capabilities of the network. With care, a well-trained network can be generated from limited data with the ability to make predictions as well as clarify the interaction of mechanisms.

3. High temperature mechanical properties are directly related to alloy microstructure. As with the relationship between processing and microstructure, microstructure and mechanical properties are subject to complex interactions, with multiple mechanisms operating simultaneously. Based on the mechanism driving the damage process, different microstructural features will affect the resulting properties. For example, small grain size improves yield strength, but increase creep deformation rates, based on the relative role of grain boundaries. However, both properties can be improved by rapid cooling from solution, which refines the γ' distribution, based on the role on the role precipitate-dislocation interaction. Crack growth resistance, on the other hand, is improved by slow cooling from solution. Materials engineers must identify the application for which the material is being used in order to tailor the microstructure to suit the

demands. Control of microstructure alloys us to efficiently improve alloy performance for a given application.

4. ANN techniques can successfully be applied to the prediction of mechanical properties. Further, although the effect of microstructure on these properties has clearly been demonstrated, it is not necessary to directly include microstructural inputs in the network. The capabilities of the ANN technique are such that effects of microstructural features on mechanical properties can be inferred from processing and compositional inputs. In this way, time and resources spent on microstructural quantification can be saved. This is a prime example of the potential contribution of machine learning techniques in the field of metallurgy. The successful generation of neural networks for prediction of mechanical properties indicates the possibilities of applications in the aeronautics industry, where optimization of service life of superalloy components contributes to improvements in cost and safety.

Research efforts based on this project are ongoing. At the time of this writing, some of these efforts are already underway and some are actively being planned. These are summarized in the following paragraphs. In addition to description of ongoing research efforts, discussion of future applications of this work is included.

1. Further creep crack growth testing will be conducted to confirm the relationship between decreased cooling rates and decreased creep crack growth rates. Testing at lower initial stress intensity parameter will allow for better-developed longer-

term tests. Test material with more highly differing serration formations would be ideal for this study. In addition, further insight on the mechanisms by which serrations might improve crack growth will be sought.

2. Additional cyclic crack growth tests should be conducted to confirm the consistent results for fatigue crack growth rate, independent of material cooling rate. Cyclic tests incorporating a dwell-time are currently underway to establish the possible creep-fatigue interactions in these materials. Multiple supersolvus microstructures are being tested. Results from these tests were not available in time for incorporation into this work.

3. The role of environment in cyclic crack growth testing is very important in the applications for which superalloys are used. To this end, NASA-funded efforts are underway to conduct fatigue testing of next-generation Ni-base disc alloys in air and vacuum. These tests should help to clarify the role oxygen in crack growth rates and shed light on the possible role of microstructure in these mechanisms.

4. Ongoing efforts by NASA, Rolls-Royce, and other engine manufacturers have been focused on the development of a process to create multiple microstructures within a single superalloy component. This process is referred to as a dual microstructure heat treatment (DMHT). Development of this capability is aimed at optimizing alloy performance in components which have seemingly contradictory demands in different areas of the part. Refinement of our

understanding of both processing-structure and structure-property relationships would facilitate these efforts. This application typifies the potential for property improvement through control of microstructure.

5. Further work will concentrate on the establishment of neural network techniques as a tool in many facets of metallurgy including, alloy development and component lifing. While this work has successful demonstrated the application of machine learning techniques to multiple scenarios with limited data sets, the true power of this tool lies in its ability to assimilate the results of much larger sets of data. In this application a neural network can consolidate the results of tests and identify trends in databases too large to be assessed by most humans. Complex interactions can be accounted for and predictions can be made with a high level of accuracy. In this way improvements on current techniques for alloy development can be made by reducing (but not eliminating) the need for experimental work. Currently, efforts are underway to apply neural network techniques to process modeling of U720 components already in service. This tool can be applied using data that has already been generated. Further refinement of this process will also allow for prediction of not just a single value, but prediction of distributions of values.

From the results of this project, and the conclusions that can be drawn from those results, several avenues of future work are suggested. These efforts are of a more speculative nature than those mentioned above.

1. Additional creep deformation testing is necessary to refine our understanding of the role of precipitates in the creep process. Further testing should encompass test temperatures above and below 704˚C, in order to develop a Larson-Miller type treatment of these results. Additional tests should also duplicate prior tests for increased statistical relevancy.

2. Further creep deformation testing should include detailed measurements of test-specimen microstructure, specifically of secondary and tertiary γ' particles, including volume fraction, using TEM techniques when necessary. Use of TEM imaging should also be pursued to document interactions between dislocations and precipitates. TEM imaging can verify the mechanism, i.e. shearing versus looping, of dislocation-obstacle interaction. These efforts should confirm a strain rate calculation that incorporates microstructural terms.

3. Hot hardness testing of fine-grained material can be conducted in order to establish the contribution of grain boundaries to hardness. Further hot hardness testing should involve similar sized indents to that used in this work, however the test material should be subsolvus superalloys with a higher density of grain boundaries. This work would also clarify whether a correlation between hot

hardness and hot tensile strength is possible, as a more comprehensive set of behaviors/mechanisms would be incorporated into the measurements.

Further, hot hardness efforts should consider the possible correlation between indent measurements and creep deformation. This would be dependent on additional creep deformation testing and would require variation of indent times and pressures. TEM imaging techniques can used to compare the relative amounts of necking or bowing of dislocations, in order to assess the similarity of mechanisms involved.

4. In this work a two dimensional assessment of grain boundary serrations has been used. The use of a three dimensional measure of roughness to assess the extent of grain boundary serrations should be considered. The potential exists for this approach to produce a more accurate measurement of this feature. Work establishing a measure of fracture surface roughness is directly applicable to this feature of microstructure. In both, the three dimensional feature is manifest in a two dimensional line or profile. Current work for this project has used the total length of this line to calculate a GBCR to characterize serrations. To use a three dimensional assessment of grain boundary serrations in the form of grain surface roughness, this total line length as a ratio to projected length is used. From the product of total profile length/projected length and a profile structure factor, ψ, a surface roughness parameter, R_s, can be calculated [45, 46]. A common limitation to both techniques exists in the possibility for different surfaces or boundaries to be represented by the same value of GBCR or R_s. However, the

potential for a three dimensional measure of "surface roughness" to provide a more accurate measure of the deviation of grain boundary (surface) from straight (smooth) recommends the further pursuit of this approach. Improved accuracy of microstructural features such as the nature of grain boundaries provides the additional benefit of refining ANN modeling techniques involving those features.

5. ANN models can be advanced by the addition of physical models to the technique. Predictions from physical models can be incorporated into the training data used in the development of the model. Physical models of thermodynamic or kinetic behavior of materials, for example, can be used to augment results from quantification or mechanical testing of materials for use as training data. In this way the accuracy of NN model predictions can be further refined, without the addition of additional physical or mechanical testing.

APPENDIX A

SEM Images of Microstructures from Heat-Treatment

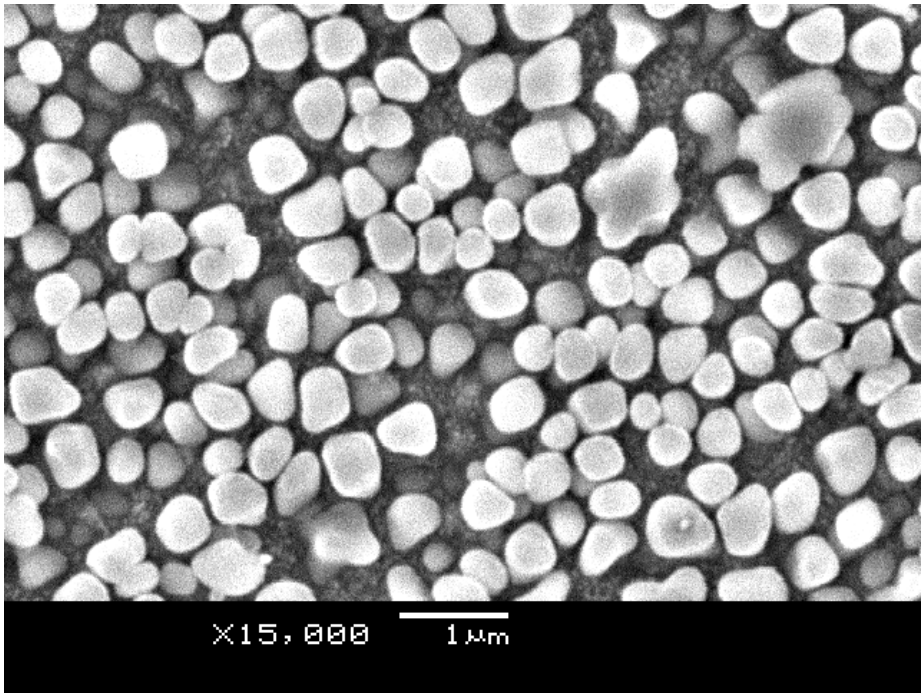

Figure 79 SEM image of LSHR specimen L1; 1165˚C solution, 0.75˚C/sec cool, 1040˚C hold.

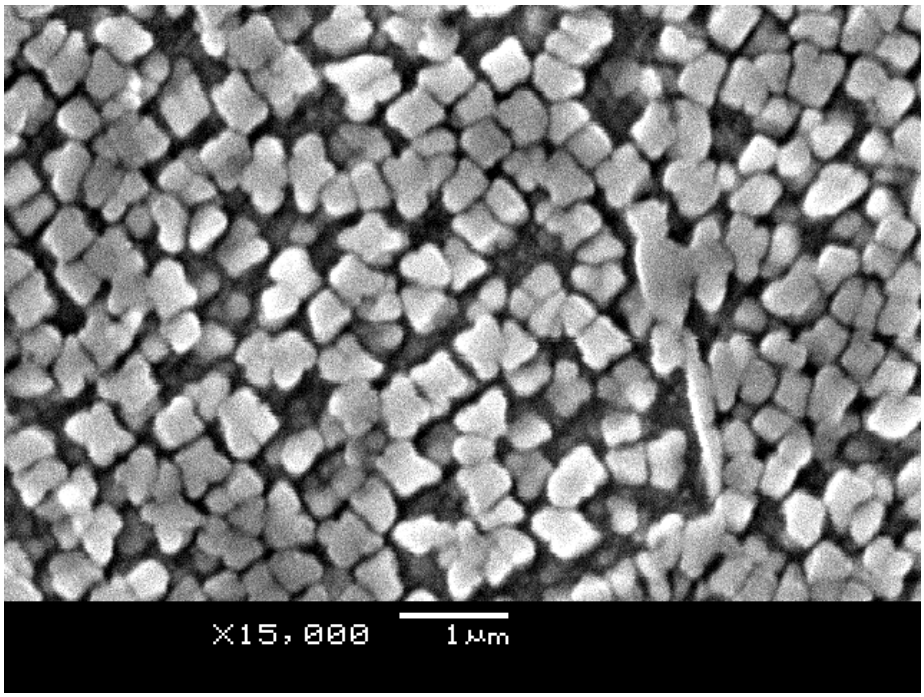

Figure 80 SEM image of LSHR specimen L2; 1165˚C solution, 0.75˚C/sec cool, 845˚C hold.

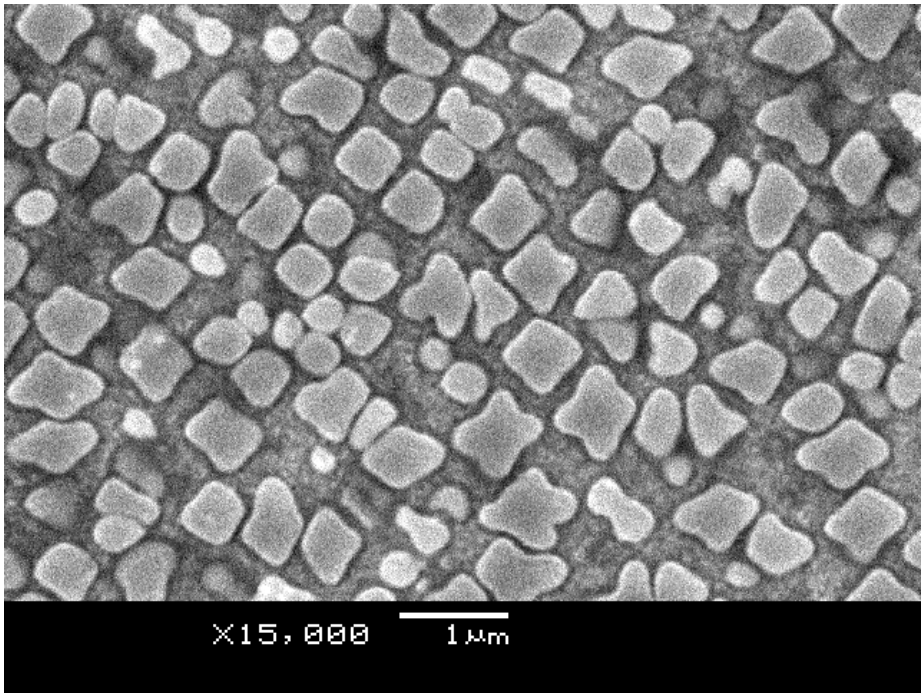

Figure 81 SEM image of LSHR specimen L3; 1165˚C solution, 0.417˚C/sec cool, 1040˚C hold.

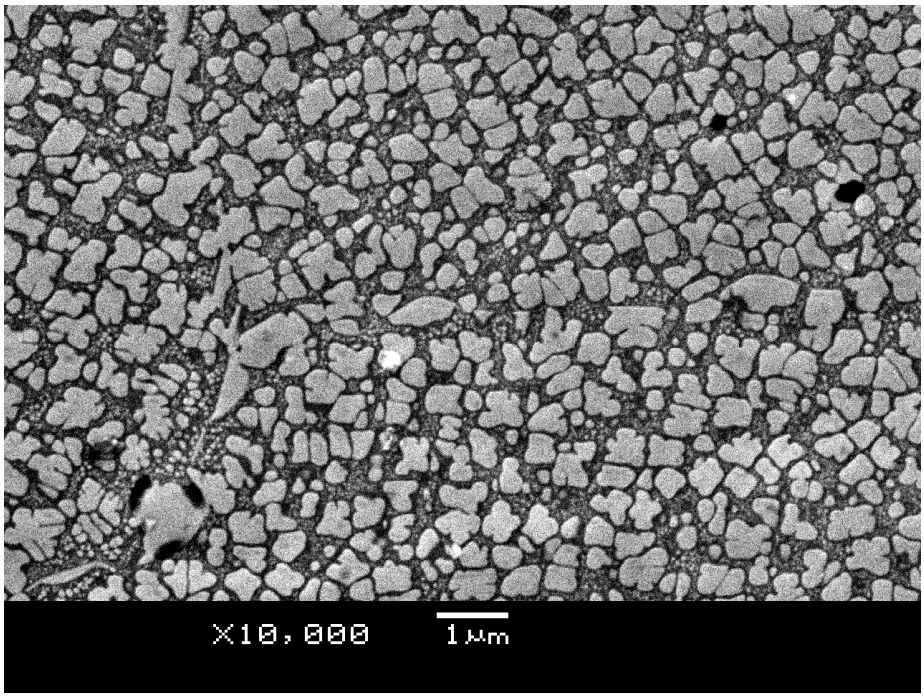

Figure 82 SEM image of LSHR specimen L3; 1165˚C solution, 0.417˚C/sec cool, 845˚C hold.

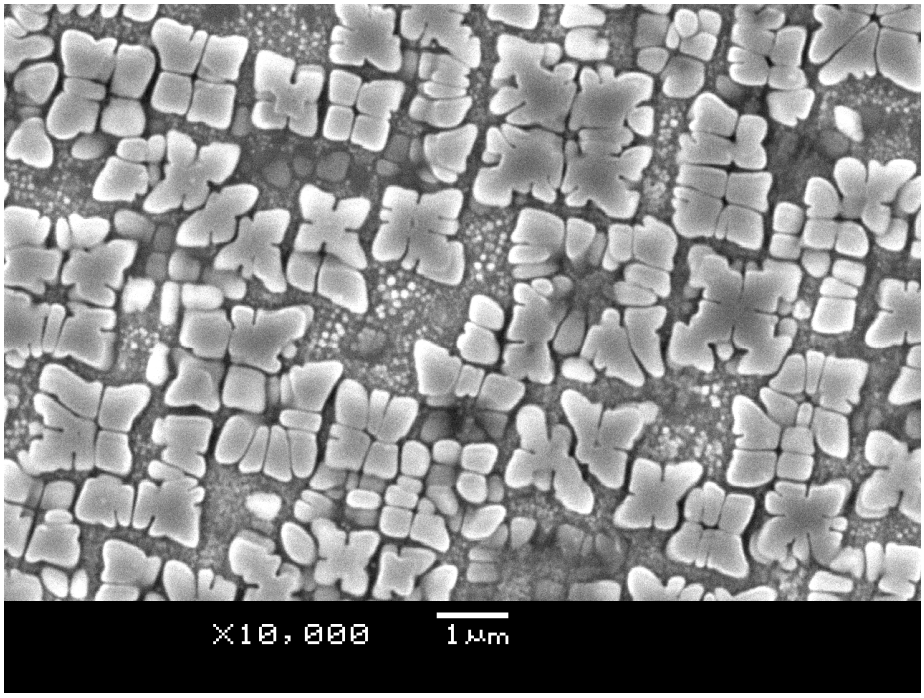

Figure 83 SEM image of LSHR specimen L5; 1165˚C solution, 0.083˚C/sec cool, 845˚C hold.

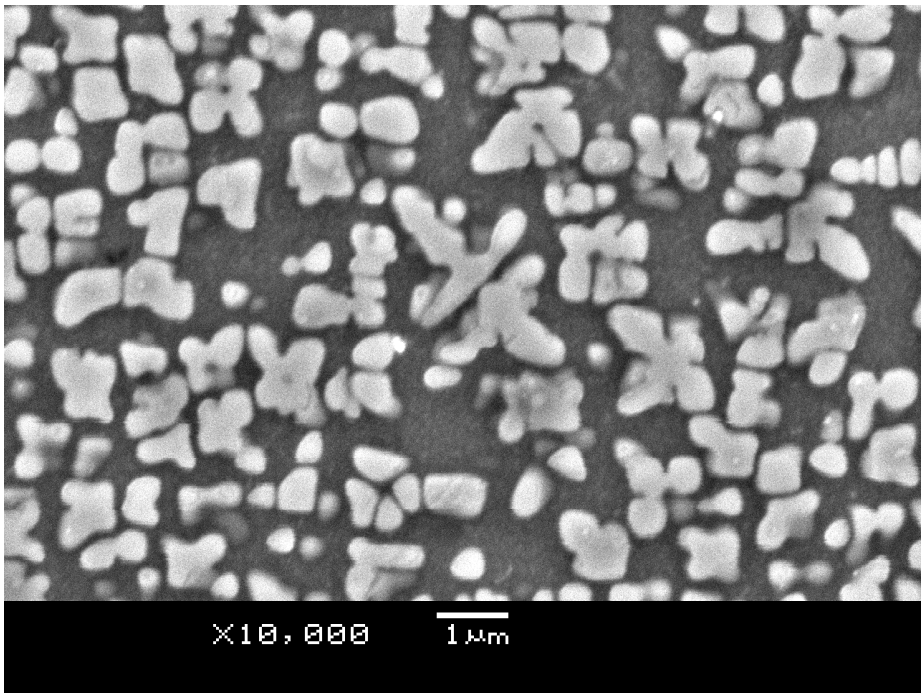

Figure 84 SEM image of LSHR specimen L6; 1165˚C solution, 0.083˚C/sec cool, 1040˚C hold.

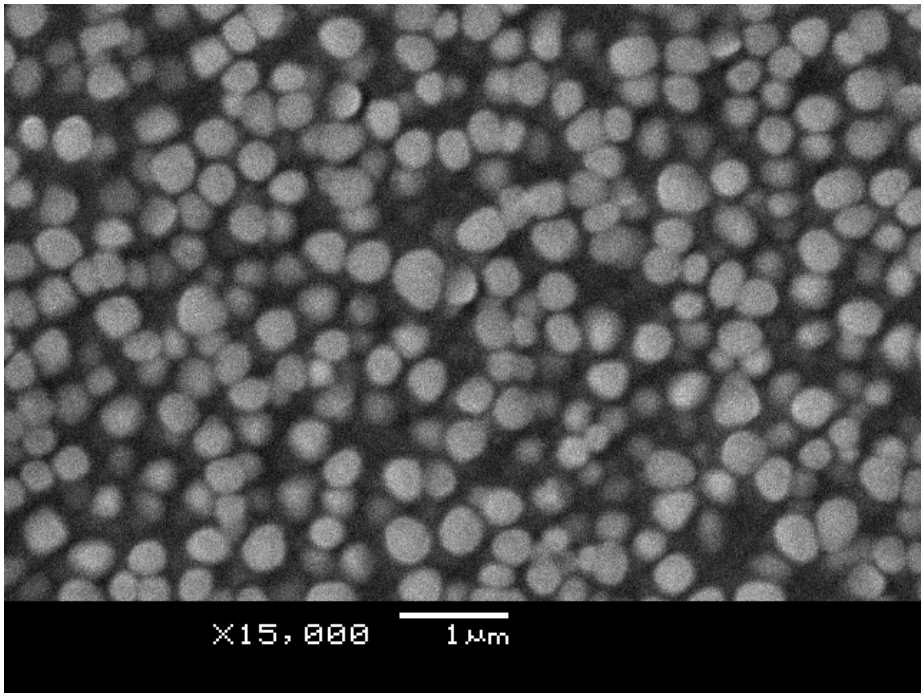

Figure 85 SEM image of LSHR specimen L7; 1182˚C solution, 0.75˚C/sec cool, 1040˚C hold.

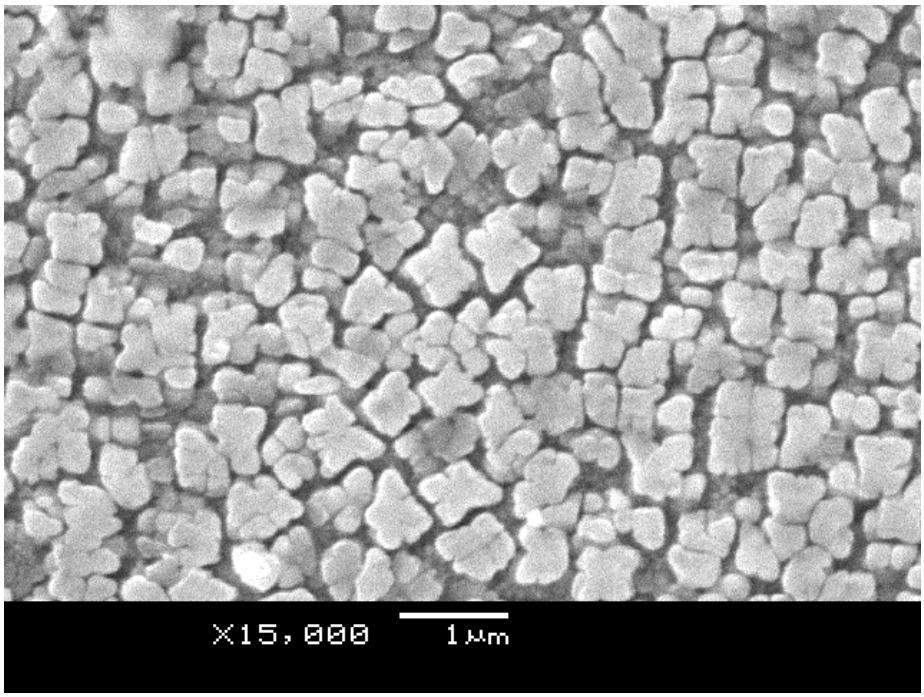

Figure 86 SEM image of LSHR specimen L8; 1182˚C solution, 0.75˚C/sec cool, 845˚C hold.

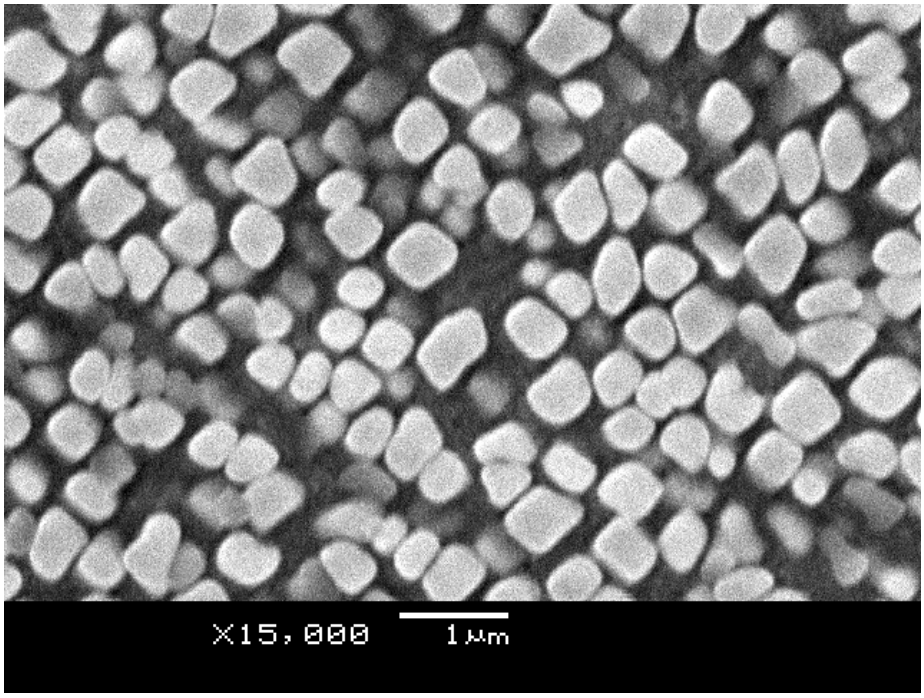

Figure 87 SEM image of LSHR specimen L9; 1182˚C solution, 0.417˚C/sec cool, 1040˚C hold.

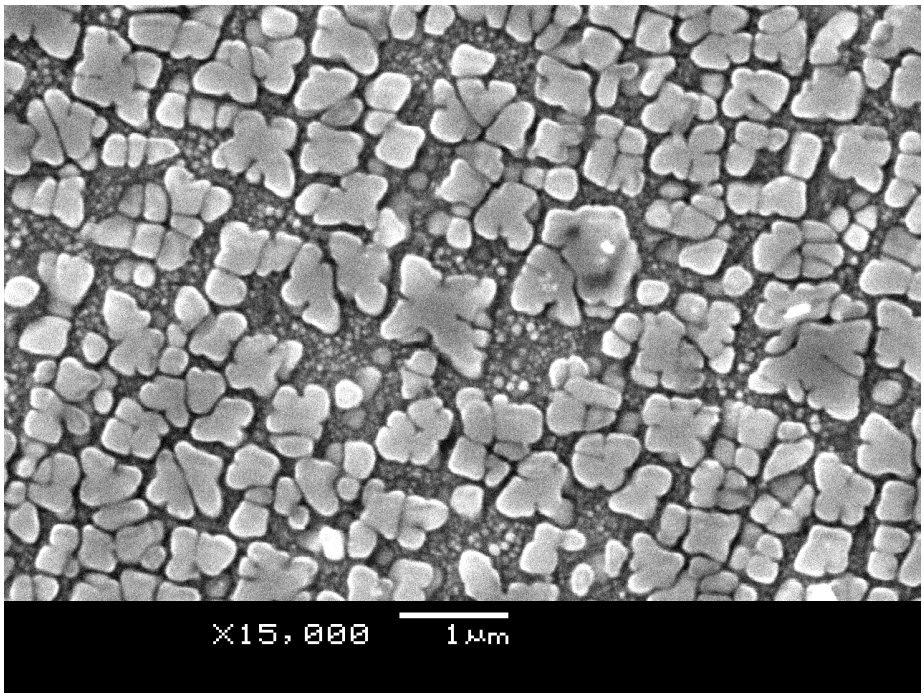

Figure 88 SEM image of LSHR specimen L10; 1182˚C solution, 0.417˚C/sec cool, 845˚C hold.

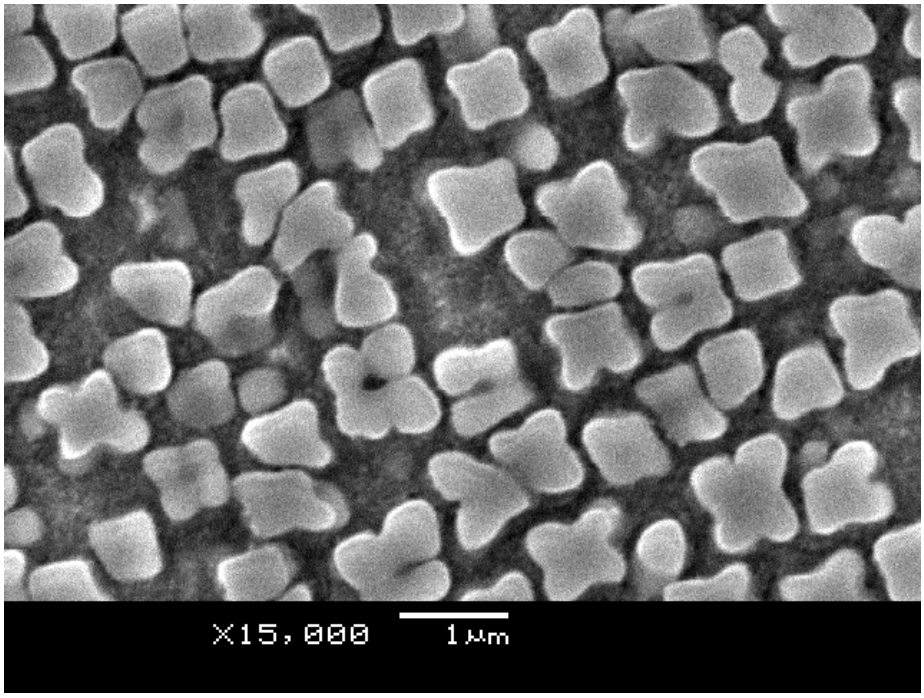

Figure 89 SEM image of LSHR specimen L11; 1182˚C solution, 0.083˚C/sec cool, 1040˚C hold.

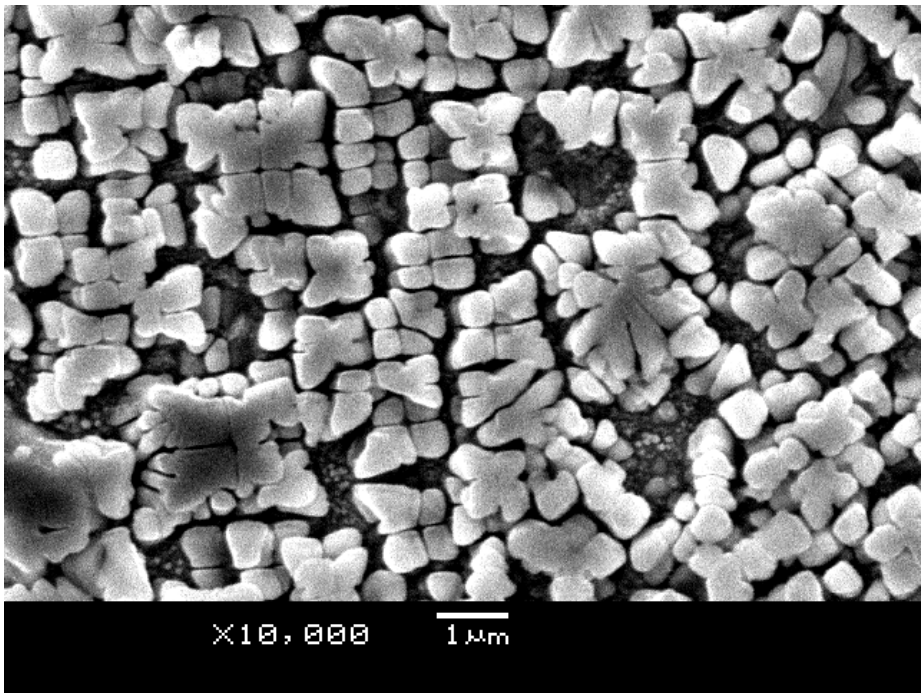

Figure 90 SEM image of LSHR specimen L12; 1182˚C solution, 0.083˚C/sec cool, 845˚C hold.

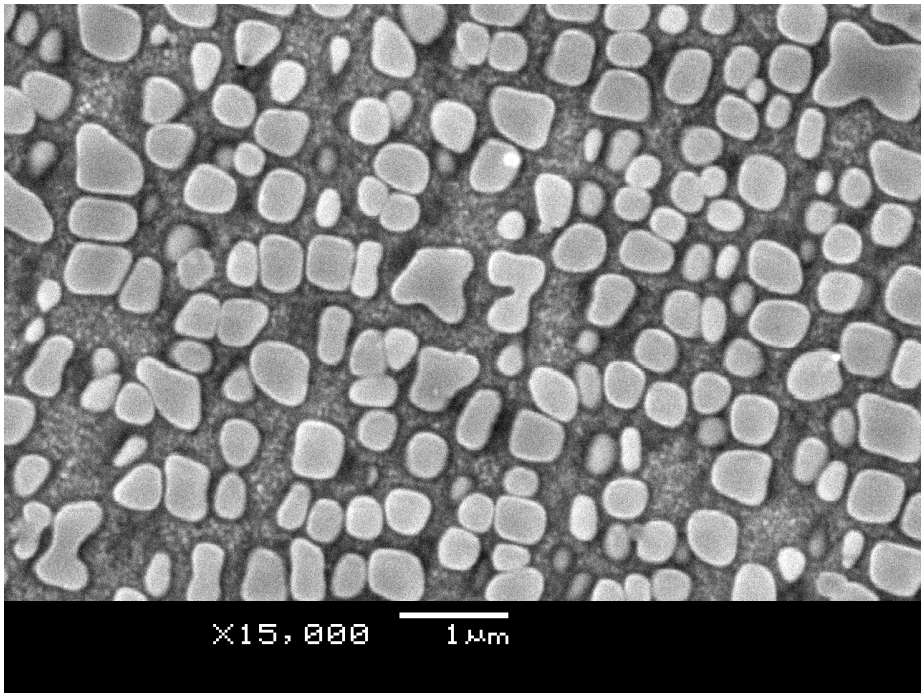

Figure 91 SEM image of LSHR specimen L13; 1199˚C solution, 0.75˚C/sec cool, 1040˚C hold.

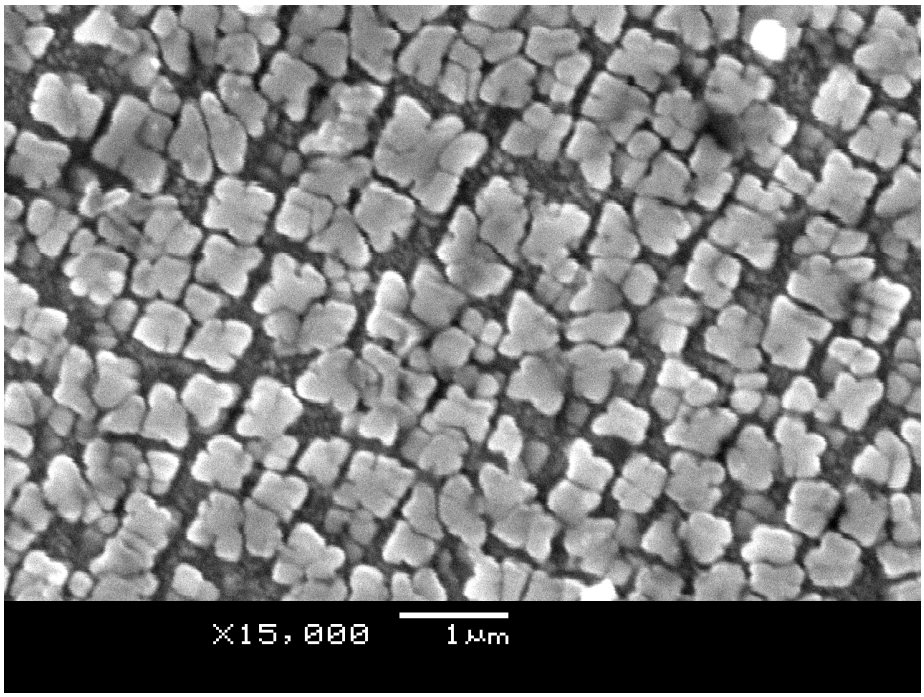

Figure 92 SEM image of LSHR specimen L14; 1199˚C solution, 0.75˚C/sec cool, 845˚C hold.

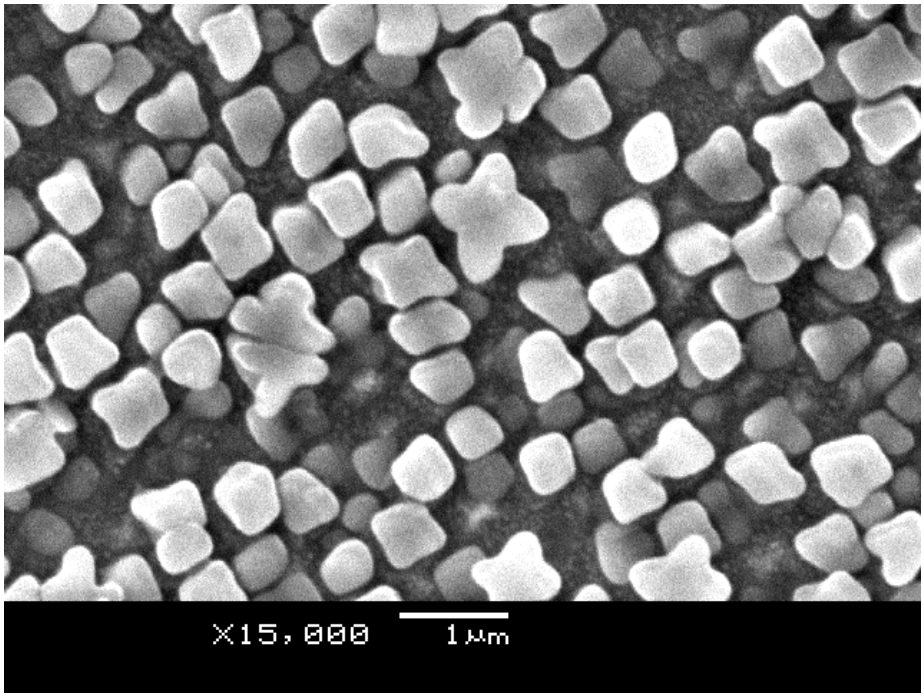

Figure 93 SEM image of LSHR specimen L15; 1199˚C solution, 0.417˚C/sec cool, 1040˚C hold.

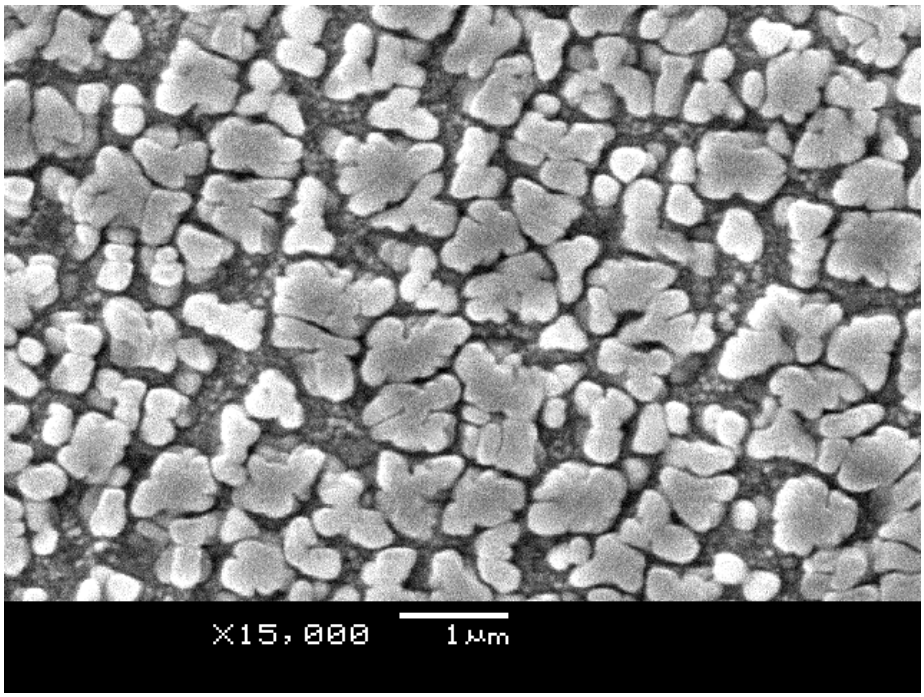

Figure 94 SEM image of LSHR specimen L16; 1199˚C solution, 0.417˚C/sec cool, 845˚C hold.

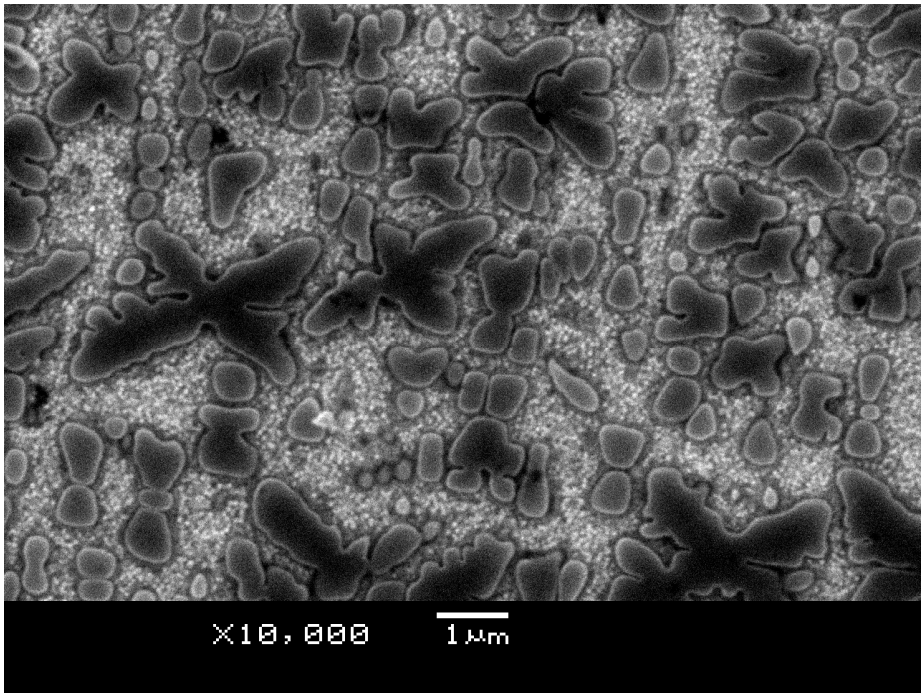

Figure 95 SEM image of LSHR specimen L17; 1199˚C solution, 0.083˚C/sec cool, 1040˚C hold.

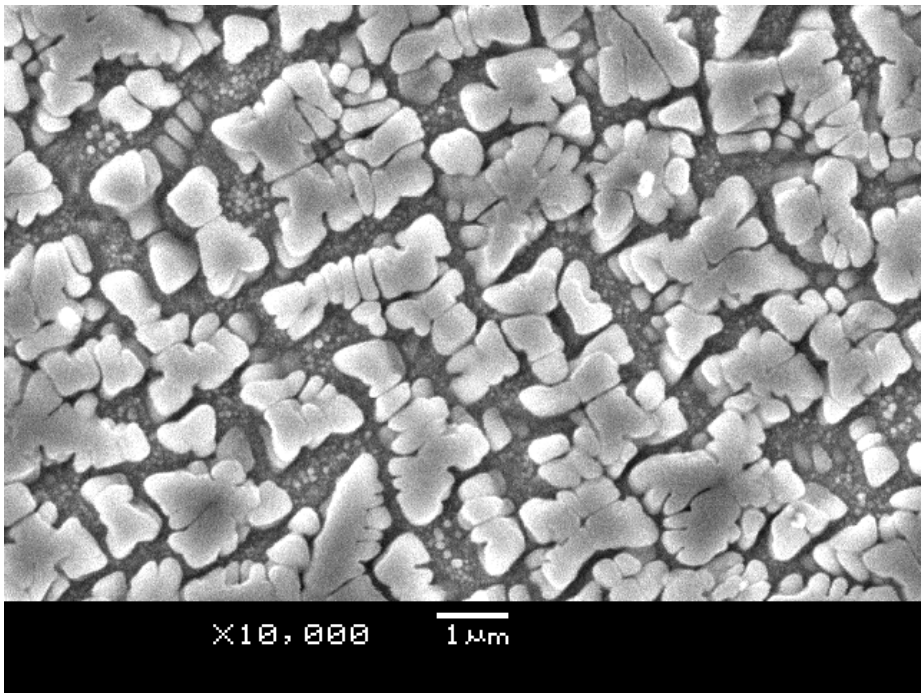

Figure 96 SEM image of LSHR specimen L18; 1199˚C solution, 0.083˚C/sec cool, 845 ˚C hold.

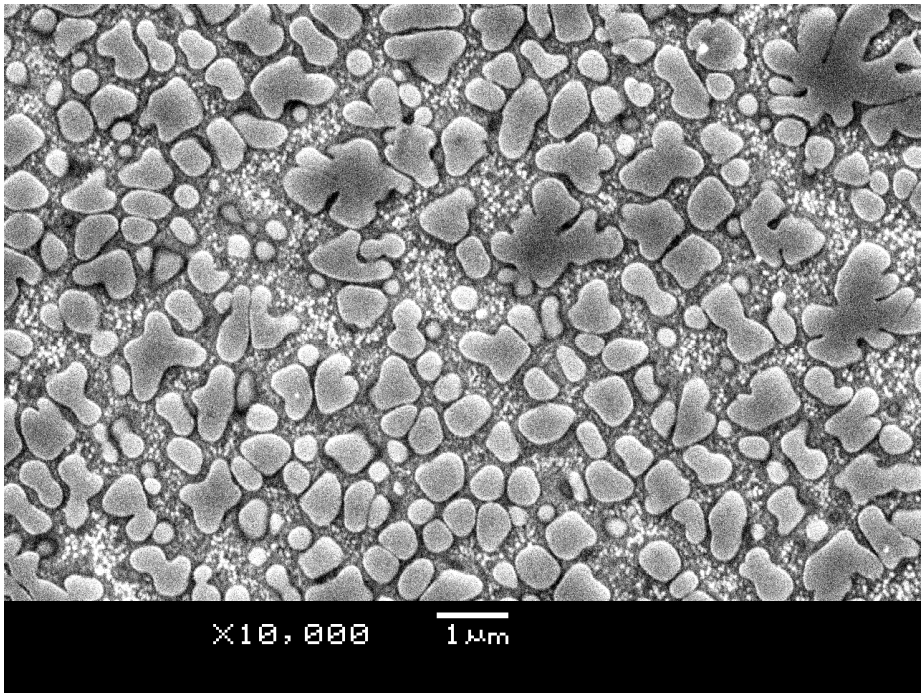

Figure 97 SEM image of Alloy10 specimen A1; 1199˚C solution, 0.75˚C/sec cool, 1040˚C hold.

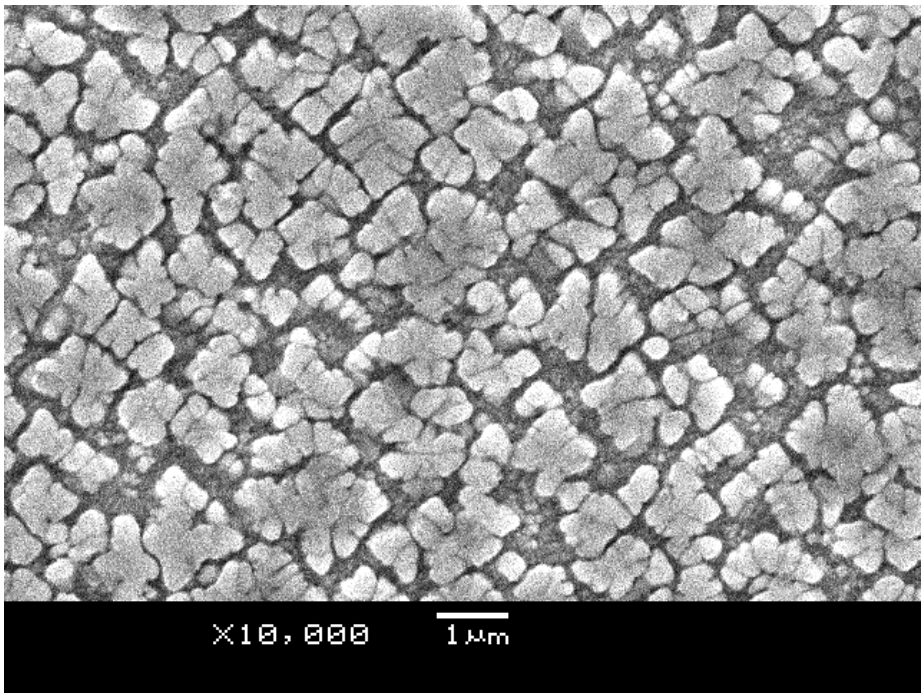

Figure 98 SEM image of Alloy10 specimen A2; 1199˚C solution, 0.75˚C/sec cool, 845˚C hold.

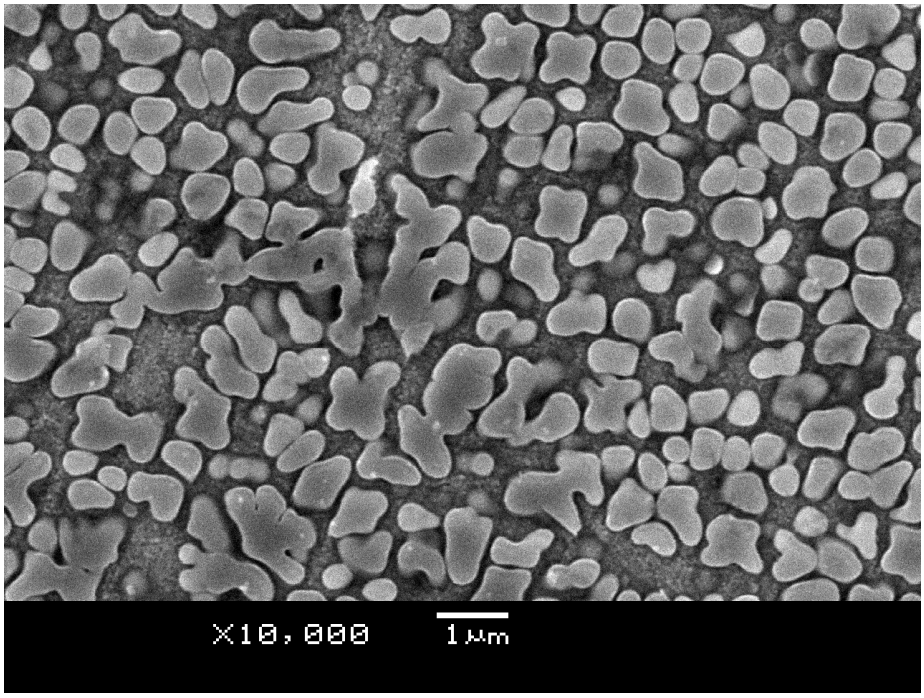

Figure 99 SEM image of Alloy10 specimen A3; 1199˚C solution, 0.417˚C/sec cool, 1040˚C hold.

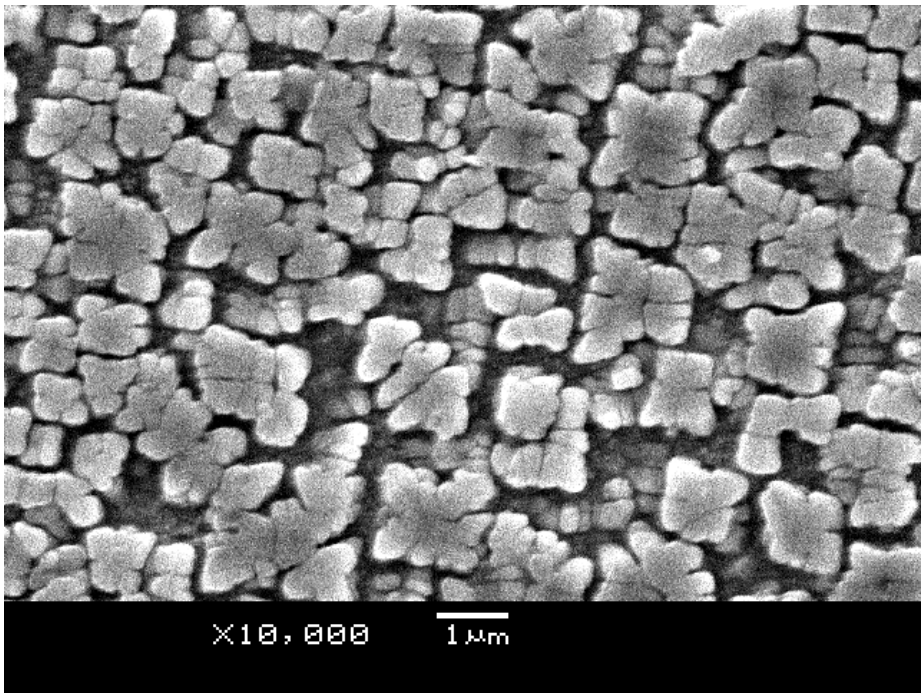

Figure 100 SEM image of Alloy10 specimen A4; 1199˚C solution, 0.417˚C/sec cool, 845˚C hold.

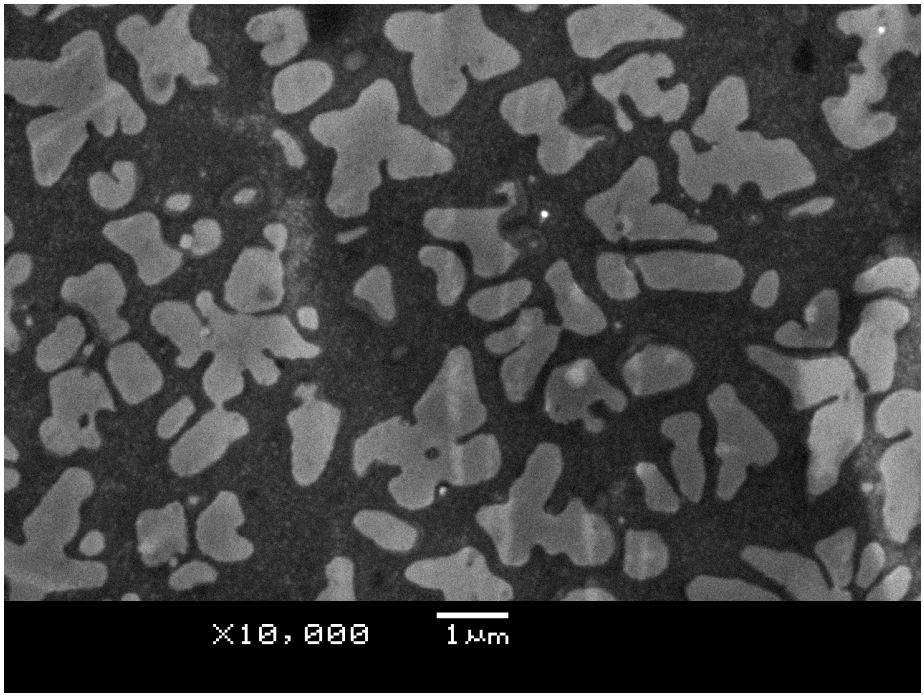

Figure 101 SEM image of Alloy10 specimen A5; 1199˚C solution, 0.083˚C/sec cool, 1040˚C hold.

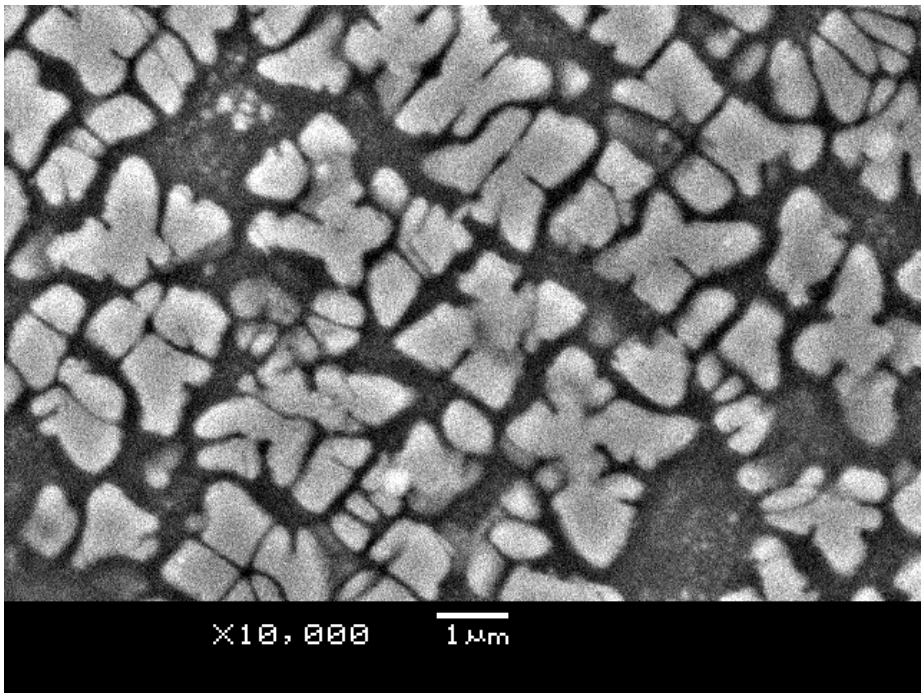

Figure 102 SEM image of Alloy10 specimen A6; 1199˚C solution, 0.083˚C/sec cool, 845˚C hold.

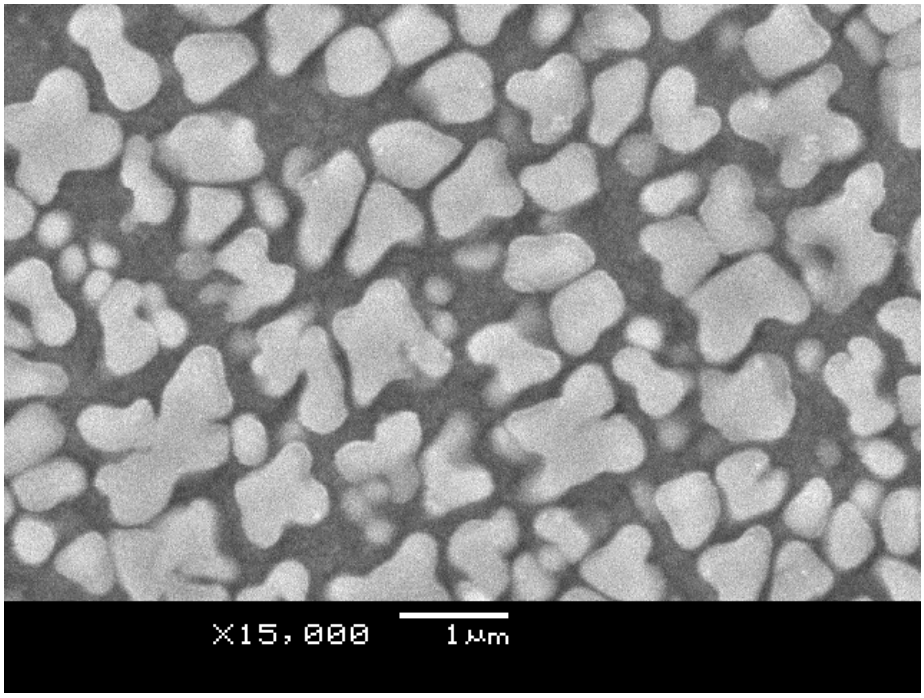

Figure 103 SEM image of Alloy10 specimen A7; 1216˚C solution, 0.75˚C/sec cool, 1040˚C hold.

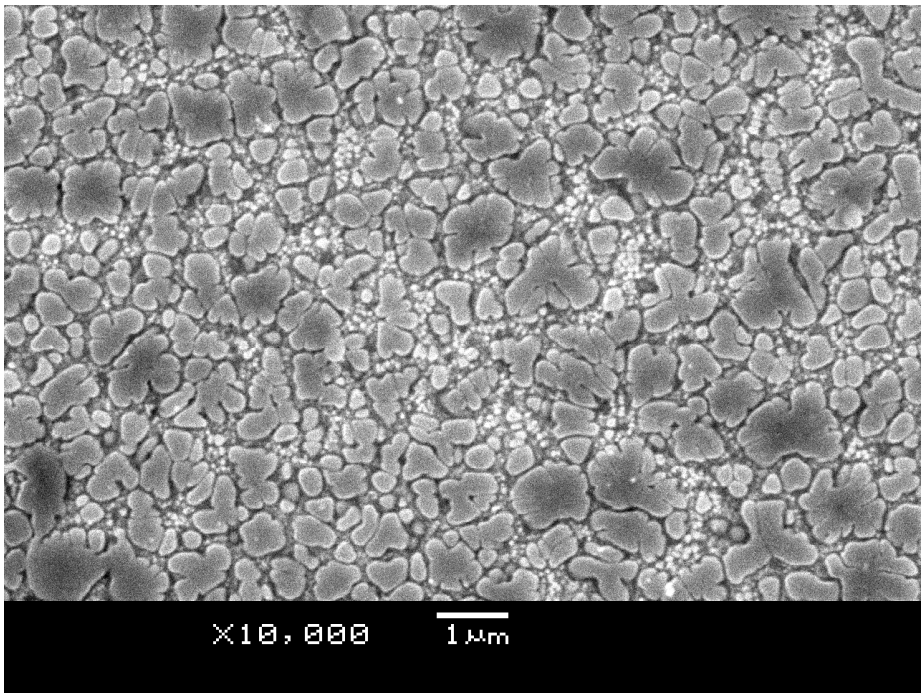

Figure 104 SEM image of Alloy10 specimen A8; 1216˚C solution, 0.75˚C/sec cool, 845˚C hold.

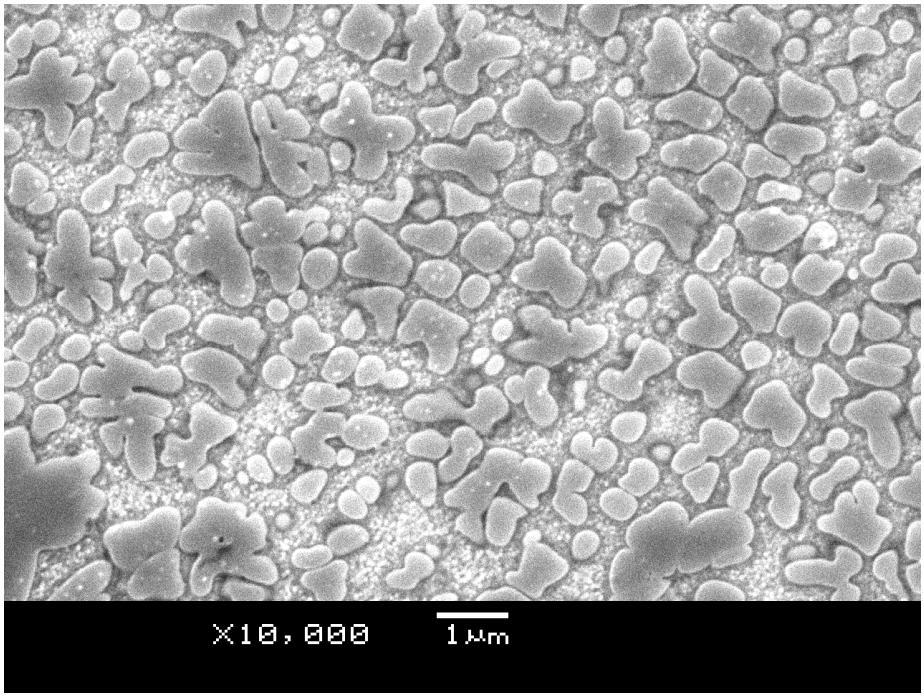

Figure 105 SEM image of Alloy10 specimen A9; 1216˚C solution, 0.417˚C/sec cool, 1040˚C hold.

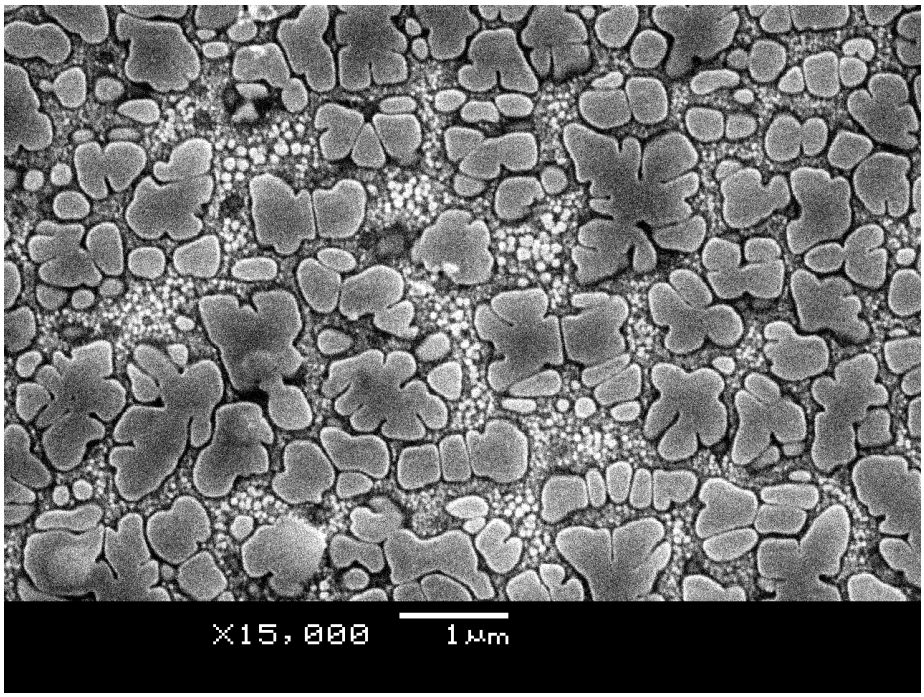

Figure 106 SEM image of Alloy10 specimen A10; 1216˚C solution, 0.417˚C/sec cool, 845˚C hold.

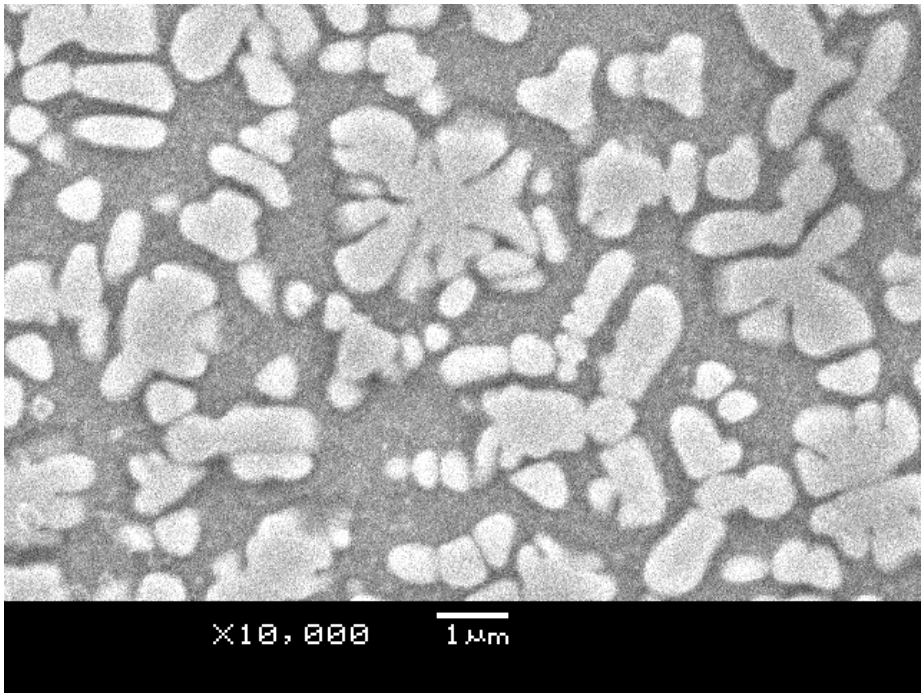

Figure 107 SEM image of Alloy10 specimen A11; 1216˚C solution, 0.083˚C/sec cool, 1040˚C hold.

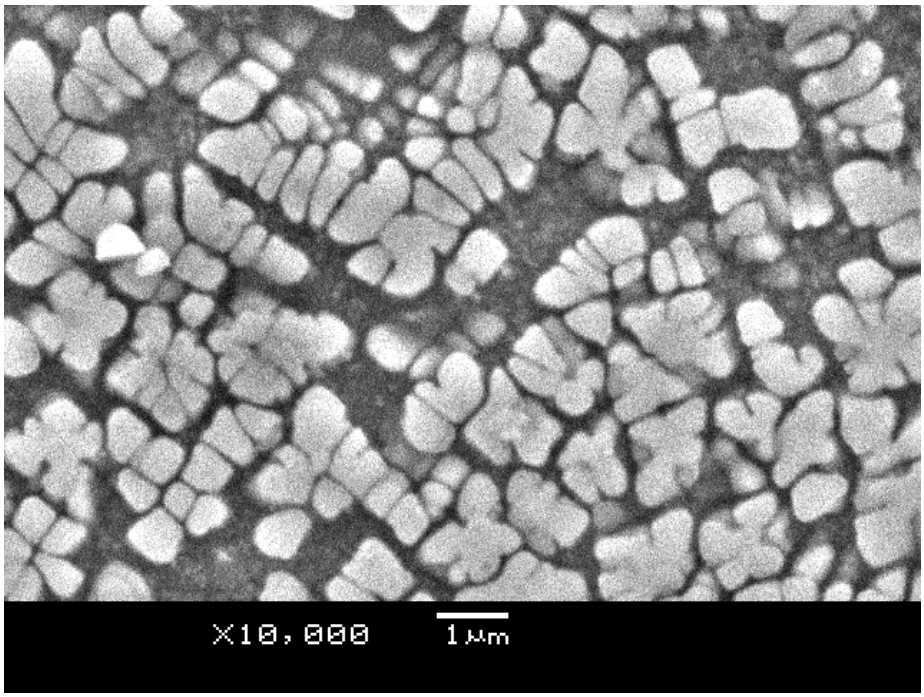

Figure 108 SEM image of Alloy10 specimen A12; 1216˚C solution, 0.083˚C/sec cool, 845˚C hold.

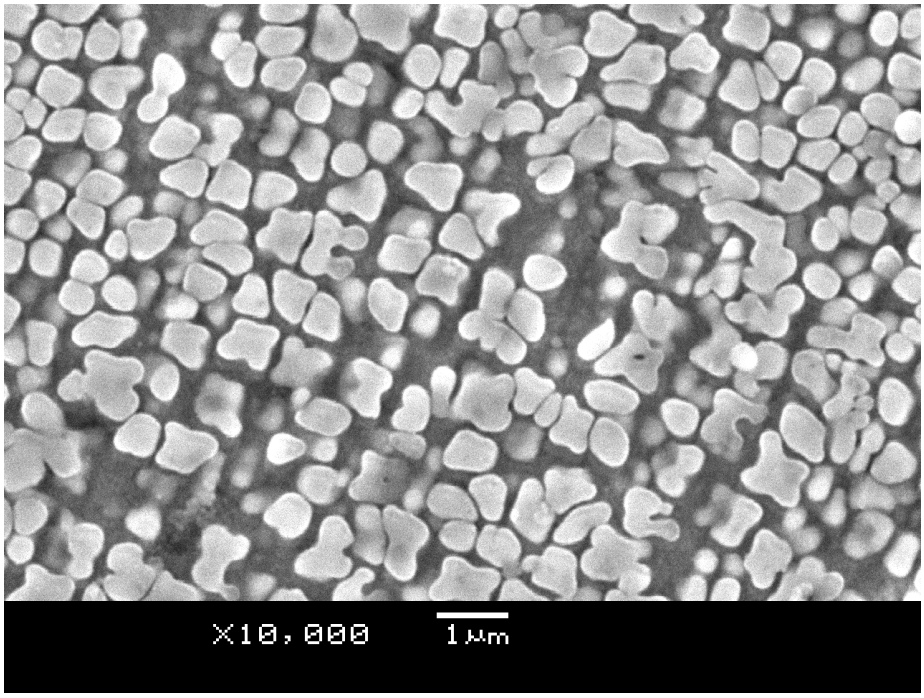

Figure 109 SEM image of Alloy10 specimen A13; 1233˚C solution, 0.75˚C/sec cool, 1040˚C hold.

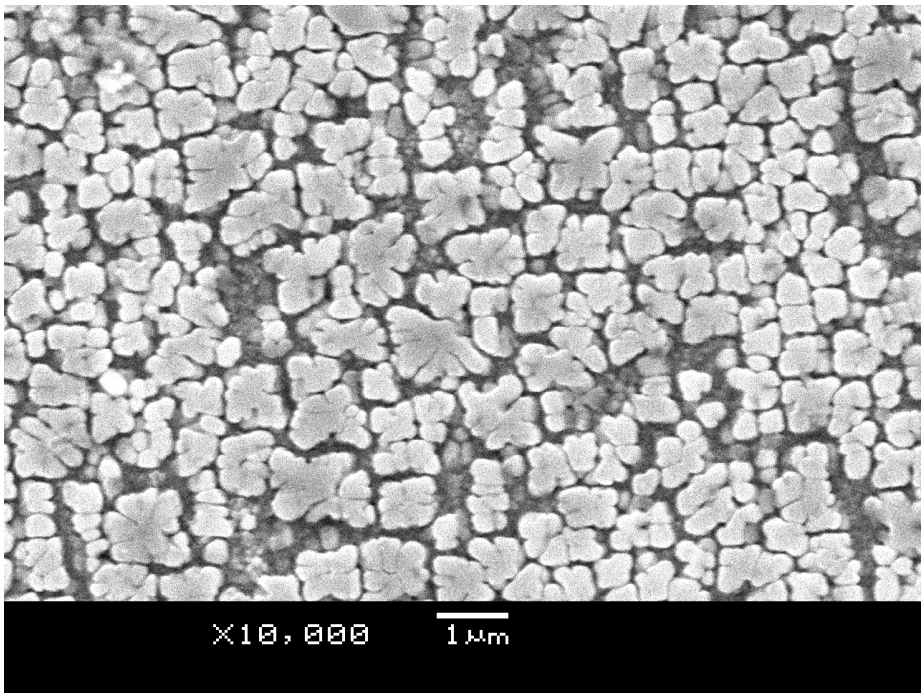

Figure 110 SEM image of Alloy10 specimen A14; 1233˚C solution, 0.75˚C/sec cool, 845˚C hold.

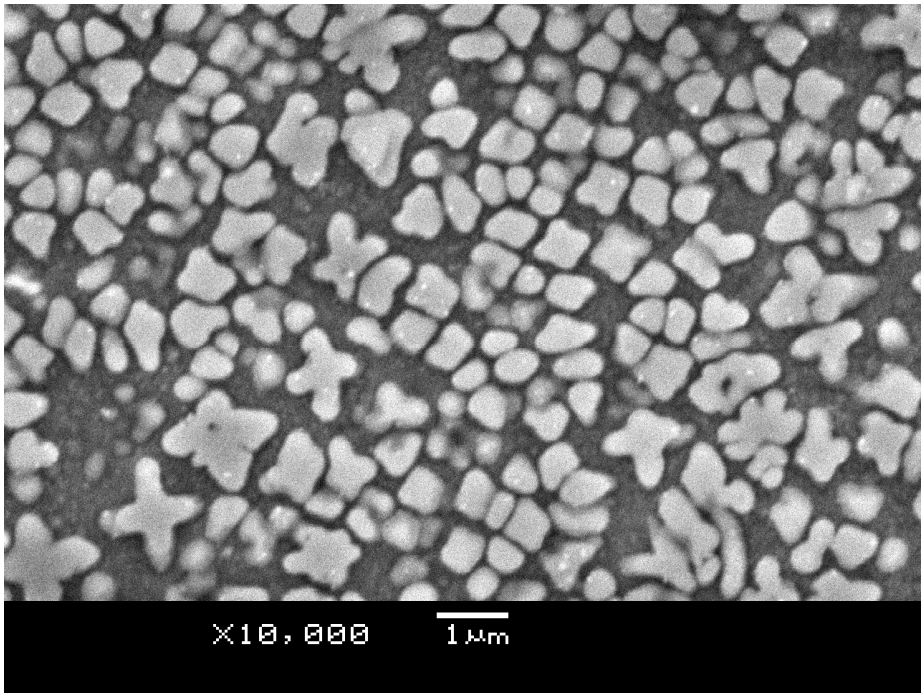

Figure 111 SEM image of Alloy10 specimen A15; 1233˚C solution, 0.417˚C/sec cool, 1040˚C hold.

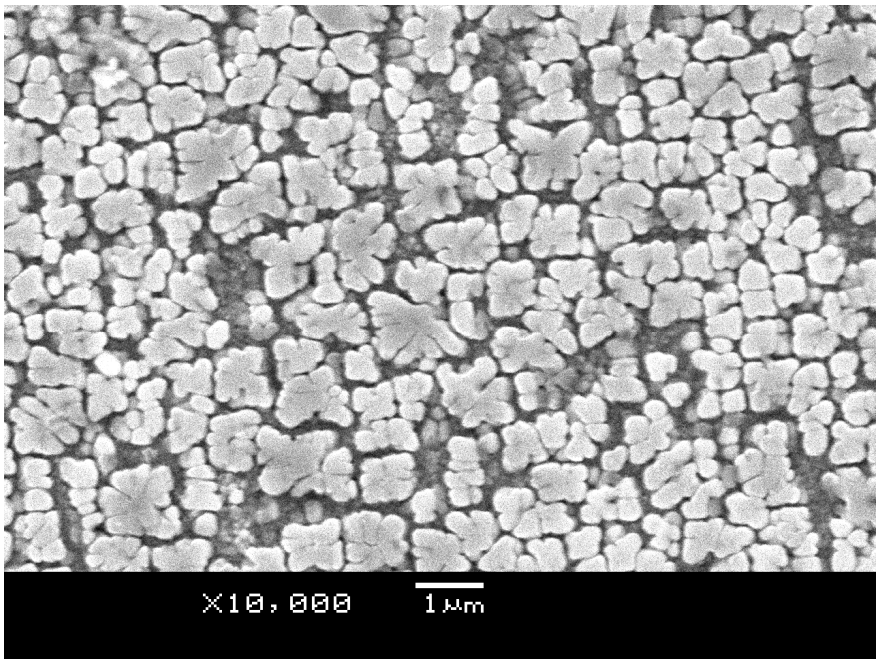

Figure 112 SEM image of Alloy10 specimen A16; 1233˚C solution, 0.417˚C/sec cool, 845˚C hold.

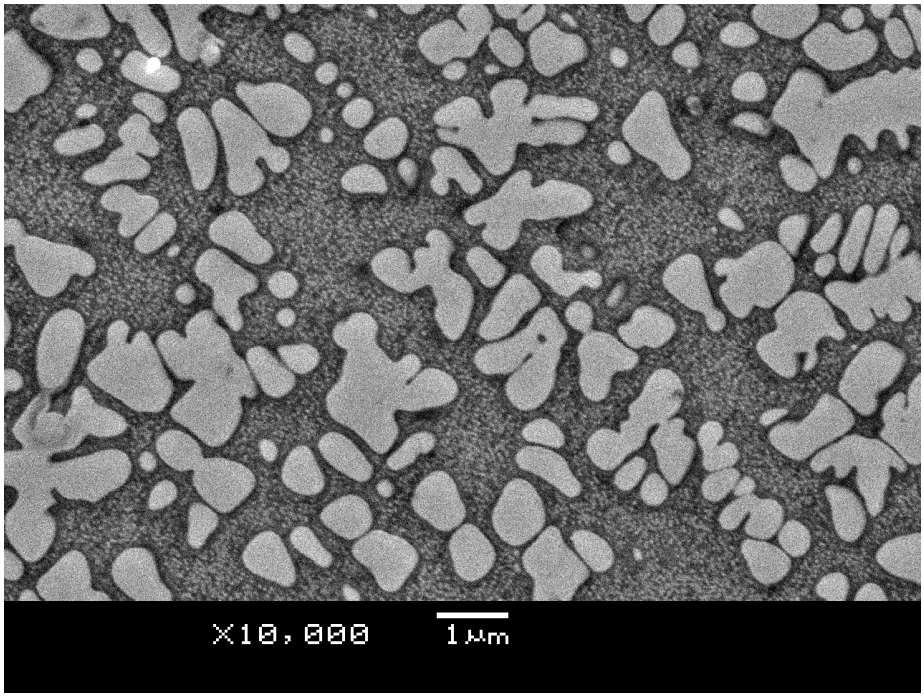

Figure 113 SEM image of Alloy10 specimen A17; 1233˚C solution, 0.083˚C/sec cool, 1040˚C hold.

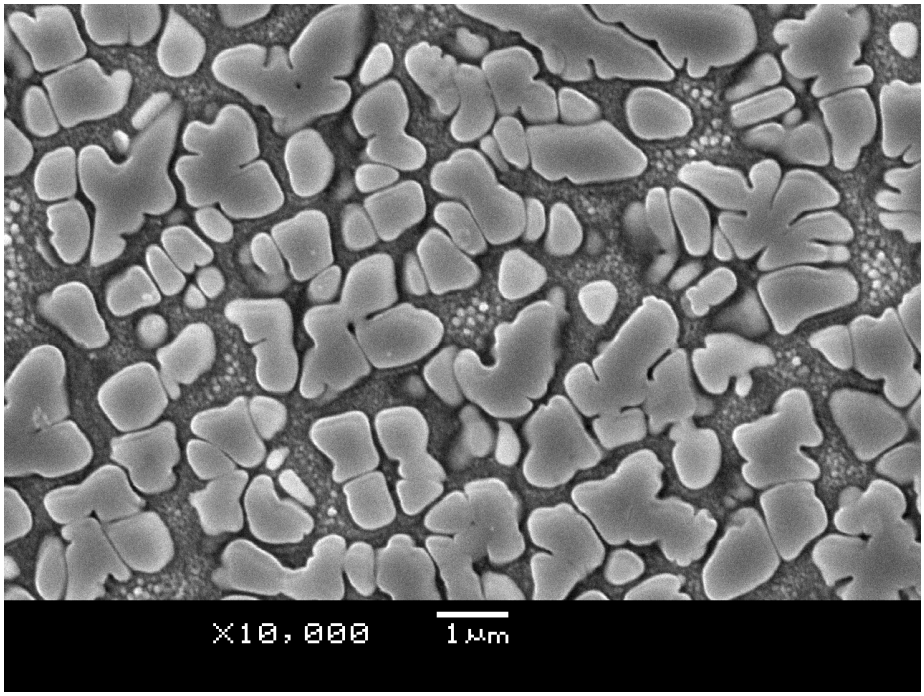

Figure 114 SEM image of Alloy10 specimen A18; 1233˚C solution, 0.083˚C/sec cool, 845˚C hold.

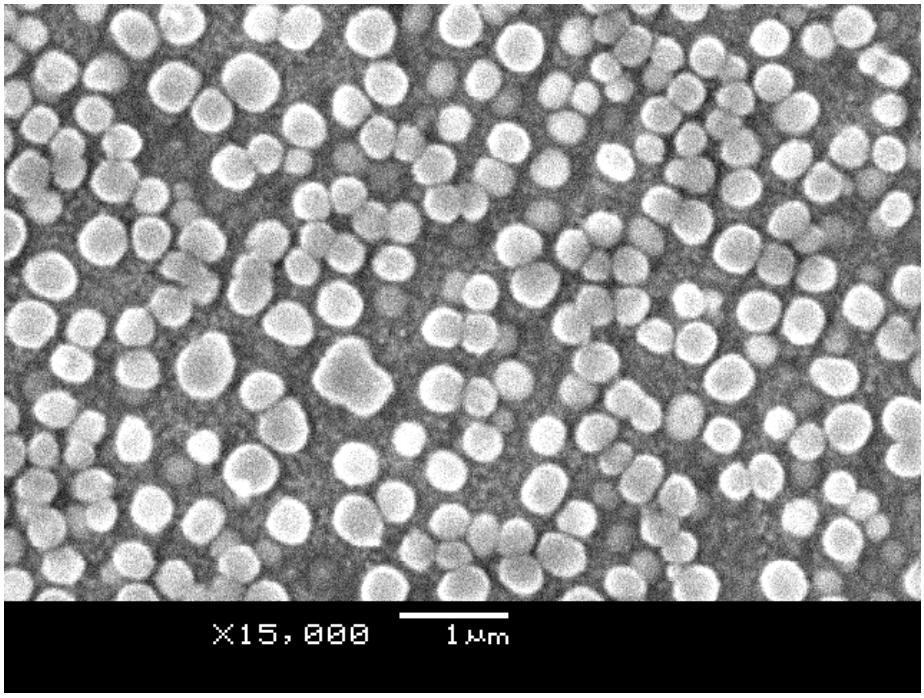

Figure 115 SEM image of RR1000 specimen R1; 1150˚C solution, 0.75˚C/sec cool, 1040˚C hold.

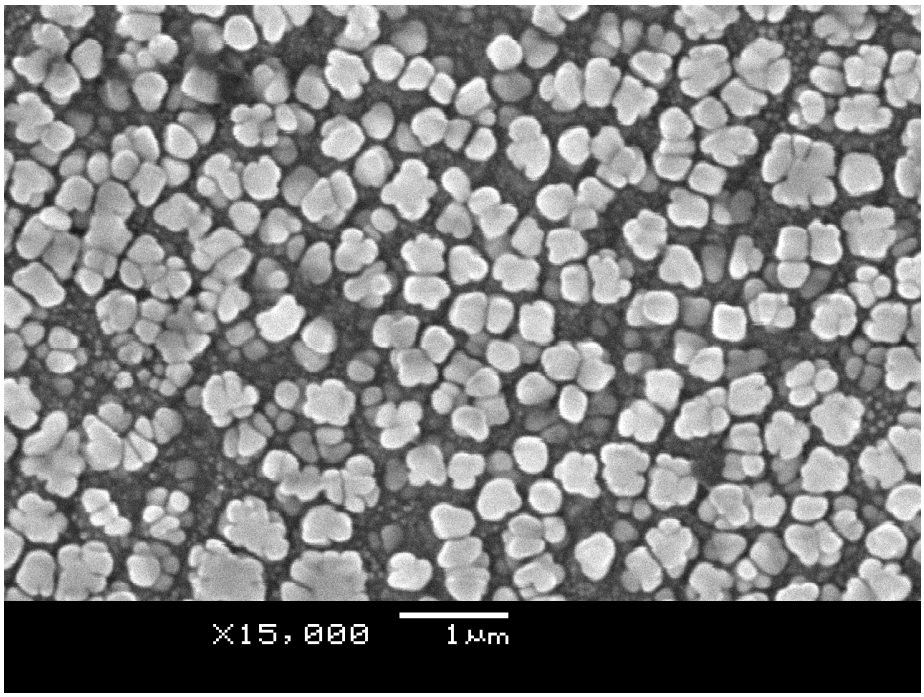

Figure 116 SEM image of RR1000 specimen R2; 1150˚C solution, 0.75˚C/sec cool, 845˚C hold.

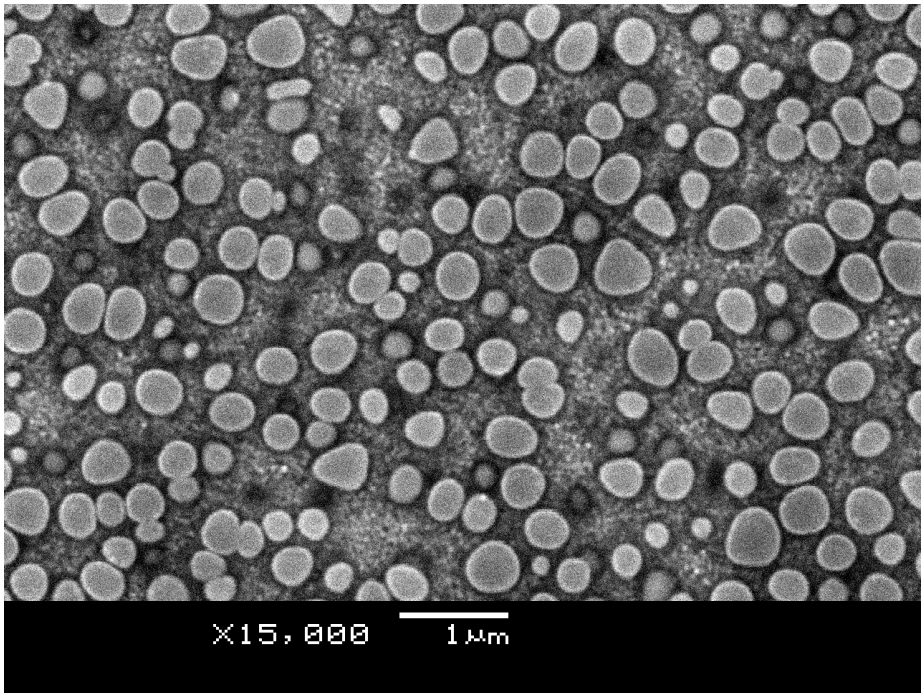

Figure 117 SEM image of RR1000 specimen R3; 1150˚C solution, 0.417˚C/sec cool, 1040˚C hold.

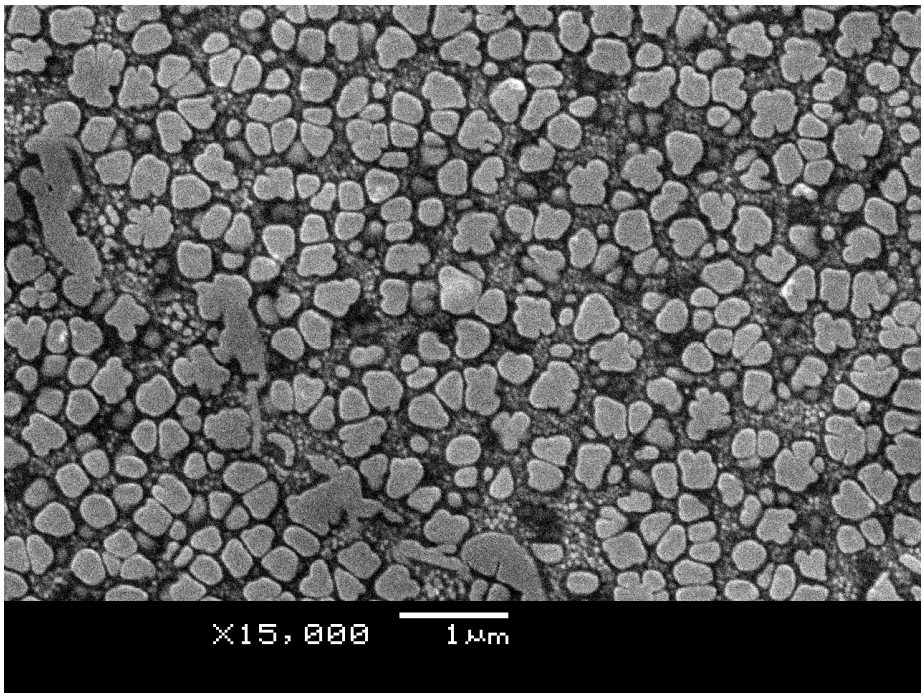

Figure 118 SEM image of RR1000 specimen R4; 1150˚C solution, 0.417˚C/sec cool, 845˚C hold.

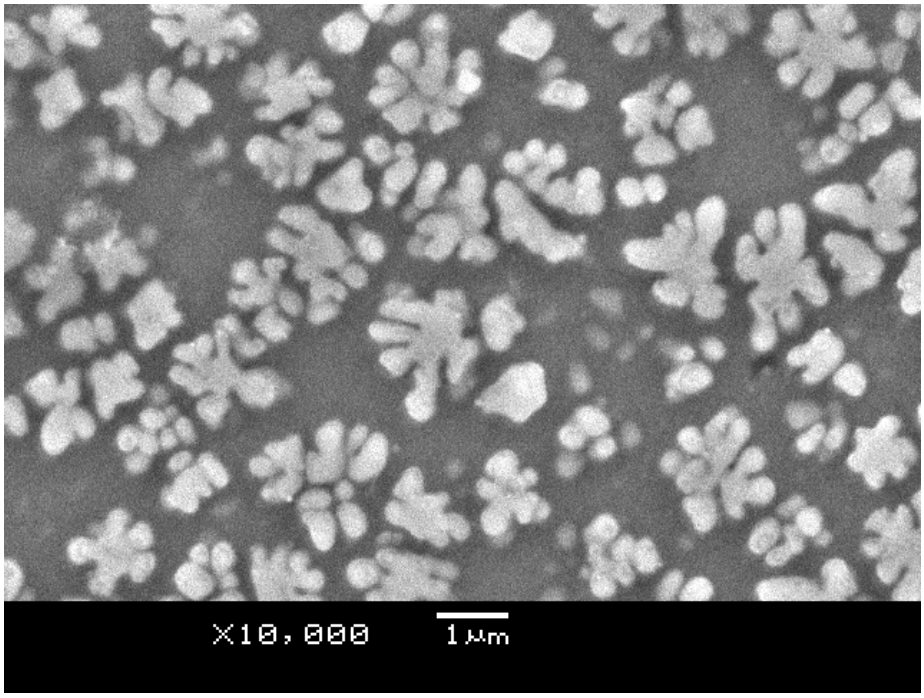

Figure 119 SEM image of RR1000 specimen R5; 1150˚C solution, 0.083˚C/sec cool, 1040˚C hold.

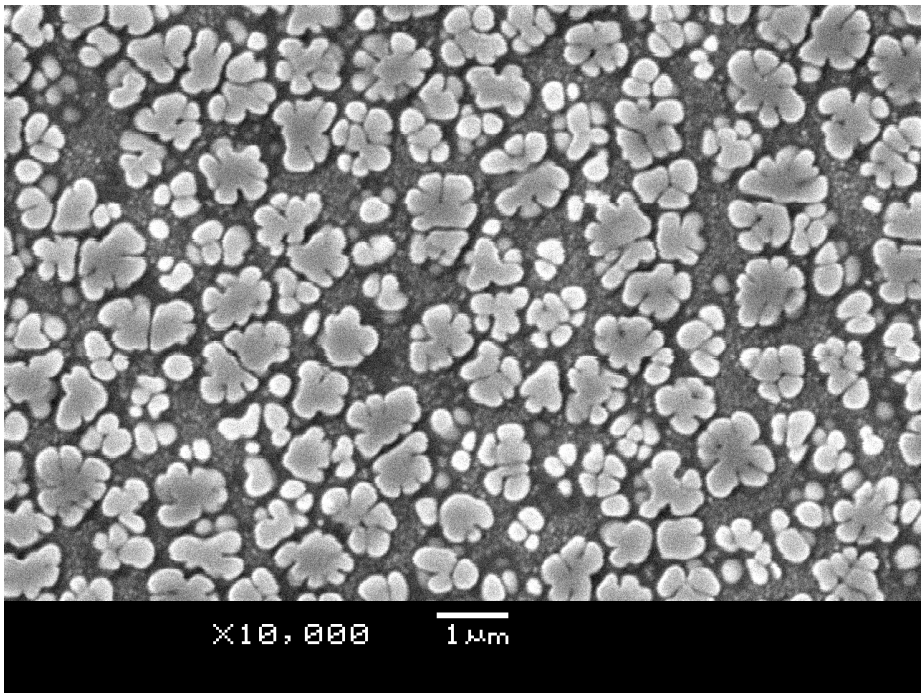

Figure 120 SEM image of RR1000 specimen R6; 1150˚C solution, 0.083˚C/sec cool, 845˚C hold.

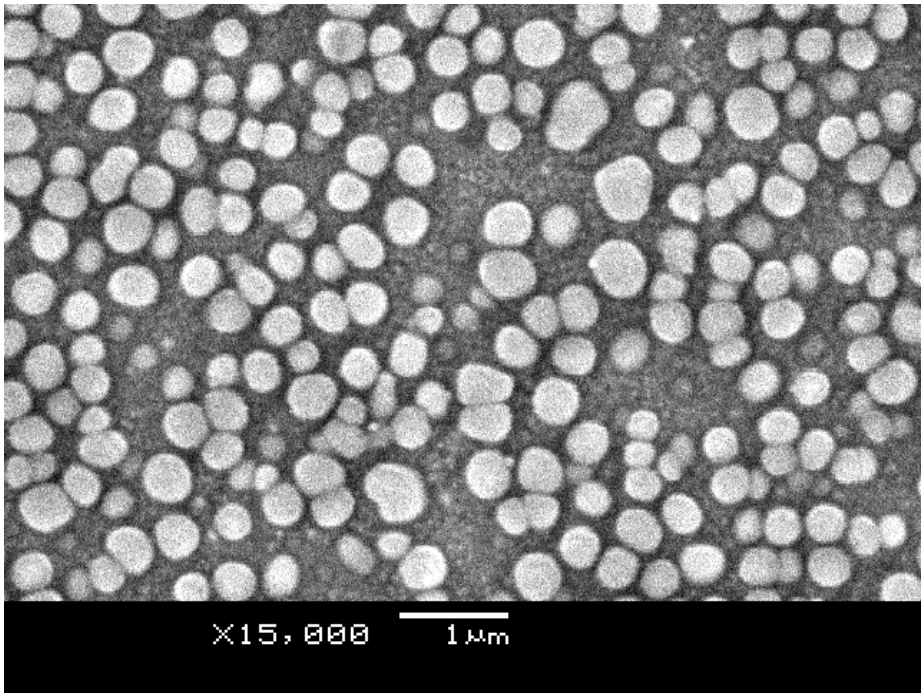

Figure 121 SEM image of RR1000 specimen R7; 1165˚C solution, 0.75˚C/sec cool, 1040˚C hold.

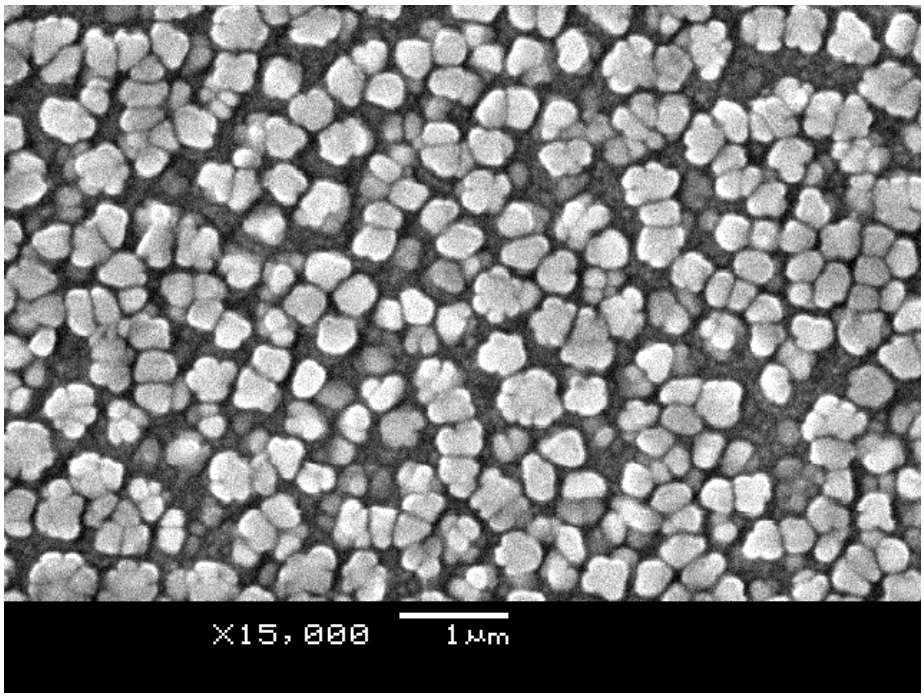

Figure 122 SEM image of RR1000 specimen R8; 1165˚C solution, 0.75˚C/sec cool, 845˚C hold.

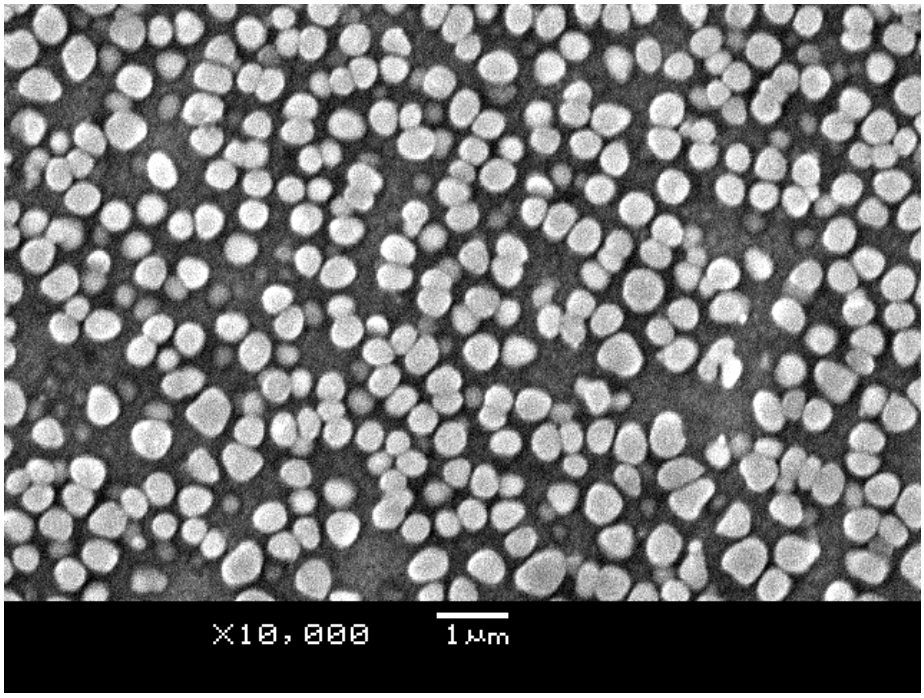

Figure 123 SEM image of RR1000 specimen R9; 1165˚C solution, 0.417˚C/sec cool, 1040˚C hold.

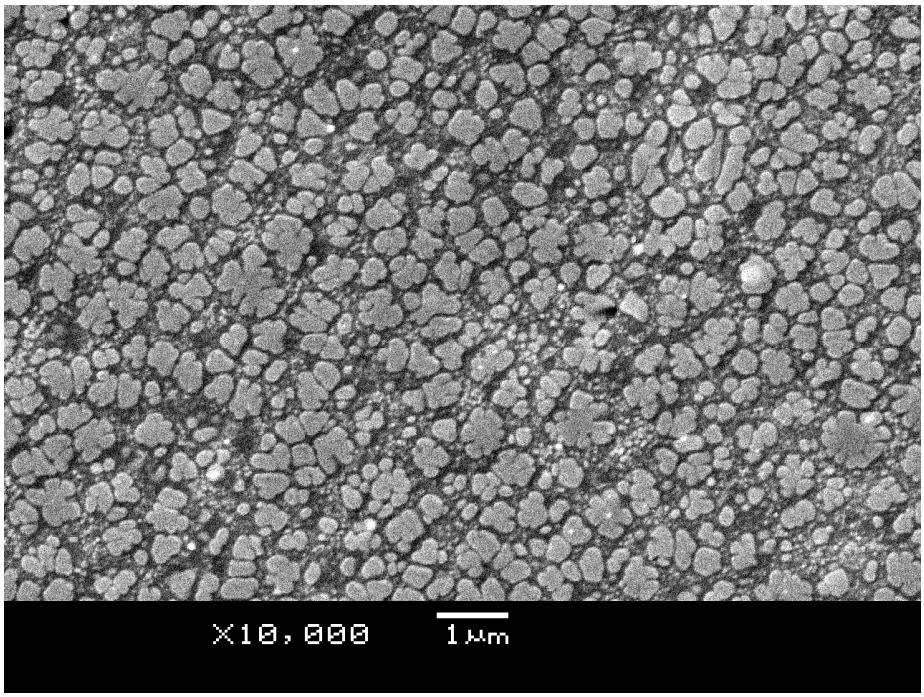

Figure 124 SEM image of RR1000 specimen R10; 1165˚C solution, 0.417˚C/sec cool, 845˚C hold.

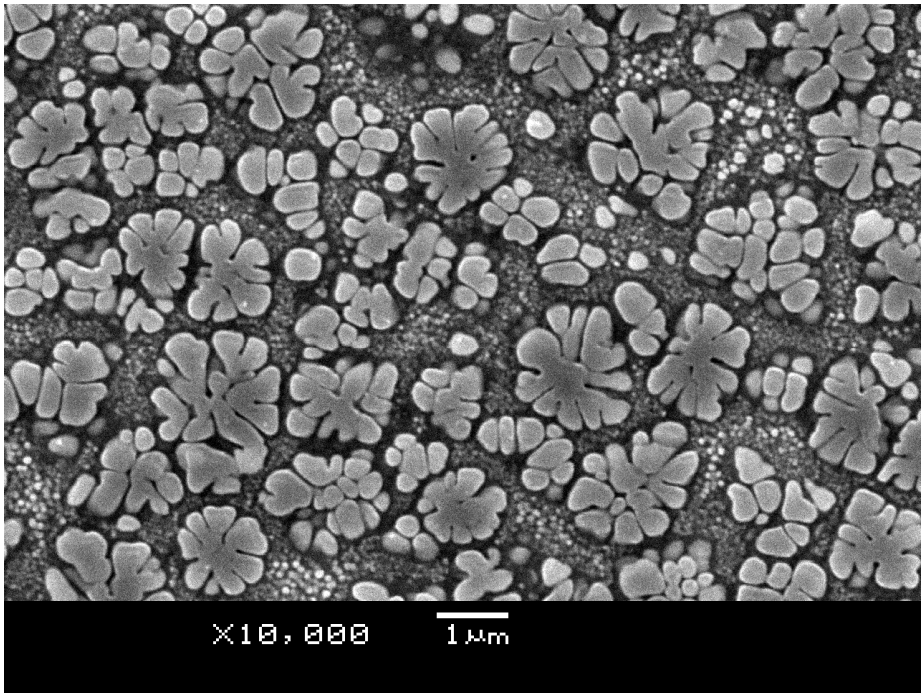

Figure 125 SEM image of RR1000 specimen R11; 1165˚C solution, 0.083˚C/sec cool, 845˚C hold.

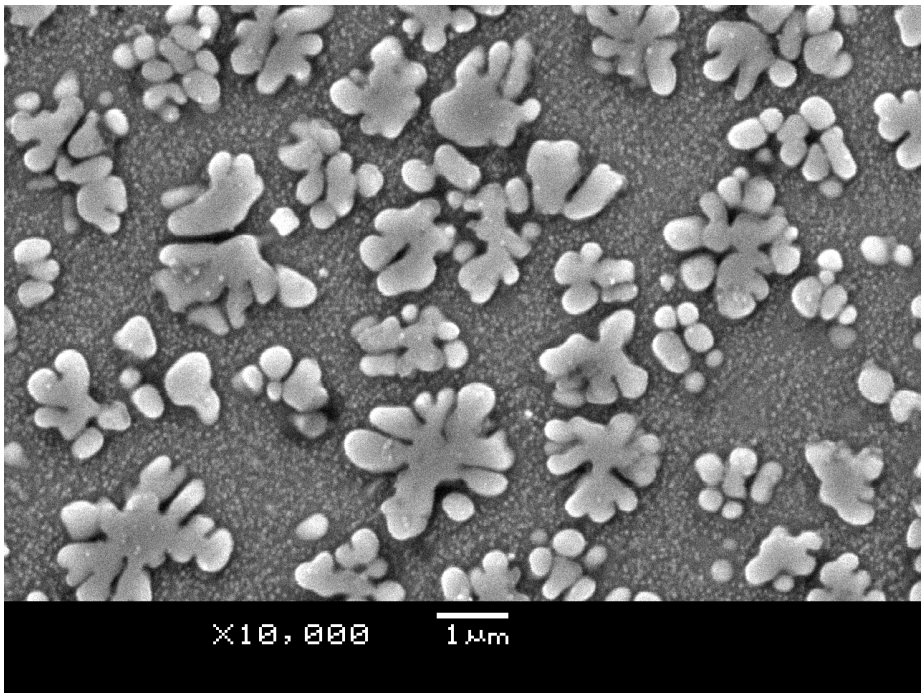

Figure 126 SEM image of RR1000 specimen R12; 1165˚C solution, 0.083˚C/sec cool, 1040˚C hold.

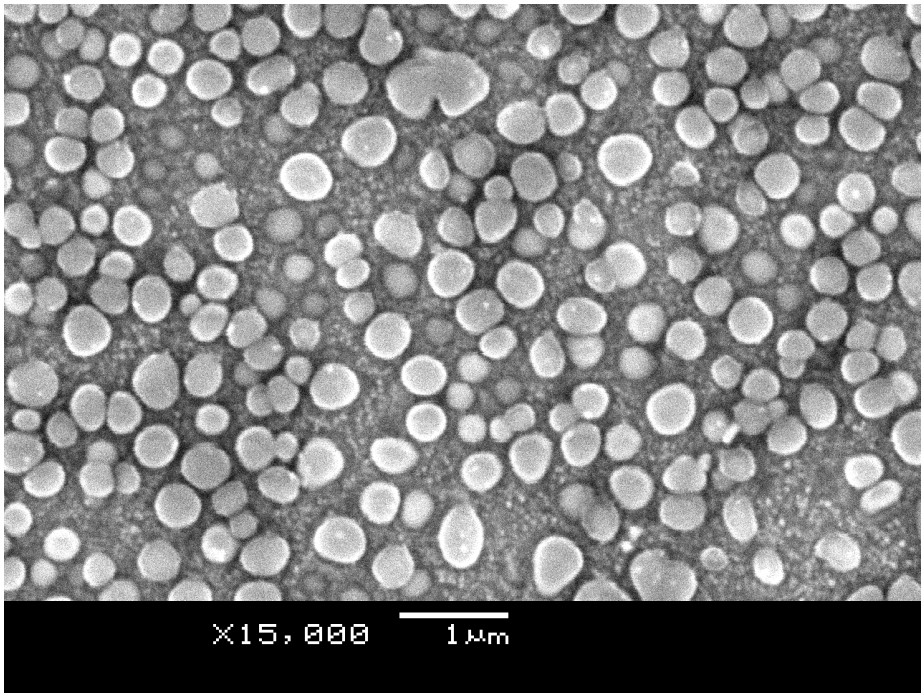

Figure 127 SEM image of RR1000 specimen R13; 1182˚C solution, 0.75˚C/sec cool, 1040˚C hold.

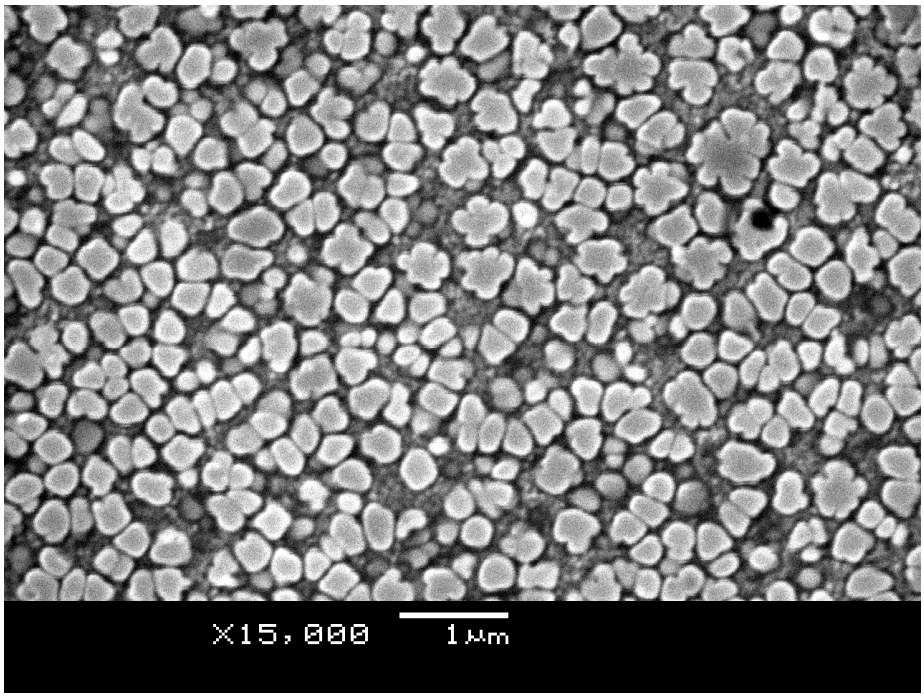

Figure 128 SEM image of RR1000 specimen R14; 1182˚C solution, 0.75˚C/sec cool, 845˚C hold.

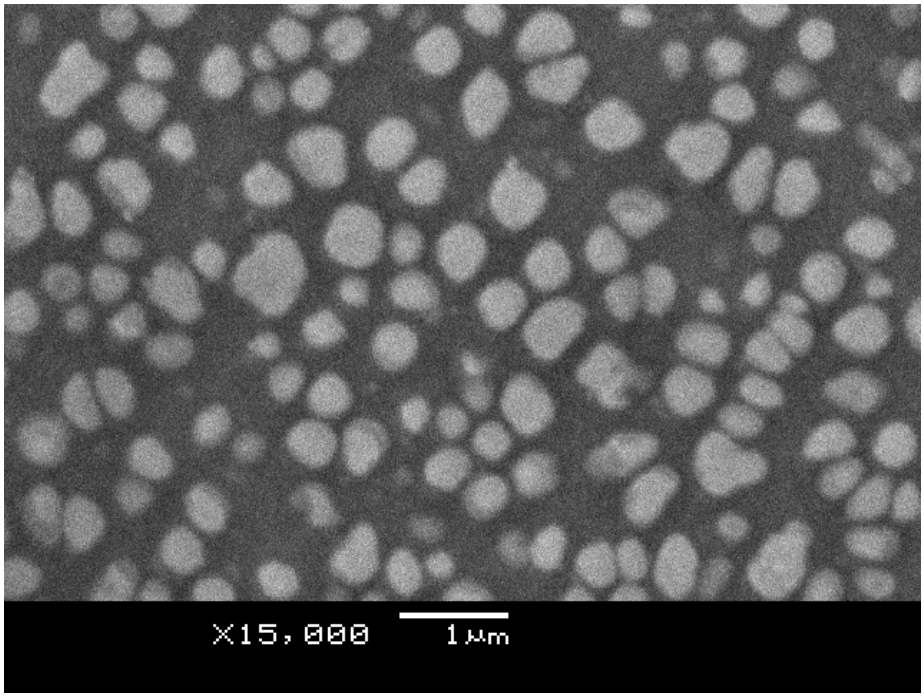

Figure 129 SEM image of RR1000 specimen R15; 1182˚C solution, 0.417˚C/sec cool, 1040˚C hold.

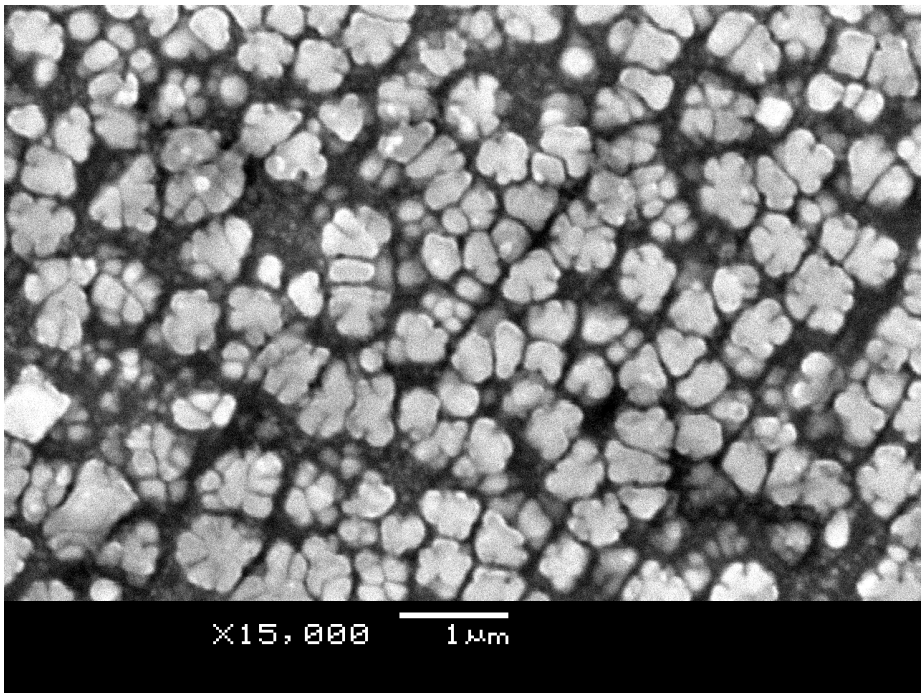

Figure 130 SEM image of RR1000 specimen R16; 1182˚C solution, 0.417˚C/sec cool, 845˚C hold.

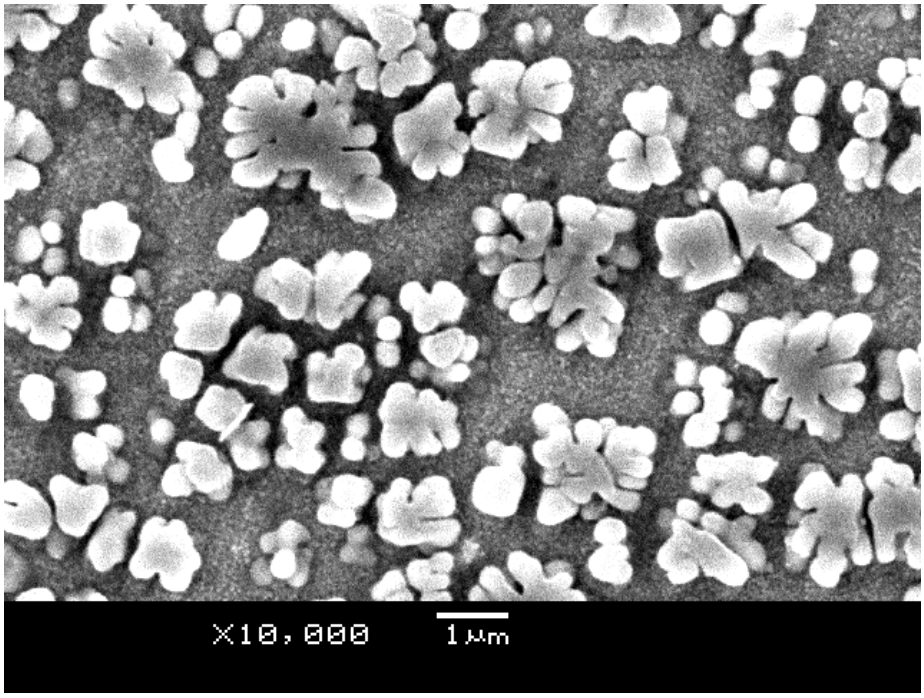

Figure 131 SEM image of RR1000 specimen R17; 1182˚C solution, 0.083˚C/sec cool, 1040˚C hold.

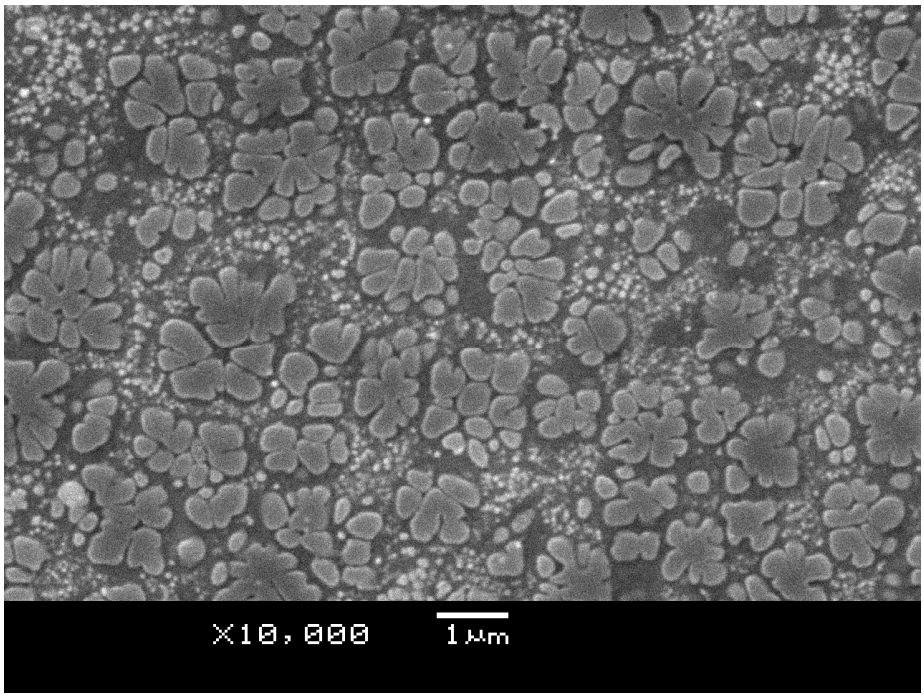

Figure 132 SEM image of RR1000 specimen R18; 1182˚C solution, 0.083˚C/sec cool, 845˚C hold.

APPENDIX B

LSHR Creep Deformation Curves

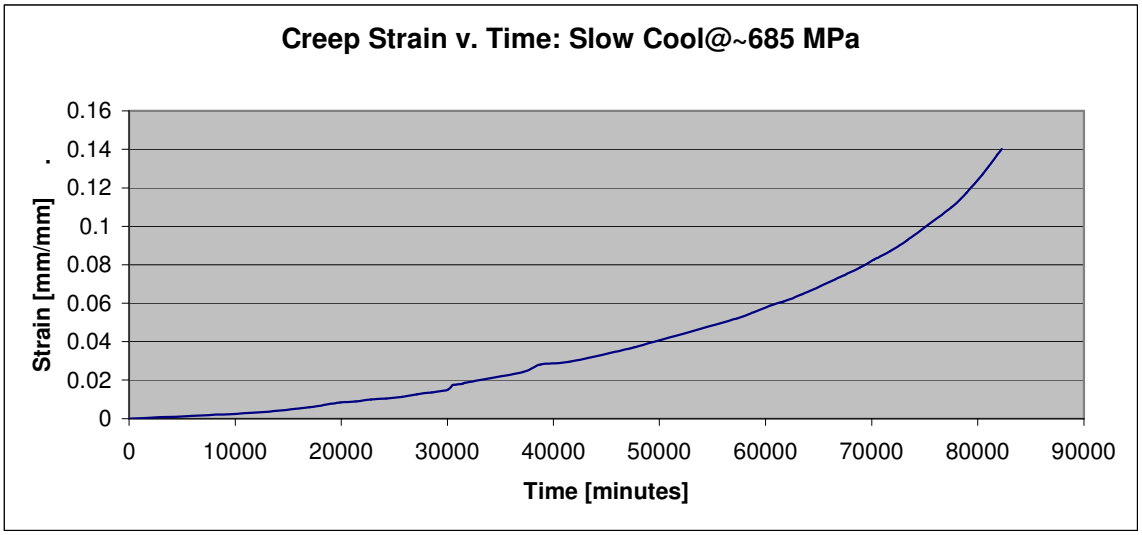

Figure 133 Creep strain versus time for LSHR Specimen M3.

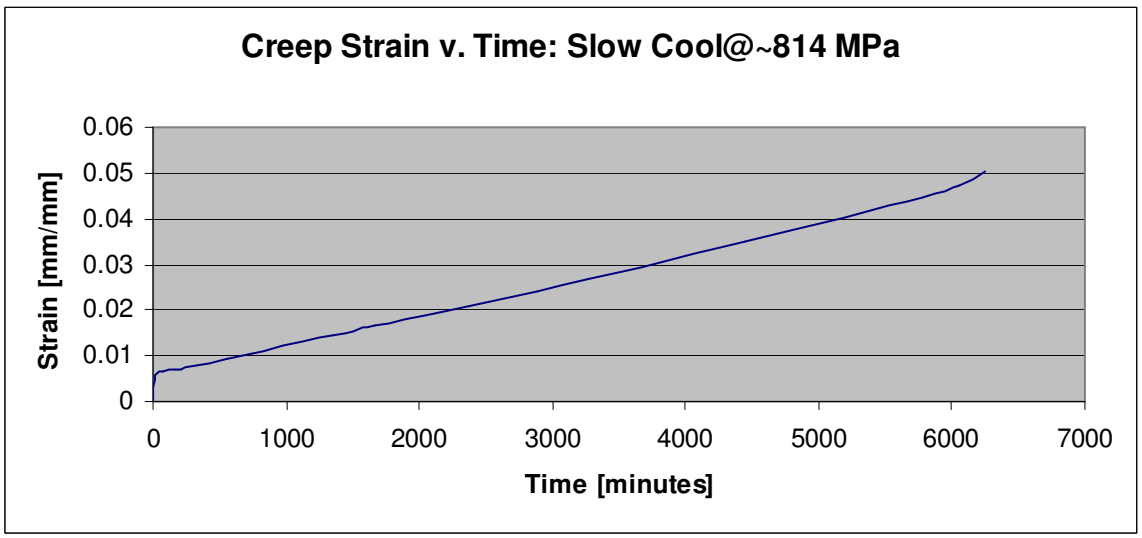

Figure 134 Creep strain versus time for LSHR Specimen B6.

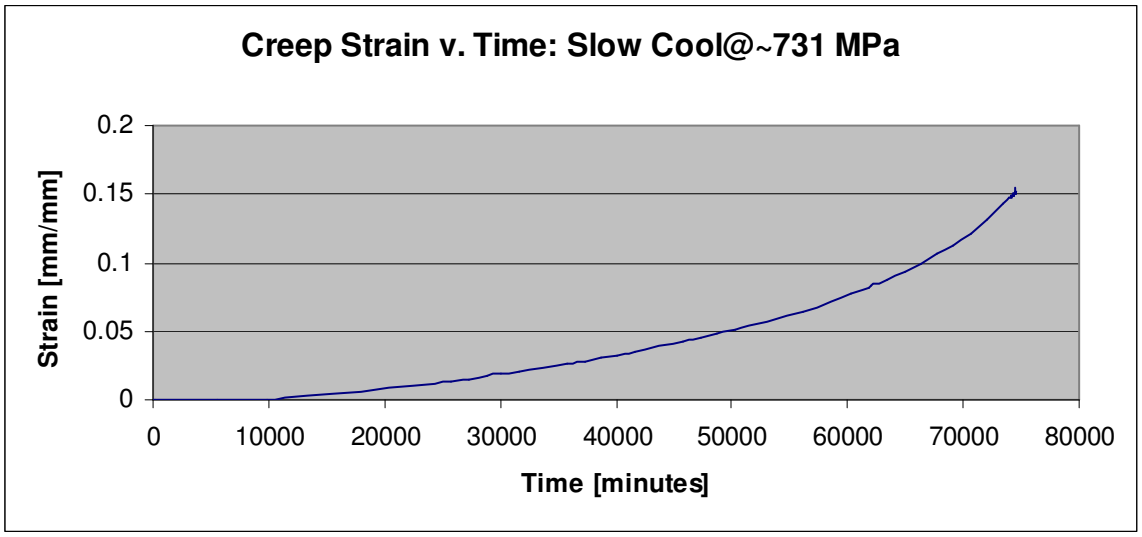

Figure 135 Creep strain versus time for LSHR SpecimenT2.

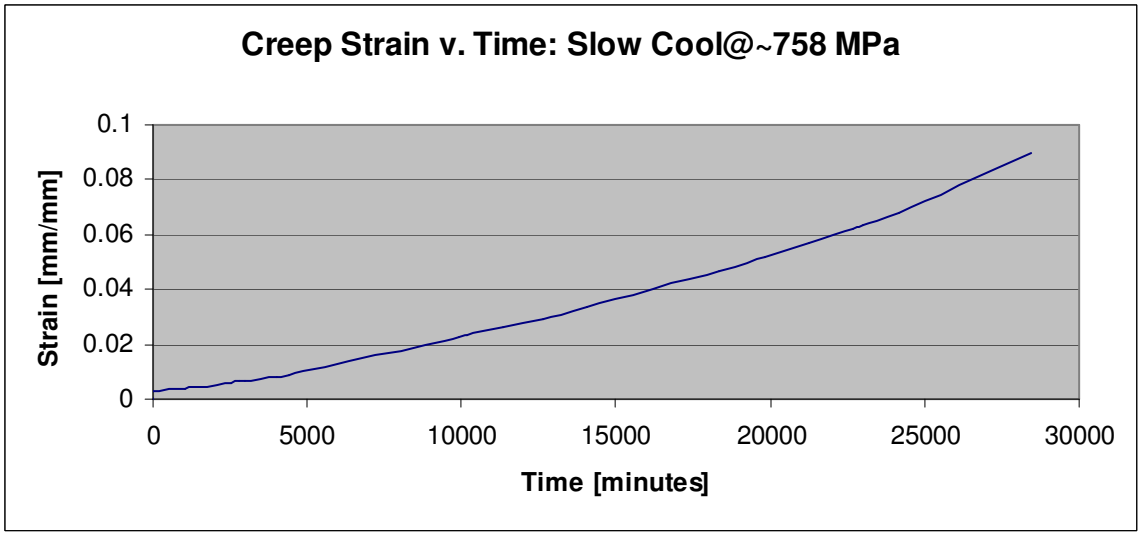

Figure 136 Creep strain versus time for LSHR Specimen M2.

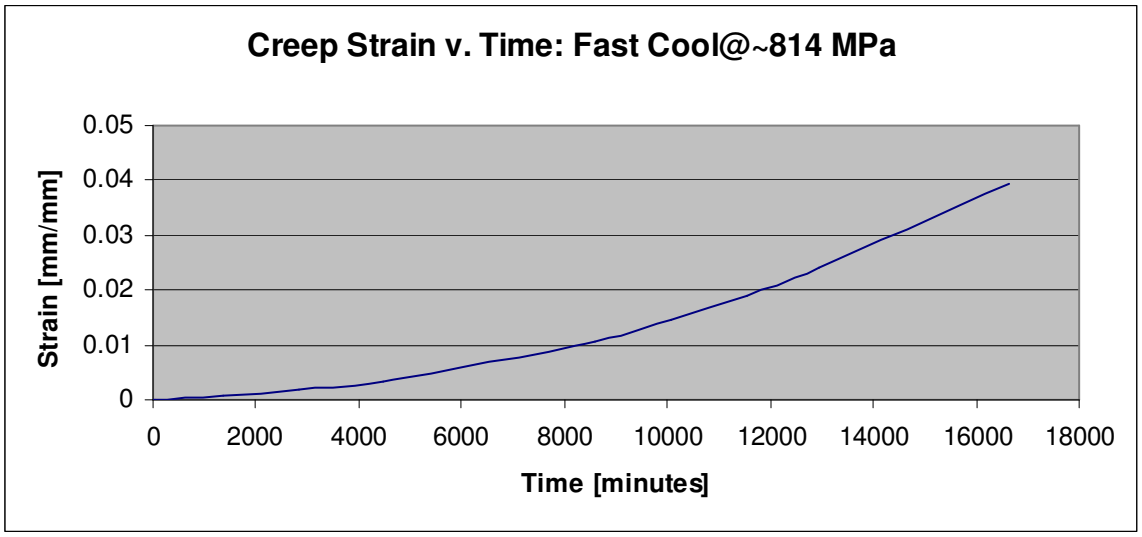

Figure 137 Creep strain versus time for LSHR Specimen T6.

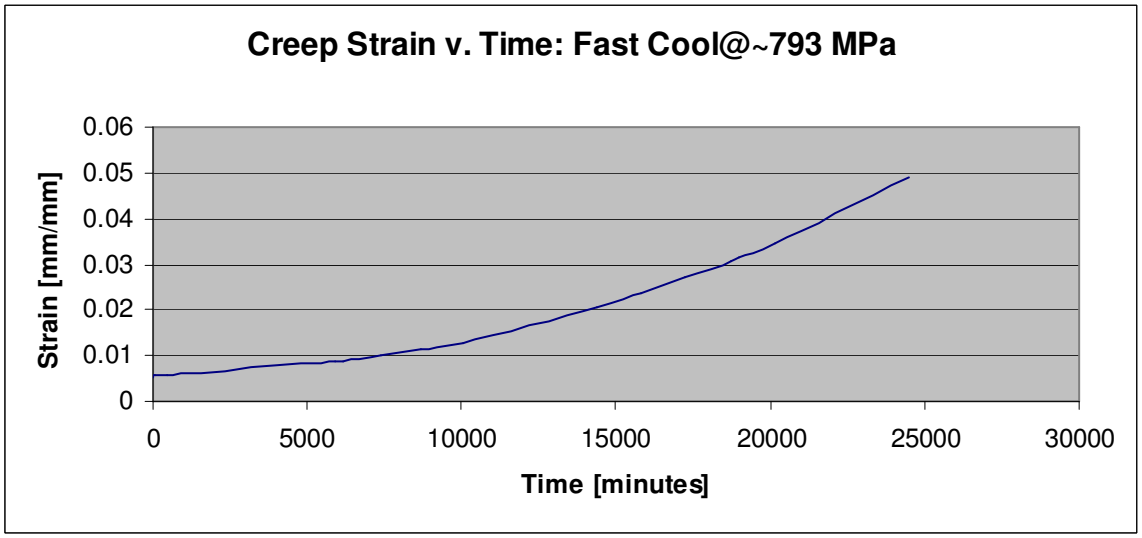

Figure 138 Creep strain versus time for LSHR Specimen M6.

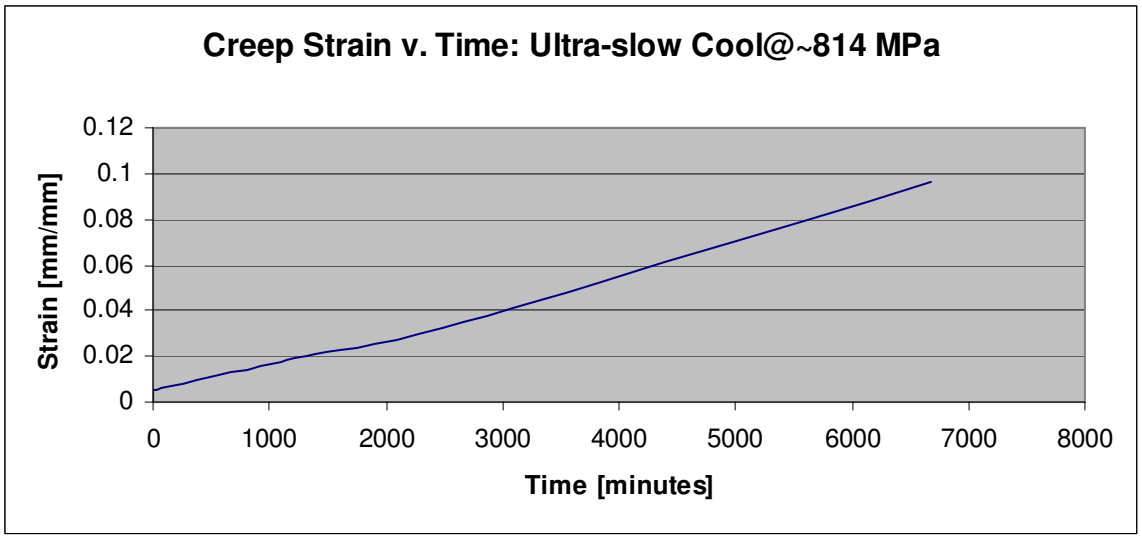

Figure 139 Creep strain versus time for LSHR Specimen B5.

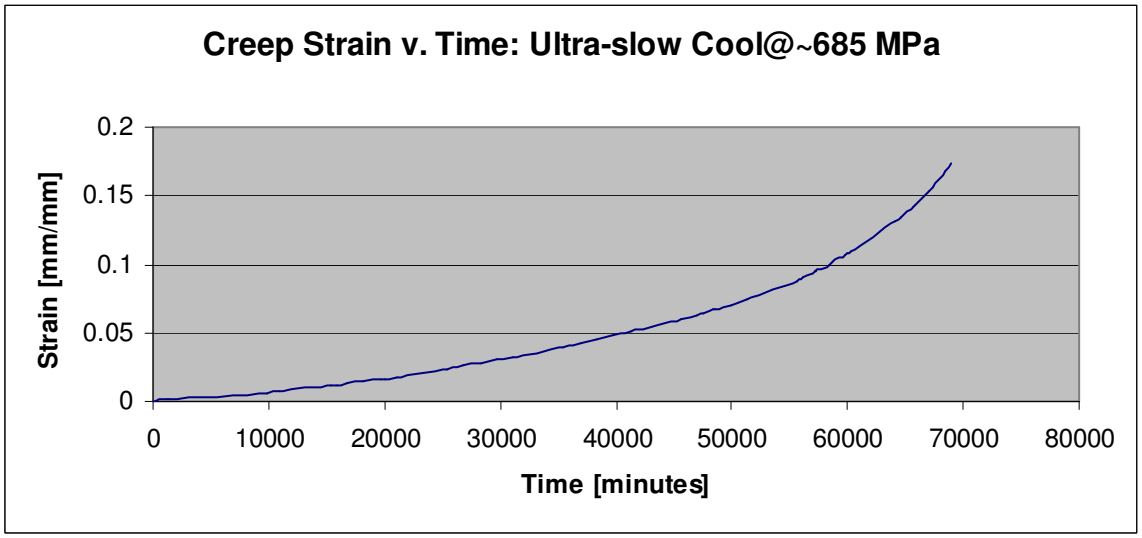

Figure 140 Creep strain versus time for LSHR Specimen T5.

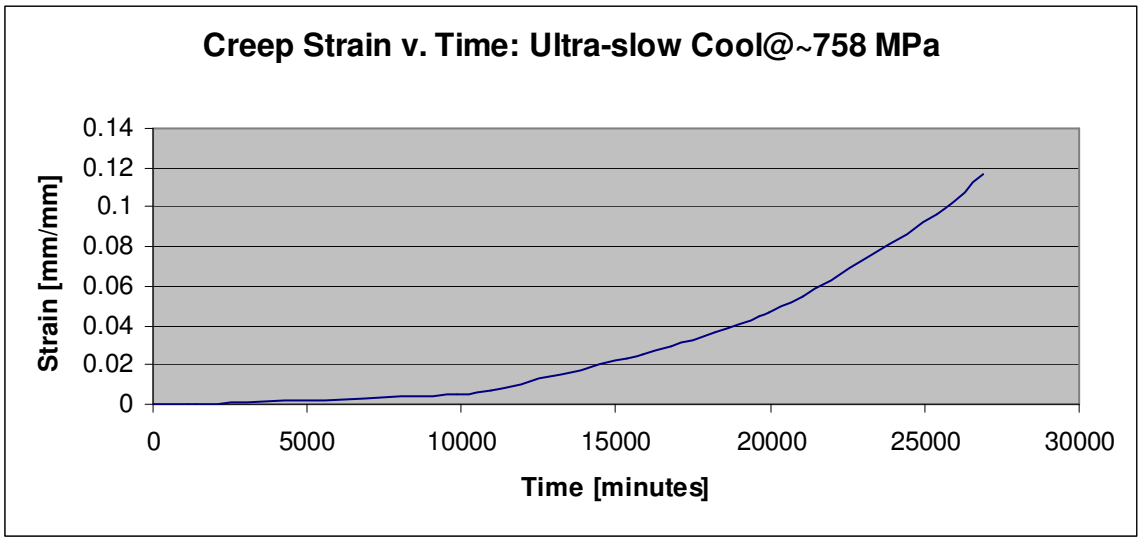

Figure 141 Creep strain versus time for LSHR Specimen M5.

REFERENCES

[1] M. Durand-Charre, The Microstructure of Superalloys, Gordon and Breach Science Publishers, 1997.

[2] *Airplane Flying Handbook*. U.S. Government Printing Office, Washington D.C.: U.S. Federal Aviation Administration. FAA-8083-3A. 2004.

[3] D. Mukherji, S. Piegert, J. Rosler, *Materials Science Forums*, **426-432**, p. 815-820, 2003.

[4] S. Reichman, D.S. Chang, "Powder Metallurgy," Superalloys II. Ed. C.T. Sims et al. John Wiley & Sons, 1987.

[5] T. Gabb, J. Gayda, J. Telesman, P. Kantzos, W. Konkel, "Realistic Subscale Evaluations of the Mechanical Properties of Advanced Disk Superalloys". NASA T/M 2003-212086, 2003.

[6] T. Gabb, J. Gayda, J. Falsey, "Forging of Advanced Disk Alloy LSHR". NASA T/M 2005-213649, 2005.

[7] T. Gabb, J. Gayda, J. Telesman, P. Kantzos, "Thermal and Mechanical Property Characterization of the Advanced Disk Alloy LSHR". NASA T/M 2005-213645, 2005.

[8] Rolls-Royce plc internal memo, 2005.

[9] M.C.Hardy, B. Zirbel, G. Shen, R. Shankar, " Developing Damage Tolerance and Creep Resistance in a High Strength Nickel Alloy for Disc Applications," Superalloys 2004, ed. K.A. Green et al., TMS, 2004.

[10] J. Telesman, P. Kantzos, J.Gayda, P.J. Bonacuse, A. Prescenzi, "Microstructural Variables Controlling Time-dependent Crack Growth in a P/M Superalloy," Superalloys 2004, ed. K.A. Green et al., TMS, 2004.

[11] J. Gayda, "Alloy10: A 1300F Disc Alloy". NASA T/M 200-210358, 2000.

[12] D.U. Furrer, "Review of U720LI Alloy and Process Development," Materials Design Approaches and Experiencs, ed. J.C. Zhao et al., TMS, 2001.

[13] E.O. Hall, *Proceedings of the Physical Society of London*, **643**, p. 747, 1951.

[14] N.J. Petch, *Journal of Iron Steel Institute of London*, **173**, p. 25, 1953.

[15] J. C. M. Li *Transactions of the Metallurgical Soc*iety *AIME*, **227**, p. 239-247, 1963.

[16] M. Chang, A.K.Koul, C. Cooper, "Damage Tolerance of P/M Turbine Disc Materials," Superalloys 1996, ed. R.D. Kissenger, et al.,TMS, 1996.

[17] N.S. Stoloff, "Fundamentals of Strengthening," Superalloys II. Ed. C.T. Sims et al. John Wiley & Sons, 1987.

[18] J. Mao, K. Chang, W. Yang, D. Furrer, K. Ray, S. Vaze, *Materials Science and Engineering A*, **332**, p. 318-329, 2002.

[19] J. Radavich, T. Carneiro, D. Furrer, J. Lemsky, A. Banik, Unpublished results.

[20] J. Schirra, P.L. Reynolds, E. Huron, K. Bain, D. Mourer, "Effect of Microstructure and Heat Treatment on the 649C Properties of Advanced P/M Superalloy Disc Materials," Superalloys 2004, ed. K.A. Green et al., TMS, 2004.

[21] D. Furrer, H. Fecht, "Microstructure and Mechanical Property Development in Superalloy U720LI," Superalloys 2000, ed. T.M. Pollack et al., TMS, 2000.

[22] H.L. Danflou, M. Macia, T.H. Sanders, T. Khan, "Mechanisms of Formation of Serrated Grain Boundaries in Nickel Base Superalloys," Superalloys 1996, ed. R.D. Kissenger, et al., TMS, 1996.

[23] H. L. Danflou, M. Marty, A. Walder, "Formation of serrated Grain Boundaries and Their Effect on Mechanical Properties in a P/M Nickel Base Superalloy," Superalloys 1992, ed. S.D. Antolovich et al., TMS, 1992.

[24] G. Dieter, Mechanical Metallurgy, McGraw-Hill Book Co., 1986.

[25] G.F. Vander Voort, Metallography: Principles and Practice, McGraw-Hill Inc., 1984.

[26] G. Sharma, R.V. Ramanujan, T.R.G. Kutty, G.P. Tiwari, *Materials Science & Engineering A*, **278**, p. 106-112, 2000.

[27] R.S. Sunder, T.R.G. Kutty, D.H. Sastry, *Intermetallics*, **8**, p. 427-437, 2000.

[28] J.H.Westbrook, *Transactions of the American Society of Metallurgy*, **45**, p. 221, 1953.

[29] H. K.D.H. Bhadeshia *ISIJ International*, **39**, p. 966-979, 1999.

[30] R.P. Cherian, L.N. Smith, P.S. Midha, *Artifical Intelligence in Engineering*, **14**, p. 39-44, 2000.

[31] D.J.C. MacKay *Neural Computation*, **4**, p. 415-447, 1992.

[32] D.J.C. MacKay *Neural Computation*, **4**, p. 448-472, 1992.

[33] M.A. Yescas *Int. J. Cast Metals Res.*, **15**, p. 513-521, 2003.

[34] H. Fujii, D.J.C. MacKay, H.K.D.H. Bhadeshia, *ISIJ Internatinal*, **36**, p. 1373-1382, 1996.

[35] ASTM Standard E112, ASTM International, 2004.

[36] ASTM Standard E930, ASTM International, 1999.

[37] ASTM Standard E8, ASTM International, 2004.

[38] ASTM Standard E92-82, ASTM International, 2003.

[39] ASTM Standard E139-00, ASTM International, 2000.

[40] ASTM Standard E1457, ASTM International, 2000.

[41] T.Cool, H.K.D.H. Bhadeshia, D.J.C. MacKay, *Materials Science & Engineering A* **223**, p. 186-200, 1997.

[42] E. Maurer, W. Castledine, F.A. Schweizer, S. Mancuso, "Development of HIP consolidated P/M Superalloys for Conventional Forging to Gas Turbine Engine Components," Superalloys 1996, ed. R.D. Kissenger, et al.,TMS, 1996.

[43] J. Mao, K. Chang, D. Furrer, "Growth Kinetics of γ' Precipitates in P/M Superalloys," Materials Design Approaches and Experiencs, ed. J.C. Zhao et al., TMS, 2001.

[44] T. Courtney, Mechanical Behavior of Materials, McGraw-Hill, 1990.

[45] A.M. Gokhale and E.E. Underwood, *Metallurgical Transactions - A*, **21A**, p. 1193-1199, 1990.

[46]A.M. Gokhale and W.J. Drury, *Metallurgical Transactions - A*, **21A**, p. 1201-1207, 1990.